

In compliance with the
Canadian Privacy Legislation
some supporting forms
may have been removed from
this dissertation.

While these forms may be included
in the document page count,
their removal does not represent
any loss of content from the dissertation.

University of Alberta

Computational Analysis of Digital Chest Radiography

by

Alexander Lun Chor Kwan



A thesis submitted to the Faculty of Graduate Studies and Research in partial fulfillment
of the requirements for the degree of Doctor of Philosophy

in

Medical Physics

Department of Physics

Edmonton, Alberta

Fall, 2003



National Library
of Canada

Bibliothèque nationale
du Canada

Acquisitions and
Bibliographic Services

Acquisitons et
services bibliographiques

395 Wellington Street
Ottawa ON K1A 0N4
Canada

395, rue Wellington
Ottawa ON K1A 0N4
Canada

Your file *Votre référence*
ISBN: 0-612-88006-0
Our file *Notre référence*
ISBN: 0-612-88006-0

The author has granted a non-exclusive licence allowing the National Library of Canada to reproduce, loan, distribute or sell copies of this thesis in microform, paper or electronic formats.

L'auteur a accordé une licence non exclusive permettant à la Bibliothèque nationale du Canada de reproduire, prêter, distribuer ou vendre des copies de cette thèse sous la forme de microfiche/film, de reproduction sur papier ou sur format électronique.

The author retains ownership of the copyright in this thesis. Neither the thesis nor substantial extracts from it may be printed or otherwise reproduced without the author's permission.

L'auteur conserve la propriété du droit d'auteur qui protège cette thèse. Ni la thèse ni des extraits substantiels de celle-ci ne doivent être imprimés ou autrement reproduits sans son autorisation.

Canada

University of Alberta
Library Release Form

Name of Author: Alexander Lun Chor Kwan

Title of Thesis: Computational Analysis of Digital Chest Radiography

Degree: Doctor of Philosophy

Year this Degree Granted: 2003

Permission is hereby granted to the University of Alberta Library to reproduce single copies of this thesis and to lend or sell such copies for private, scholarly or scientific research purposes only.

The author reserves all other publication and other rights in association with the copyright in the thesis, and except as herein before provided, neither the thesis nor any substantial portion thereof may be printed or otherwise reproduced in any material form whatever without the author's prior written permission.

Dated: May 26th, 2003.

University of Alberta

Faculty of Graduate Studies and Research

The undersigned certify that they have read, and recommend to the Faculty of Graduate Studies and Research for acceptance, a thesis entitled **Computational Analysis of Digital Chest Radiography** submitted by Alexander Lun Chor Kwan in partial fulfillment of the requirements for the degree of Doctor of Philosophy in Medical Physics.

Dr. J.A. Seibert (External Examiner)

Dated: 16 May, 2003

To Ada... for everything.

“Just as even the ablest professional baseball player cannot expect to get a hit much more often than one out of every three times he comes to bat, so a sizable number of research projects, governed merely by the law of averages, are bound to produce nothing profitable at all.”

Philip A. Fisher

Abstract

Studies have shown that a large percentage of malignant lung nodules detected on chest radiographs are overlooked on previous examination(s). One of the causes for this higher error rate is the superimposition of anatomic structures such as ribs and soft tissues, which obstruct the true visual examination of the underlying soft tissue in the radiographs. Therefore, the dual-energy subtraction method is developed to numerically remove the bone from digital chest radiograph, thus improving diagnostic capabilities.

The dual-energy subtraction technique is based on the fact that the attenuation of x-rays is different for different materials (bone versus soft tissues) and different x-ray energies. Hence with images from two different energy levels, one should be able to compute the thickness of the bone and eliminate them from the original image(s) numerically. A number of studies have demonstrated the feasibility of this technique; however, all of these works are based on the global subtraction method. Hence, the signal-to-noise ratio (SNR) in the inter-rib regions of the subtracted images is reduced, which leads to a reduction in the diagnostic capability of the chest radiographs in these regions.

The purpose of this research is to improve the current dual-energy subtraction method by enhancing (or at least maintaining) the diagnostic capability of the whole digital chest radiograph. Our method is a pseudo global/localization approach, achieved by subtracting only the chest regions that are obstructed by the bone structures. The procedures involved can be summarized into the following steps:

1. Decompose the dual energy images into soft-tissue and bone-only images by employing the traditional global subtraction technique.
2. Identify the rib structures by locating the upper and lower rib edges utilizing the bone-only image computed in Step #1.
3. Numerically remove the rib structures identified in step #2 from the original radiograph(s) by utilizing the rib thickness information calculated in Step #1.

Step #1 is required because the soft tissues in the images are hindering the detection procedure. Also, a new bone equivalent material (consisting of polyvinyl chloride and aluminum) and a soft tissue mimicking material (consisting of water and Lucite) have also been examined in an attempt to offer better approximations for the dual-energy subtraction techniques. Based on the experimental results, the current approach is a good starting point for the identification of bone structure in a digital chest radiograph. It is a good starting point because it uses a unique combination of image enhancement tools and edge detection algorithms that together minimize the problems presented by low SNR images. Further improvement of either contrast enhancement and/or edge detection processes will most likely not improve significantly upon the process used here. Improvement will come from either higher detective quantum efficiency image receptors and/or x-ray sources (both in terms of dual energy separation and photon flux). Consequently, additional work will be required before the technique can be confidently incorporated into a clinical dual-energy subtraction algorithm.

Acknowledgements

The completion of this project would not be possible without the help from many individuals. First of all, I would like to express my deepest thanks and appreciation to Dr. Larry J. Filipow for all his supports and suggestions. I would also like to thank Dr. D. Frey and Mr. Eugene Mah at the Medical University of South Carolina for providing the images used in the initial phase of this project. Special thanks is given to Dr. S. Halls at the Cross Cancer Institution for the utilization of the Fuji dual-energy subtraction radiographic system, as well as Mr. D. Bridgeman and Ms. M. Horden for the assistance in the acquisition of the radiographic images. Finally, I would like to thank my Dad for giving me the freedom to pursue my interest, and to my wife Ada for giving me one of the biggest joys of my life – Aiden.

Table of Contents

Chapter 1.	Introduction	1
Chapter 2.	Review of the Dual-Energy Subtraction Technique	8
2.1.	Review of Dual-Energy Radiograph	12
2.1.1.	Fundamentals of X-ray Interactions	13
2.1.2.	Fundamentals of Computed Radiography	15
2.1.3.	Fundamentals of Dual-Energy Radiography	17
2.2.	Review of Dual-Energy Subtraction Algorithms	20
2.3.	Disadvantages of the Global Dual-Energy Subtraction Algorithm	24
Chapter 3.	New Equivalent Materials for the Dual-Energy Decomposition Algorithm	28
3.1.	New Bone Equivalent Material (BEM)	31
3.1.1.	Theoretical Considerations for the new BEM	32
3.1.2.	Experimental Verification of the new BEM	38
3.2.	A Different Soft Tissue Equivalent Material	45
Chapter 4.	Current Approach	49
4.1.	The Canny Edge Detector	51
4.2.	The Yanowitz and Bruckstein Image Segmentation Method	54
4.3.	Binary Operation	57
4.4.	Software	60
Chapter 5.	Results and Discussion	61
5.1.	The Canny Edge Detector	62
5.2.	The Yanowitz and Bruckstein Image Segmentation Method	92
5.3.	Binary operation	103
5.4.	The Bisection Results	111
5.5.	The Reconstructed Image	125

Chapter 6.	Conclusion	133
Chapter 7.	Future Research	137
Chapter 8.	References	143
Appendix I	Fitting of Rib Edges	150
Appendix II	Reverse MUSICA	157
Appendix III	Reading the DICOM File	162
Appendix IV	Digital Chest Phantom	165
Appendix V	Automatic quantitative low contrast analysis of digital chest phantom radiographs	176

List of Figures

1.1.	The Age-Standardized Mortality Rates (SMR) for the Canadian male population.	2
1.2.	The Age-Standardized Mortality Rates (SMR) for the Canadian female population.	3
1.3.	Lung cancer incidence and mortality rate versus tobacco consumption 20 years earlier for the Canadian population.	4
2.1.	Subtraction of dual-energy images utilizing weighting factors.	9
2.2.	Some possible patient movements for sequential dual-energy acquisition.	10
2.3.	A typical 125 kVp X-ray spectrum.	12
2.4.	The photostimulable luminescence process.	16
2.5.	The “sandwich” single-exposure dual-energy acquisition setup.	17
2.6.	The spectra exposing the two different imaging plates.	19
2.7.	An overview of the aluminum/Lucite decomposition technique.	22
2.8.	An overview of the pseudo-global/local subtraction algorithm.	27
3.1.	The ratio of the linear attenuation coefficients of some possible bone equivalent materials with respect to cortical bone.	29
3.2.	Linear attenuation coefficient ratios of some possible tissue equivalent materials with respect to soft tissue.	29
3.3.	The ratio of the linear attenuation coefficient of the proposed bone equivalent materials with respect to bone.	34
3.4.	The ratio of the coherent scattering coefficient of the proposed bone equivalent materials with respect to bone.	34
3.5.	The ratio of the photoelectric absorption coefficient of the proposed bone equivalent materials with respect to bone.	35
3.6.	The ratio of the Compton scattering coefficient of the proposed bone equivalent materials with respect to bone.	35

3.7.	The x-ray spectra exposing the first imaging plate after passing through different bone equivalent materials.	36
3.8.	The x-ray spectra exposing the second imaging plate after passing through different bone equivalent materials.	37
3.9.	The ideal narrow-beam geometry for the experimental determination of the linear attenuation coefficient.	38
3.10.	Pictures of shields used for the attenuation coefficient determination experiment.	40
3.11.	Estimation of the Compton edge and other non-photopeak contributions in the spectra in the bone equivalent material attenuation experiment.	42
3.12.	An illustration of the area in the photopeak used for attenuation calculation.	42
3.13.	The step wedge constructed using aluminum and PVC.	43
3.14.	An illustration of the water block.	45
3.15.	The ratio of the linear attenuation coefficient of the water block with respect to soft tissue.	47
3.16.	The x-ray spectra exposing the two imaging plates after passing through 10 cm of different soft tissue equivalent materials.	48
4.1.	A pair of Prewitt operators used for edge detection.	51
4.2.	The Canny edge detectors.	53
4.3.	The Laplacian operator.	55
4.4.	An illustration of the threshold values for a horizontal profile.	56
4.5.	A 21×21 double-triangular mask for the ranking filter employed to eliminate the missing component in the segmented image due to the noise in the bone-only image.	58
4.6.	A demonstration of the ability of the ranking filter.	59
5.1.	The anthropomorphic chest phantom.	62
5.2.	An illustration of the noise reduction capability of the median filter.	63

5.3.	An illustration of the ideal edges for a section of the phantom radiography.	65
5.4.	An illustration of the locations of the four areas of interest in the anthropomorphic chest phantom image.	67
5.5.	The edge detected image of the anthropomorphic chest phantom employing the Prewitt filter.	68
5.6.	The edge detected image of the anthropomorphic chest phantom employing the Sobel filter.	69
5.7.	The edge detected image of the anthropomorphic chest phantom employing the Laplacian of the Gaussian function.	70
5.8.	The edge detected image of the anthropomorphic chest phantom employing the Canny filter with hysteresis threshold.	71
5.9.	An illustration of the locations of the four areas of interest in the real patient image.	72
5.10.	The edge detected real patient image employing the Prewitt filter.	73
5.11.	The edge detected real patient image employing the Sobel filter.	74
5.12.	The edge detected real patient image employing the Laplacian of the Gaussian function.	75
5.13.	The edge detected real patient image employing the Canny filter with hysteresis threshold.	76
5.14.	The edge detected image of the anthropomorphic chest phantom employing the Canny edge detector with $\sigma = 1$.	79
5.15.	The edge detected image of the anthropomorphic chest phantom employing the Canny edge detector with $\sigma = 3.5$.	80
5.16.	The edge detected image of the anthropomorphic chest phantom employing the Canny edge detector with $\sigma = 7$.	81
5.17.	The edge detected real patient image employing the Canny edge detector with $\sigma = 1$.	82
5.18.	The edge detected real patient image employing the Canny edge detector with $\sigma = 3.5$.	83

5.19.	The edge detected real patient image employing the Canny edge detector with $\sigma=7$.	84
5.20.	The figure of merit of the phantom edge image detected with the Canny edge detector for different sigma values.	85
5.21.	An illustrated of the region of interest for the edge detected image without the shoulder region.	86
5.22.	The edge detected image of the anthropomorphic chest phantom employing the Canny edge detector with $T_h = 0.0065$.	87
5.23.	The edge detected image of the anthropomorphic chest phantom employing the Canny edge detector with $T_h = 0.015625$ (default value).	88
5.24.	The edge detected image of the anthropomorphic chest phantom employing the Canny edge detector with $T_h = 0.025$.	89
5.25.	The figure of merit of the phantom edge image detected with the Canny edge detector using different upper threshold values.	90
5.26.	The figure of merit of the phantom edge image detected with the Canny edge detector using different lower threshold values.	91
5.27.	An illustration of the final solution computed utilizing two different initial guesses.	94
5.28.	An illustration of the enhanced mask.	95
5.29.	The segmented anthropomorphic chest phantom image utilizing the original Laplacian mask.	97
5.30.	The segmented anthropomorphic chest phantom image utilizing the enhanced mask.	98
5.31.	The segmented real patient image utilizing the original Laplacian mask.	99
5.32.	The segmented real patient image utilizing the enhanced mask.	100
5.33.	The difference image, computed by subtracting the Laplacian from the enhanced mask for the anthropomorphic chest phantom.	101
5.34.	The difference image, computed by subtracting the Laplacian from the enhanced mask for the real patient image.	102

5.35.	The segmented anthropomorphic chest phantom image operated with both the dual-triangular mask and dilation procedures.	105
5.36.	The segmented anthropomorphic chest phantom image processed with the dual-triangular mask procedure only.	106
5.37.	The differences between the segmented anthropomorphic chest phantom image processed by a mixture of dual-triangular mask and dilution verses dual-triangular mask alone.	107
5.38.	The segmented real patient image processed with both the dual-triangular mask and dilution procedures.	108
5.39.	The segmented real patient phantom image processed with the dual-triangular mask procedure only.	109
5.40.	The differences between the segmented real patient phantom image processed by a mixture of dual-triangular mask and dilution verses dual-triangular mask alone.	110
5.41.	The original bone-only phantom image.	113
5.42.	The identified bone structure of Figure 5.41.	114
5.43.	The original bone-only real patient A image.	115
5.44.	The identified bone structure of real patient A.	116
5.45.	The original bone-only real patient B image.	117
5.46.	The identified bone structure of real patient B.	118
5.47.	The original bone-only real patient C image.	119
5.48.	The identified bone structure of real patient C.	120
5.49.	The original bone-only real patient D image.	121
5.50.	The identified bone structure of real patient D.	122
5.51.	The original bone-only real patient E image.	123
5.52.	The identified bone structure of real patient E.	124
5.53.	The reconstructed soft tissue image for patient A.	126

5.54.	The reconstructed soft tissue image for patient B.	127
5.55.	The reconstructed soft tissue image for patient C.	128
5.56.	The reconstructed soft tissue image for patient D.	129
5.57.	The reconstructed soft tissue image for patient E.	130
5.58.	The reconstructed soft tissue image for patient A with a simple gray-level matching.	132
6.1.	The different in the number of non-attenuated photon passing through 15 cm of soft tissue compared with 14 cm of soft tissue plus 1 cm of cortical bone.	135
7.1.	The photon spectrum exposing the second image plate after passing through different filter materials.	138
7.2.	The probability of Compton scattering exposing the second imaging plate resulting from different filter materials.	138
A1.1.	The processed rib edge.	150
A1.2.	Parabolic fitting of the processed rib edge.	151
A1.3.	Power fitting of the processed rib edge.	152
A1.4.	Logarithmic fitting of the processed rib edge.	152
A1.5.	Second order polynomial fitting of the processed rib edge.	153
A1.6.	Fourth order polynomial fitting of the processed rib edge.	153
A1.7.	Parabolic fitting of another processed rib edge.	154
A1.8.	Parabolic and elliptical fitting of another processed rib edge.	155
A1.9.	An illustration of some missing rib edge.	156
A2.1.	Sub-sampling of the filtered image.	157
A2.2.	An illustration of the MUSICA's ability to enhance subtle details.	159
A2.3.	An illustration of the reverse MUSICA's ability to suppress subtle details.	161
A4.1.	The simulated bone structure layer for the digital phantom.	166

A4.2.	The simulated soft tissue layer for the digital phantom.	166
A4.3.	The simulated heart layer for the digital phantom.	167
A4.4.	The simulated abdomen layer for the digital phantom.	167
A4.5.	The simulated wire mesh for the digital phantom.	168
A4.6.	An illustration of the original spectrum and a gaussian noise added spectrum.	169
A4.7.	The reconstructed absorption curve for the CR plate.	170
A4.8.	The digital phantom image.	171
A4.9.	A gray-level histogram of the digital phantom image.	172
A4.10.	The digital phantom image with scattering noise added.	173
A4.11.	The gray-level distribution of the DP image with approximated scattering noise.	174
A4.12.	The gray-level distribution of a real chest radiograph.	175

List of Tables

3.1.	Table of gamma energies of interest and half-lives for the four isotopes used in the experimental verification of the bone equivalent material.	39
3.2.	Distance between isotopes, the “perfect” shield and the detector in the bone equivalent material verification experiment.	39
3.3.	A table of linear attenuation coefficients for theoretical cortical bone, theoretical aluminum versus PVC thickness with mixture ratio of 1:2, and the experimentally measured values of this mixture for the four different isotopes listed in Table 3.1.	43
A2.1.	A demonstration of MUSICA enhancing ability.	158
A2.2.	A demonstration of reverse MUSICA suppression ability.	160

1. Introduction

Lung cancer is one of the leading causes of premature death due to cancers for the population of North America.¹⁻³ In fact, it is expected to account for about 28% of all cancer deaths in the United States¹ and Canada² in 2001. While the mortality rate due to lung cancer has been on the decline for the male population in North America in the last decade, the rate for the female population has been increasing steadily.¹⁻³ These are illustrated in Figs. 1.1 and 1.2 which show the age-standardized mortality rates for different type of cancers for the male and female population in Canada since 1970. This variation in the trends may be associated with the change in the smoking habits of the population, since there is a correlation between smoking and mortality rate due to lung cancer in Canada as illustrated in Fig. 1.3. While smoking has declined steadily since the 1960's for Canadian men aged 15 and over, the decline for the female population did not begin until 15 years later (late 1970's).⁴

So why is lung cancer so deadly? To begin with, lung cancers can be divided into two major groups: small cell lung cancer and non-small cell lung cancer. Small cell lung cancer, which accounts for about 20% of all lung cancer, tends to grow and spread very quickly.¹ As with many other types of cancer, surgical resection is the treatment of choice for lung tumors.^{5,6} However, this technique is limited to localized tumors, and for tumors that have a propensity to spread, such as small cell lung cancer, the only available treatment options are radiation or chemotherapy.⁶ Another reason that may account for the high mortality rate of lung cancer is the fact that the symptoms for early stage lung cancer tend to be nonspecific (such as coughing or chest pain).^{5,7} Consequently, a tumor is generally detected at a later stage and hence incurable.

So, how important is the ability to detect lung tumors at the earliest stage possible? The answer is very important: the earlier a tumor is detected, the more likely it will be localized and resected completely. In fact, the survival probability following the resection of earlier stage lung cancer is significantly higher than the more advanced (non-resectable) stages.^{5,6} This is shown in Melamed et al.'s study⁵, where the survival probability after 5 years for stage 1 resected patient is about 80%, compare to about 5% for stage 3 non-resectable patient.

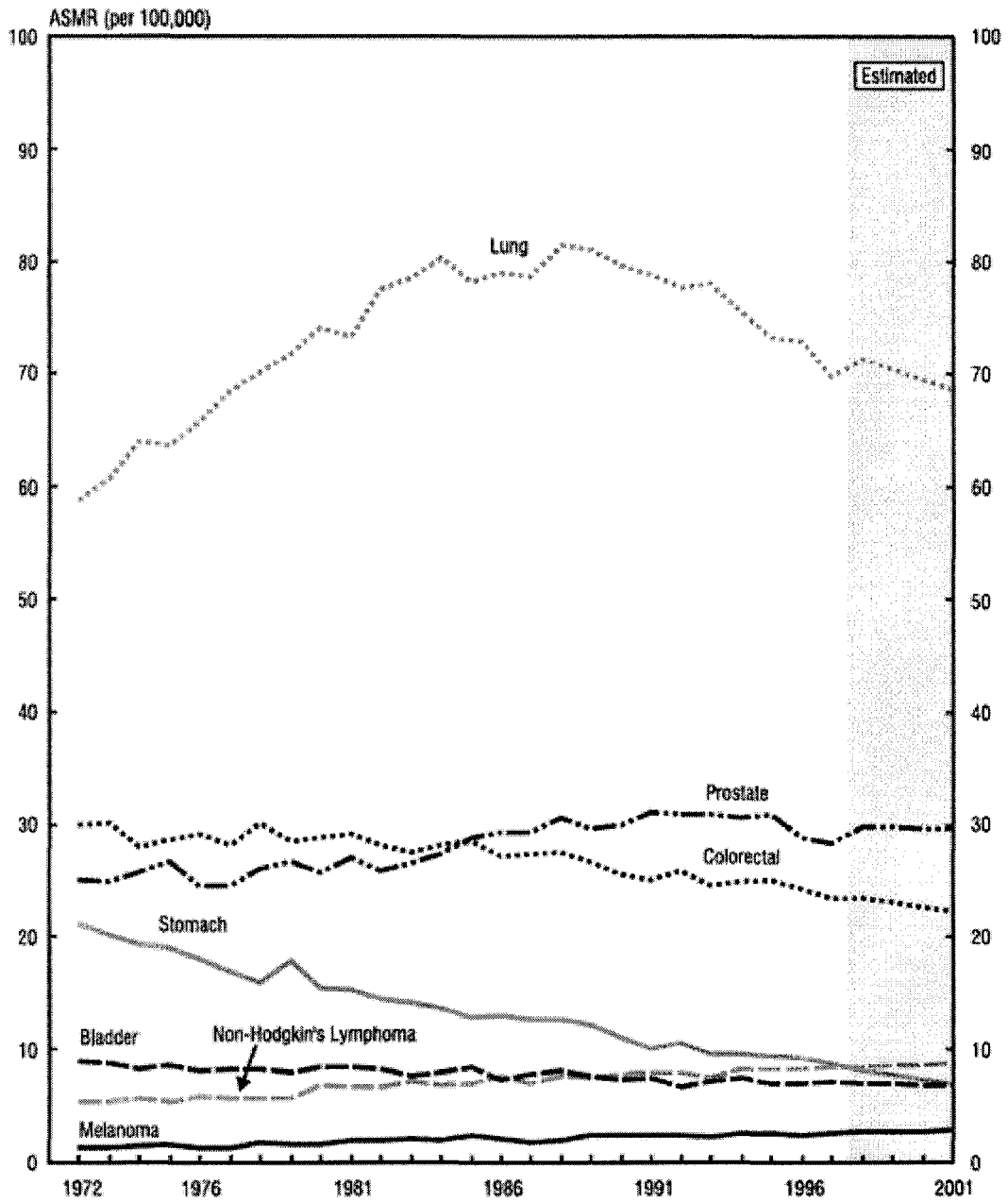


Figure 1.1. The Age-Standardized Mortality Rates (SMR) for the Canadian male population. The Rates are standardized to the age distribution of the 1991 Canadian population. (Reprinted permitted from **Canadian Cancer Statistics 2001²**)

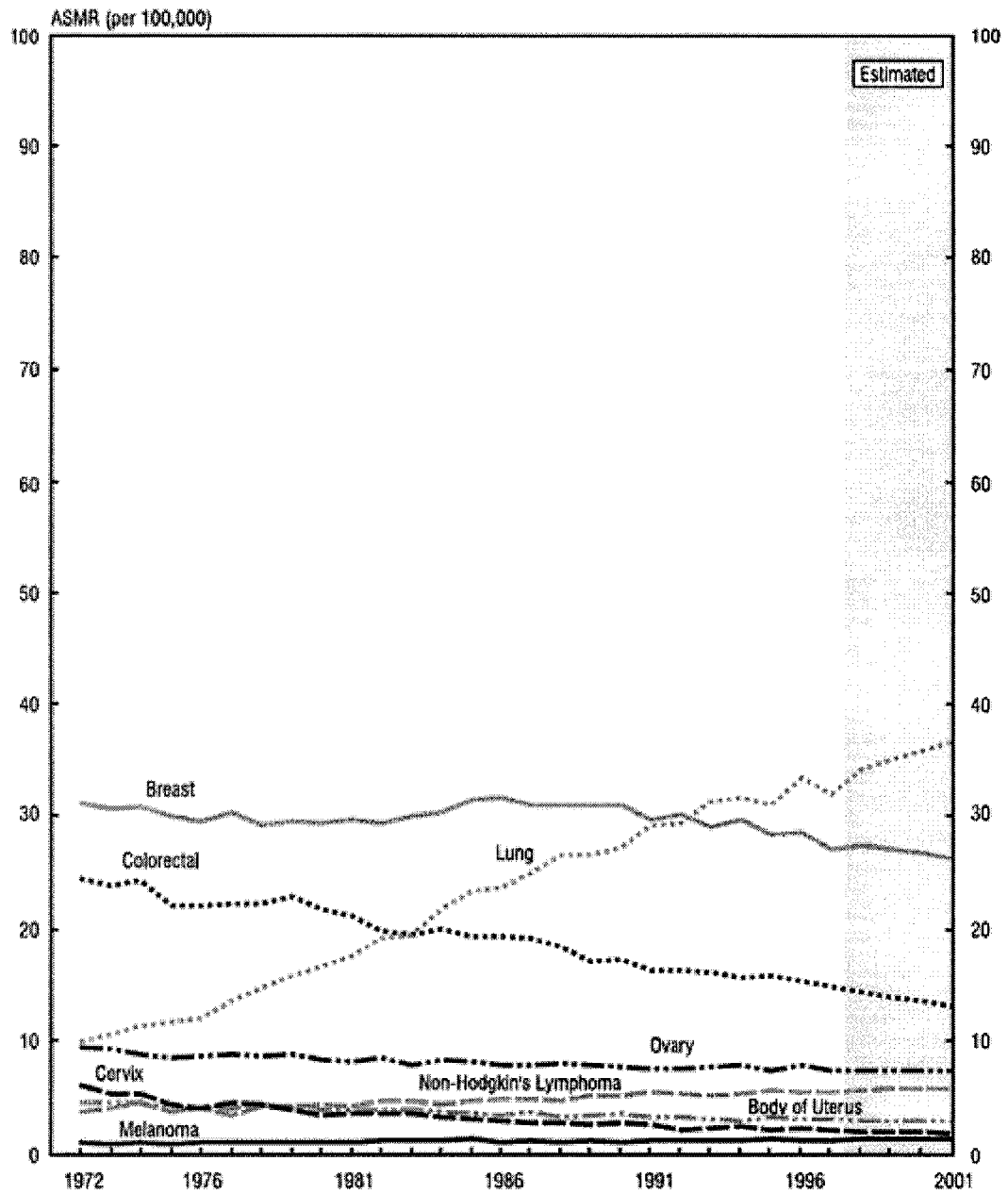


Figure 1.2. The Age-Standardized Mortality Rates (SMR) for the Canadian female population. The Rates are standardized to the age distribution of the 1991 Canadian population. (Reprinted permitted from **Canadian Cancer Statistics 2001**²)

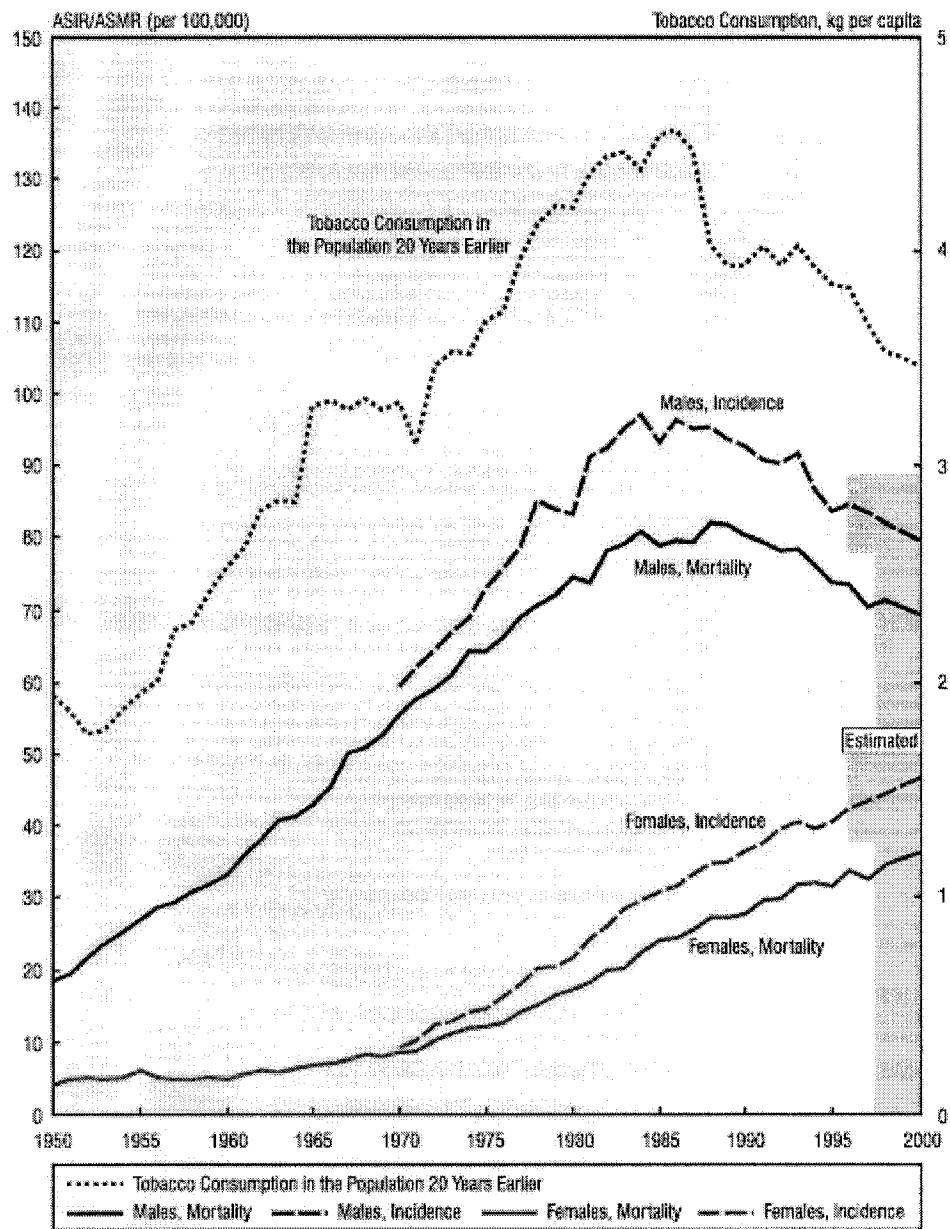


Figure 1.3. Lung cancer incidence and mortality rate versus tobacco consumption 20 years earlier for the Canadian population. The Rates are standardized to the age distribution of the 1991 Canadian population. (Reprinted permitted from **Canadian Cancer Statistics 2000⁴**)

Since early detection is so important for lung tumor, one would expect a regular screening procedure (similar to mammography) would exist. However, this is not the case. Procedures that can confirm the existence of the tumor with a high degree of certainty such as bronchoscopy and needle biopsy are very time consuming. Computerized tomography (CT) scanning tends to have limited access. On top of this, CT scanning is a high radiation modality. Lastly, position emission tomography (PET) scanning is expensive, since it involves the injection of radioactive isotopes (position emitter) into the body. As a result, none of these procedures are suitable for a mass screening procedure, which would potentially need to screen hundreds of thousands of people annually. While a number of studies have examined the feasibility of utilizing chest radiograph(s) for lung cancer screening^{5,6,8-10}, the results are still inconclusive.

One of the reasons that radiographic screening may be ineffective is that a large percentage of malignant lung nodules detectable on chest radiographs are overlooked during examination(s).^{9,11} In fact, the error rate for the detection of early stage lung cancer may be as high as 50%.¹¹ One of the causes for this high error rate is the superimposition of anatomic structures such as ribs and soft tissues, which obstruct the true visual examination of the underlying soft tissue in the radiographs.¹¹⁻¹³ Therefore, technique(s) that can reduce and/or eliminate such superimposition should improve the effectiveness of chest radiography as a screening procedure. One such technique is the dual-energy subtraction method which can numerically remove the ribs from digital chest x-rays, thus improving the diagnostic capabilities of the radiograph.

The dual-energy subtraction method is based on the fact that the attenuation of x-ray photons is both matter (bone versus soft tissues) and energy dependent. Theoretically, therefore, with images from two different energy levels, one should be able to estimate the thickness of the bones and eliminate them from the original image(s) numerically, producing a soft-tissue only image. Conversely, one can also utilize the thickness information and generate a bone only image. A number of studies have demonstrated the feasibility of this technique¹⁴⁻²¹. However, all this work is based on the global subtraction method, which implies that every pixel in the final (displayed) image has been manipulated. Thus, two disadvantages exist: Firstly, any calcified lung nodules will be treated as bone material and will not be displayed on the soft tissue image. The

consequence of this is two images (soft tissue image and bone only image) may have to be viewed to ensure all the nodules are identified, although almost all calcified nodules are considered benign. Secondly, subtraction of images will always increase the noise and reduce the signal-to-noise ratio (SNR) of the final image(s). This pose a concern for the inter-rib (between rib) regions of the chest radiograph since there is no obstruction in these areas and therefore the subtraction will reduce the diagnostic capability of these regions by reducing the SNR with no advantage associated with it.

Purpose of this research is to determine if the bone structure and only the bone structure can be accurately removed from routine dual-energy chest images acquired using current technology and typical clinical setting. If achievable, this will improve the current dual-energy subtraction method by enhancing (or at least maintaining) the diagnostic capability of the whole digital chest radiograph. Our method is a pseudo global/localization approach, achieved by eliminate only the signal due to the bone structure in chest regions. The procedures involved in accomplishing this task can be summarized into the following steps:

1. Decompose the dual-energy images into soft-tissue and bone-only images by employing the traditional global subtraction technique.
2. Identify the rib structures by locating the upper and lower rib edges utilizing the bone-only image computed in step #1.
3. Numerically remove the signal due to the rib structures identified in step #2 from the original radiograph(s) by utilizing the rib thickness information calculated in step #1. An alternative is to replace the rib structures with soft tissue signal to produce a more uniform final image.

Following this introduction, Chapter 2 of this dissertation will review the theory behind radiography and the global dual-energy subtraction method. In Chapter 3, a new bone equivalent material and a different water equivalent material will be introduced to enhance the accuracy of the subtracted results. Chapter 4 presents a detailed discussion of the pseudo global/localization dual-energy subtraction method, while the results of this

new approach will be examined in Chapter 5. Finally, the strength and limitation of this subtraction technique will be discussed in Chapter 6.

2. Review of the Dual-Energy Subtraction Technique

As mentioned in Chapter 1, the dual-energy subtraction method is employed to enhance the diagnostic capabilities of chest radiographs by eliminating the superimposition of anatomic structures such as ribs and soft tissues. This will potentially increase the accuracy for the detection of early stage lung cancer using digital chest radiographs, and may lead to the deployment of digital chest radiography as a cost effective mass screening test for lung tumors.¹⁰

The dual-energy subtraction method is not a new idea. In fact, Kruger et al. had demonstrated the feasibility of this technique by subtracting two analog films exposed using two different x-ray spectra back in 1981.¹⁴ Since these two film-screen pairs have to be hand picked to provide the best tissue suppression and bone isolation, the Kruger's method is very limiting in terms of film-screen selections. Thus, dual-energy subtraction methods did not become viable until the introduction of digital radiography.²²⁻²³

The digital radiographic revolution began with the introduction of film digitizers, which convert the optical density of an analog film into a digital image by examining the amount of light transmitted through a film.²⁴⁻²⁵ The digitizers were soon superseded by computed radiography (CR).²⁶⁻²⁸ In CR, the conventional analog film is replaced by a photostimulable phosphor (PSP) plate. The PSP captures and stores the incident x-ray photons, producing a latent image. This latent image is read by a reader where the PSP is stimulated by the laser to luminesce. The luminescent light is subsequently captured by a photomultiplier tube and converted into a digital image.

Lately, another type of digital radiographic system has been gaining a lot of attention. This system is being referred to as direct radiography (DR).²⁹⁻³⁴ As the name implies, DR systems convert the incident x-ray photons directly into an electrical signal by means of semiconducting materials such as amorphous selenium. The advantage of DR is that it is potentially able to achieve better contrast resolution, or the ability to distinguish different objects with close attenuation properties, when compared to CR.

With digital radiography, the subtraction component of the dual-energy decomposition method is readily achievable. This is because it is much easier to subtract

two numerical values for every pixel in an image than to subtract two analog films. The next few paragraphs will summarize some of the highlights that have occurred so far.

In 1986, Nishitani et al. demonstrated a dual-energy subtraction method that utilized CR.¹⁵ In this method, two images are acquired sequentially at two different x-ray energies. Afterward, each pixel in the images are multiplied individually by a weighting factor which is predetermined from prior experiences, and then subtracted to produce the soft tissue and bone only images using the following¹⁶

$$D = HD_h - LD_l + C, \quad (2.1)$$

where D_l , D_h and D are the digital values of the low energy, high energy and final images respectively. L and H are the weighting factors and C is a constant. These processes are illustrated in Fig. 2.1.

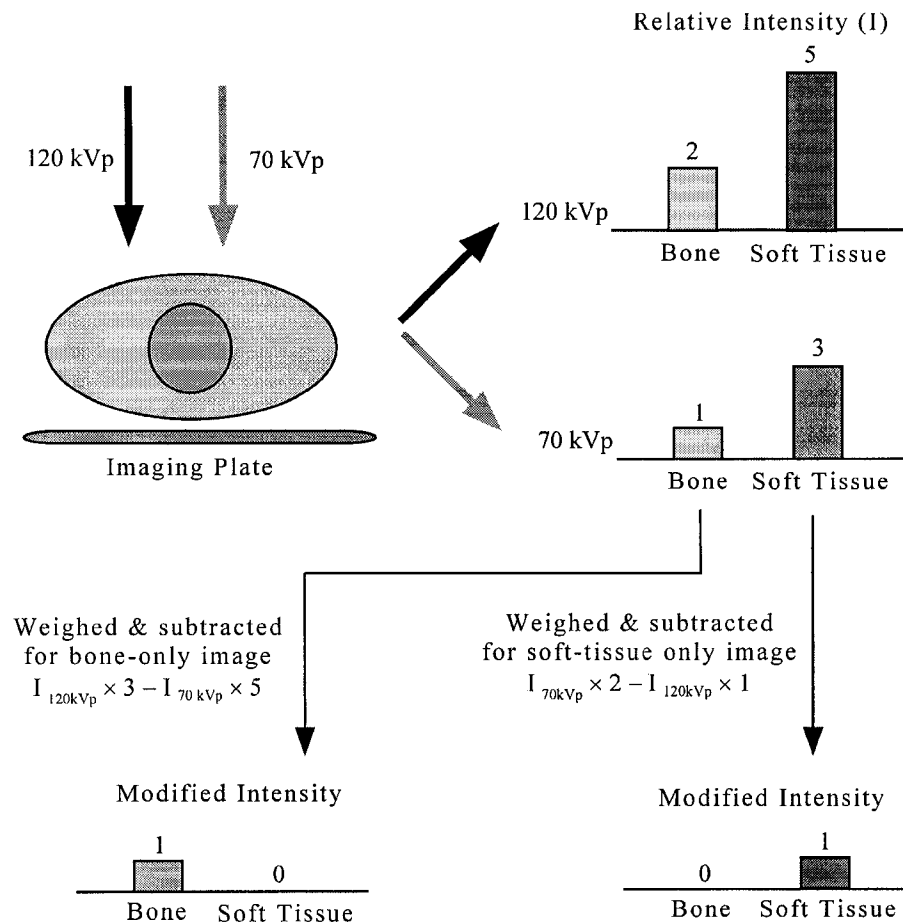


Figure 2.1. Subtraction of dual-energy images utilizing weighting factors.

One of the problems with acquiring the two images sequentially is that patient movement(s) may (and often does) occur between exposures, leading to possible artifact after subtraction. A few types of patient motion are illustrated in Fig. 2.2.³⁵ Although some of these movements can be easily corrected for, others (such as breathing) may require more complex operation such as spatial transformation due to the non-rigid nature of this motion, which will likely involve some sort of gray-level interpolation for some of the pixels in the final image. This leads to the question of the accuracy of the final image due to the interpolation, and may lead to possible legal concerns.

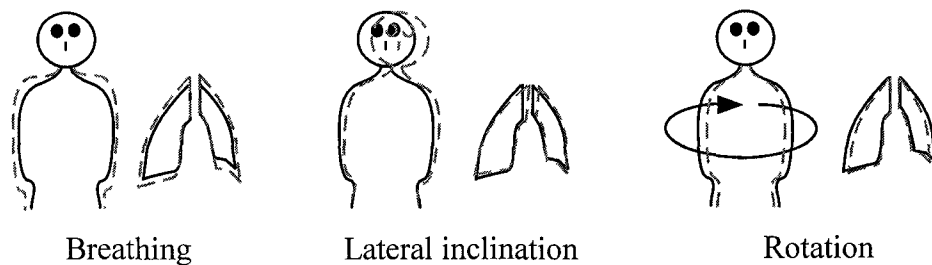


Figure 2.2. Some possible patient movements for sequential dual-energy acquisition.

To overcome this concern, a single-exposure dual-energy subtraction method has been developed. In this method, two image receptors (PSP) are exposed at the same time, with a filter (usually a thin piece of copper or a couple of PSP plates) sandwiched between the two imaging plates.¹⁶ The idea behind this concept is very simple. The first plate will receive the full x-ray spectrum that exited the patient body, while the second plate will intercept the remaining x-ray spectrum that does not get attenuated by the first receptor and sandwiched filter. Since higher energy x-ray photons attenuate less than lower energy x-ray photons, the second PSP plate will receive mostly higher energy photons (due to beam hardening), hence producing the dual-energy images required using only a single exposure. Clinical studies have demonstrated the superior quality of the single-shot dual-energy subtracted images over plain CR images for the detection of pulmonary nodules.¹⁷

One of the concerns with the utilization of the weighting factors is that it does not, unfortunately, provide any quantitative information with regard to the tissue, so a new subtraction method has been proposed. In this method, the dual-energy images are decomposed into two basis images.³⁶ These basis images are usually material equivalent images of bone and soft tissues, such as aluminum and Lucite. The soft tissue image (or the bone only image) is then computed by combining these two basis images linearly. Stewart and Huang¹⁸⁻¹⁹ demonstrated the feasibility of applying the decomposition method to single-exposure dual-energy images. To enhance the accuracy and resolution of this decomposition method, Cardinal and Fenster³⁷ approximated the dual-energy equations with conic and cubic surface equations.

The single-exposure dual-energy decomposition algorithm is chosen as the starting platform for this research project, since this method has been proven to work clinically. Therefore, the remainder of this chapter will be devoted to a more thorough examination of the theories and ideas behind this technique. The next section (2.1) will review some of the theories behind x-ray radiography, from fundamental matter-photon interaction to single-exposure dual-energy image acquisition. Section 2.2 examines some of the concepts behind the image decomposition method, as well as some of the techniques current available. Finally, Section 2.3 of this chapter will consider some of the problems with regard to the current subtraction methods, and how these concerns may be addressed and/or improved by the pseudo-global/local dual-energy subtraction technique proposed in this dissertation.

2.1. Review of Dual-Energy Radiograph

W.C. Roentgen first discovered x-rays in 1895.³⁸ The most common way to produce x-ray are by accelerating electrons through a large potential difference in vacuum and directing them to strike a (metal) target. Two different types of x-ray photons will be generated by this method: characteristic x-rays and Bremsstrahlung radiation. A characteristic x-ray is produced when an orbital electron in an atom jumps from a higher energy orbit to a lower energy vacancy (from an outer shell to an inner shell), releasing a photon with very distinct energy, equal to the difference in binding energies of the two orbits. Due to this, characteristic x-rays will appear as very sharp peaks in the x-ray spectrum. On the other hand, Bremsstrahlung radiation is produced when the striking electrons decelerate inside the target materials, releasing a broad continuous spectrum of x-rays in the process. A 125 kVp x-ray spectrum, generated by the tungsten anode spectral model using interpolating polynomials³⁹ with 5% kV ripple and 3 mm of Al filtration, is illustrated in Fig. 2.3.

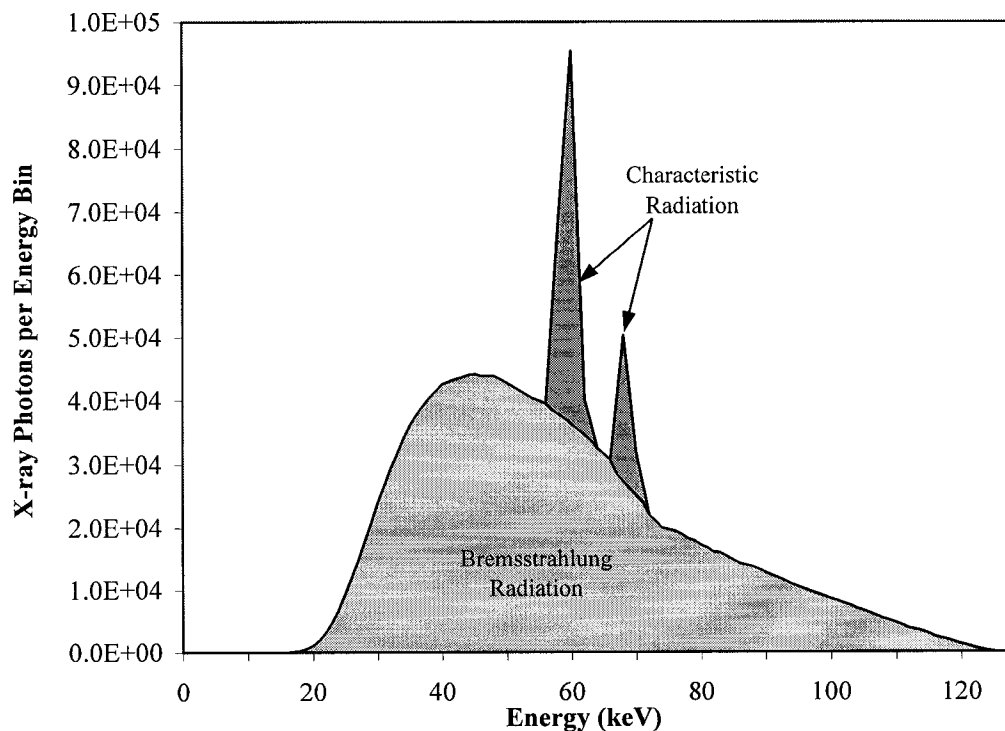


Figure 2.3. A typical 125 kVp x-ray spectrum.

2.1.1. Fundamentals of X-ray Interactions

There are four major types of interactions that may occur when photons travel through matter. They are:

1. **Coherent Scattering (or Rayleigh Scattering)** – This type of interaction occurs when the photon is scattered with essentially no energy loss and a very small scattered angle. This type of interaction is often referred to as elastic scattering, and will account for less than 5% of interactions in the diagnostic energy range.⁴⁰
2. **Photoelectric Absorption** – For this interaction, the energy of the incoming photon is completely absorbed by an orbital electron. Consequently, the electron will gain enough energy to escape from the atom, producing a photoelectron and an empty orbital shell. Clearly, the energy of the incident photon will have to be equal to or greater than the binding energy of the orbital electron in order for the interaction to occur, with the excess energy converted to the kinetic energy of the photoelectron. The electron shell vacancy caused by the ejection of the photoelectron will be filled by an outer shell electron due to its lower energy state, producing characteristic x-rays and/or Auger electrons in the process. Experiments have shown that maximum absorption of the incoming photons occurs when the electron is tightly bound and the energy of the photons is equal to the binding energy of the shell. Lastly, the photoelectric interaction is inversely proportional to the energy of the incident photons.⁴¹
3. **Compton Scattering** – In this interaction, the incident photon interacts with an outer shell or loosely bound electron, transferring some of its energy to the electron in the process. The energy gained by the electron will be utilized to overcome the weak binding energy of the atom, as well as converted to the kinetic energy of the electron. As a result, a scattered photon, with less energy than the original photon and traveling in a different direction, and a scattered electron with

kinetic energy will be produced by this event. Experiments have demonstrated that Compton Scattering is the most important interaction in soft tissue for photons in the energy range of 100 keV to 10 MeV.⁴¹

4. **Pair Production** - This process occurs when a photon with sufficient energy interacts with the nucleus of the atom, producing a positron and electron in the process. Since both the positron and electron have a rest mass equivalent of 0.511 MeV, the incident photon energy has to be greater than or equal to 1.022 MeV for this interaction to occur.

Since the typical energies utilized in diagnostic radiology are in the range of 30 to 150 keV, photoelectric absorption and Compton scattering will be the most important interactions to be considered, while pair production will not occur.

To produce a radiograph, the x-ray photons generated have to traverse through the body of the patient and captured by the image receptor (i.e. screen or PSP). In order to be able to produce a useful image, the attenuation (or interaction) of the x-ray photons with different tissues such as soft tissue and bone have to be different. Luckily, this is the case. Theoretically, the number of transmitted photons from a monoenergetic x-ray beam in an ideal narrow beam geometry traveling through a single medium is governed by

$$N = N_o e^{-\mu x}, \quad (2.2)$$

where N is the number of photons transmitted, N_o is the number of incident photons, x is the thickness of the material and μ is the linear attenuation coefficient of the medium. The linear attenuation coefficient represents the probability per unit distance of a photon interacting with any of the given matter, and is a combination of the different types of interactions that may occur

$$\mu = \sigma_R + \tau + \sigma. \quad (2.3)$$

Here σ_R is the linear attenuation coefficient due to coherent scattering interaction, τ is the linear attenuation coefficient due to photoelectric effect, while σ is the linear attenuation coefficient due to the Compton scattering interaction.

Since a human body is composed of more than one medium, Eq. 2.2 has to be modified in order to estimate the number of photons that will be transmitted. To begin with, let us assume that the body is composed of two components: the soft tissue and the

bone. Utilizing Eq. 2.2, the number of photons transmitted through the soft tissue (first component) is

$$N_{\text{after soft tissue}} = N_o e^{-\mu_{\text{soft tissue}} x_{\text{soft tissue}}} . \quad (2.4)$$

And the number of photons that are transmitted through the bone (second component) after being attenuated by the soft tissue is

$$N = N_{\text{after soft tissue}} e^{-\mu_{\text{bone}} x_{\text{bone}}} . \quad (2.5)$$

By combining Eqs. 2.4 and 2.5 we obtain

$$N = \left(N_o e^{-\mu_{\text{soft tissue}} x_{\text{soft tissue}}} \right) e^{-\mu_{\text{bone}} x_{\text{bone}}} ,$$

or

$$N = N_o e^{-(\mu_{\text{soft tissue}} x_{\text{soft tissue}} + \mu_{\text{bone}} x_{\text{bone}})} . \quad (2.6)$$

Therefore for a general m component transmission

$$N = N_o e^{-\sum_{i=1}^m \mu_i x_i} . \quad (2.7)$$

Finally since the x-rays utilized in the clinical setting will be a spectrum of energies instead of a monoenergetic beam as illustrated in Fig. 2.3, the total number of photons transmitted through a body consisting of m components is

$$N_{\text{total transmitted}} = \int_{E=0}^{E_{\text{max}}} N(E) dE = \int_{E=0}^{E_{\text{max}}} N_o(E) e^{-\sum_{i=1}^m \mu_i(E) x_i} dE . \quad (2.8)$$

2.1.2. Fundamentals of Computed Radiography

Once the x-ray photons exit from the body of the patient, an imaging plate is used to capture them and convert it to a useful image. CR imaging plates (which are based on the photostimulable phosphor technique) are utilized in this project. The receptor on the CR plate is usually composed of europium activated barium fluorohalide compounds (i.e. BaFBr:Eu²⁺). When x-ray photons ionize the phosphor molecule, a valence electron from the Eu²⁺ ion is excited into the conduction band, producing an Eu³⁺ ion in the process. This electron is then trapped by the halogen vacancies at a higher energy metastable state, producing a latent image. Once exposure is completed, the CR plate is transferred to a

laser reader for readout. During the readout, the plate is scanned by a laser beam. When the energy of the laser photon is absorbed by the fluorine (F_{center}), excitation occurs which leads to the release of the captured electron to the conduction band. This electron may then recombine with the Eu^{3+} ion to produce an Eu^{2+} ion, and luminesce in the process. The complete photostimulable luminescence process is illustrated in Fig. 2.4.⁴² The light given off by this luminescence process is usually in the green, blue or ultraviolet range, and is linearly proportional to the amount of x-rays absorbed.²⁸ The luminescence light is filtered and collected by a photomultiplier tube (PMT). The PMT converts the light collected into an electronic signal, which can be amplified and converted into a digital signal. This digital signal can then be processed and/or displayed by a computer.

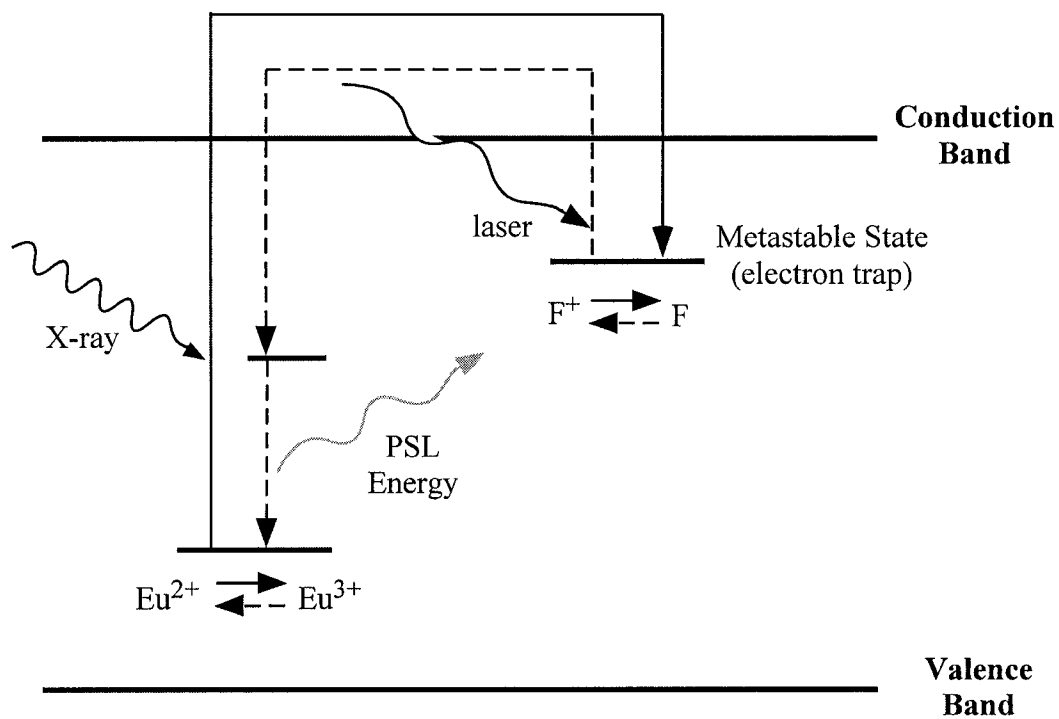


Figure 2.4. The photostimulable luminescence process.

2.1.3. Fundamentals of Dual-Energy Radiography

As the name implies, dual-energy radiography is the acquisition of two radiographic images at different energy levels, which is required in techniques such as dual-energy subtraction. These images can be acquired in a number of ways, with the two most popular methods being sequential and single-exposure dual-energy acquisitions. As mentioned before, the sequential method acquires the images one after the other at different energy levels. The advantages of this technique are the ease of setup as well as lower (mostly scattering) noise in the higher energy image when compared to the single-exposure technique. However, patient motion between exposures as illustrated in Fig. 2.2 is a major problem with this method, since some of these movements such as breathing can not be easily corrected for due to the nature of the non-rigid transformation.

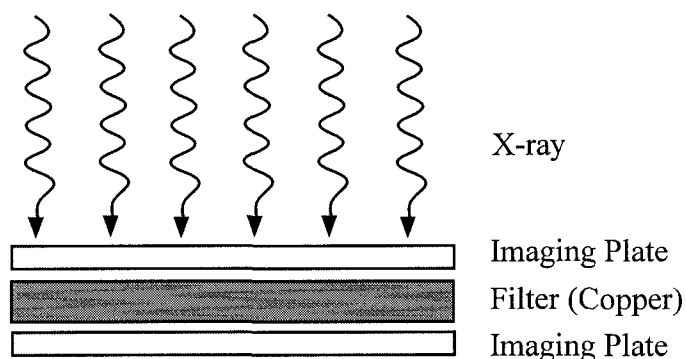


Figure 2.5. The “sandwich” single-exposure dual-energy acquisition setup.

The single-exposure dual-energy acquisition method eliminates the motion concern by acquiring both images at the same time. This is achieved by “sandwiching” a filter (such as Cu or additional PSP plates) between the image receptors, and exposing the assembly in a single exposure. This is illustrated in Fig. 2.5. Obviously, the image receptors in front of the filter will be exposed to the full spectrum of the incident x-rays, while the receptors behind the filter will be exposed only to the filtered (or higher energy)

spectrum. To illustrate the difference in these two spectra, the x-ray spectrum shown in Fig. 2.3 was used to compute the follow energy spectra:

- 1) First passing through 10 cm of lung tissue (to simulate the spectrum exposing the first imaging plate), and
- 2) Secondly, passing through 10 cm of lung tissue, one PSP plate with assumed density thickness (ρt) of $0.1 \frac{\text{g}}{\text{cm}^2}$,⁴³ and a 1 mm Cu filter (to simulate the spectrum exposing the second imaging plate).

The results are shown in Fig. 2.6. The mass attenuation coefficients utilized in these calculations are obtained using data from the NIST web site.⁴⁴ The imaging plate utilized in this theoretical calculation is assumed to be composed of BaFBr. The Eu^{2+} ion is ignored in the calculation since only a miniscule amount is present in the receptor. Finally, the mass attenuation coefficient for a mixture such as the imaging plate is calculated using a simple additivity formula⁴⁵

$$\left(\frac{\mu}{\rho}\right)_{\text{mixture}} = \sum_i f_i \left(\frac{\mu}{\rho}\right)_i, \quad (2.9)$$

where μ/ρ is the mass attenuation coefficient and f_i is the fractional weight of the i th atomic constituent. From Fig. 2.6, one can observe that the copper filter will harden the x-ray spectrum. In other words, the mean energy of the x-ray spectrum has shifted from about 67 keV for the first imaging plate to about 82 keV for the second imaging plate, an increase of about 15 keV in mean photon energy.

Since an imaging plate and a filter is placed in front of the high-energy image receptor, the amount of scattering photons received by the second imaging plate will be greater, while the amount of primary photons will be reduced when compared with the first imaging plate. This will translate to a decrease in the SNR of the high-energy image due to an increase in noise and decrease in signal. This is one of the major disadvantages of the single-exposure dual-energy acquisition method. Another minor concern is that this method is harder to set up when compared with the sequential method. This is because the sandwich has to be packaged into a cassette, and time consuming manipulation is required if a regular CR cassette is to be utilized.

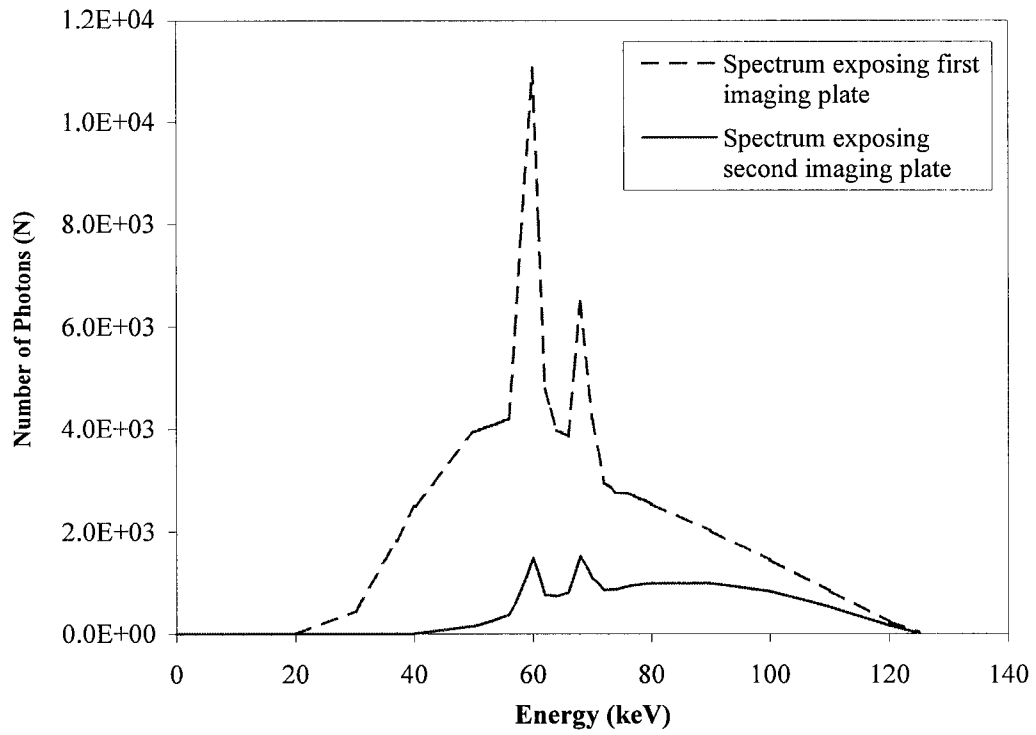


Figure 2.6. The spectra exposing the two different imaging plates.

2.2. Review of Dual-Energy Subtraction Algorithms

Once the dual-energy images are acquired, the subtraction algorithm can be applied to produce the soft tissue only and/or bone only images. The two most popular subtraction algorithms are the weighted subtraction algorithm (WSA) and the basis decomposition algorithm (BDA). The WSA is standard in the Fuji CR dual-energy subtraction system¹⁵, and is illustrated in Fig. 2.1. In this algorithm, an appropriate weighting factor is multiplied with the relative intensity of every pixel in each of the images. These modified images are then subtracted to produce the appropriate soft tissue and/or bone only images. Obviously, accurate determination of these weighting factors is very important, and is currently predetermined through prior experience as discussed before. The major disadvantage of the weighting factor approach is that it does not offer any quantitative information with regard to the tissue properties, such as bone density. Hence, the basis decomposition method has been developed.

The dual-energy decomposition was first developed for computerized tomography (CT) scanning back in the 1970's.^{36,46-48} The concept behind this approach is very simple. Recall from Section 2.1.1., experiments had shown that the photoelectric interaction is inversely proportional to the energy of the incident photons, and the probability of photoelectric interaction can be approximated using the following

$$\tau = \frac{c_1}{E^3}. \quad (2.10)$$

Here τ is the linear attenuation coefficient due to photoelectric interaction, c_1 is a constant that is material dependent and E is the energy of the x-ray photons.

On the other hand, Compton scattering depends on both the electron density (since this may be viewed as an electron-photon interaction) and the energy of the incident photons. The probability of Compton scattering can be computed using the Klein and Nishina cross section⁴⁵

$$\sigma = c_2 \left\{ \frac{1+\alpha}{\alpha^2} \left[\frac{2(1+\alpha)}{1+2\alpha} - \frac{\ln(1+2\alpha)}{\alpha} \right] + \frac{\ln(1+2\alpha)}{2\alpha} - \frac{1+3\alpha}{(1+2\alpha)^2} \right\}. \quad (2.11)$$

Here σ is the linear attenuation coefficient due to Compton scattering, c_2 is another material dependent constant, and α is defined as

$$\alpha = \frac{E}{m_0 c^2}. \quad (2.12)$$

Here E is energy of the incident photons, while $m_0 c^2$ is the rest mass of the electron and is equal to 0.511 MeV.

From Eqs. 2.10 and 2.11, one can observe that the energy (E) dependence for the photoelectric effect and Compton scattering is different. Therefore with two monoenergetic x-ray beams (such as those produced by two different radioactive isotopes), one can easily calculate (or decompose) the contributions from the photoelectric effect (c_1) and/or Compton scattering (c_2). However, this approach has two drawbacks. Firstly, the incident photons are not monoenergetic for most radiographic systems. Therefore, the two constants (c_1 and c_2) cannot be determined analytically unless the original x-ray spectra are known. Secondly, due to the non-linear nature of the attenuation equation (Eq. 2.2), scattering radiation cannot be easily accounted for in this decomposition. To overcome these concerns, Alvarez and Macovski³⁶ have suggested determining these coefficients by first measuring the x-rays transmitted through materials with known attenuation coefficients, and then numerically determining these unknown values using a least square fitting.

In 1981, Lehmann et al.⁴⁹ applied the decomposition algorithm to digital radiography using aluminum and Lucite as basis materials. As will be shown in Chapter 3, aluminum and Lucite are considered to be bone and soft tissue equivalent materials respectively due to their similar attenuation properties with respect to bone and soft tissue. In 1989, Stewart¹⁸ utilized this decomposition method in a single-exposure dual-energy subtraction CR system. In his method, different thicknesses of aluminum and Lucite were irradiated, and a calibration (look-up) table was constructed by logging the gray-levels from the high and low energy images. Afterward, the patient images were decomposed into aluminum equivalent and Lucite equivalent images by looking up the amounts of material required utilizing the look-up table generated above. Finally, a linear recombination of these basis images is required to produce the soft tissue and bone only images. A flowchart for this decomposition algorithm is illustrated in Fig. 2.7.

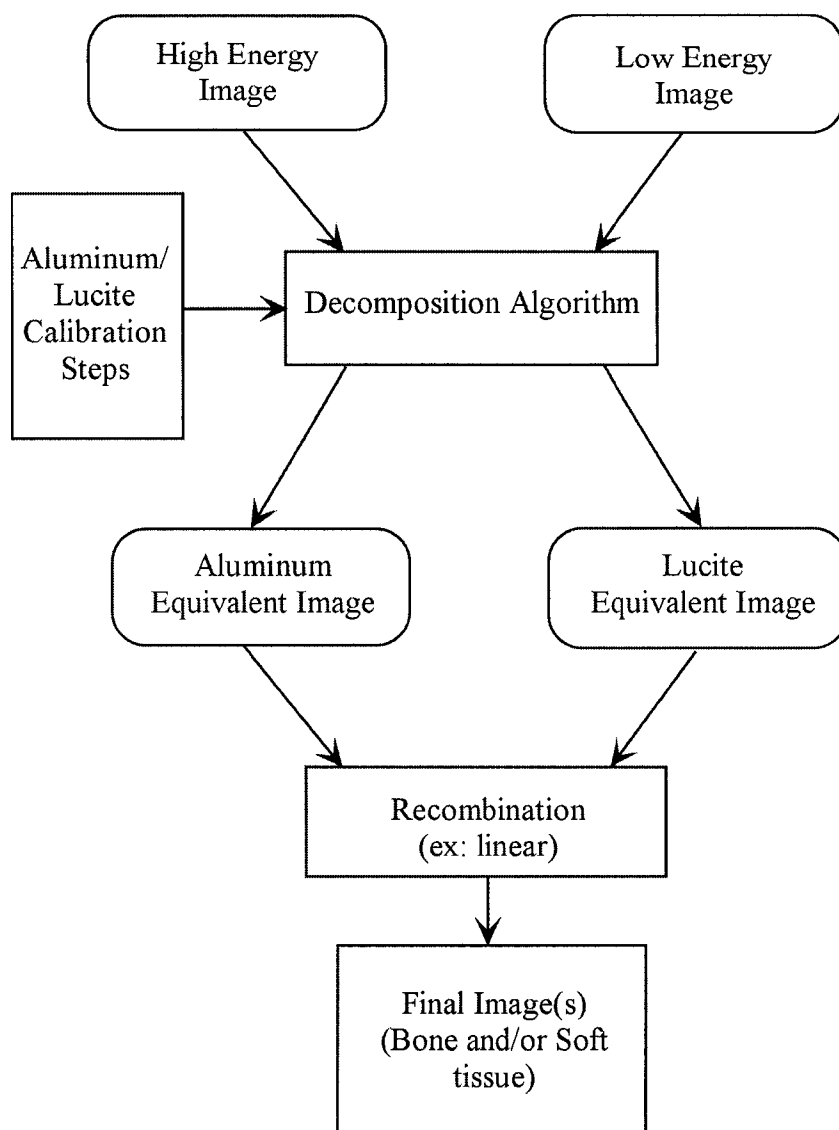


Figure 2.7. An overview of the aluminum/Lucite decomposition technique.

Since the gray-levels of the digital image are not linearly proportional to the incident exposure, a look-up table constructed from the gray-levels of the image may not be able to produce the appropriate material equivalent images. This is because in order to display the large range of exposures required in a chest radiograph, the relationship between the gray-level (Q) and exposure (E) is typically a semi-logarithmic function. (i.e. $Q = a \log(E) + b$ where a and b are constants.) As a result, a large change in E may produce only a small change in the Q value. This is a concern with the Stewart method

described above. Consequently, Stewart and Huang¹⁹ have modified the procedure by utilizing the exposure instead of simply the gray-level in the calibration table. This should eliminate the ill-conditioned nature of the decomposing algorithm because of the ambiguity due to the gray-level look-up. Also, two 12:1 grids, placed perpendicular to each other, are employed to reduce the scattering radiation.

Even with these improvements, however, the sizes of the steps as well as the amount of quantum noise in the data limit the accuracy of the decomposition. To enhance the accuracy and resolution of the decomposition method, Cardinal and Fenster³⁷ have proposed the use of conic and cubic surface equations (a convergent Taylor series expansion with limited terms) to approximate the dual-energy equations. In this method, the signals from each imaging plate of different aluminum and Lucite thickness are approximated using a conic equation (F) such that

$$F = \frac{2A}{B + \sqrt{B^2 + 4AC}}, \quad (2.13)$$

where

$$A = a_0 + a_1 t_{Al} + a_2 t_{Lu} + a_3 t_{Al}^2 + a_4 t_{Al} t_{Lu} + a_5 t_{Lu}^2, \quad (2.14)$$

$$B = 1 + b_1 t_{Al} + b_2 t_{Lu}, \quad (2.15)$$

$$C = c_0. \quad (2.16)$$

Here t_{Al} and t_{Lu} are the thickness of the aluminum and Lucite materials respectively, while a , b and c are coefficients resulting from the fitting. With this method, not only is an accuracy of 1 μm in material thickness is achievable, but extrapolation beyond the calibrated region is possible as well.

2.3. Disadvantages of the Global Dual-Energy Subtraction Algorithm

As mentioned in the introduction, there are two major disadvantages with the global dual-energy subtraction algorithm. The first one is that any calcified lung nodules will be treated as bone material and will be displayed on the bone image, and the second one is that of the decrease in SNR of the final image(s). This section will examine each of these concerns in more detail.

Although the presence of calcification within a solitary pulmonary nodule may be considered as sign of being a benign lesion,¹¹ there may be exceptions to this rule. Therefore, it is important for a radiologist to identify all the nodules. However, with the global dual-energy subtraction algorithm, all the calcified nodules will be treated as bone components due to their calcium content; as a result, these calcified nodules will be displayed in the bone-only images after the subtraction. Hence, in order to identify all the nodules, a radiologist will have to review both the soft tissue and bone-only images. In other words, the workload of the radiologist would increase unless another method of displaying these two images is developed.

The decrease in the SNR of the final image(s) is another disadvantage of the global subtraction algorithm. This is due to the fact that when one subtract two values with independent uncertainties, the maximum error in the resulting values is the sum of the two uncertainties.⁵⁰ For example, given two pixels with values $x \pm \partial x$ and $y \pm \partial y$, where x and y are the two measured values and ∂x and ∂y are the two respective uncertainties, then for

$$z = x - y, \quad (2.17)$$

the maximum error in z will be

$$\partial z_{\max} = \partial x + \partial y. \quad (2.18)$$

Therefore, one would expect the subtracted image to be noisier than the original low or high energy images. In addition, due to the filtering required to create the high energy image for the single-exposure dual-energy acquisition, one would expect the higher energy images to be noisier. This is due to 1) the additional scattering from the filter, and 2) increasing quantum mottle (or noise) due to the reduction in the number of photons reaching the second imaging plate. Consequently, one would expect the subtracted image

to contain more noise when compared to a normal chest radiograph. On the other hand, the removal of the bone structure will reduce the latitude (or range of gray-level) required to display the chest radiograph. This will allow an increase in contrast for the subtracted soft tissue radiograph, and should enhance the diagnostic conspicuity of the soft tissue radiograph when compare to the conventional chest x-ray.

These concerns can be addressed and/or improved by applying the dual-energy subtraction technique proposed in this dissertation. The method is a pseudo global/local approach where only the ribs that are obstructing the visual examination of the underlying soft tissue in the radiographs are subtracted. An overview of this pseudo-global/local subtraction algorithm as initially intended is illustrated in Fig. 2.8. In this approach, the low and high energy images are first decomposed into the soft tissue and bone-only images using the normal global subtraction method. However, the basis materials that are utilized in the decomposition are a composition of aluminum with PVC and Lucite blocks filled with water. It is because these materials, as will be examined in the next chapter, are closer to the x-ray attenuation properties of bone and soft tissue respectively. This should reduce the complexity of the decomposition of the low- and high-energy images into the basis images since this transformation is generally nonlinear. Once the bone-only image is computed, a detection algorithm is employed to isolate the bone structure from the background of the image, which would indicate the location of the bone on the image. Finally, equipped with the bone location information, the algorithm will decompose (subtract) only the areas on the images that are covered with bone. A more detail discussion of this detection algorithm is presented in Chapter 4. However, due to the ability to access a dual-energy subtraction radiographic unit (FCR XU-D1) from Fuji Medical System (Tokyo, Japan) in the later part of this project, the standard bone images outputted by the unit will be utilized instead of computing the decomposition using the new equivalent materials.

The two concerns with the global subtraction method can be addressed by the current approach as follows:

- 1) Since the ribs (bones) in the thorax are generally larger in size than calcified nodules, the calcified nodules in the bone-only image that are not covered could be easily filtered out by some detection algorithm

and not be removed in the second (local) subtraction. As for the nodules that are covered by ribs, one may be able to account for them by recognizing the fact that a rib (at least the body of it) is a flat bone structure whose thickness will not vary significantly from its surroundings. Consequently, a large local variation in the thickness of ribs during the global subtraction should indicate the existence of a calcified nodule. This problem can then be “corrected for” by estimating the thickness of each rib using the surrounding rib thickness with a correction algorithm, and subtract only this estimated thickness in the second subtraction.

- 2) Since only the areas that are covered with bone are subtracted in this pseudo algorithm, the SNR in the interrib area (area not covered by ribs) is preserved. And although the SNR in the areas covered by bone will be reduced after the subtraction, the removal of the bones should increase the diagnostic conspicuity of the radiograph in these areas. Hence the overall diagnostic capability of the image(s) produced using this pseudo method should be higher than both the normal (non-subtracted) chest radiograph and the global subtracted image.

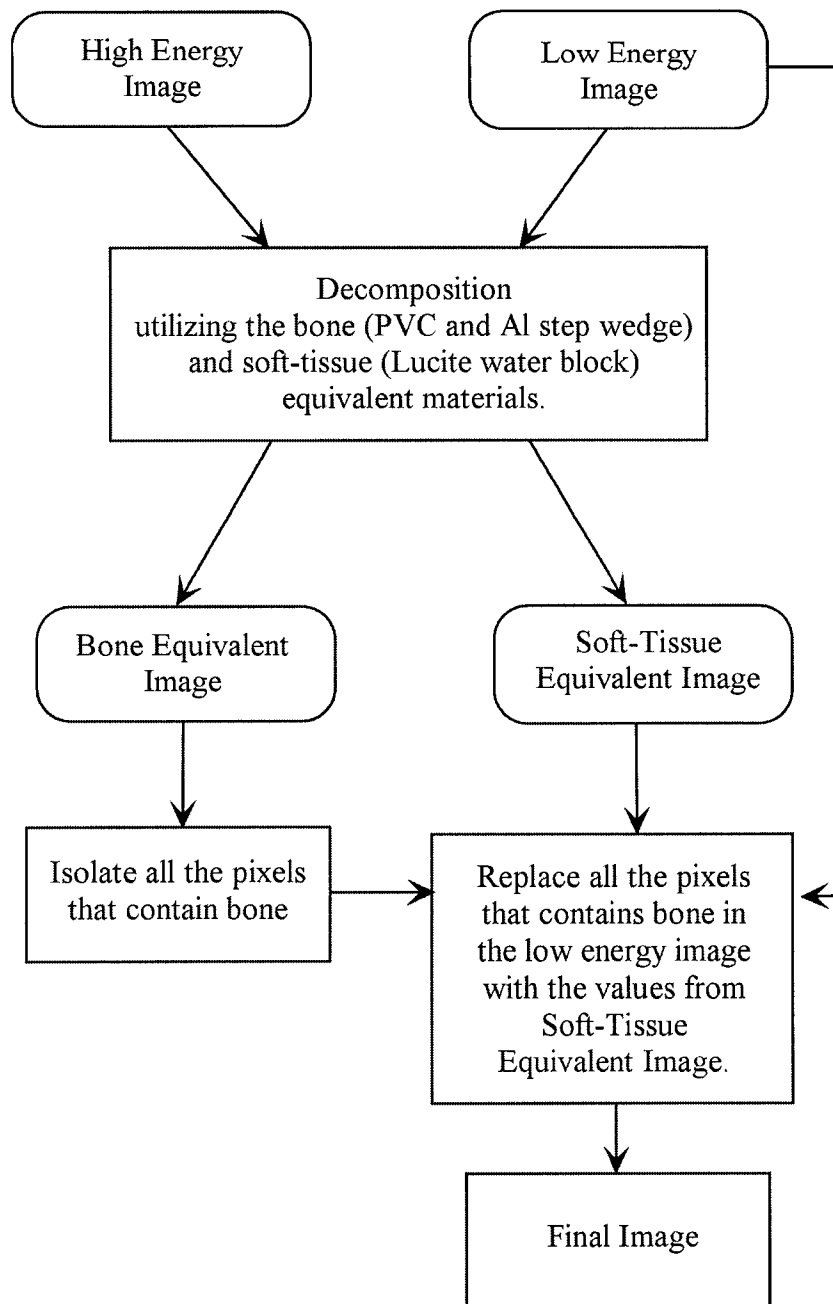


Figure 2.8. An overview of the pseudo-global/local subtraction algorithm.

3. New Equivalent Materials for the Dual-Energy Decomposition Algorithm

Due to the fact that the dual-energy decomposition algorithms require the use of bone and soft tissue equivalent materials, the accuracy of the resultant subtracted images greatly depends on the ability of the equivalent materials to mimic the x-ray attenuation property of the respective tissue. Currently, aluminum is the material of choice for bone equivalent material. This is mainly because the atomic number of aluminum is 13, which closely resembles the effective atomic number of (approximately) 12.5 for bone. Therefore, one would expect the attenuation properties of both materials would be similar in the photoelectric region. Also, aluminum is stable and readily available in various shapes, sizes and thicknesses. This would allow very flexible design as well as quick construction of imaging phantoms.

However, although the attenuation properties of aluminum and bone should be similar in the photoelectric region, there is no guarantee this will be the case in the Compton region. The aluminum-to-bone linear attenuation coefficient ratio (μ_{Al}/μ_{bone}), as well as the ratio of a few other possible bone equivalent materials, is illustrated in Fig. 3.1. For this Figure, the bone mass attenuation coefficient is computed using Eq. 2.9, with a composition by fractional weight of 3.4% hydrogen, 15.5% carbon, 43.5% oxygen, 0.1% sodium, 0.2% magnesium, 10.3% phosphor, 0.3% sulfur and 22.5% calcium as indicated in the ICRU (International Commission on Radiation Units and Measurement) Report 44.⁵¹ The linear attenuation coefficients are then calculated by multiplying the mass attenuation coefficient with the density of cortical bone (1.920 g/cm^3).

From Fig. 3.1, one can observe that aluminum is only a fair bone equivalent material. The linear attenuation coefficient ratio has a range from 1.2 at 40 keV to about 1.3 at 125 keV. Although aluminum is able to mimic the attenuation property of bone better than most other equivalent materials at lower energy regions as expected, silicon and B-100, a bone equivalent plastic, are better at higher energies.

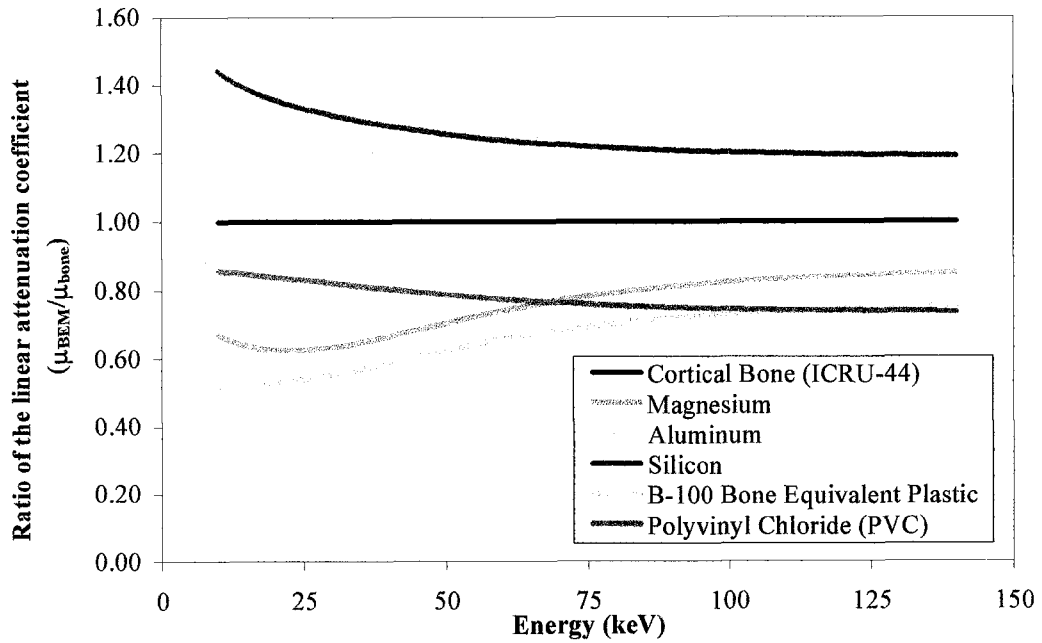


Figure 3.1. The ratio of the linear attenuation coefficients of some possible bone equivalent materials with respect to cortical bone.

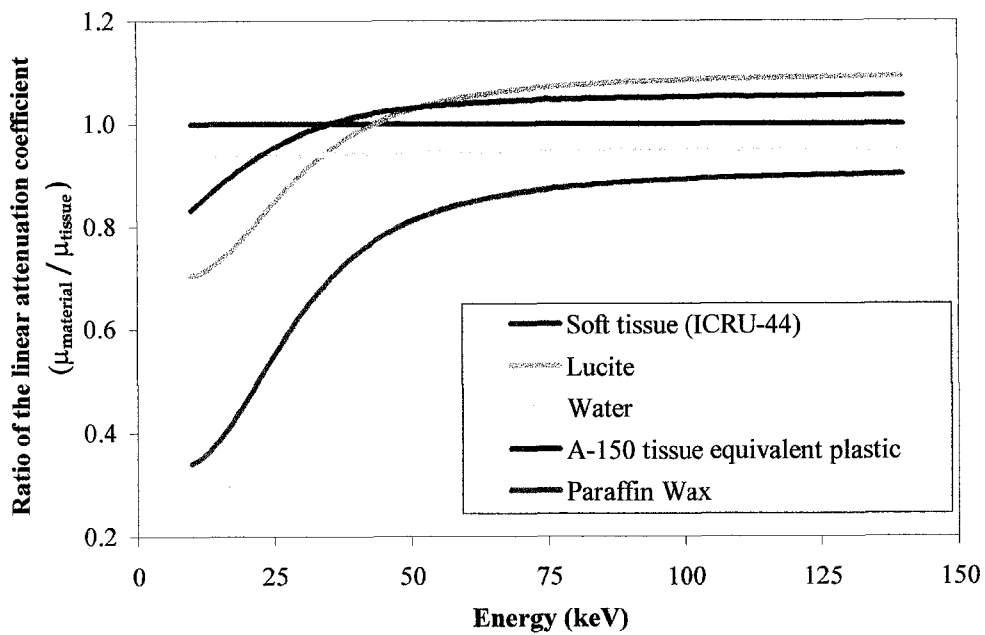


Figure 3.2. Linear attenuation coefficient ratios of some possible tissue equivalent materials with respect to soft tissue.

Similarly, Lucite is the material normally used to imitate soft tissue. Again this is mainly due to the stability, availability and attenuation properties of Lucite. The linear attenuation coefficient ratios of Lucite, as well as a few other possible soft tissue equivalent materials, verses soft tissue are shown in Fig. 3.2. In this Figure, the soft tissue composition from ICRU Report 44⁵¹ is used to calculate the soft tissue mass attenuation coefficient, which consists of 10.2% hydrogen, 14.3% carbon, 3.4% nitrogen, 79.8% oxygen, 0.2% sodium, 0.3% phosphor, 0.3% sulfur, 0.2% chloride and 0.3% potassium.

From Fig. 3.2, one can observe that although Lucite is a better soft tissue equivalent material than Paraffin Wax, water is the best overall choice. Unfortunately, water cannot be easily used to construct phantoms, or models, due to its fluid nature; therefore, some compromise will be required. In the next section (3.1), a new type of bone equivalent material, composed of aluminum and PVC, will be examined. This material has the ability to mimic the attenuation property of bone to a higher accuracy when compared to aluminum alone, and is both stable and readily available. Section 3.2 will examine a soft tissue equivalent material which have been used in our facility for QC testing for many years, consisting of hollow Lucite blocks filled with water. This SEM has the ability to simulate the attenuation property of soft tissue better than Lucite or water alone at energies above 40 keV.

3.1. New Bone Equivalent Material (BEM)

As indicated in the previous section, aluminum is only a fair BEM. Therefore, a new type of BEM consisting of aluminum and PVC (polyvinyl chloride) will be examined in this section. This composition has the ability to mimic the attenuation properties of bone to a higher degree of accuracy when compared to aluminum or PVC alone, and should enhance the accuracy of the decomposition method when utilized.

Due the fact that aluminum and PVC are the only two materials to be utilized in this BEM, Eq. 2.7 can be simplified to

$$N = N_o e^{-(\mu_{Al} x_{Al} + \mu_{PVC} x_{PVC})}. \quad (3.1)$$

Since only the attenuation properties of the final combined mixture is of interest

$$N = N_o e^{-\mu_{mixture} x_{mixture}}. \quad (3.2)$$

By combining Eqs. 3.2 and 3.3 and simplifying, one obtains

$$\mu_{mixture} = \frac{\mu_{Al} x_{Al} + \mu_{PVC} x_{PVC}}{x_{mixture}}. \quad (3.3)$$

Obviously, one would like this $\mu_{mixture}$ to be as close to μ_{bone} as possible.

So why combine aluminum and PVC for the new BEM? Part of the answer can be obtained by reviewing Fig. 3.1 and Eq. 3.3. Firstly, Eq. 3.3 may be viewed as a formula that averages the linear attenuation coefficient of the two materials weighted by the fractional thickness. Therefore, by utilizing two materials that have mirrored values (above and below the required attenuation coefficient) throughout the required energy range, one should be able to produce a composition that has the same linear attenuation coefficient as the ideal values. From Fig. 3.1, one can observe that PVC and aluminum fit this description relatively well. Secondly, one would also prefer to choose materials that are both stable and readily available in different shapes, sizes and thicknesses. Here, aluminum and PVC both fit this constraint perfectly.

Finally, in order to be a good BEM in the diagnostic radiology energy range, not only should the total linear attenuation (μ) be the same as that of bone, but also the linear attenuation coefficient due to coherent scattering interaction (σ_R), the photoelectric effect (τ) and the Compton scattering interaction (σ) as well. This is because these are the

interactions that could occur in the diagnostic energy range, and obviously a good BEM should be able to match each of these interactions to that of bone.

3.1.1. Theoretical Considerations for the new BEM

Once the basic materials for the new BEM have been selected, the appropriate thickness of aluminum and PVC needs to be chosen such that the proper bone attenuation properties can be computed. Clearly, the thickness of the material one chooses should be readily available; therefore, the thickness ratio for aluminum versus PVC is chosen to be 1:2, 1:1 and 2:1 in these calculations. The total linear attenuation coefficients for these three ratios are shown in Fig. 3.3, while the coherent scattering, photoelectric and Compton scattering interaction cross sections are illustrated in Figs. 3.4, 3.5 and 3.6 respectively. From these Figures, one can observe that the 1:1 aluminum to PVC thickness ratio is the best ratio for mimicking the attenuation properties of cortical bone for the overall attenuation and Compton scattering, while the 1:2 thickness ratio is better for the elastic scattering. Finally, the 2:1 aluminum to PVC thickness is closer to the photoelectric absorption property of cortical bone.

To illustrate the effect the BEMs have on the x-ray spectra exposing the two imaging plates, the x-ray spectrum shown in Fig. 2.3 is used to compute the follow two energy spectra similar to Section 2.1.3:

- 1) First passing through the BEM (to simulate the spectrum exposing the first imaging plate), and
- 2) Secondly, passing through the BEM, one PSP plate and 1 mm of Cu filter (to simulate the spectrum exposing the second imaging plate).

Three BEM materials are selected for this calculation. They are aluminum, the 1:1 aluminum to PVC thickness ratio, and the 1:2 aluminum to PVC thickness ratio. Although the 1:1 thickness ratio is closer to the ideal bone linear attenuation coefficient, the 1:2 thickness ratio is more linear throughout the energy range of interest (30 to 140 keV), which implies that it should be easy to correct for. The thickness for these BEMs are set to 1 cm, except for the 1:2 thickness ratio which has a thickness of about 1.08 cm.

This slightly larger thickness for the 1:2 ratio is needed to correct for the “constant” lower values of the 1:2 ratio when compared to the bone coefficient (the attenuation coefficients of the 1:2 Al-to-PVC thickness ratio are about 0.93 times of μ_{bone} for the diagnostic energy range). The results are shown in Fig. 3.7 for the first spectrum, and Fig. 3.8 for the second spectrum. From Figs. 3.7a and 3.8a, one can observe that the two proposed BEMs (1:1 and 1:2 Al-to-PVC thickness ratio) are better than or equal to aluminum for the diagnostic energy range. And from Figs. 3.7b and 3.8b, one can observe that the 1:2 thickness ratio is able to approximate the number of photons (N) exposing the plates to a higher of degree of accuracy when compared to the 1:1 ratio for the energy range of 55 keV and above. Since more of the photons of the x-ray spectra exposing the two plates will be of this higher energy range as illustrated in Fig. 3.7a and 3.8a, the 1:2 aluminum-to-PVC thickness with correction should be the better choice.

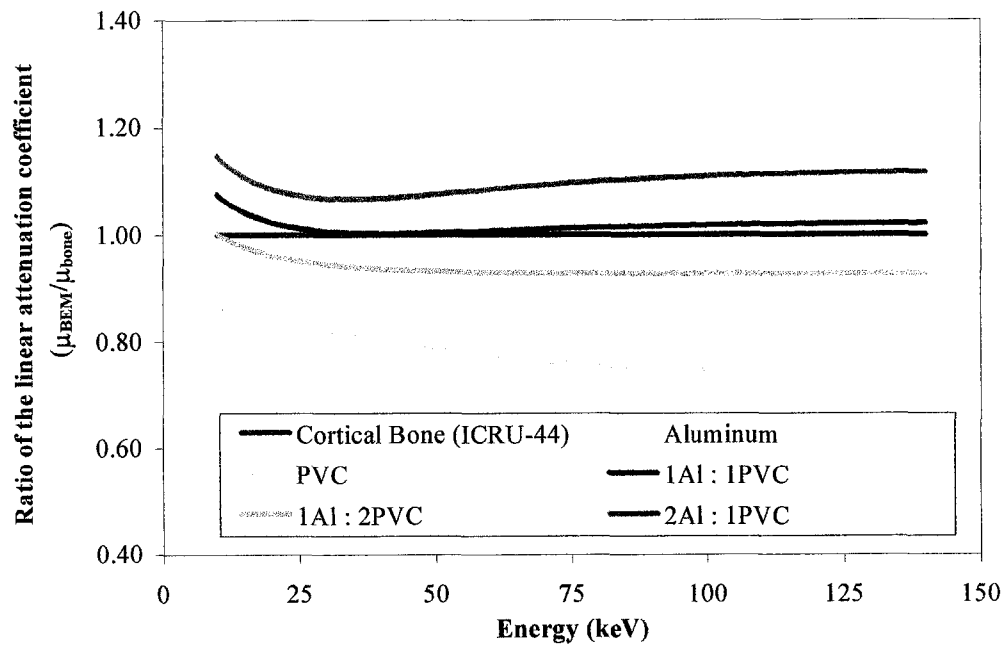


Figure 3.3. The ratio of the linear attenuation coefficient of the proposed bone equivalent materials with respect to bone.

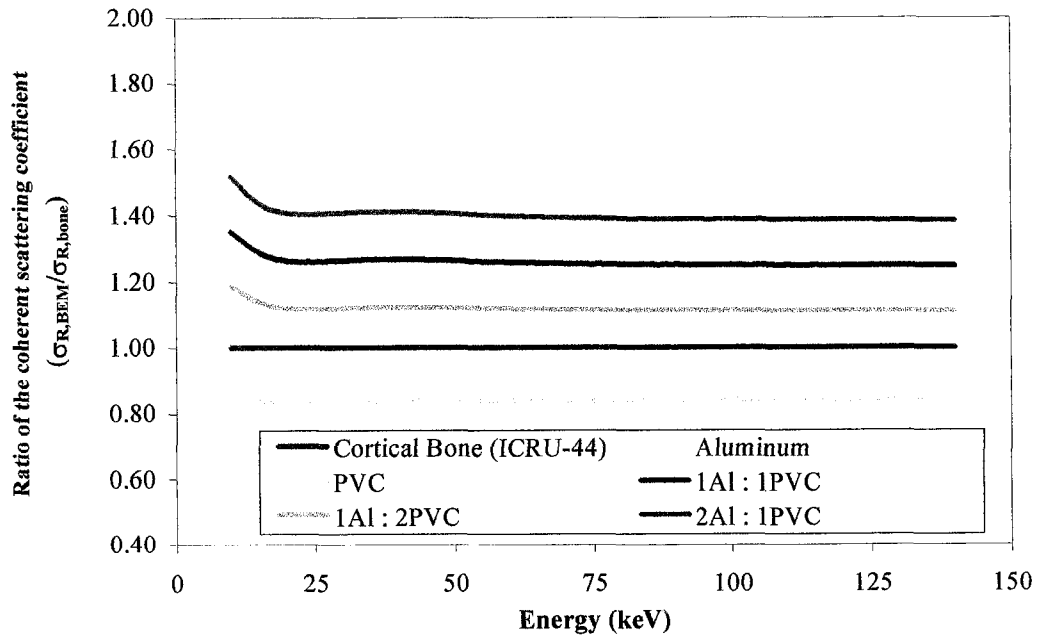


Figure 3.4. The ratio of the coherent scattering coefficient of the proposed bone equivalent materials with respect to bone.

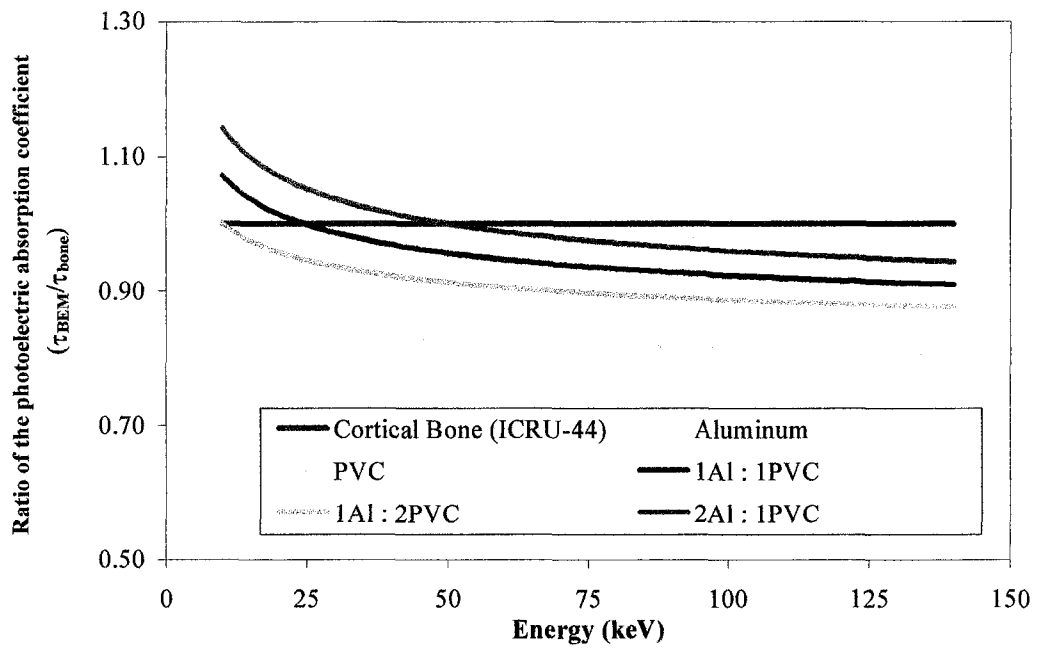


Figure 3.5. The ratio of the photoelectric absorption coefficient of the proposed bone equivalent materials with respect to bone.

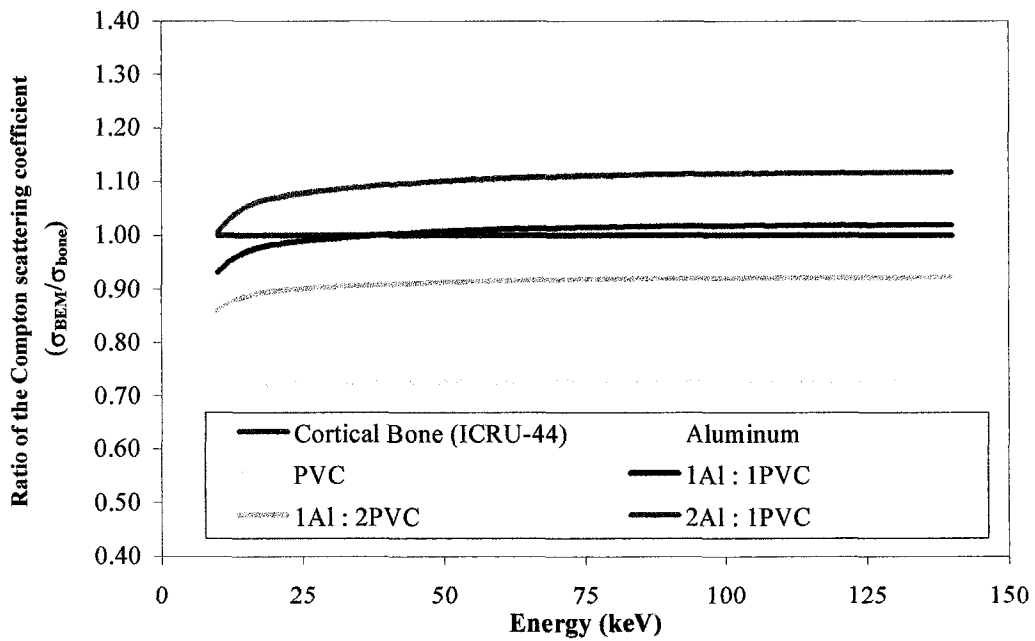
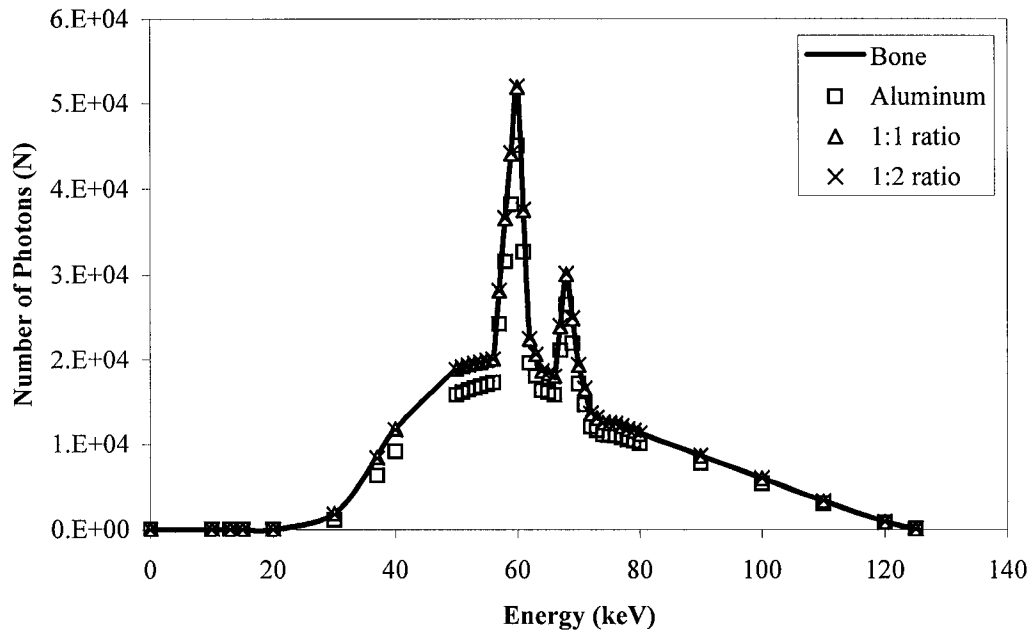
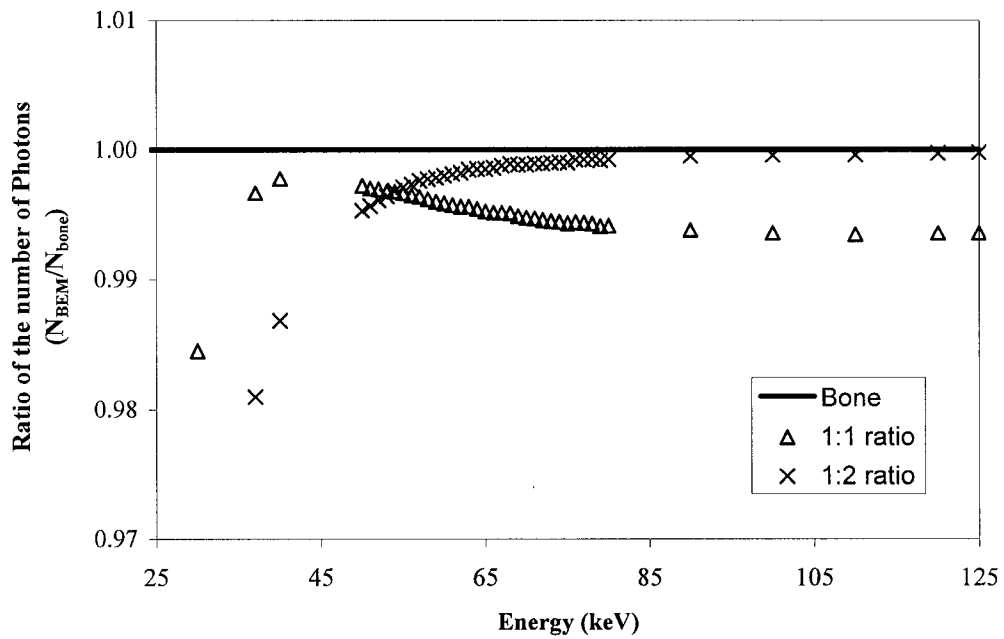


Figure 3.6. The ratio of the Compton scattering coefficient of the proposed bone equivalent materials with respect to bone.

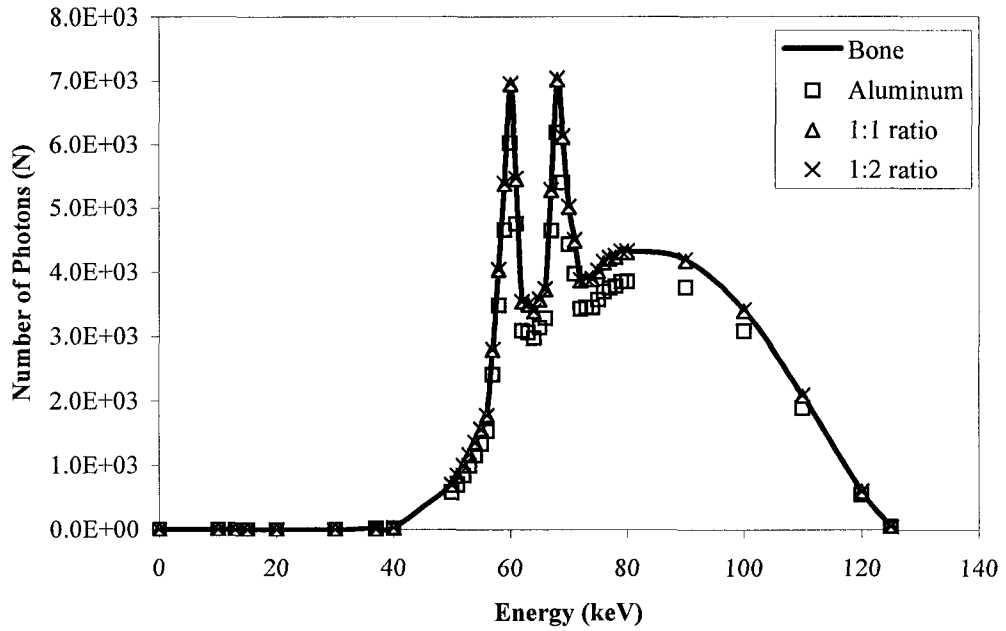


(a)

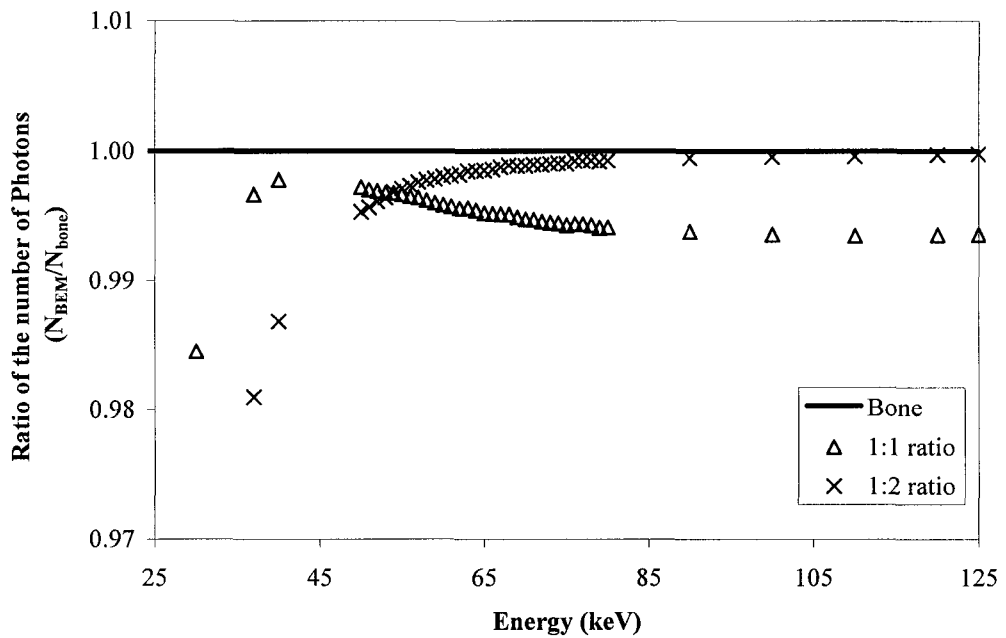


(b)

Figure 3.7. The x-ray spectra exposing the first imaging plate after passing through different bone equivalent materials. (a) All three bone equivalent materials. (b) A detailed comparison (ratio) of the 1:1 and 1:2 Al-to-PVC thickness materials.



(a)



(b)

Figure 3.8. The x-ray spectra exposing the second imaging plate after passing through different bone equivalent materials. (a) All three bone equivalent materials. (b) A detailed comparison (ratio) of the 1:1 and 1:2 Al-to-PVC thickness materials.

3.1.2. Experimental Verification of the new BEM

For the experimental verification of the linear attenuation coefficients of the new BEM, an aluminum versus PVC thickness ratio of 1:2 is selected. This is because linear attenuation coefficients of the 1:2 thickness ratio are slightly more linear at the higher range (50 kV and above) as mentioned in the last section. Since the pixel values on the radiograph will be an integrated signal of all these energies, a linear response (such as the 1:2 aluminum to PVC thickness ratio linear attenuation coefficient) should be easier to account for. Also for thinner thickness, the ratio of 1:2 should provide more strength to the phantom (step wedge). In this experiment, the 1/8" Alloy 1100 Aluminum (88685K1) and 1/4" Type I PVC (8747K114) from McMaster-Carr (www.mcmaster.com) are used.

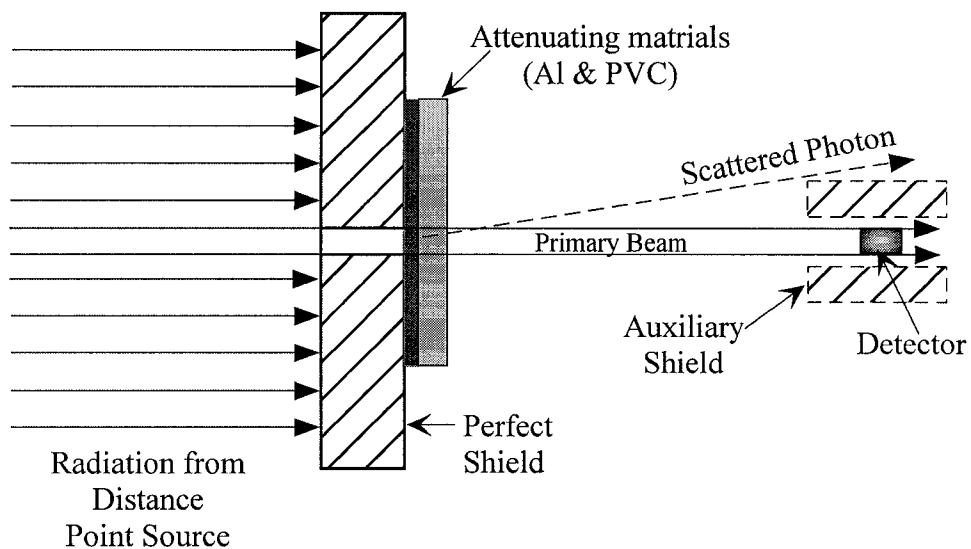


Figure 3.9. The ideal narrow-beam geometry for the experimental determination of the linear attenuation coefficient.

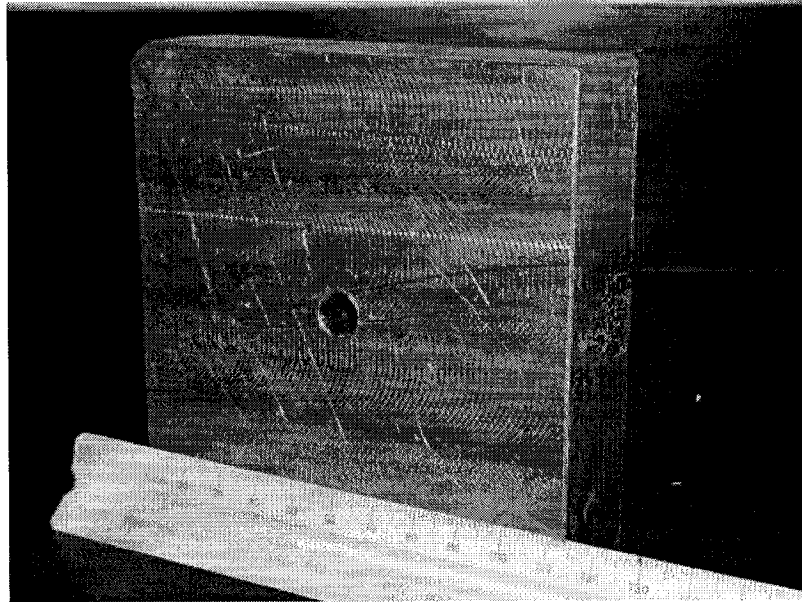
The setup of this experiment is based on the narrow-beam attenuation of uncharged radiation in Chapter 3 of Attix⁴⁵, and is illustrated in Fig. 3.9. Four different radioactive isotopes are used. They are ²⁴¹Am, ⁵⁷Co, ⁶⁷Ga and ^{99m}Tc, and are chosen due to the fact that at least one of the higher probability decay gammas are within the diagnostic energy range. These gamma energies, as well as their half-lives, are listed in Table 3.1. The data are obtained from a freeware called **Radiation Decay** by Charles Hacker.⁵²

Table 3.1. Table of gamma energies of interest and half-lives for the four isotopes used in the experimental verification of the bone equivalent material.

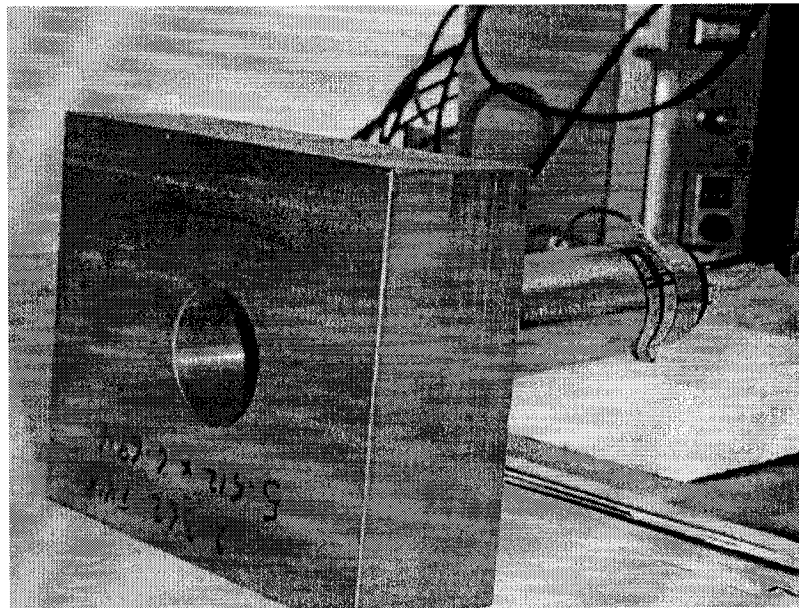
Isotope	Gamma Energy (keV)	Half-life
²⁴¹ Am	60	432 years
⁵⁷ Co	122	270 days
⁶⁷ Ga	93	3.3 days
^{99m} Tc	141	6 hrs

Table 3.2. Distance between isotopes, the “perfect” shield and the detector in the bone equivalent material verification experiment.

Isotope	Source to Shield Distance (cm)	Shield to Detector Distance (cm)
²⁴¹ Am	216	206
⁵⁷ Co	98	98.5
⁶⁷ Ga	98	98.5
^{99m} Tc	150	170



(a)



(b)

Figure 3.10. Pictures of shields used for the attenuation coefficient determination experiment. (a) The “perfect” shield. (b) The auxiliary shield.

The distance from the isotopes to the “perfect” shield is roughly about the same as the distance from the shield to the detector, and is different for each isotope depending on the activity. These distances are listed in Table 3.2. The “perfect” shield used in this experiment is composed of a piece of lead that is about 3 cm in thickness. A hole of 1 cm in diameter is drilled through the center of the lead to allow the gamma rays to pass through. A picture of this shield is shown in Fig. 3.10a. Finally, the photons are detected using a 1.5” diameter by 3” length NaI crystal coupled to a photomultiplier tube connected to a multi-channel analyzer. The NaI crystal is also shielded with another piece of lead that is about 6 cm in thickness as illustrated in Fig. 3.10b.

Each linear attenuation calculation required two different counts. This is because the count with and without the attenuating material are needed (N & N_o respectively) as shown in Eq. 3.2. An acquisition time of 400 seconds was used to obtain each count. Two data sets, or runs, were acquired for the ^{241}Am source, and 4 runs were acquired for the rest of the isotopes. The background count (with no radioactive isotopes present) was also acquired, and was subtracted from the spectra. Finally, the Compton edge was approximated using a linear estimation technique and removed. An example of the estimation of the Compton edge is illustrated in Fig. 3.11.

Once the spectra are obtained and corrected for, the linear attenuation coefficient calculation can be computed. Here, N and N_o are obtained by summing from the maximum values in the photopeak to the upper full width half maximum (FWHM) values as shown in Fig. 3.12. This is to reduce the Compton edge contribution in the lower half of the photopeak that may not be approximated accurately by the linear estimation. Also, due to the short half-life of the $^{99\text{m}}\text{Tc}$ isotopes, the counts for these runs were decay adjusted. The average calculated linear attenuation coefficients for these four isotopes are listed in Table 3.3. From this table, one sees that experimentally determined linear attenuation coefficients are close to but slightly less than the theoretical values. This is expected since the narrow-beam setup is only valid for the ideal case, and will never be able to eliminate all of the scattered photons.⁴⁵ Therefore, one would expect the experimentally determined linear attenuation coefficient to be slightly smaller due to the increase in N from scattered photons.

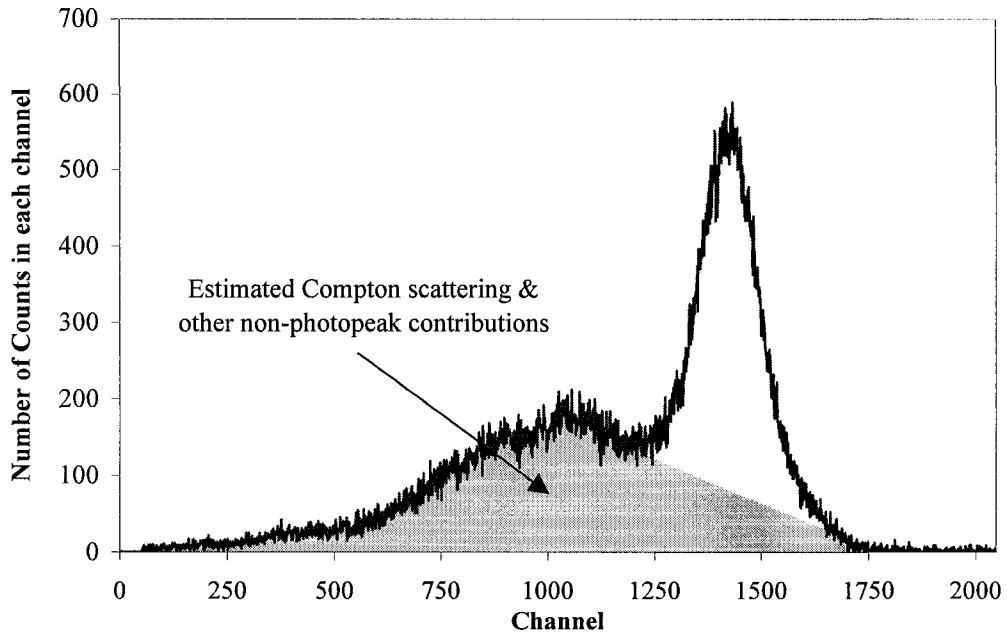


Figure 3.11. Estimation of the Compton edge and other non-photopeak contributions in the spectra in the bone equivalent material attenuation experiment.

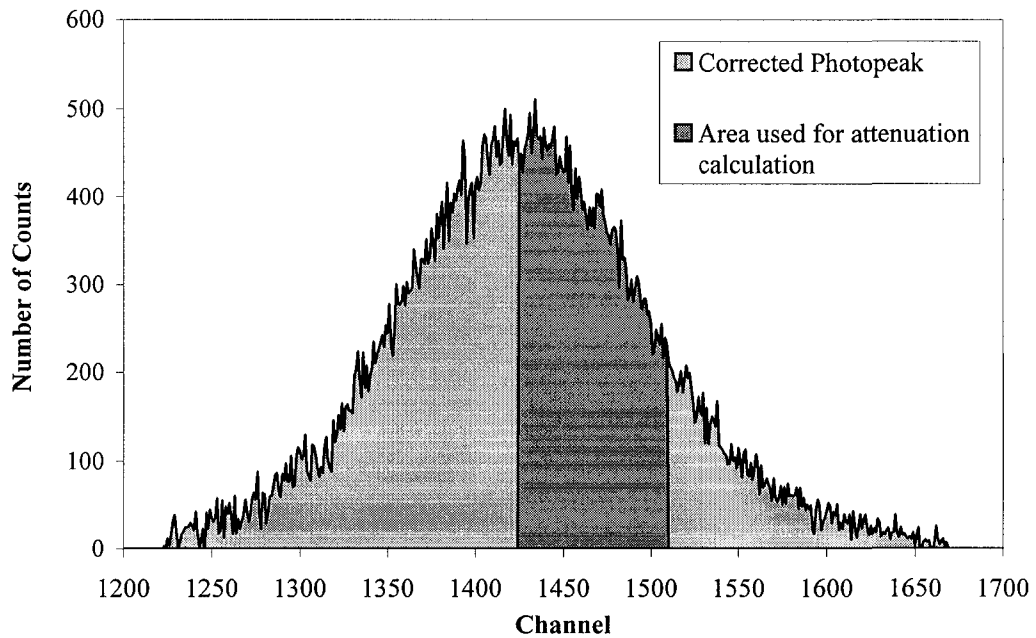


Figure 3.12. An illustration of the area in the photopeak used for attenuation calculation.

Table 3.3. A table of linear attenuation coefficients for theoretical cortical bone, theoretical aluminum versus PVC thickness with mixture ratio of 1:2, and the experimentally measured values of this mixture for the four different isotopes listed in Table 3.1.

Isotopes	<i>μ bone, theoretical (cm⁻¹)</i>	<i>μ mixture, theoretical (cm⁻¹)</i>	<i>μ mixture, experimental (cm⁻¹)</i>
²⁴¹ Am	0.604	0.56	0.548 ± 0.005
⁵⁷ Co	0.315	0.29	0.260 ± 0.007
⁶⁷ Ga	0.376	0.35	0.34 ± 0.02
^{99m} Tc	0.293	0.27	0.26 ± 0.03

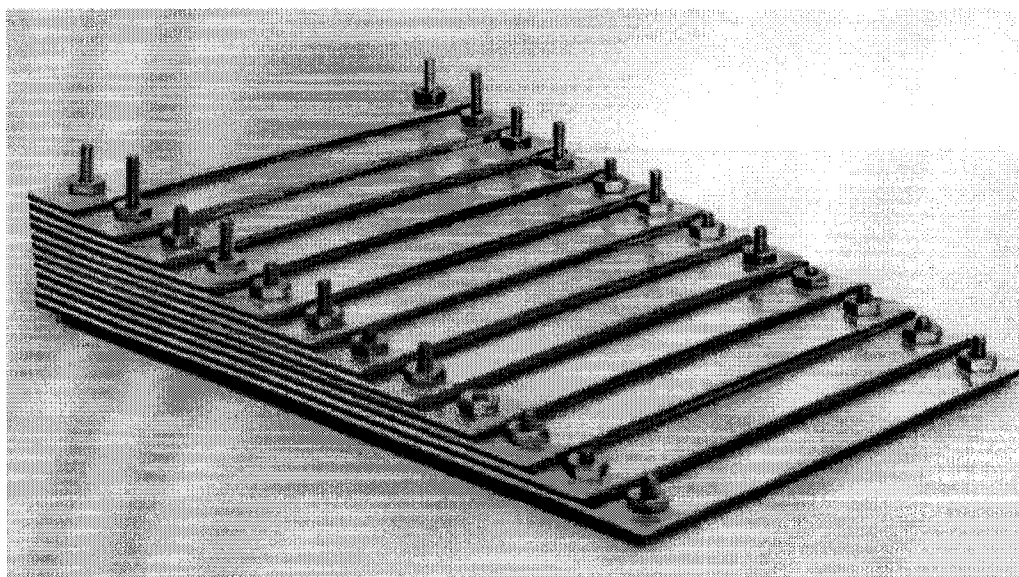


Figure 3.13. The step wedge constructed using aluminum and PVC.

With these results, the 1:2 aluminum-to-PVC thickness ratio is selected for the construction of a step wedge that will be used as the BEM for future experiments. For the construction of the step wedge, 0.032" Alloy 1100 aluminum (88685K17) and 1/16" Type I PVC (8747K145) sheets were once again purchased from McMaster-Carr. This combination will provide a thickness of 0.0945", or about 2.4 mm, between steps. The step wedge is constructed by layering the aluminum and PVC sheets on top of each other to ensure an even "mixing" of the two materials, and to simplify the construction. A total of 12 steps are included in the step wedge, providing a thickness range of 0.0945" to 1.134" (about 2.4 to 28.8 mm). An illustration of the step wedge is shown in Fig. 3.13.

3.2. A Different Soft Tissue Equivalent Material

As mentioned in the introduction to this Chapter, a different type of SEM (soft tissue equivalent material) will be introduced in this section. This SEM consists of a hollow Lucite block filled with water. The Lucite block is fabricated using 2mm Lucite sheets for five sides, with the 6th side (where the drain screw is located) being of 6 mm thickness. The outer dimensions of a single water block are 200 mm wide by 100 mm long by 12 mm thick. Thirty of these blocks are constructed for a thickness range of 1.2 cm to 36 cm. One is illustrated in Fig. 3.14.

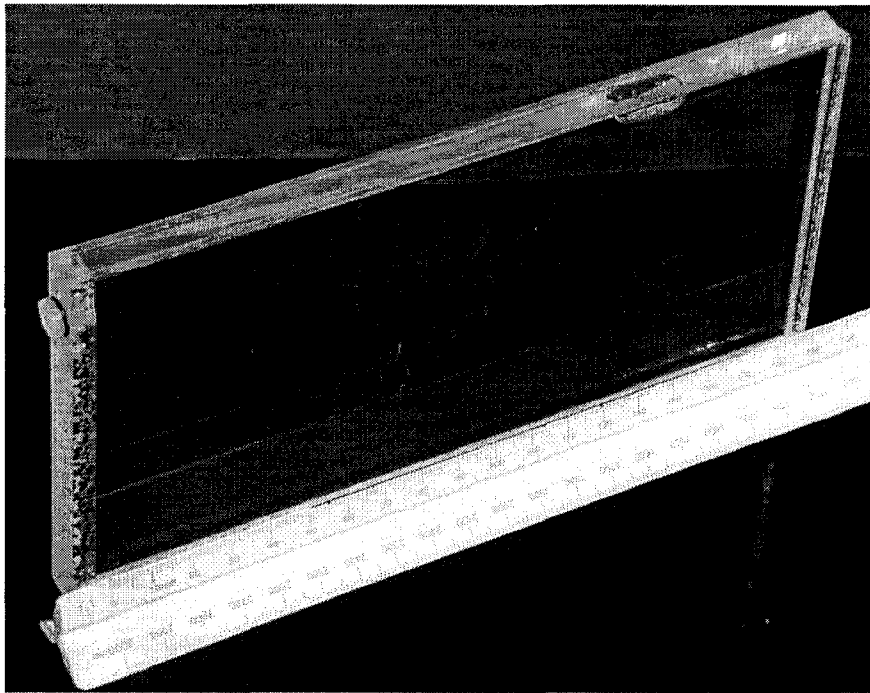


Figure 3.14. An illustration of the water block.

Since the experimental results are similar to the theoretical calculations for bone equivalent material, and the fact that the isotopes needed for the experimental determination of the linear attenuation coefficients are not readily available, only the

theoretical calculation for the linear attenuation coefficient will be examined in this section. If one focus on the center of the water block (the edges are composed of Lucite only), the center is consist of 4 mm of Lucite and 8 mm of water. This will modify Eq. 3.3 to:

$$\begin{aligned}\mu_{water\ block} &= \frac{4\mu_{Lucite} + 8\mu_{water}}{12} \\ \mu_{water\ block} &= \frac{\mu_{Lucite} + 2\mu_{water}}{3}\end{aligned}\quad (3.4)$$

The result of this computation is illustrated in Fig. 3.15. Here the μ of the soft tissue is computed using the soft tissue composition from ICRU-44⁵² as mentioned before. From this Figure, one can observe that the μ of the water block is closer to the ideal soft tissue ratio than Lucite, water or A-150 for the higher energy region, but A-150 and water is slightly better for the lower energy region. However, only a small amount of x-rays from this lower energy region will penetrate and exit the object (such as the patient). Therefore, one would expect the water block to be a more effective soft tissue equivalent material when compared to the A-150 soft tissue equivalent plastic. (Water will not be considered as a SEM by itself since it is obviously very difficult to build a phantom using water alone.)

Once again to illustrate the effect of the SEMs on the x-ray spectra exposing the two imaging plates, the x-ray spectrum shown in Fig. 2.3 is used to compute the follow two energy spectra similar to Section 3.1.1:

- 1) First passing through 10 cm of SEM (to simulate the spectrum exposing the first imaging plate), and
- 2) Secondly, passing through 10 cm of SEM, one PSP plate and 1 mm of Cu filter (to simulate the spectrum exposing the second imaging plate).

Three SEM materials are selected for this calculation. They are Lucite, A-150 plastic and the water block. The results are illustrated in Fig. 3.16. From this Figure, one can observe that the water block spectrum overestimates the number of non-attenuated photons while the A-150 plastic and Lucite underestimate it. Overall, the water block is slightly more accurate when compared to the other two materials as expected.

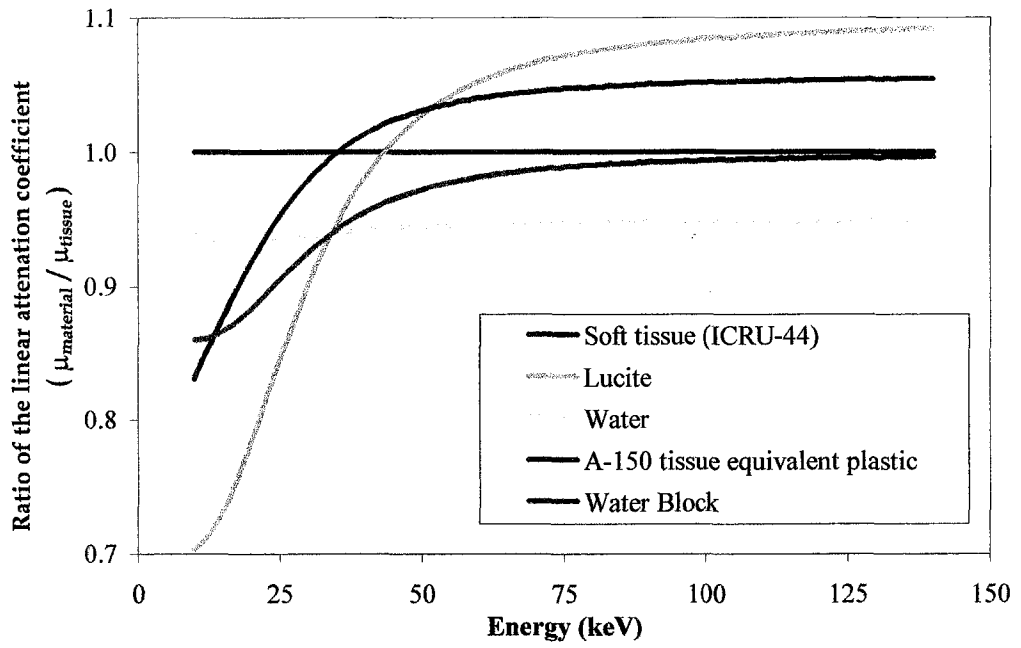
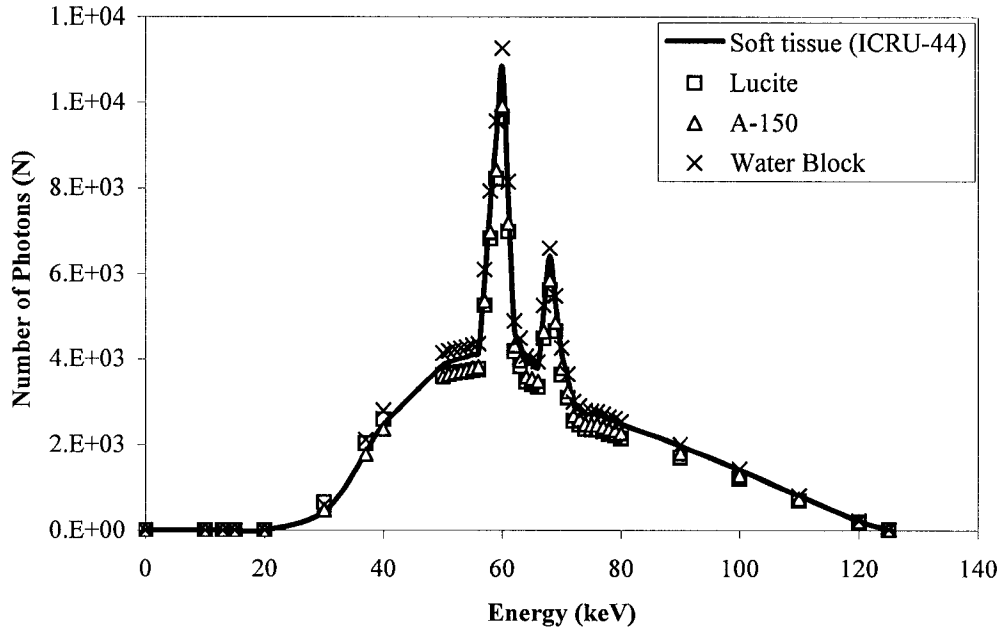
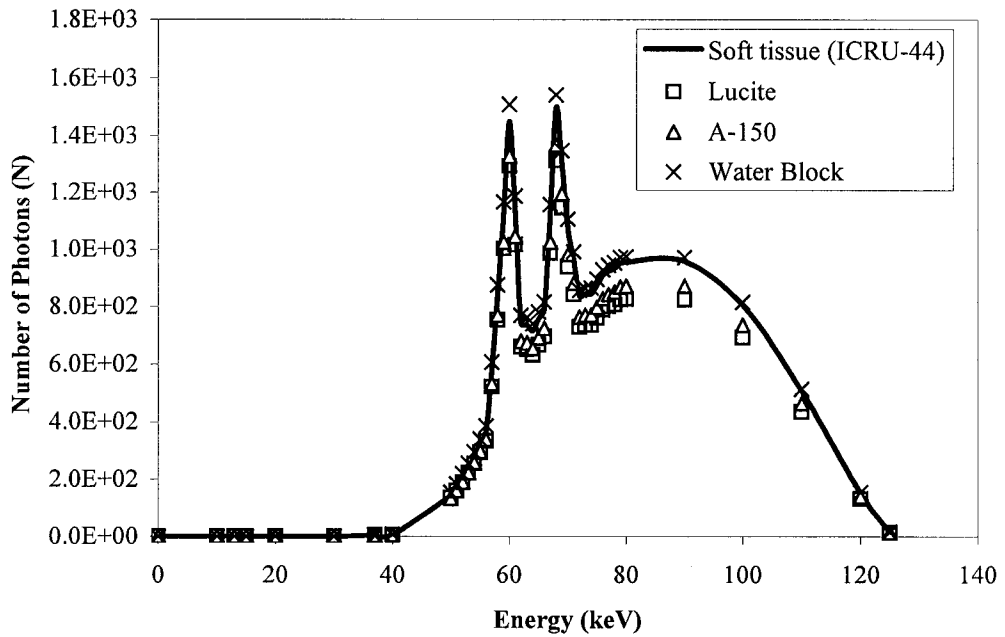


Figure 3.15. The ratio of the linear attenuation coefficient of the water block with respect to soft tissue.



(a)



(b)

Figure 3.16. The x-ray spectra exposing the two imaging plates after passing through 10 cm of different soft tissue equivalent materials. (a) Spectrum exposing the first imaging plate. (b) Spectrum exposing the second imaging plate.

4. Current Approach

As mentioned in Chapter 2, the bone images from the Fuji dual-energy subtraction radiographic unit (FCR XU-D1) is being utilized for the current project. This simplifies the procedures by eliminating the need to decompose the low and high energy images, but may reduce the accuracy of the subtracted images when compared to the decomposition utilizing the equivalent materials shown in the last Chapter.

The detection of ribs in chest radiography has been attempted for some time. This is because the rib structure interferes with many computer-aided diagnosis (CAD) schemes by producing false positive identification.^{53,54} Back in 1973, Toriwaki et al.⁵⁵ tried to identify the ribs by first detecting their edges with an edge detector, and then fitting the profile of the edges with a parabolic equation. In 1977, Wechsler and Sklansky⁵⁶ improved the fitting method by using a mixture of parabolic and elliptical equations for each fit. However, these processes are not very accurate for the larger digital images produced by modern digital radiographic units. In 1988, Powell et al.⁵⁷ proposed the use of a shift-variant sinusoidal pattern to identify the inter-rib spaces

$$f(x) = A \cos\left(\frac{2\pi x}{d(x)} + \varphi\right), \quad (4.1)$$

where $f(x)$ is the sinusoidal background-corrected profile, A is the amplitude of the profile, x is the pixel location, $d(x)$ is the rib plus inter-rib distance at x and φ is the phase term. Although this method works well in locating the region of interest in the inter-rib spaces, it does not identify the ribs. Finally in 1996, Carrascal et al.⁵⁸ attempted to identify the rib edges by first enhancing the inferior and superior rib edges separately. The enhanced images were thresholded⁵⁹ to 80% and the local maxima located. These maxima were then used to reconstruct the rib edges.

One of the problems with many of the above approaches is that the underlying soft tissues in a radiograph interfere with the detection of the rib boundaries. Consequently, the current approach will utilize the bone-only image obtained from the global subtraction method. This should eliminate the interference problem. The Canny edge detector⁶⁰ will be used to locate the rib boundaries. Once the edges are identified, they are used in a segmentation method proposed by Yanowitz and Bruckstein⁶¹ to

separate the bones from the rest of the image. The segmentation method is used because the usual fitting algorithm (as illustrated in Appendix I) will restrict the fit into a predefined equation or parameters, which may reduce the accuracy of the result. Lastly, the missing bone sections in the segmented binary (black and white) image are filled in using a simple binary operation.

At this point in time, one may be wondering why a global detection method utilizing artificial intelligence (such as a neural network) is not used for the identification of the bone structure. This is mainly due to two reasons. Firstly to account for the small variation in human structures, a large database (or amount of images), will be required to train the neural network. Secondly due to the small variation between images, the probability exists that the neural network may miss a small portion of the bone structure. Consequently, this approach will not be used at the current time.

4.1. The Canny Edge Detector

Throughout the years, a number of methods have been introduced to identify edges in an image, since it is one of the most practical applications in image segmentation. The most common method for edge detection is the use of gradient operators. These operators are based on the idea that the gray-levels on the two sides of an edge are distinct. Therefore, by computing these differences between the gray-levels, one should be able to identify the edges. One example of an early edge detector are the Prewitt operators⁶² as illustrated in Fig. 4.1, which are simply a pair of gradient operators. The problem with gradient operators is that they are sensitive to noise, hence any variation in the gray-level may be identified as an edge.

-1	0	1
-1	0	1
-1	0	1

(a)

-1	-1	-1
0	0	0
1	1	1

(b)

Figure 4.1. A pair of Prewitt operators used for edge detection. (a) The Prewitt operator in the x direction. (b) The Prewitt operator in the y direction.

In order to overcome the problem of the gradient edge detector, John Canny⁶⁰ suggested that an ideal edge detector should contain the following three criteria:

1. The edge detector should be able to locate all edges with minimum error. In other words, the detector should detect only edges, without missing any.

2. The detected edge pixels should be as close to the actual edge as possible.
3. The edge detector should eliminate multiple responses from the same edge.

Unfortunately, these criteria are too complex to provide an analytical solution. Fortunately, the derivative of a two-dimensional Gaussian function is a good approximation to the solution. Additionally, the convolution of the derivative of the two-dimensional Gaussian function is separable. This reduces the edge detector into two simpler one-dimension operators, one in the x-direction (G_x) and one in the y-direction (G_y)

$$G_x = \left(-\frac{N_x}{\sigma^2} \right) e^{-\left(\frac{x^2}{2\sigma^2}\right)}$$

$$G_y = \left(-\frac{N_y}{\sigma^2} \right) e^{-\left(\frac{y^2}{2\sigma^2}\right)}$$
(4.2)

Here x and y is the location of the pixel, σ is the standard deviation, or the spread, of the distribution and N is the normalization factor. These operators are illustrated in Fig. 4.2. Once a mask is calculated, it is convolved with the image (A) to produce the x component edge image (A'_x) and the y component edge image (A'_y)

$$A'_x = \sum_{m=1}^M \sum_{n=1}^N A(m,n)G_x(x-m,y-n)$$

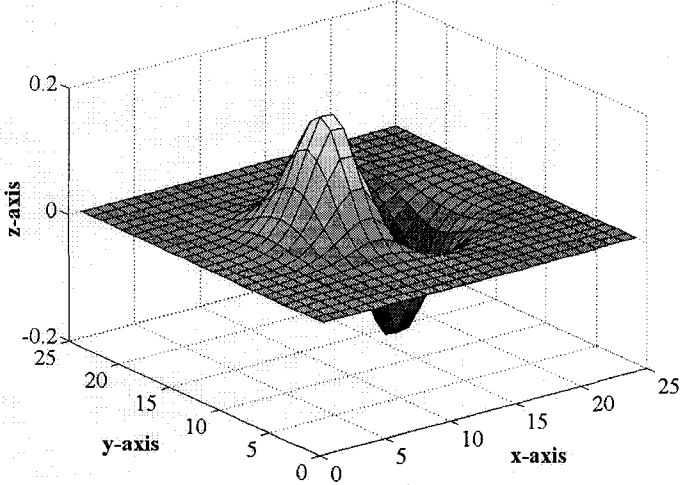
$$A'_y = \sum_{m=1}^M \sum_{n=1}^N A(m,n)G_y(x-m,y-n)$$
(4.3)

Here M is the total number of pixels in the x direction and N is the total number of pixels in the y direction for image A . To acquire the final edge image (A'), these two directional edge images are combined using the root mean square method

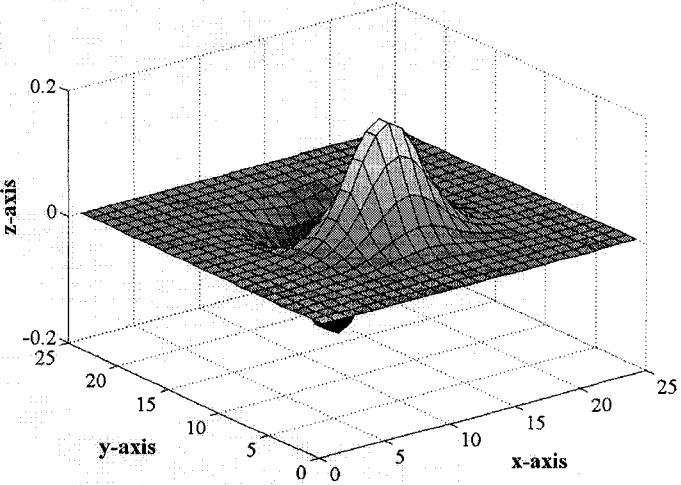
$$A' = \sqrt{(A'_x)^2 + (A'_y)^2}$$
(4.4)

To increase the accuracy of the edge detector, the hysteresis thresholding method was proposed by Canny. Here two thresholding levels, one high (T_h) and one lower (T_l), are used. The pixels that are higher than T_h are assumed to be an edge in the first iteration, while pixels with gradient magnitude that is higher than T_l and are next to an

identified edge pixel are kept in the subsequent iterations. The pixels remaining after the iterations are the edge pixels detected by the Canny edge detector. A detailed discussion of this detector may also be found in Section 1.4 of Parker.⁶³



(a)



(b)

Figure 4.2. The Canny edge detectors. (a) The x axis operator. (b) The y axis operator.

4.2. The Yanowitz and Bruckstein Image Segmentation Method

Once the edge pixels are extracted, the typical approach is to fit these pixels with some predefined function (such as a combination of parabolic and elliptical equations for each rib edge as suggested by Wechsler and Sklansky⁵⁶). Since there is no guarantee that the ribs can be defined by some predefined function(s), such constraint(s) should be avoided. Instead, the image segmentation method as proposed by Yanowitz and Bruckstein⁶¹ will be employed here to separate the bone structure from the rest of the radiograph.

This segmentation method utilizes the edge pixel detected to produce a threshold value for each individual pixel, or a threshold surface. The threshold surface is needed because a single threshold level will not be able to isolate all the bone structure due to the huge amount of noise and the possible uneven background in a typical bone only subtracted image. The segmentation procedure can be summarized into the following:

1. Locating the local maxima, or the edge pixels.
2. Computing the threshold surface with the gray-level of the edge pixels detected in Step #1.
3. Segmenting the image using the threshold surface produced in Step #2.
4. Removing the false positive objects with a validation process.

Since Step #1 will be implemented with the Canny edge detector, this discussion will start with Step #2. The threshold surface may be generated with a number of different approaches, but one of the simpler solutions is obtained when the surface satisfies the Laplacian equation as shown by Yanowitz and Bruckstein. Consequently, the Laplacian operator, as illustrated in Fig. 4.3, will be used to interpolate the threshold surface.

To calculate the threshold surface, one begins by creating a matrix (or image) that contains the values of the edge pixels and boundary conditions, while the rest of the pixels are set to zero. This matrix is then convolved with the Laplacian operator. Once the convolution is completed, it is added to the original image. Then the values of the edge and boundary pixels are adjusted to the original values since these are the interpolation points and already possess the correct values. The convolution and correction procedures will be repeated (or iterated) until the change in the matrices are

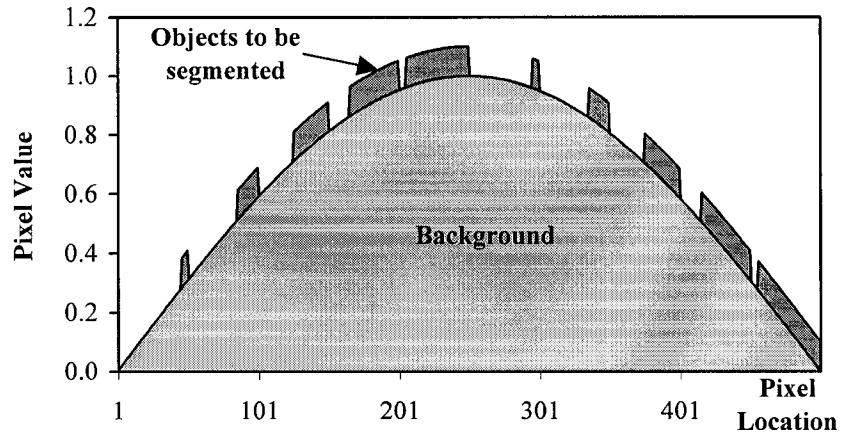
less than some predefined value (such as a small percentage of the total value). The segmentation process for a horizontal profile is illustrated in Fig. 4.4. Although the iteration process is very straightforward, a huge amount of time may be required. Therefore, Yanowitz and Bruckstein suggested the use of the successive over-relaxation method⁶⁴ to speed up the iteration process.

0	-1	0
-1	4	-1
0	-1	0

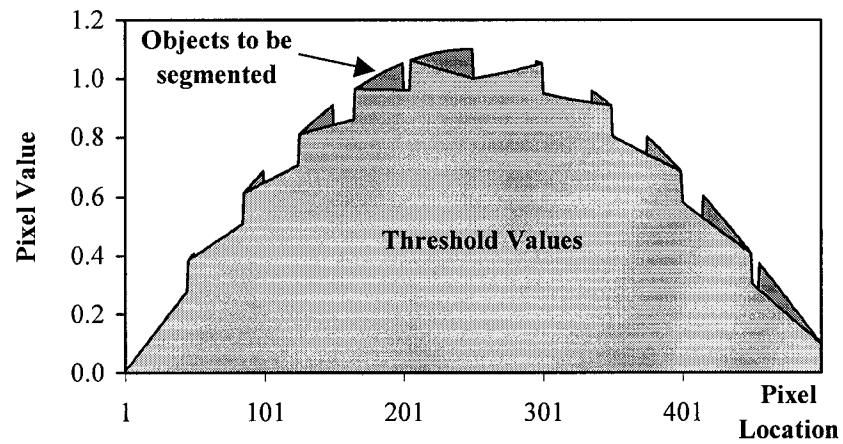
Figure 4.3. The Laplacian operator.

For this study, the Dirichlet boundary condition is used; that is, the value at all four boundaries will be provided. To obtain these values, the one-dimensional Prewitt operator is applied to each of the boundaries, with the endpoints of each boundary set to equal to the values of the bone image at that location. The boundary conditions are obtained when a line satisfying the one-dimensional Laplacian equation is produced by iteration.

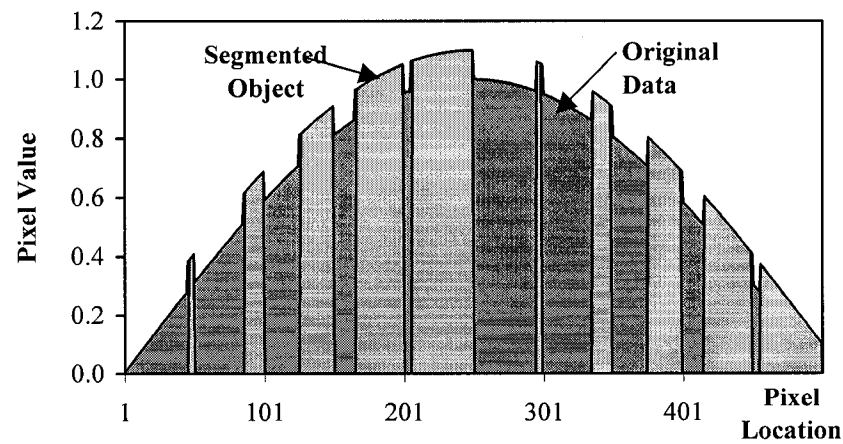
Once the threshold surface is computed, the image can be segmented. In this step, the pixel in the original image with value greater than the threshold is assigned a value of one, while the rest of the pixels will be assigned a value of zero. After the segmentation, a validation process may be applied to eliminate the objects that are falsely identified. One validation method is to first identify all the separate (non-connected) components in the bisected image. Then the average edge pixel value for each individual component is calculated, and objects with value less than some threshold are eliminated.



(a)



(b)



(c)

Figure 4.4. An illustration of the threshold values for a horizontal profile. (a) The original profile. (b) The threshold values computed from the Laplacian equation. (c) The segmented components of the original profile.

4.3. Binary Operation

Once the image has been segmented, an additional operation will be required. This is due to the huge amount of noise contained in the bone image inherited from the dual-energy subtraction procedure, which causes two problems: 1) The noise may interfere with the edge detection process, and lead to part of the bone edges missing in the edge detected image. Although the segmentation process may compensate this problem, a more robust solution may be needed. 2) The noise level may also hinder the segmentation process, which may result in the missing of some small parts (such as a few pixels) of the bone structure throughout the segmented image.

To overcome these concerns, a ranking filter with a double-triangular mask is used. A typical 21×21 double-triangular mask is illustrated in Fig. 4.5. The application of the ranking filter is as follows:

1. The filter mask is multiplied with the binary image on an area-by-area basis similar to the convolution procedure.
2. The resulting matrix, which should contain only ones and zeros, will be sorted, or ranked, from the smallest value (zero) to the largest value (one). This will result in a vector that contains all zeros in the beginning and ones in the end.
3. The values at a particular location of this vector will be used to replace the value at the segmented image.

The ability of the ranking filter with the double-triangular mask to bridge the gaps for four lines with different slopes is illustrated in Fig. 4.6. As one can observe, this ranking filter is employed to fill in gaps that are within $\pm 45^\circ$ from the x axis of the image. The $\pm 45^\circ$ from the x axis are chosen because the problem rib areas in the bisected image are usually within this range, and they are the main interest of this investigation. Also from Fig. 4.6, one may observe that the ranking filter will expand the edges slightly.

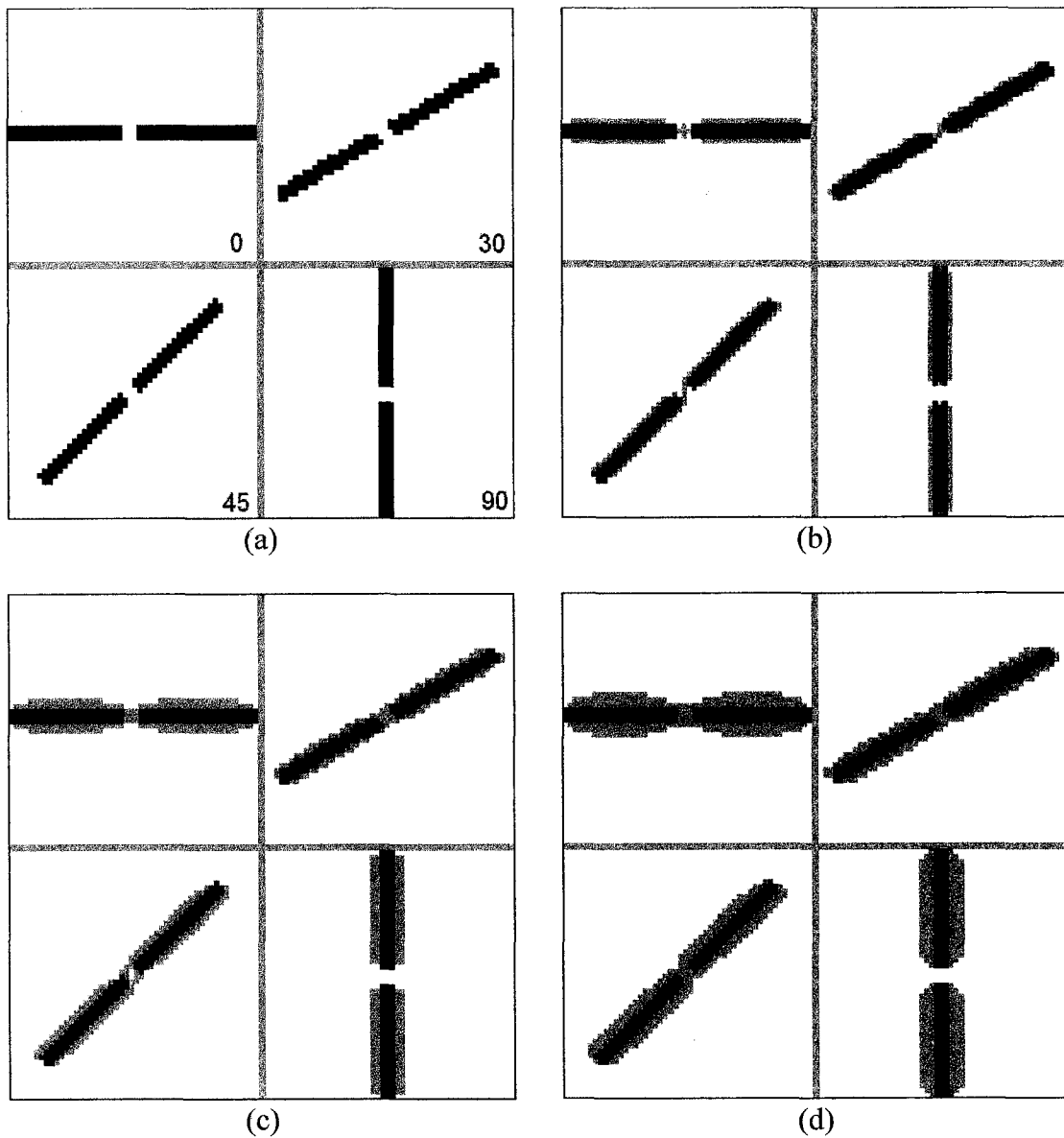


Figure 4.6. A demonstration of the ability of the ranking filter. Four lines are shown in each Figure. The angles with respect to the x-axis for these four lines are 0° , 30° , 45° and 90° as indicated on Figure (a). Here the pixel in black is the original line, the light purple pixels near the original line are the pixels that were filled in, while the red pixels are the ones that were removed. A 5×5 double-triangular mask with a rank order of 12 is utilized here. (a) Original image. (b) After one iteration. (c) After two iterations. (d) After three iterations.

4.4. Software

The algorithms employed in this dissertation are programmed in Matlab Version 5.3 (The MathWorks, Inc., Massachusetts, U.S.A.). Although slower than most other programming languages such as C/C++ in terms of execution time, Matlab is chosen due to its ability to handle matrix manipulation with ease. Operations such as convolution can be applied with a simple call to the “*conv2*” function. Since execution time is less important than the ability to modify the algorithms on-the-fly, Matlab is the ideal programming language for the current study. All computations were performed on a 667 MHz Pentium III PC running Windows NT Version 4.0.

5. Results and Discussion

As discussed in the last chapter, the technique employed to segment the bone structure in the bone-only image from the Fuji dual-energy subtraction system is as follows:

1. The edges of the bone structure are detected using the Canny edge detector.
2. A threshold surface fitting the Laplacian equation is computed and used to segment the bone-only image.
3. The gaps and holes in the bisected image are filled in with a ranking filter.

In this chapter, the results from each of these procedures will be examined. In Section 5.1, the ability of the Canny edge detector will be investigated, while the results from the threshold surface segmentation process will be discussed in Section 5.2. The results of the binary operation will be presented in Section 5.3. In these three sections, one phantom and one real patient image will be used to study the effect of the different processes. Two different images are chosen because the response of each process may be different between different images, and compromises may have to be made. This is also why a theoretical examination is not included, since an optimized process for a theoretical image may not work well with other images. After the identification processes have been optimized, they will be applied to a number of different phantom and real patient images in Section 5.4, while the final reconstructed soft tissue will be shown in Section 5.5.

5.1. The Canny Edge Detector

In this section, the edge-detected image of the bone-only radiographic images for an anthropomorphic chest phantom and a real patient will be examined for various edge detectors and parameters. The chest phantom (34-7002-0826-6) is manufactured by 3M, and is illustrated in Fig. 5.1. Before the edge detector is applied to the image, the bone image is first processed by a 7×7 median filter to reduce the noise in the image. (A median filter is a noise reduction filter that operates by replacing the gray-level of the each pixel in the image with the median of the gray-levels in the predefined neighborhood.) The size of the median filter is a compromise between maximum noise reduction (larger size) and minimum loss of edge pixels (smaller mask). The ability of the median filter is demonstrated in Fig. 5.2 for a section of the real patient chest radiograph. The edge detector utilized for this Figure is the default Canny edge detector found in Matlab. From this Figure, one can observe that the median filter did significantly reduce the noise in the edge-detected image.

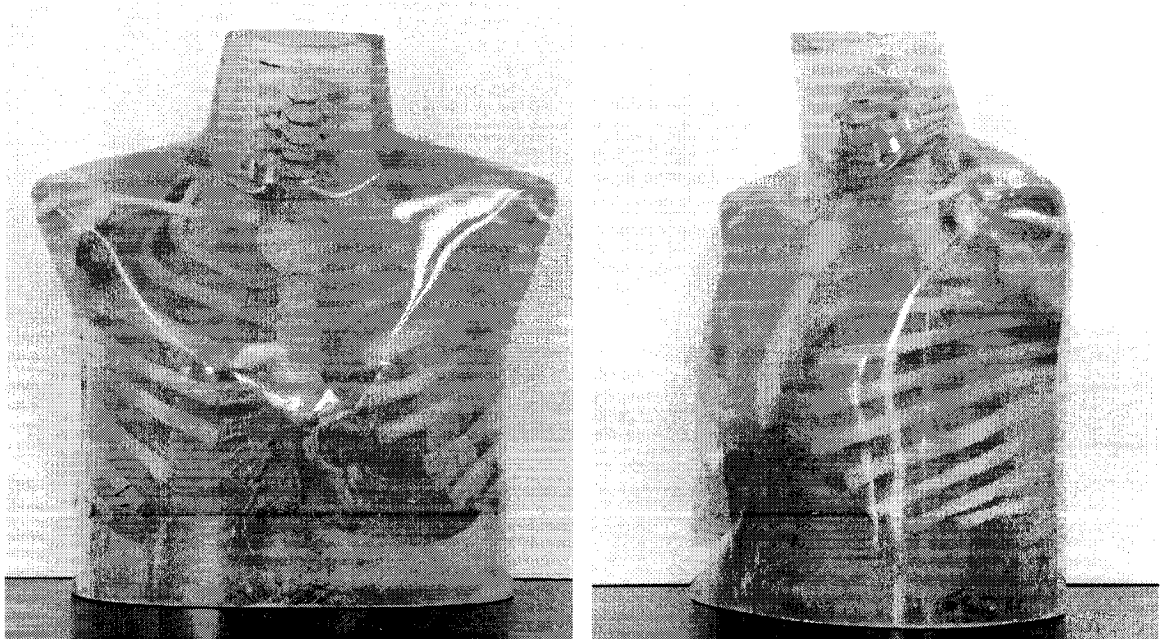


Figure 5.1. The anthropomorphic chest phantom.

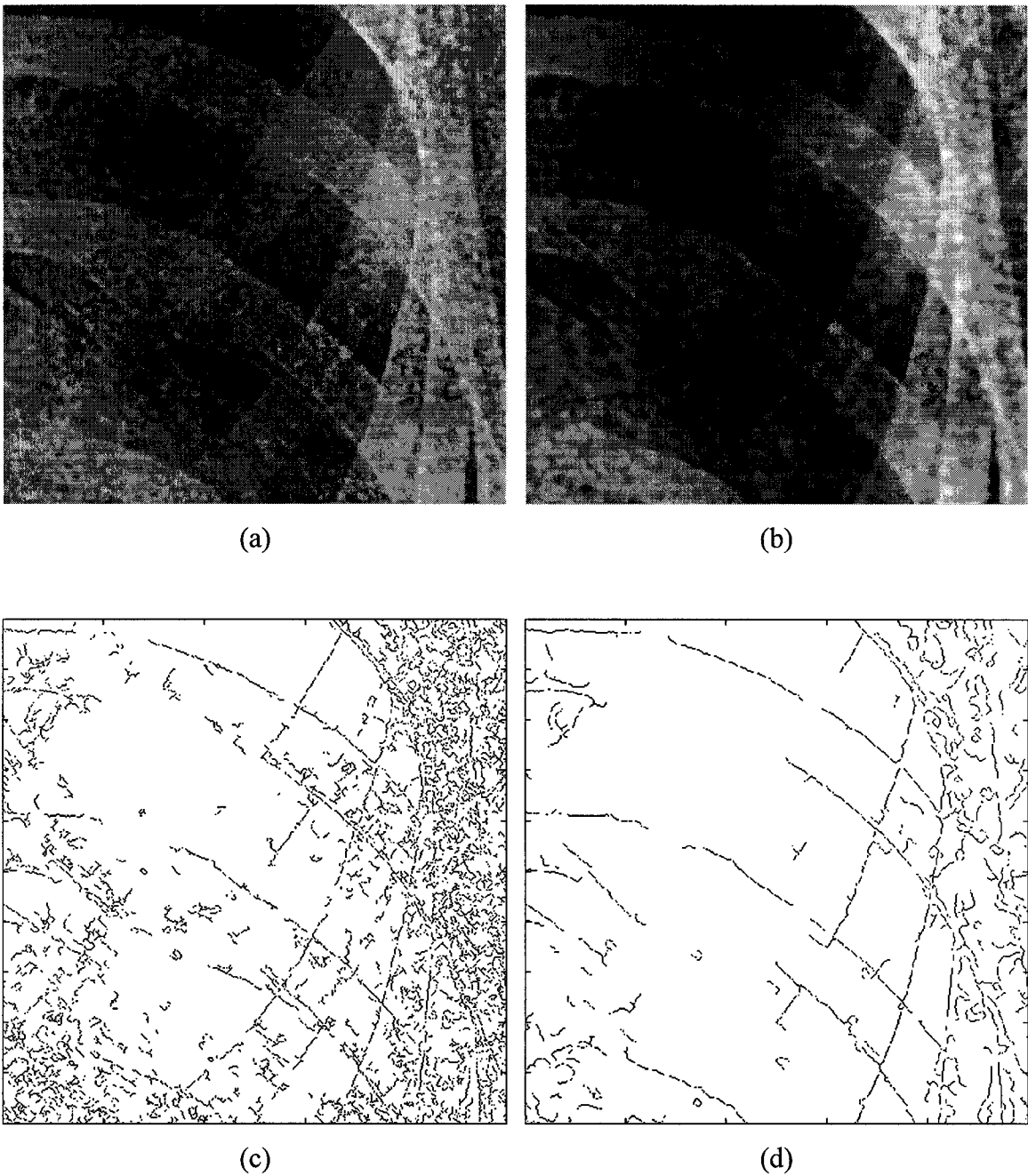


Figure 5.2. An illustration of the noise reduction capability of the median filter. (a) The original image. (b) The median filtered image. (c) The edge-detected image of a. (d) The edge-detected image of b.

To provide a quantitative analysis of the median filtered edge image (and the subsequent edge images), Pratt's figure of merit (FM) of edge quality is used⁶⁵

$$FM = \frac{\sum_{i=1}^{I_A} \frac{1}{1 + \alpha (d(i))^2}}{\max\{I_A, I_I\}} \quad (5.1)$$

Here I_A is the actual number of edge pixels detected, I_I is the ideal number of edge pixels and d is the distance between the i th detected pixel and the actual edge pixel. The constant α is a scaling factor that provides a relative weighting between smeared and thin but offset edges, and is set to 1/9 (as indicated by Pratt). Clearly for a perfect edge detector, the distances for all the detected and actual edge pixels will be zero. As a result, the figure of merit will be one (assuming all edge pixels are detected), and the edge detected image with a higher merit will have a FM value closer to 1.

In order to utilize Eq. 5.1, the location of the ideal edge pixels will need to be known. These locations are obtained by manually tracing the edge of a section (500×500 pixels) of the original phantom images. The resulting edge pixels, superimposed onto the original radiography, are shown in Fig. 5.3. Although some errors are expected on the exact location of the edge pixels, this should nevertheless provide a rough estimate of merit of the edge detected image. The next step is to calculate the distance (d) between the detected pixel and the actual edge pixel. In order to compute this distance, one will need to pair up the detected and the actual edge pixel, a tedious task. Instead, this distance is approximated as the distance between the detected and the nearest edge pixel.

With these approximations, FM is computed for the original (Fig. 5.2c) and the 7×7 median filtered (Fig. 5.2d) Canny edge detected image. The results are 0.5096 and 0.5962 respectively. These demonstrate that the median filtered edge detected image is better than the original edge detected image as observed in Fig. 5.2.

After the median filtering, the two radiographic images are processed with four different edge detectors:



Figure 5.3. An illustration of the ideal edges for a section of the phantom radiography. The ideal edges are illustrated as the white lines in the image.

- 1) The Prewitt edge detector as illustrated in Fig. 4.1.
- 2) The Sobel edge detector, which is similar to the Prewitt detector but with a smoothing feature added.
- 3) The Laplacian of the Gaussian function.
- 4) The Canny edge detector with hysteresis threshold.

These four detectors are chosen because they are readily available in Matlab, and will be applied with their default settings. (The optimization of the detector will be performed once the best edge detector is identified.) Since the edges in the detected image are too fine to display properly as a whole image, only four smaller sections will be illustrated here. The locations for these four regions of interest are depicted in Fig. 5.4 for the anthropomorphic chest phantom. The resulting edge detected images for these four processes are then illustrated in Figs. 5.5 to 5.8. Similarly, the original bone-only radiographic image of the real patient with the four regions of interest is shown in Fig. 5.9, and the resulting edge detected images for the four processes are illustrated in Figs. 5.10 to 5.13.

From Figs. 5.5 and 5.6, one can observe that the Prewitt and Sobel filters do a very poor job in detecting the edges of ribs that are relatively flat. On the other hand,

these edge detectors were able to detect the edges where the curvature of the ribs is at its maximum. Lastly, the noise level in the edge-detected image is relatively low for these two filters. Fig. 5.7 depicts the result from the Laplacian of the Gaussian function. Here, the amount of rib edges detected is slightly better than the Prewitt or the Sobel masks. However, the amount of noise contained in the detected image is also higher. Also, double identification of the same edge, as indicated by the two sets of edges for the same bone edge, is clearly visible.

The results using the Canny edge detector are illustrated in Fig. 5.8. Here the amount of edge detected is better than with the other detectors. Also the amount of noise observed is less than the Laplacian of the Gaussian function. Similar results can be observed for the real patient images as illustrated in Figs. 5.10 to 5.13. Based on these results, one can conclude that the Canny edge detector would be the better choice for the current application. The figure of merit is also computed for a section of the edge detected phantom image (Fig. 5.3) for these four detectors. The results are 0.4171, 0.4225, 0.4729 and 0.5962 for the Prewitt, Sobel, Laplacian of the Gaussian, and Canny edge detector respectively. Clearly, the Canny edge detector outperforms all the other three edge detectors, as observed.

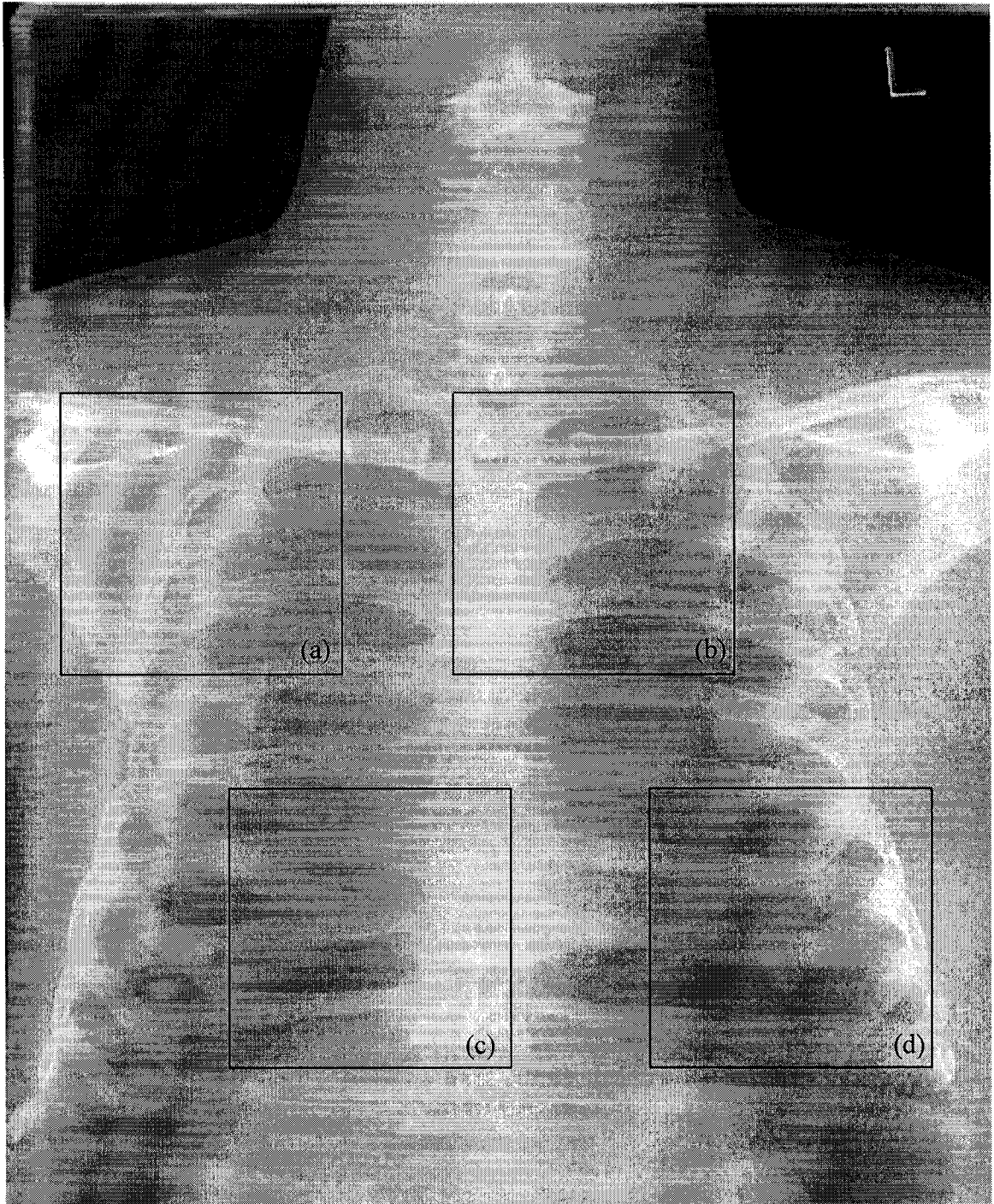


Figure 5.4. An illustration of the locations of the four areas of interest in the anthropomorphic chest phantom image. Here the letters “a”, “b”, “c” and “d” denote the four regions of interest.

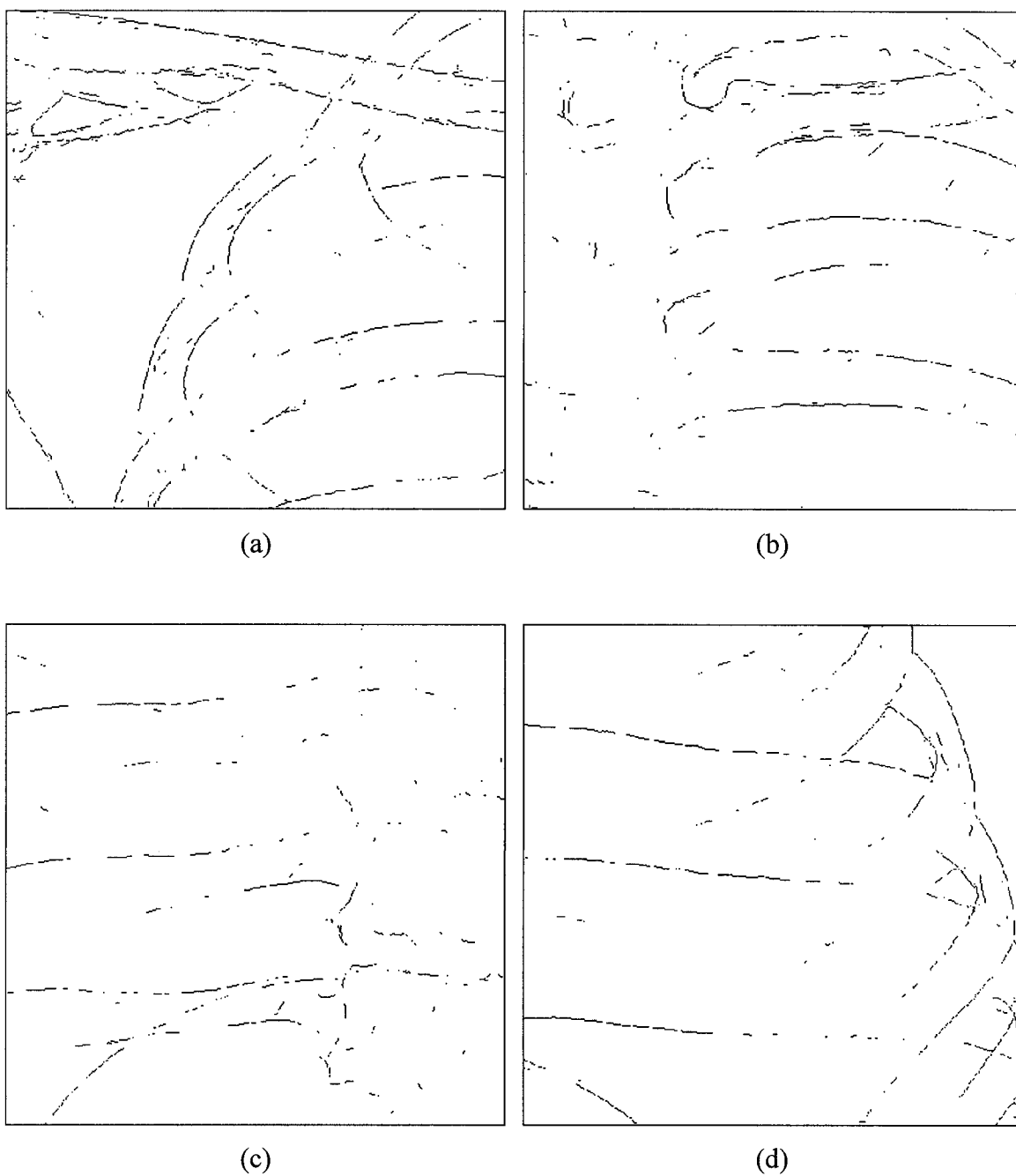


Figure 5.5. The edge detected image of the anthropomorphic chest phantom employing the Prewitt filter. Here (a) to (d) correspond to the edge detected image of (a) to (d) in Fig. 5.4.

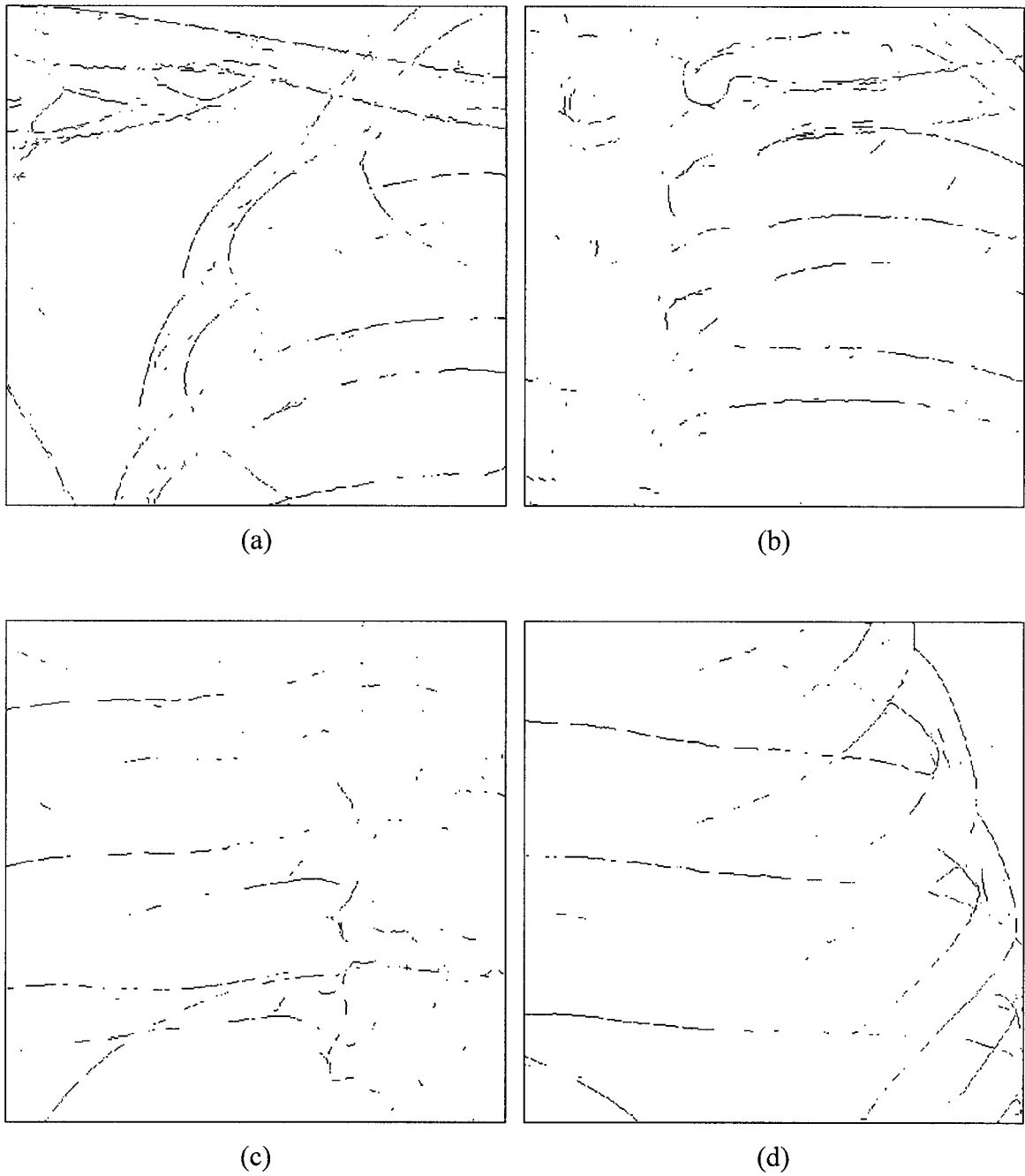


Figure 5.6. The edge detected image of the anthropomorphic chest phantom employing the Sobel filter. Here (a) to (d) correspond to the edge detected image of (a) to (d) in Fig. 5.4.

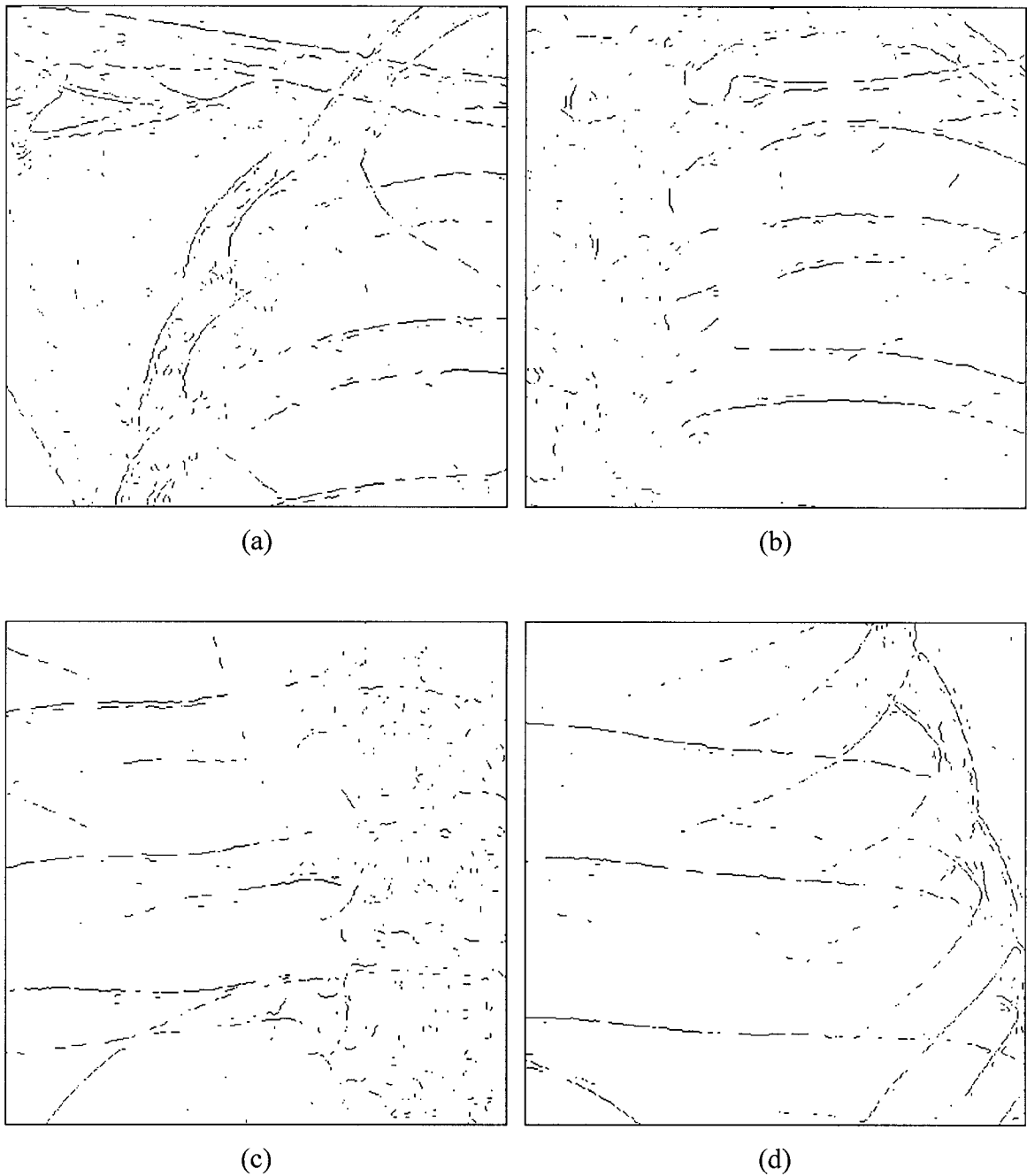


Figure 5.7. The edge detected image of the anthropomorphic chest phantom employing the Laplacian of the Gaussian function. Here (a) to (d) correspond to the edge detected image of (a) to (d) in Fig. 5.4.

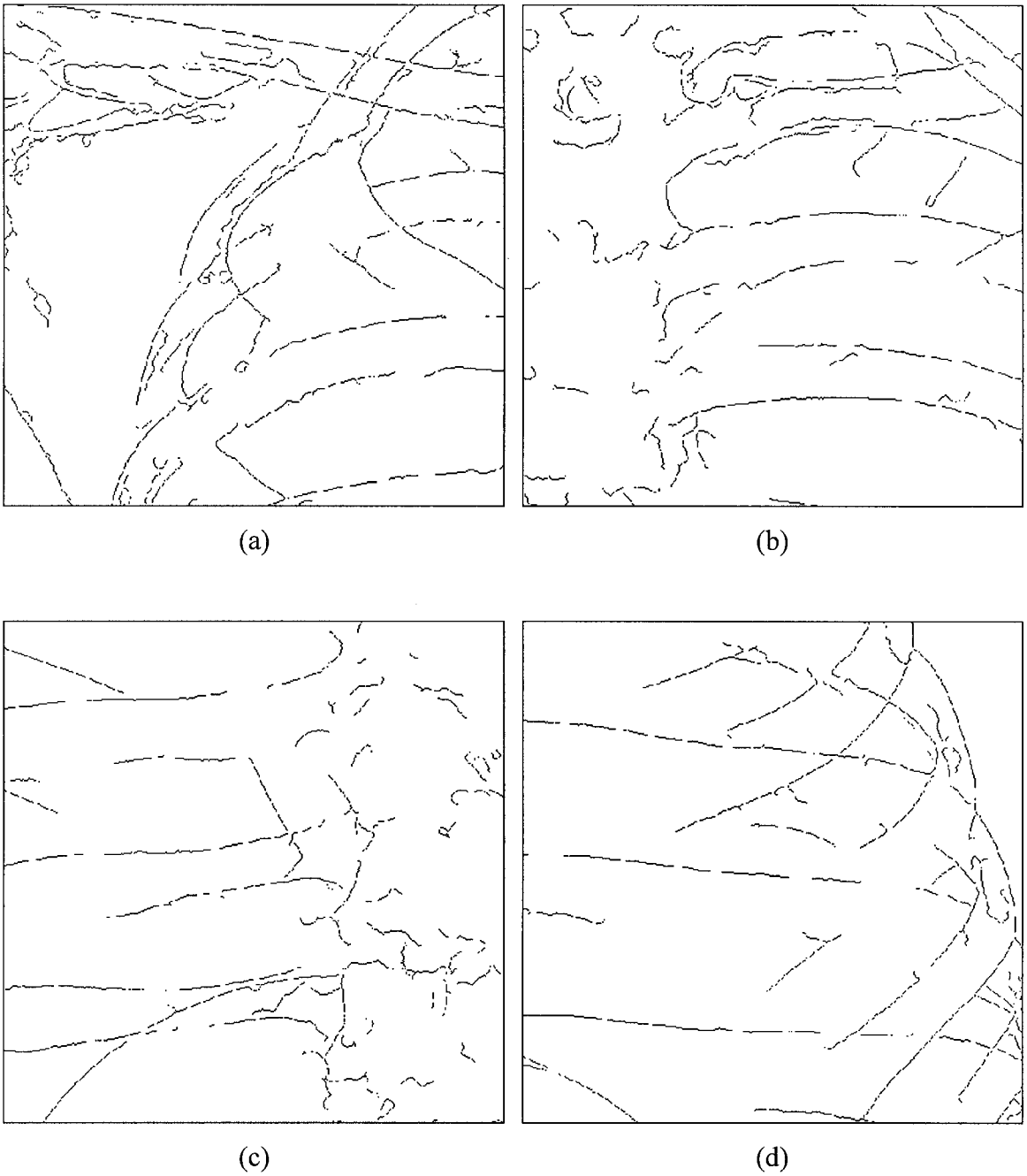


Figure 5.8. The edge detected image of the anthropomorphic chest phantom employing the Canny filter with hysteresis threshold. Here (a) to (d) correspond to the edge detected image of (a) to (d) in Fig. 5.4.



Figure 5.9. An illustration of the locations of the four areas of interest in the real patient image. Here the letters “a”, “b”, “c” and “d” denote the four regions of interest.

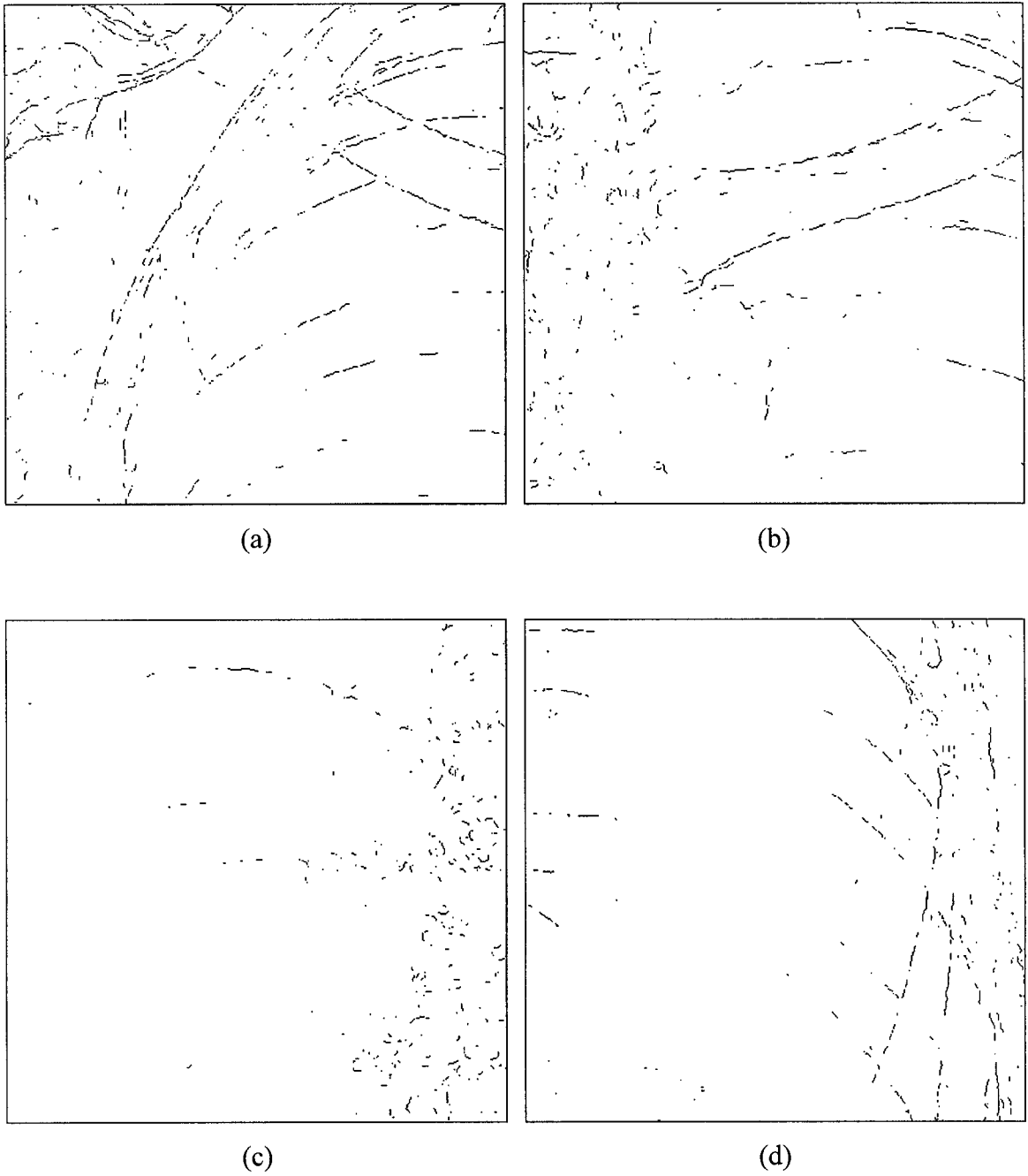


Figure 5.10. The edge detected real patient image employing the Prewitt filter. Here (a) to (d) correspond to the edge detected image of (a) to (d) in Fig. 5.9.

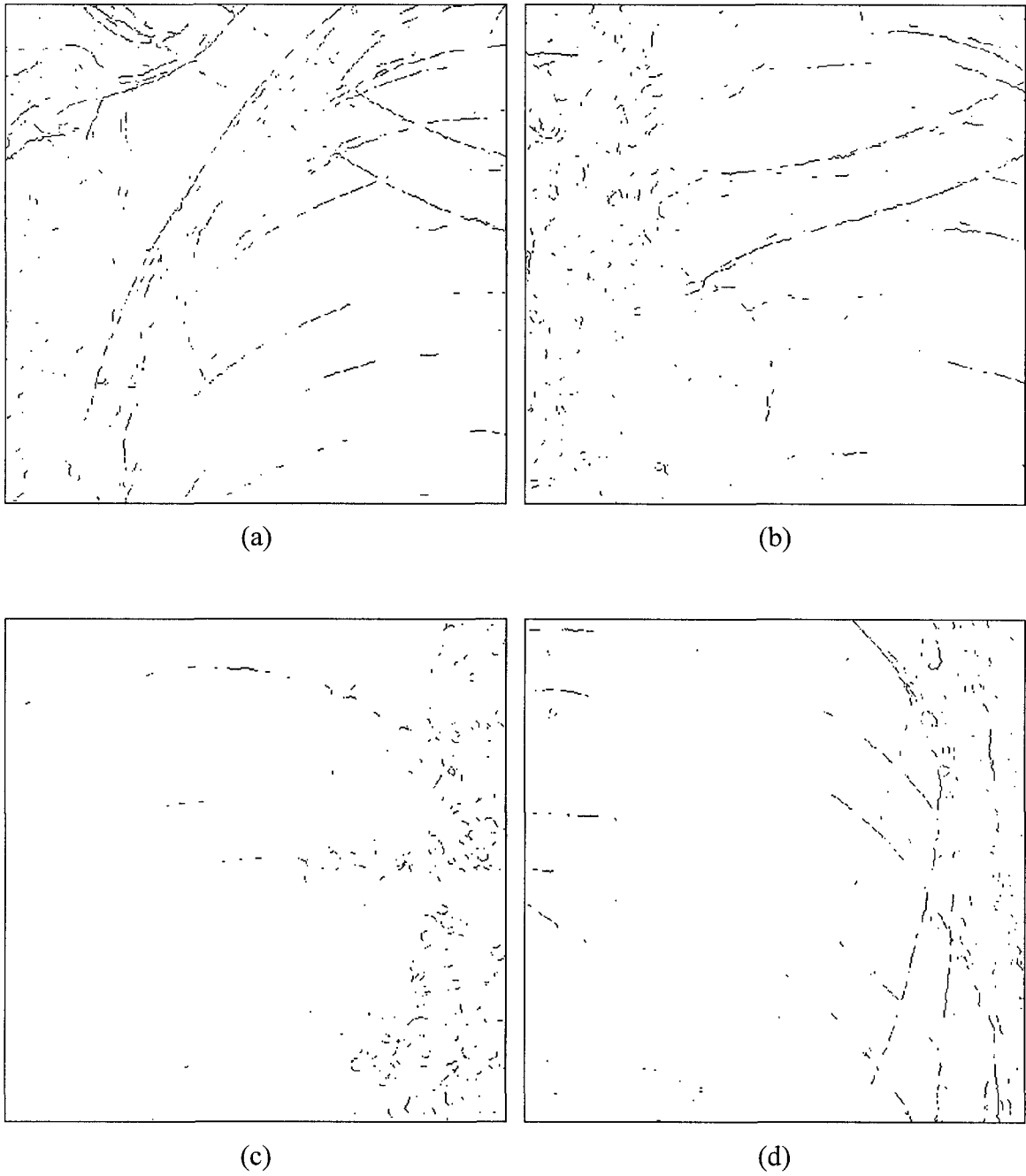


Figure 5.11. The edge detected real patient image employing the Sobel filter. Here (a) to (d) correspond to the edge detected image of (a) to (d) in Fig. 5.9.

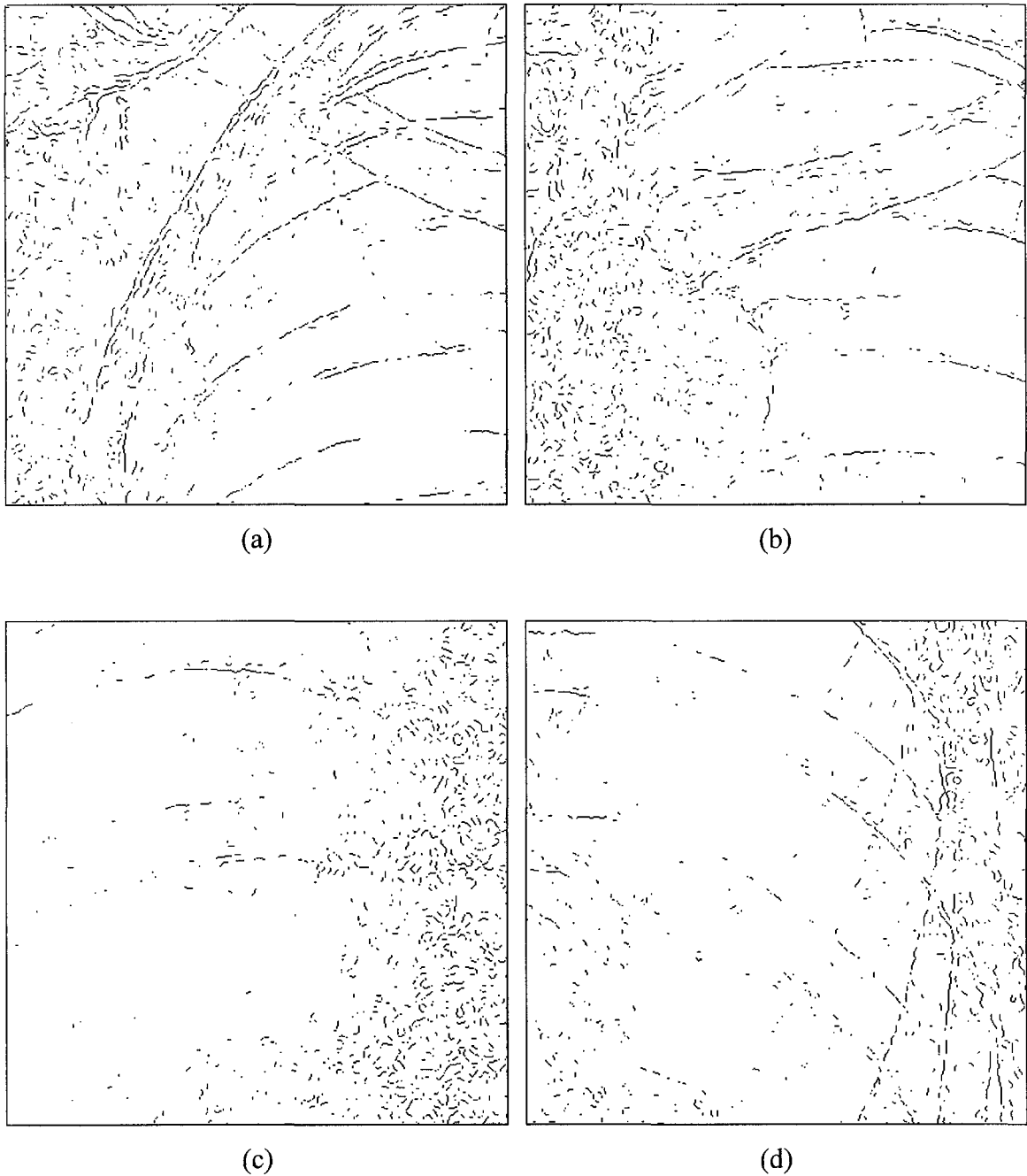
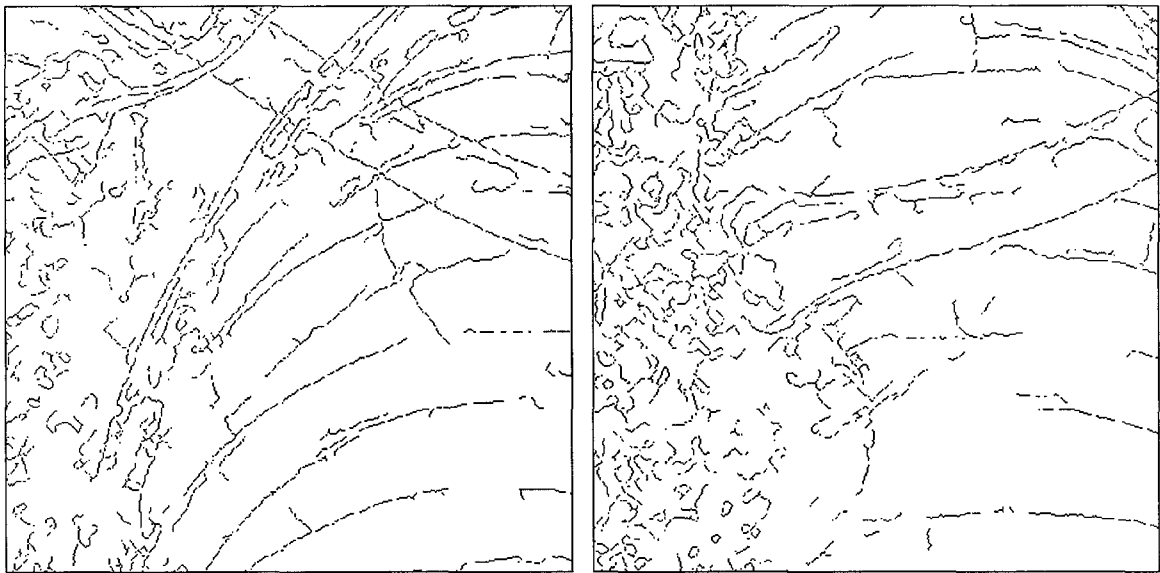
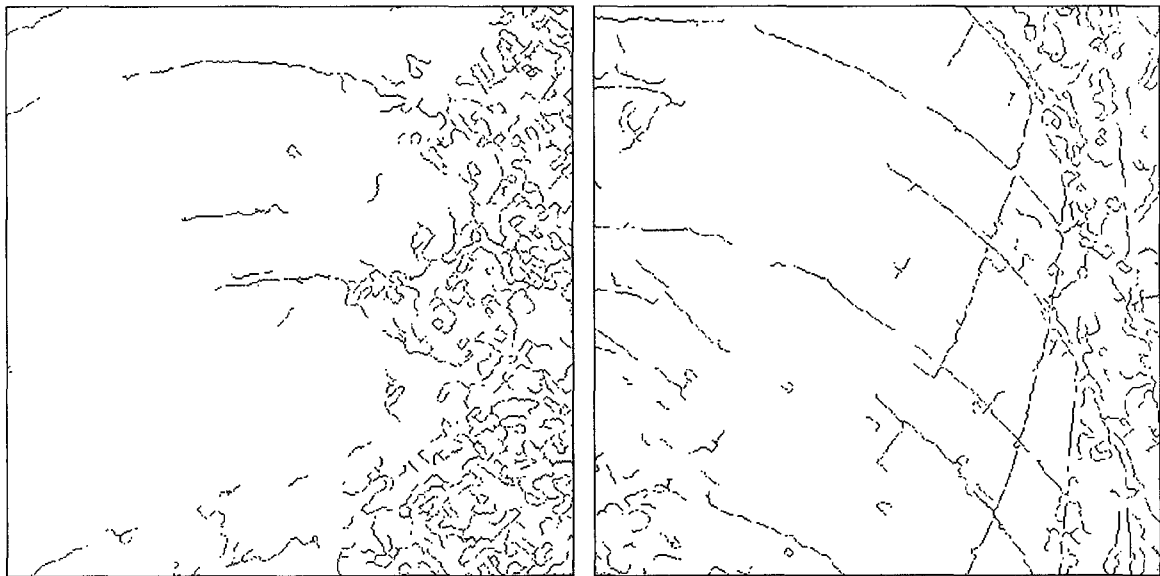


Figure 5.12. The edge detected real patient image employing the Laplacian of the Gaussian function. Here (a) to (d) correspond to the edge detected image of (a) to (d) in Fig. 5.9.



(a)

(b)



(c)

(d)

Figure 5.13. The edge detected real patient image employing the Canny filter with hysteresis threshold. Here (a) to (d) correspond to the edge detected image of (a) to (d) in Fig. 5.9.

Although the edge detection ability of the Canny edge detector using the default setting is good, there may be room for improvement. Three adjustable settings exist within the Canny edge detector. They are:

- 1) σ , or the spread of the Gaussian function, which has a default value of one.
- 2) T_h , or the upper threshold level, which is adjusted automatically for each image in Matlab, and
- 3) T_l , or the lower threshold level, and is also adjusted automatically for each image.

Although a number of σ 's have been examined to optimize the Canny edge detector for the current study, only three of the more representative values will be depicted here in Figs. 5.14 to 5.16 for the anthropomorphic chest phantom, and in Figs. 5.17 to 5.19 for the real patient radiograph. In Matlab, the size of the filter will be adjusted automatically with respect to the sigma value, since a larger sigma implies a bigger filter. The sigma values for Figs. 5.14 and 5.17 are equal to one, which is the default setting for the Canny edge detector in Matlab. The T_h and T_l for all these Figures are kept at the default values for σ equal to 1. From Figs. 5.14 and 5.17, one can observe that some of the rib edges are not detected when compared with the other images processed with larger sigma values. However, the noise level in Figs. 5.14 and 5.17 is very low. On the other hand, more rib edges are identified in Figs. 5.15 and 5.18 ($\sigma = 3.5$), with more noise included in these two images. Finally, the amount of noise in Figs. 5.16 and 5.19 ($\sigma = 7$) is slightly less than Figs. 5.15 and 5.18, but with less posterior rib edges detected. Also, the edges detected with σ equals to 7 tend to be a bit softer than the ones detected with $\sigma = 3.5$. This is because the Canny edge detector utilizes the Gaussian function to reduce the noise in the image, which may also affect the rib edges by removing some of the edge pixels (similar to the median filter).

The figures of merit are computed for the sigma range of 0.5 to 10, and are illustrated in Fig. 5.20. In this Figure, two different *FMs* are computed: one for the normal (whole) edge image and the second for the edge image with the shoulder region removed as illustrated in Fig. 5.21. This second *FM* is computed because the ribs are the main regions of interest for the current study. From Fig. 5.20, one can observe that the

optimal sigma range for the detection of the whole section is about 1 to 1.5, while for the ribs only image, it is about 2 to 4. Based on these observations, the sigma value equal to 3.5 is chosen for the subsequent analysis since it proved a good compromise between good rib edge detection capability and minimum (rib edge) manipulation.

For the upper and lower threshold values, one would expect a higher threshold value corresponding to a less noisy image, but with more of the bone edges eliminated. This is because a higher threshold value corresponds to a higher cutoff level. Conversely, a lower threshold value will maintain more of the identified bone edges, but at the expense of more noise. These expectations are proven in Figs. 5.22 to 5.24 for the phantom radiograph. The default value for Matlab for this particular image is 0.015625, and is illustrated in Fig. 5.23. From these three Figures, one can observe that the default value provides a good balance between noise suppression and preservation of the detected bone edge. Similar results (not shown) were observed for the real patient image with different T_h values, as well as for the phantom and real patient images with different T_l values. On top of these observations, the figures of merit are also computed for different values of T_h and T_l . The results are shown in Figs. 5.25 and 5.26 respectively. From these two Figures, one can observe that the optimal T_h for the ribs only image is about .015, which is close to the default value of 0.015625 from Matlab. For the optimal T_l value, the range of 0.000 to 0.006 produces the highest FM values for the rib only image. Since the T_l value dictates the amount of noise remaining on the image, one should utilize the largest T_l value possible. As a result, T_l equal to 0.006 will be the better choice, which is close to the default value of 0.00625 used in Matlab. Based on these observations and computed FM values, the default T_h and T_l values are selected for use in the subsequent analysis.

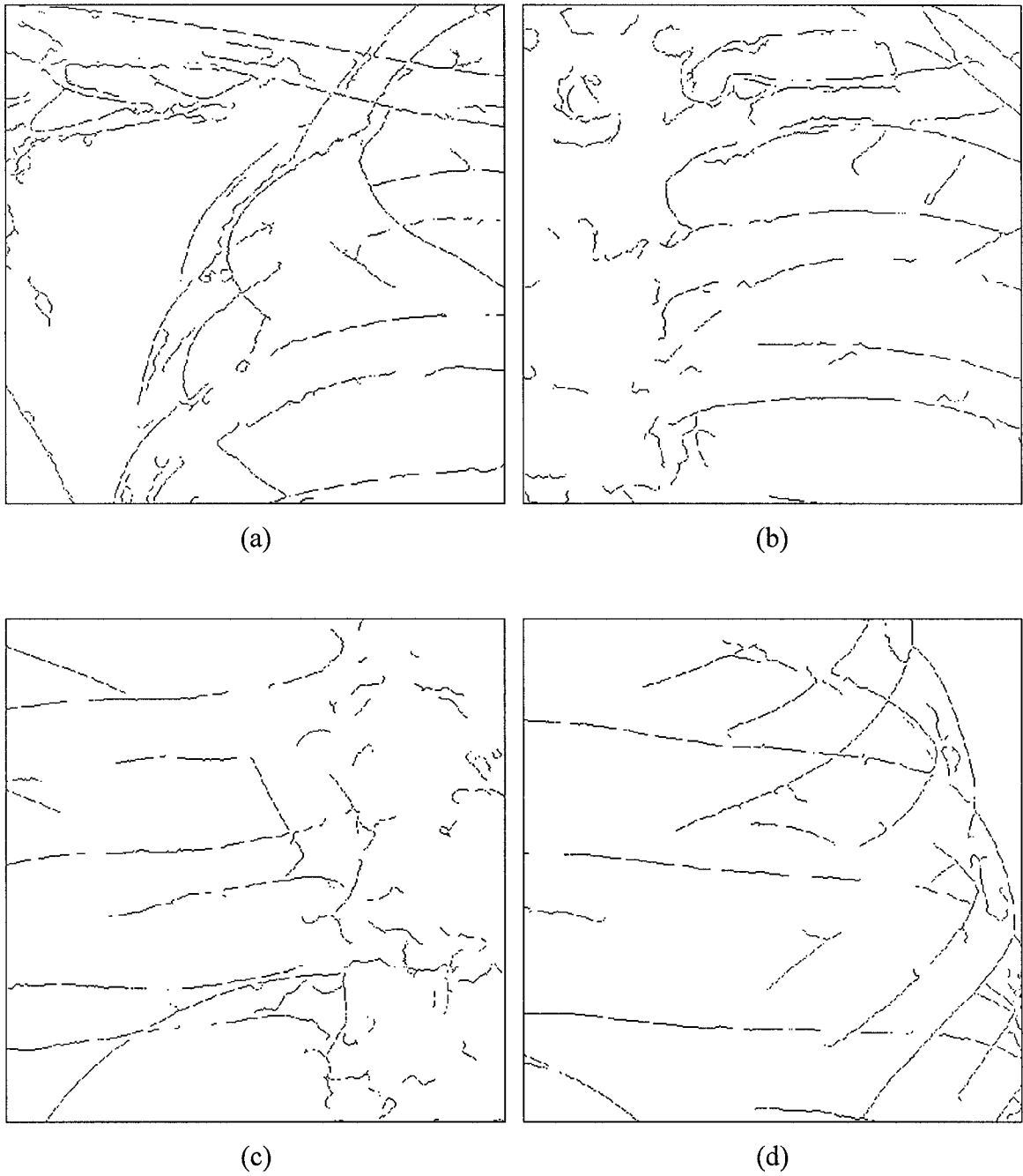


Figure 5.14. The edge detected image of the anthropomorphic chest phantom employing the Canny edge detector with $\sigma = 1$. Here (a) to (d) correspond to the edge detected image of (a) to (d) in Fig. 5.4.

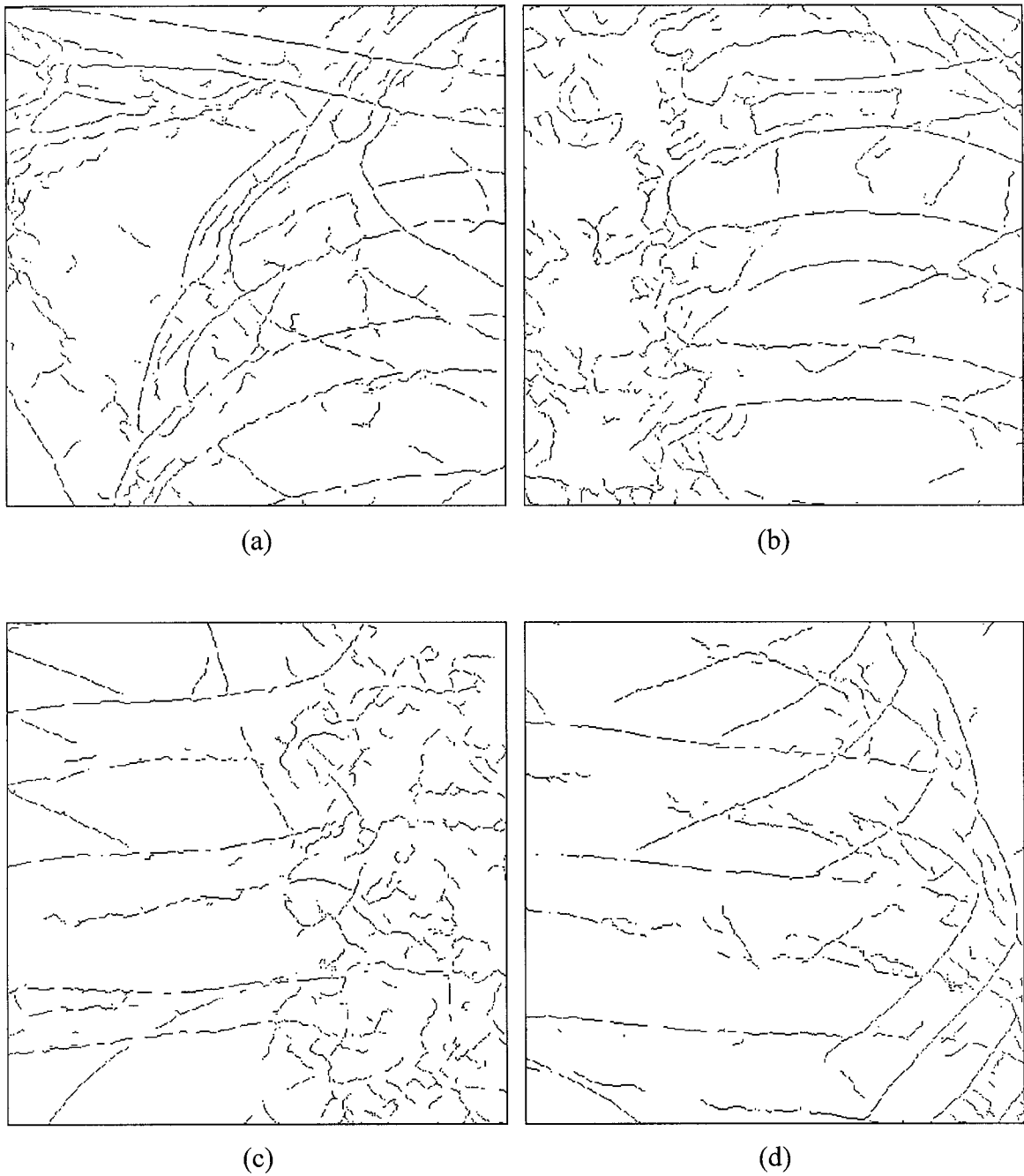


Figure 5.15. The edge detected image of the anthropomorphic chest phantom employing the Canny edge detector with $\sigma = 3.5$. Here (a) to (d) correspond to the edge detected image of (a) to (d) in Fig. 5.4.

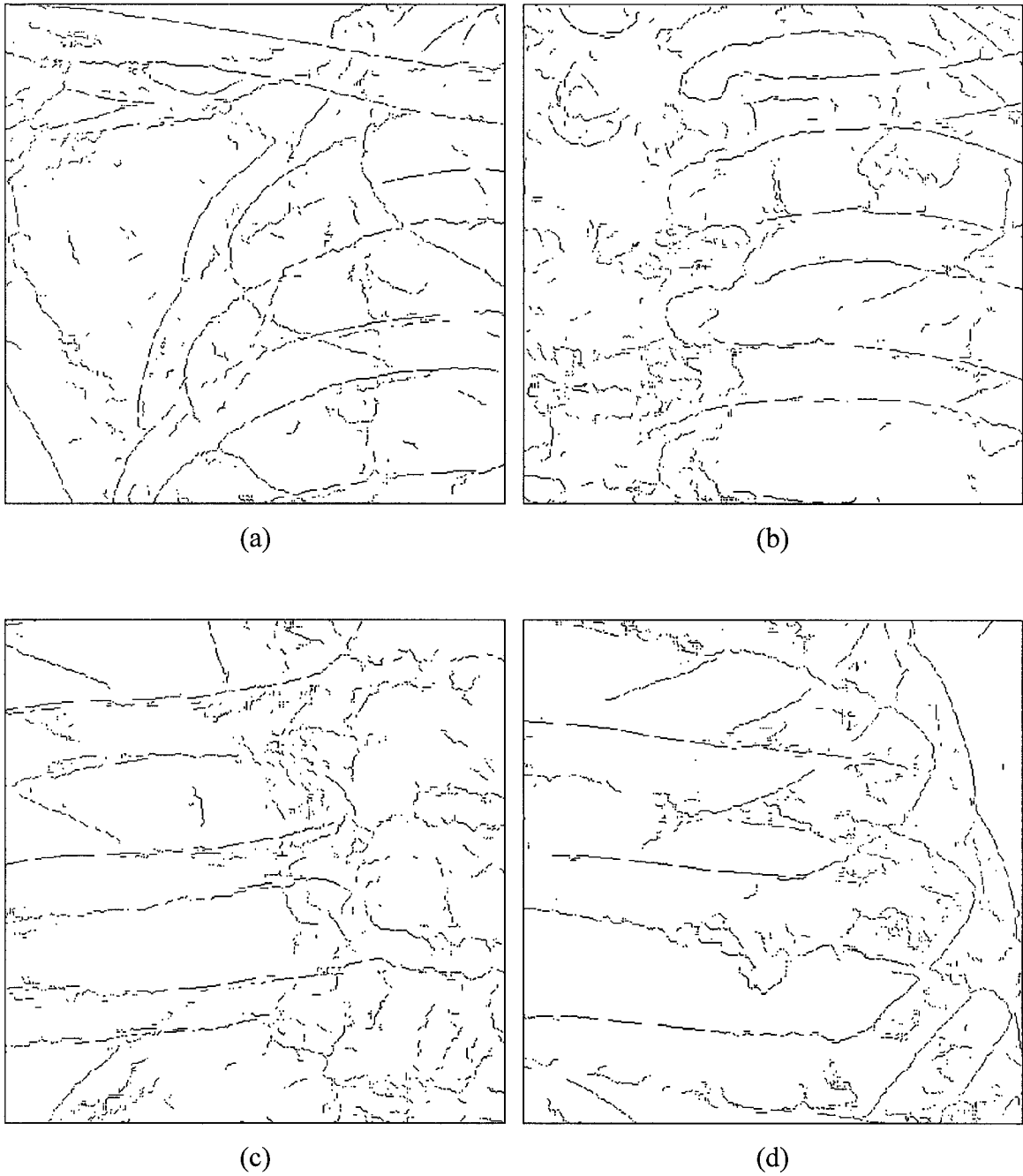


Figure 5.16. The edge detected image of the anthropomorphic chest phantom employing the Canny edge detector with $\sigma = 7$. Here (a) to (d) correspond to the edge detected image of (a) to (d) in Fig. 5.4.

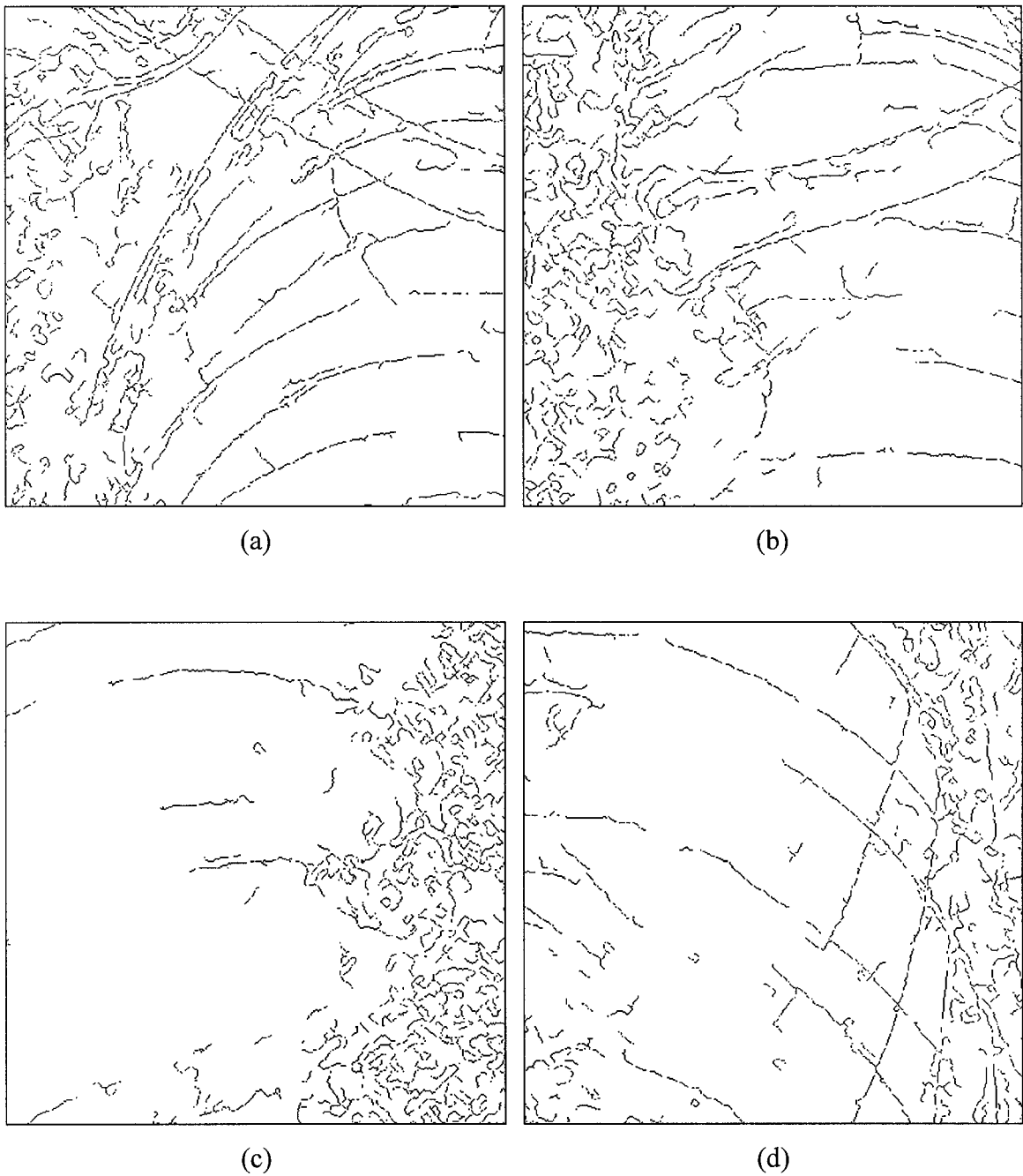


Figure 5.17. The edge detected real patient image employing the Canny edge detector with $\sigma=1$. Here (a) to (d) correspond to the edge detected image of (a) to (d) in Fig. 5.9.

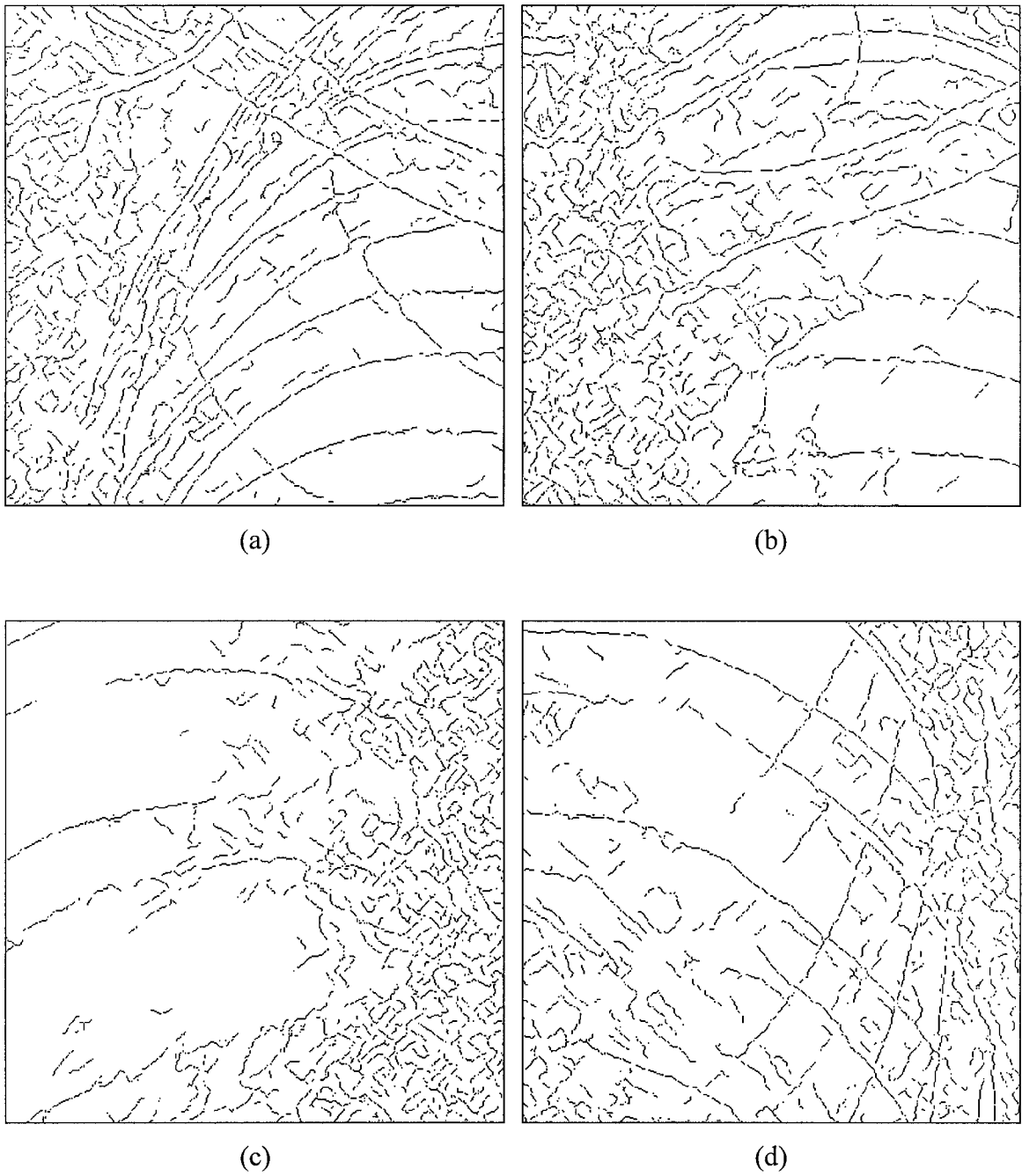


Figure 5.18. The edge detected real patient image employing the Canny edge detector with $\sigma = 3.5$. Here (a) to (d) correspond to the edge detected image of (a) to (d) in Fig. 5.9.

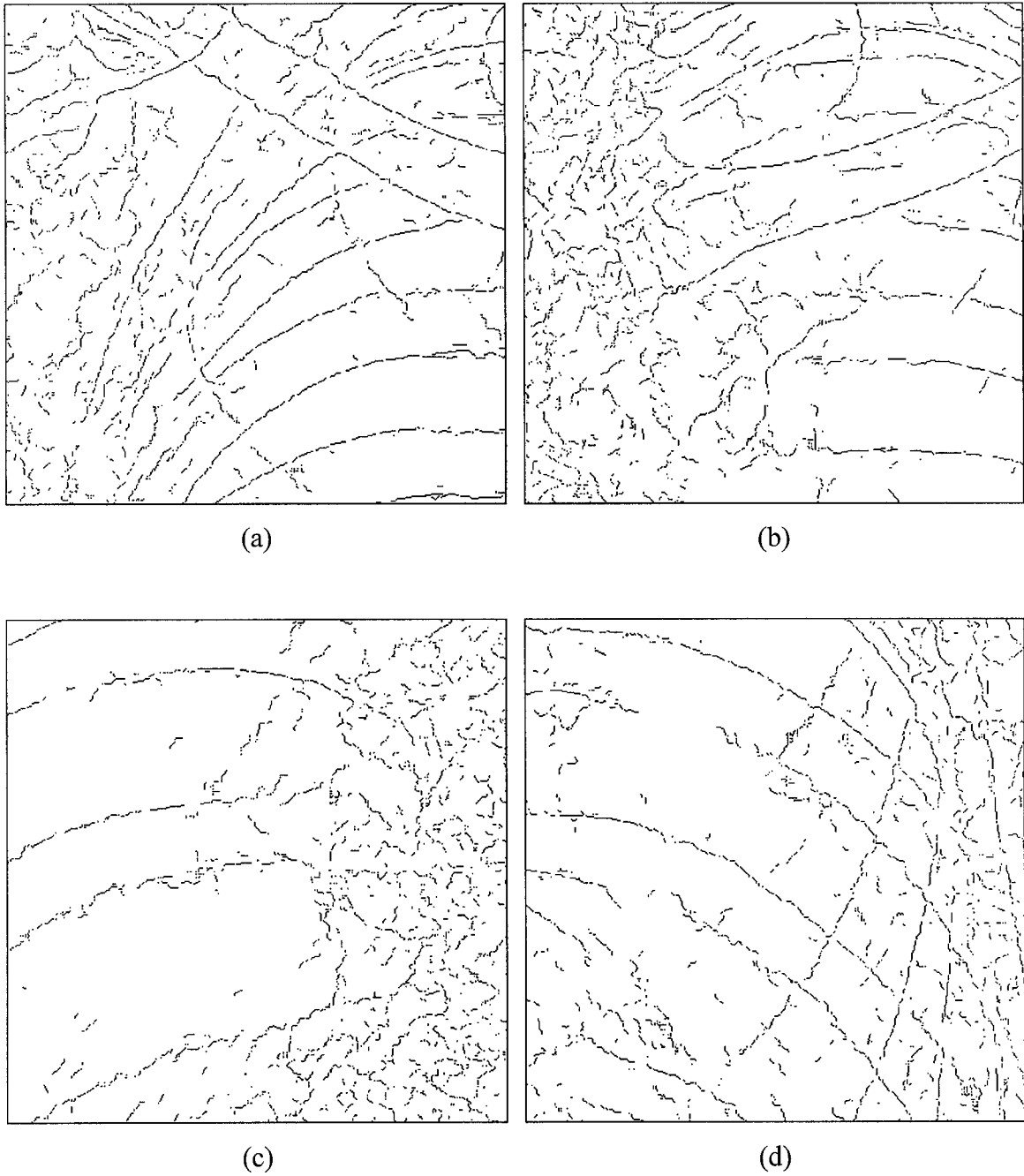


Figure 5.19. The edge detected real patient image employing the Canny edge detector with $\sigma = 7$. Here (a) to (d) correspond to the edge detected image of (a) to (d) in Fig. 5.9.

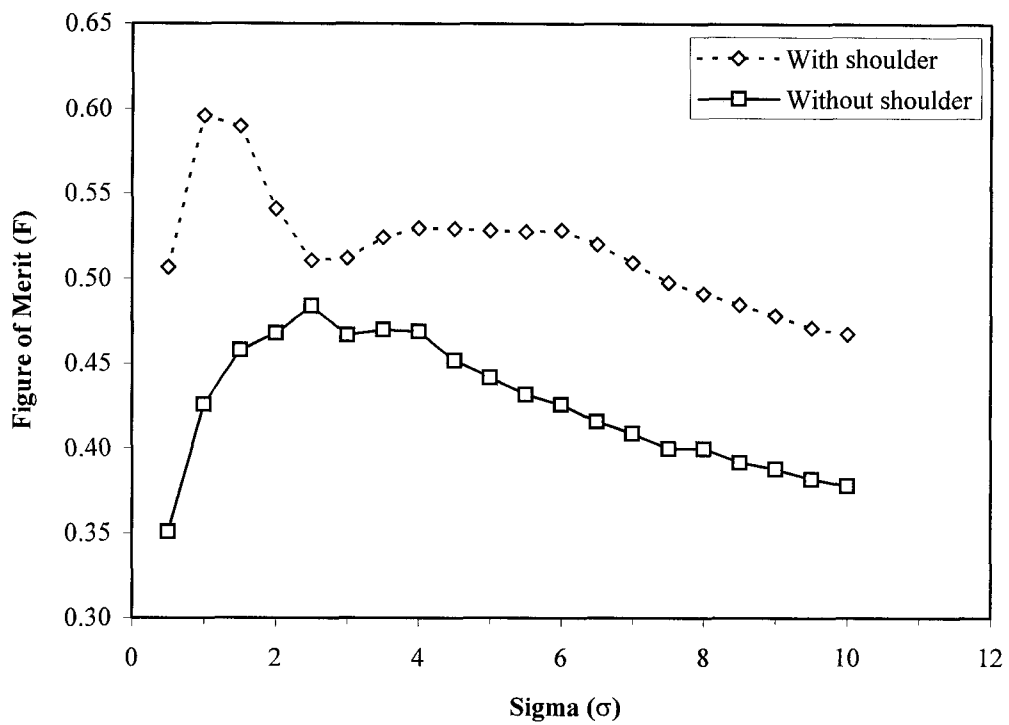


Figure 5.20. The figure of merit of the phantom edge image detected with the Canny edge detector for different sigma values.

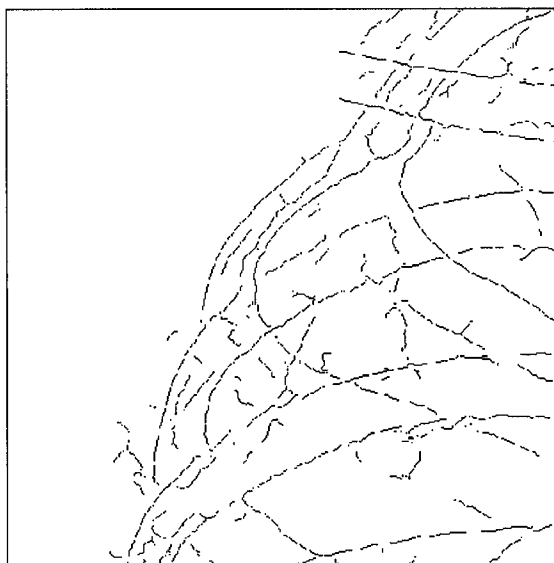


Figure 5.21. An illustration of the region of interest for the edge detected image without the shoulder region.

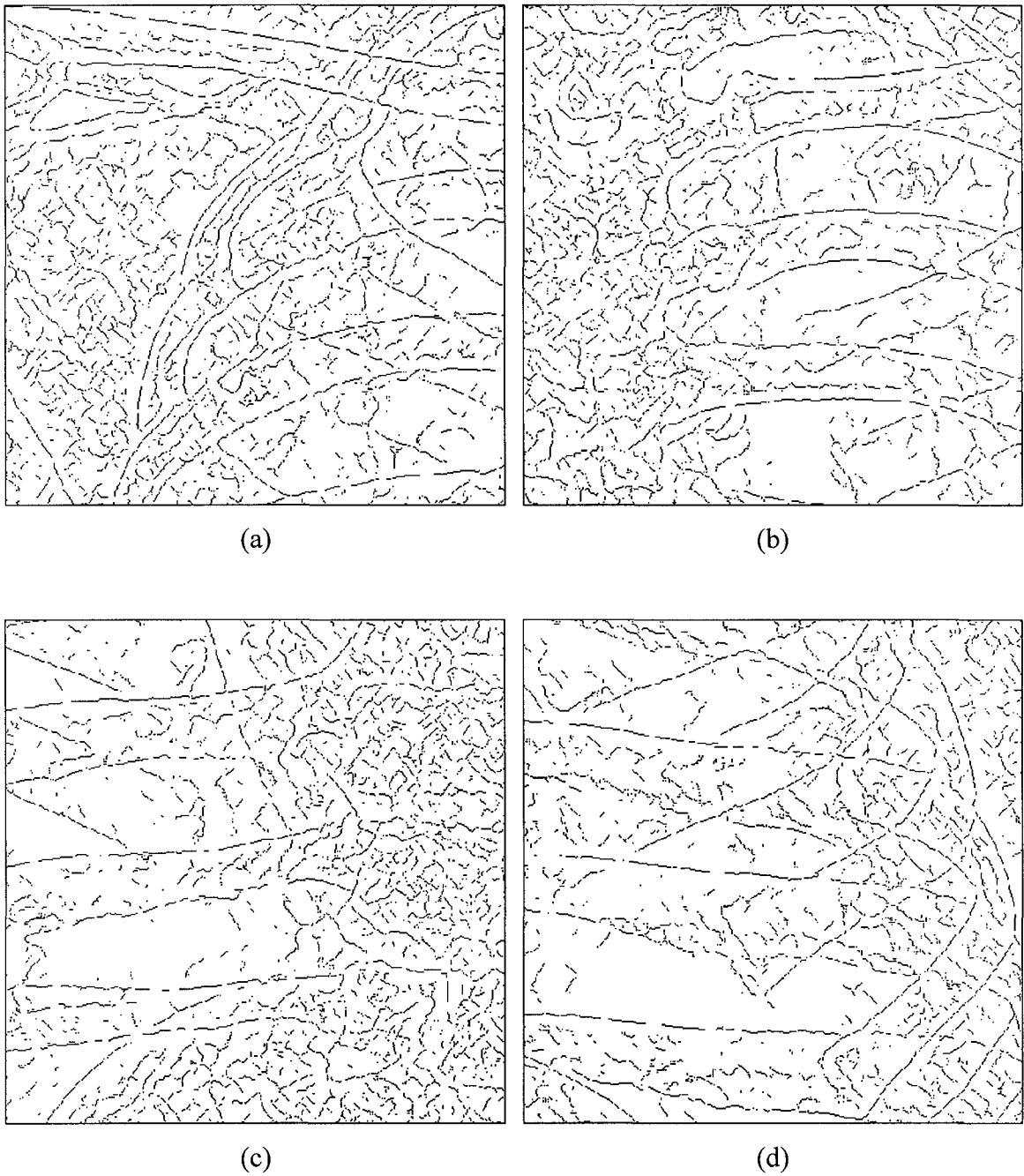


Figure 5.22. The edge detected image of the anthropomorphic chest phantom employing the Canny edge detector with $T_h = 0.0065$. Here (a) to (d) correspond to the edge detected image of (a) to (d) in Fig. 5.4.

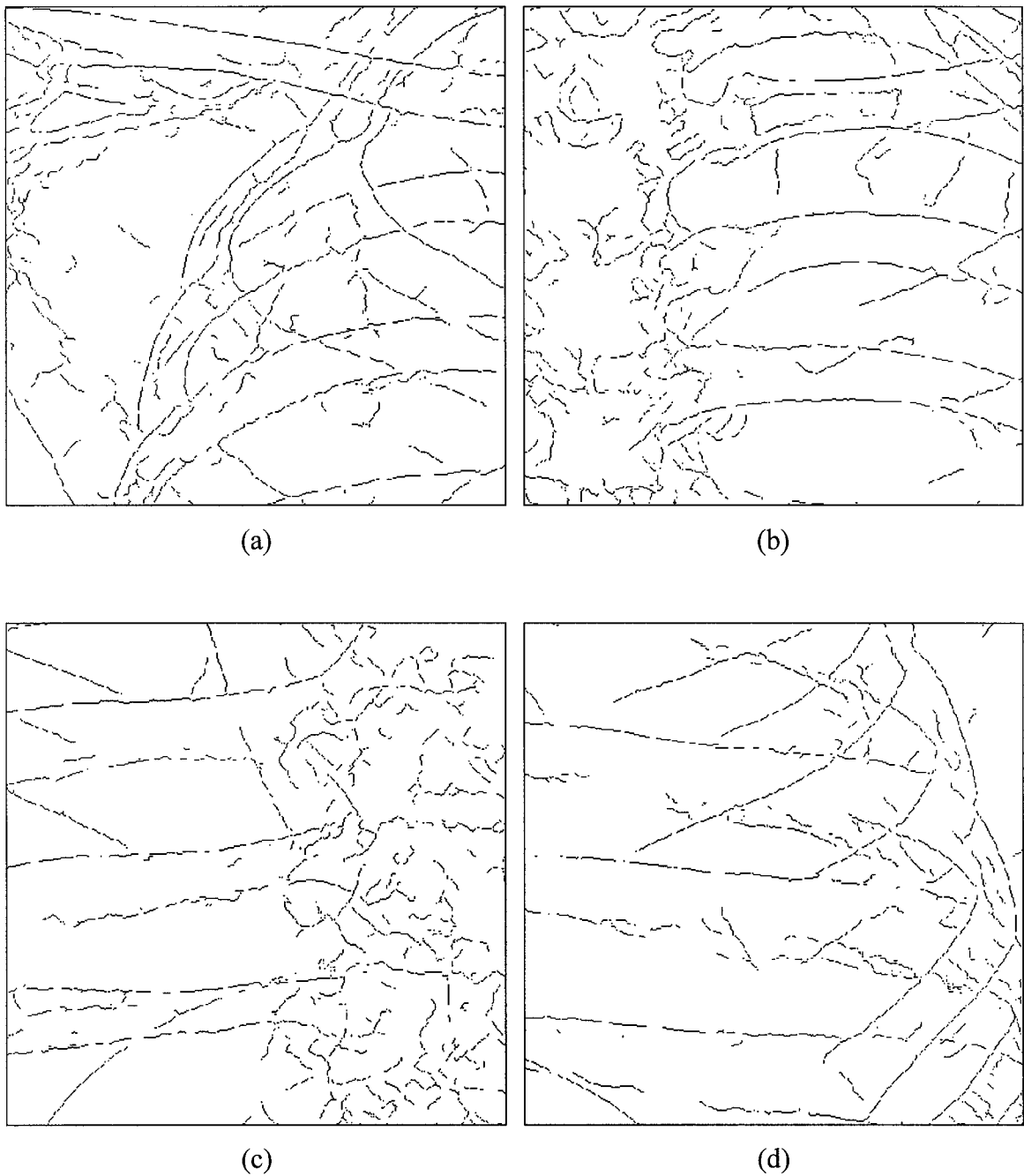


Figure 5.23. The edge detected image of the anthropomorphic chest phantom employing the Canny edge detector with $T_h = 0.015625$ (default value). Here (a) to (d) correspond to the edge detected image of (a) to (d) in Fig. 5.4.

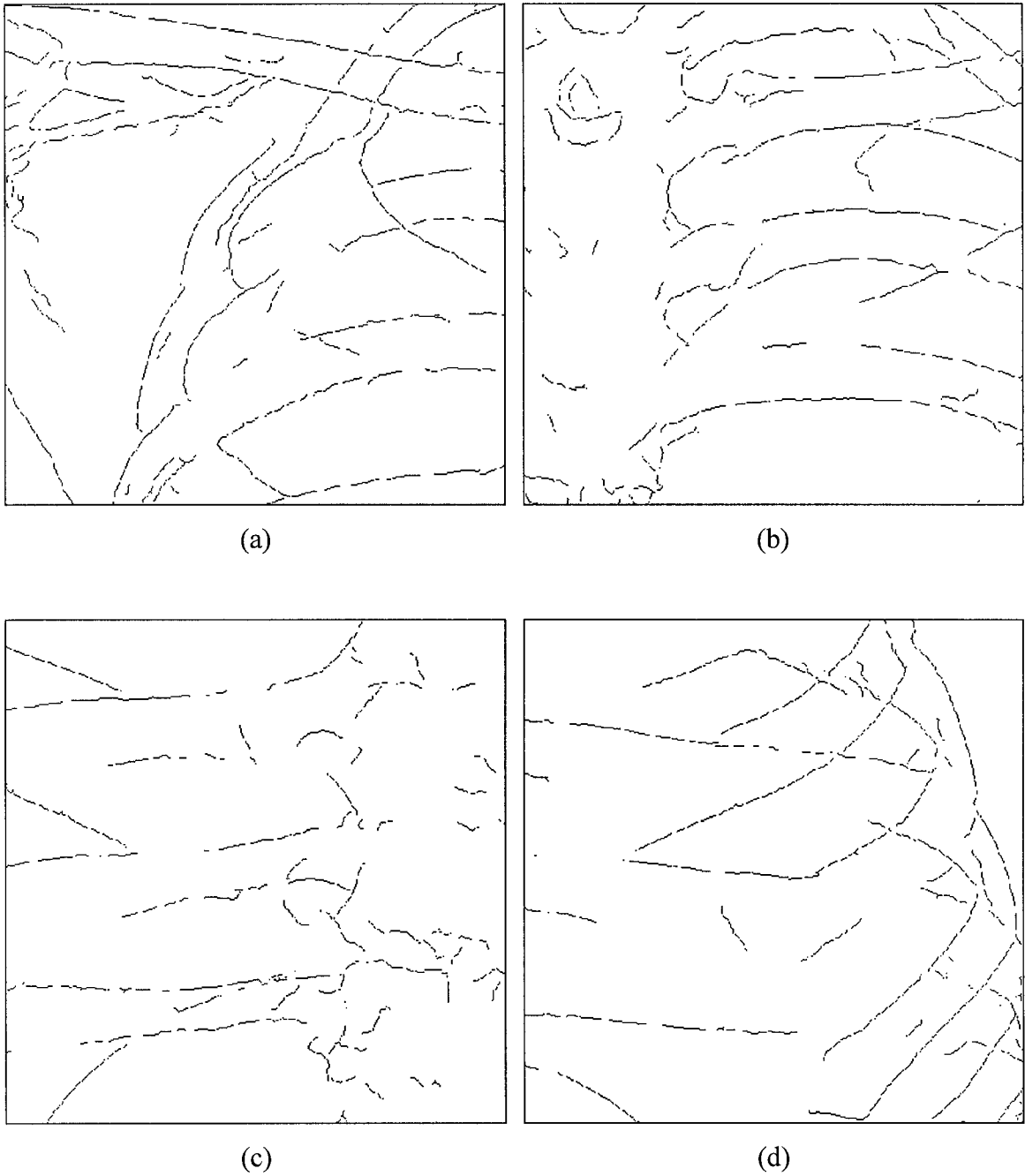


Figure 5.24. The edge detected image of the anthropomorphic chest phantom employing the Canny edge detector with $T_h = 0.025$. Here (a) to (d) correspond to the edge detected image of (a) to (d) in Fig. 5.4.

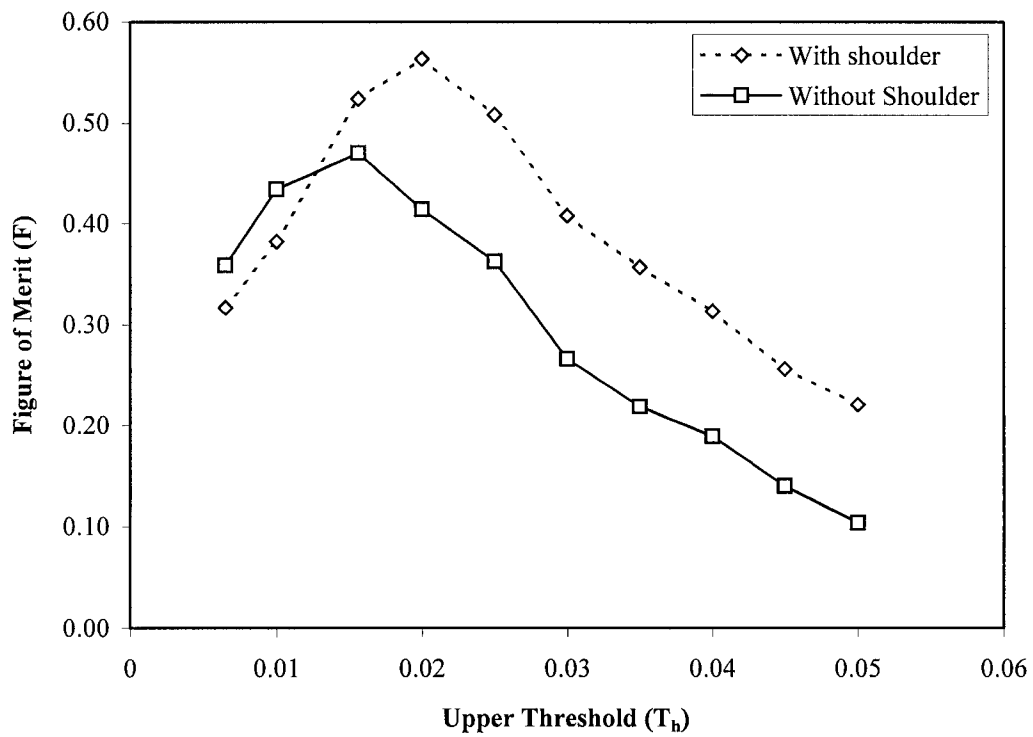


Figure 5.25. The figure of merit of the phantom edge image detected with the Canny edge detector using different upper threshold values.

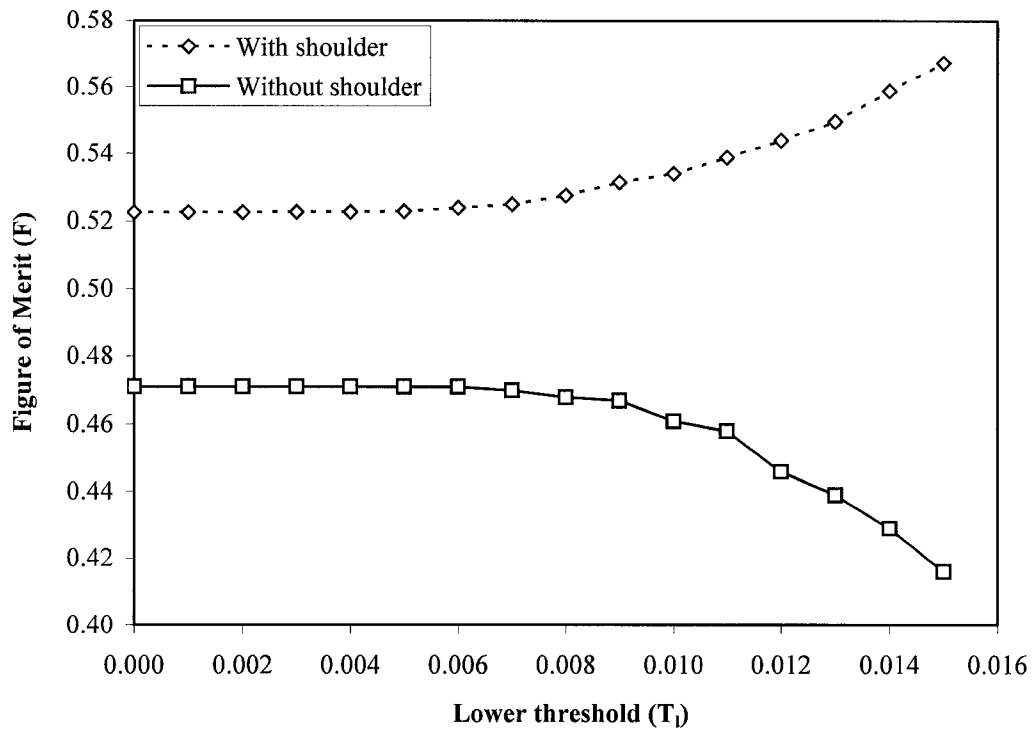


Figure 5.26. The figure of merit of the phantom edge image detected with the Canny edge detector using different lower threshold values.

5.2. The Yanowitz and Bruckstein Image Segmentation Method

In this section, the results from the threshold surface segmentation method will be examined. The anthropomorphic chest phantom and real patient images will first be processed with the Canny edge detector employing the parameters discussed in Section 5.1. Before the threshold surface can be calculated, one needs to provide the boundary conditions. The four boundary conditions (the four sides of an image) are computed using the following procedures:

- 1) The edges in each boundary are detected using the one dimensional Prewitt detector. The Prewitt detector is chosen because it is one of the simplest edge detectors and can be easily applied for the one-dimensional cases.
- 2) The values of the threshold line at the two endpoints of each boundary, as well as with the edge points identified in Step #1, are set to the values at these locations, while the rest of the threshold line is set to a value of zeros. The values at the endpoints and edge pixels are fixed for the subsequent iteration since these values are expected to be correct.
- 3) The threshold line is iterated until it satisfies the one dimensional Laplacian Equation. The iteration will terminate when the total absolute difference between the threshold line of the current iteration and previous iteration is less than some arbitrary small value. For this experiment, the cutoff value is set to 0.1, or one tenth of a gray-level.

After these four boundary conditions are calculated, the four boundaries are treated similarly to the edge pixels detected by the Canny edge detector.

Although the iteration process in Step 3 can be applied in a straightforward fashion, it does take a long time to converge. However, based on the empirical results, the values of the threshold line between the two edge pixels are observed to be between the two nearest edge pixels' values. Therefore, one should be able to speed up the iteration process by providing a more realistic estimate of the values between the edge

pixels instead of zeros. The values are chosen to be the average value of the two edge pixel values. These estimates provide two benefits:

- 1) The iteration will converge faster since the difference between the initial guesses and the true solution is less, due to the more realistic estimate.
- 2) The results are more likely to be closer to the true solution with the more realistic estimate, since the iteration starts at a closer distance to the true values.

The benefit as mentioned in Step #2 is illustrated in Fig. 5.27. Here the iteration is stopped when the total absolute difference between the current and previous threshold line is less than or equal to 1. From this Figure, one can observe that the final solution of the more realistic estimate has a higher threshold value than the original value for the first part of the line (point 0 to 500), while the final solution with the initial guess filled with zeros is lower. This implies that the solution of the more realistic estimate is able to eliminate the first part of the line after thresholding, while the zero initial guess solution cannot. Since this portion of the line is the background area on top of the shoulder, it is safe to assume that the solution of the more realistic estimate is closer to the true threshold. Lastly, the zero initial guess requires a time of about 700 seconds to complete the iteration, while the more realistic estimate is complete in less than 10 seconds. These trials showed that a reduction in iteration time by a factor of 70 is achievable by simply providing a better initial guess.

Due to these benefits, a more realistic estimate of the pixel values for all the pixels in the image should also be provided before the iteration. However, to provide a more realistic guess is difficult due to the two dimensional nature of an image. To simplify, each of the vertical profiles in the image will be treated as a line and the value is estimated using the average value of the two nearest edge pixels. The reason that the vertical profile is chosen is because the width of bone (ribs) in the vertical profile is in general shorter than in the horizontal direction, hence the estimate should be closer to the true value due to the smaller variation between the two edge pixels.

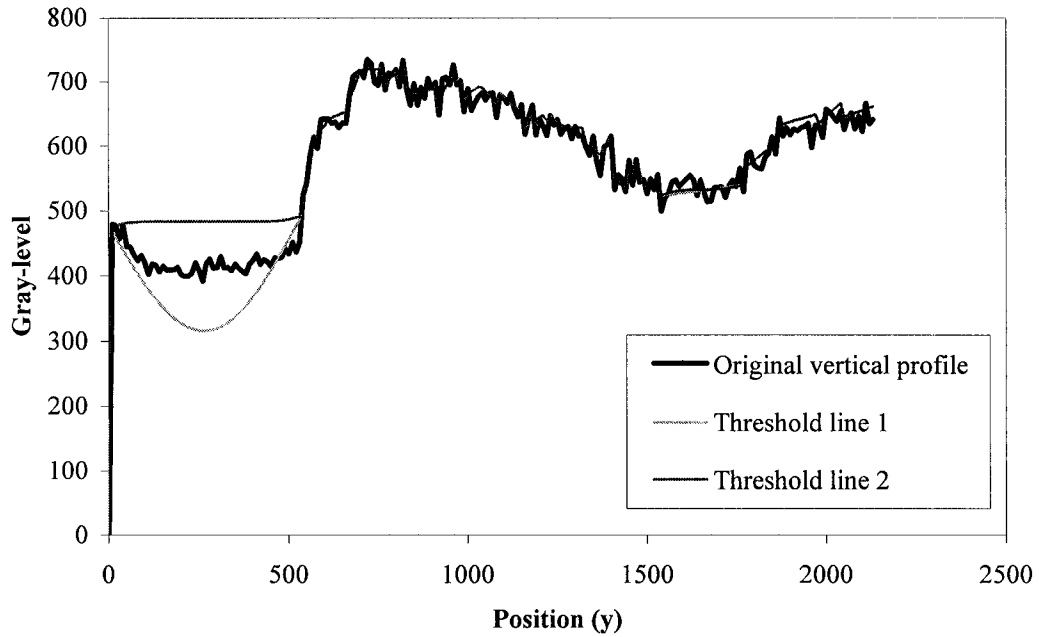


Figure 5.27. An illustration of the final solution computed utilizing two different initial guesses. Here Threshold Line 1 employs the zero initial estimates, while Threshold Line 2 uses the average value estimates.

Once the initial estimates for the threshold surface is calculated, one can compute the threshold surface that satisfies the Laplacian equation by convoluting the surface with the mask shown in Fig. 4.3 until a solution is produced. However from Fig. 4.3, one can observe that the Laplacian equation only provides solutions in the x and y directions, or lines with slope of 0° and 90° with respect to the horizontal line. In order to expand the coverage of the mask, a slightly different mask was employed in the iteration. This 3×3 mask is illustrated in Fig. 5.28. From this Figure, one can observe that the mask is designed to estimate solutions for the $\pm 45^\circ$ angles, as well as the 0° and 90° angles.

As mentioned in Section 4.2, utilization of the successive over-relaxation method is suggested to speed up the iteration procedure. However, this method contains a disadvantage in that the differences between subsequent iterations may increase instead of decrease. This makes estimating the end of convergence very difficult. This difficulty, combined with the fact that the iteration takes about 12 hours to complete for a

2140×1760 image using the normal iteration method when the more realistic estimate is provided, led to the decision that the successive over-relaxation method will not be employed in the current study. Lastly, two convergence criteria were imposed in this segmentation. The first one occurs when the absolute difference between the previous and current iteration, or the error, is less than 500, or about 0.01% of the number of pixels in the image. The second criterion occurs when the error from the current iteration is the same as the error from 500 previous iterations. This second criterion gives an estimate of whether the iteration is progressing or not. The algorithm will stop when one of these two criteria is satisfied.

-1	-1	-1
-1	8	-1
-1	-1	-1

Figure 5.28. An illustration of the enhanced mask.

The result of the segmentation process using the original Laplacian mask (Fig. 4.3) and the enhanced mask (Fig. 5.28) are illustrated in Figs. 5.29 and 5.30 respectively for the anthropomorphic chest phantom image, and in Figs. 5.31 and 5.32 for the real patient radiograph. Here the white pixels are the locations that the segmentation process identified as bone. Fig. 5.33 is obtained by subtracting the image in Fig. 5.29 from the image in Fig. 5.30, while Fig. 5.34 is computed by subtracting the image in Fig. 5.31 from the image in Fig. 5.32. Thus, the white pixels shown in these two Figures are the extra areas identified as bone structure by the enhanced mask. From Figs. 5.33 and 5.34, one can observe that the enhanced mask is able to detect slightly more of the rib edges

when compared with the original mask, which confirms the improved capability of this enhanced mask.

From Figs. 5.30 and 5.32, it is evident that a few holes in the bone structures are not being identified as bone. These gaps are larger for the anterior ribs. These holes are due to the noise in the original bone image, which causes the following two problems (as mentioned in Chapter 4):

- 1) The noise may interfere with the edge detection process, and lead to part of the bone structure being missed from the edge detected image. This is illustrated in Fig. 5.23 where some of the bone (rib) edges are missing. The anterior ribs are especially affected. This may be due to the placement of those ribs in a typical AP chest examination, where the posterior ribs are closer to the x-ray tube than the anterior ribs. Consequently, the signal-to-noise ratio (SNR) of the anterior ribs is lower because of the increased quantum mottle due to the reduction in x-ray photons, and the hardening of the x-ray beam caused by the attenuation of the x-ray photons through the body tissue.
- 2) The noise level may also hinder the segmentation process, which can produce the holes in the segmented bone structure. This is caused by the fact that the noise may reduce the gray-level of a number of the pixels in the bone structure below the threshold level.

As a result, a binary operator will be employed in the next section to try to address these problems.

Another observation from Figs. 5.30 to 5.32 is that some of the boundaries in these images are identified as bone structure. This is due to the fact that the original images contain a step near the edge as illustrated in Figs. 5.4 and 5.9, and is especially visible on the left side of these images. Luckily, this concern can be overcome by careful collimation during the acquisition stage, or removed manually from the image before the processing. Lastly, the boundary of the Lucite is clearly visible on the phantom image. This may be caused by the fact that the global dual-energy subtraction algorithm from the Fuji system is unable to differentiate Lucite from bone very well, and is not a concern for real patient images.



Figure 5.29. The segmented anthropomorphic chest phantom image utilizing the original Laplacian mask.

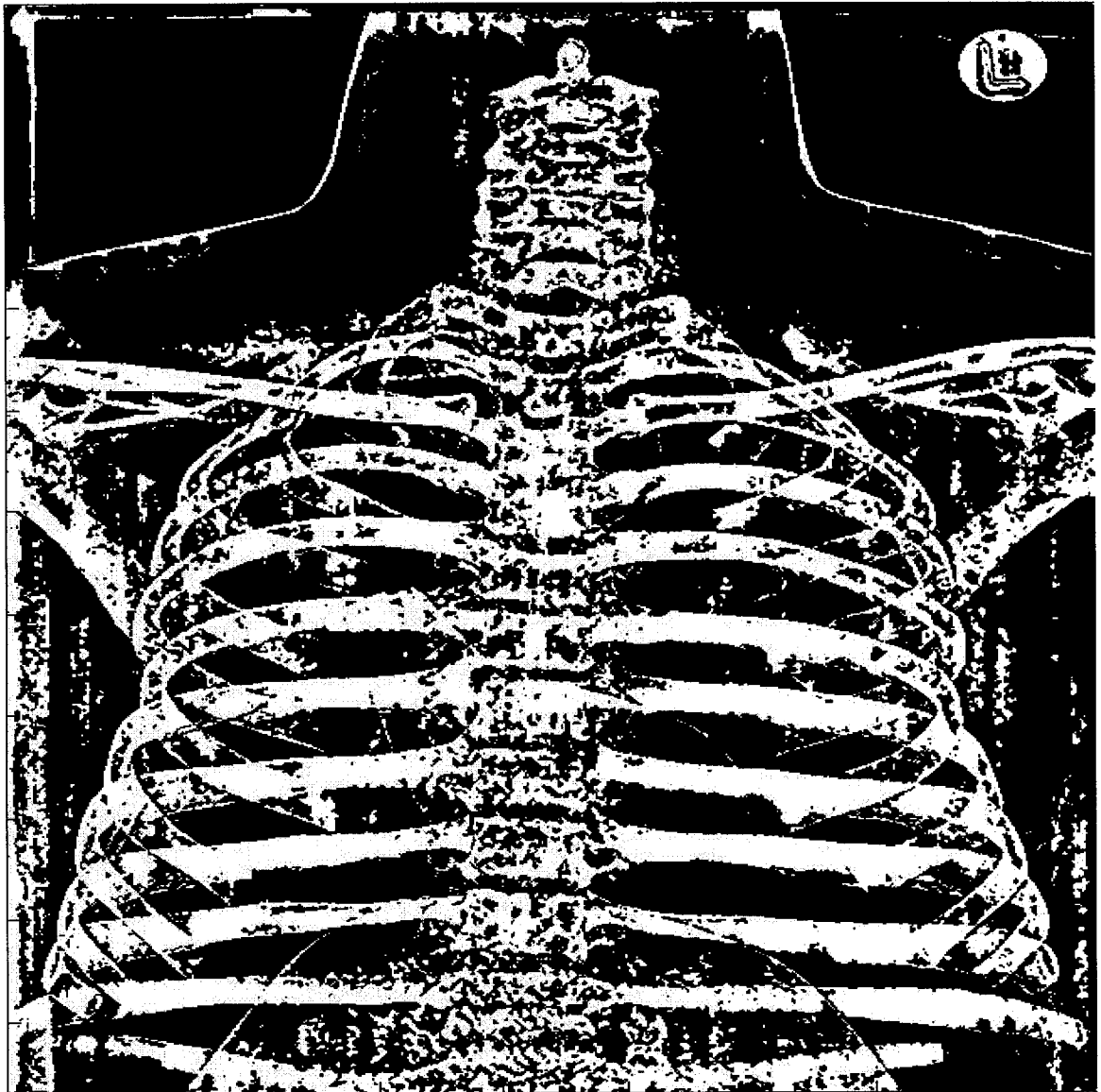


Figure 5.30. The segmented anthropomorphic chest phantom image utilizing the enhanced mask.

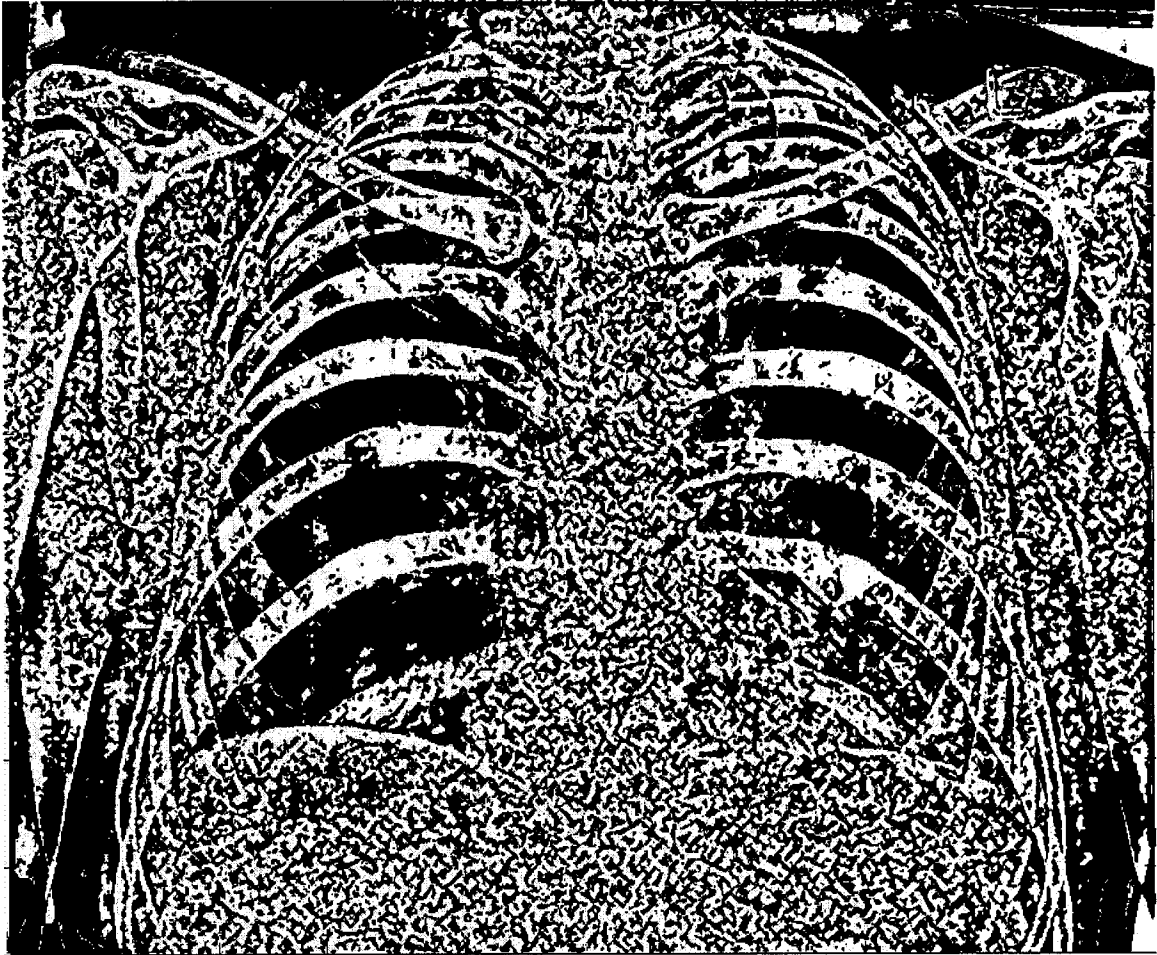


Figure 5.31. The segmented real patient image utilizing the original Laplacian mask.

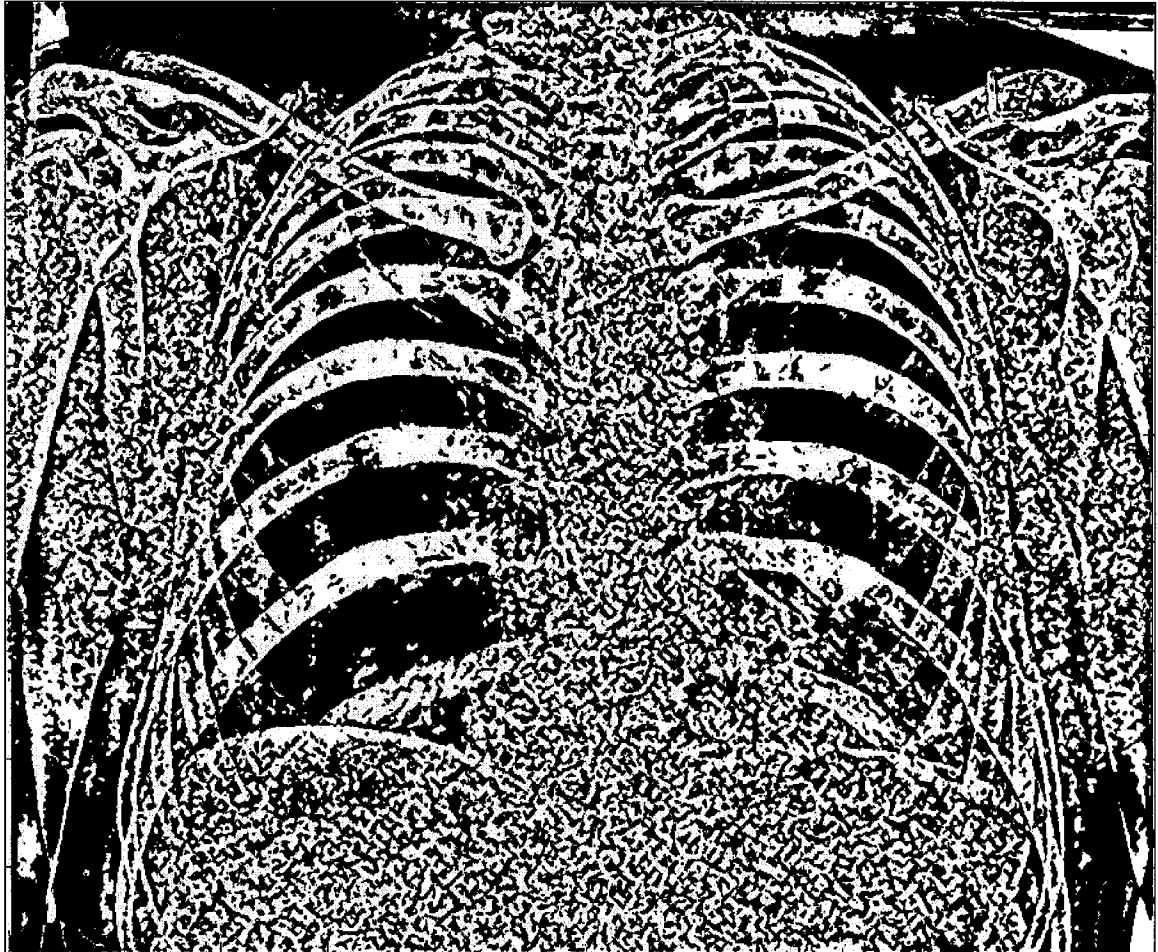


Figure 5.32. The segmented real patient image utilizing the enhanced mask.

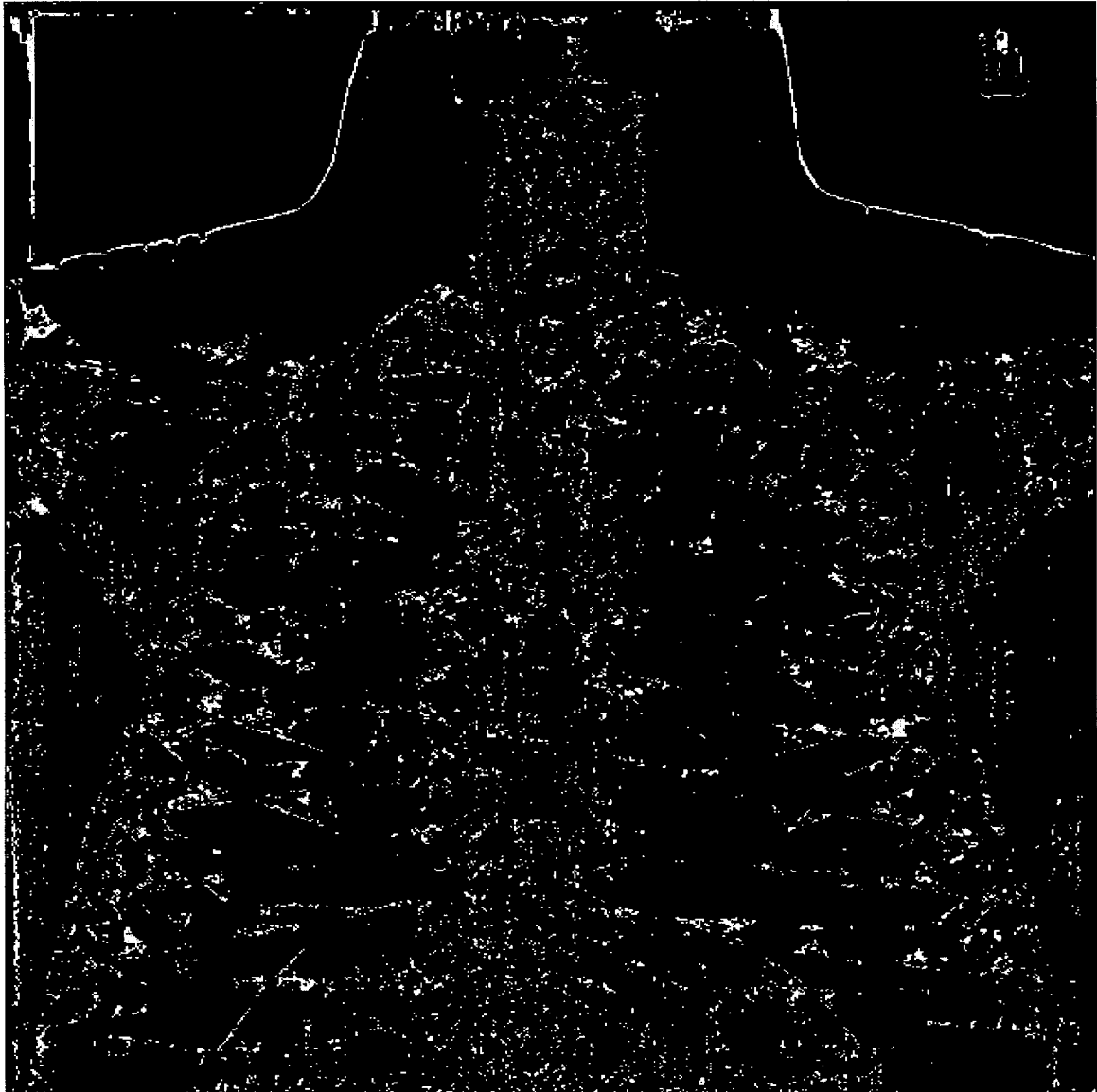


Figure 5.33. The difference image, computed by subtracting the Laplacian from the enhanced mask for the anthropomorphic chest phantom. Here the white pixels are the extra area correctly identified by the enhanced mask as bone structure.



Figure 5.34. The difference image, computed by subtracting the Laplacian from the enhanced mask for the real patient image. Here the white pixels are the extra area correctly identified by the enhanced mask as bone structure.

5.3. Binary Operation

As mentioned in the previous section, a binary operator is used to overcome the two concerns generated by the noise in the subtracted bone images. The idea behind the procedure is explained in Section 4.3, while a typical 21×21 dual-triangular mask is shown in Fig. 4.5. At this stage, one may be wondering why this mask is used to fill in the gaps and holes missing in the segmented image instead of a dilation operation, which also expands the boundary of the image. Dilation is a binary morphological operation that causes the original object to grow larger. It is achieved by first obtaining the reflection of the dilation mask (B), and then translating this reflection over the image (A). The dilation of A by B is obtained by filling in all the zero pixels covered by the reflection that contain at least one nonzero element when the image and the reflection overlap. The reason for selecting the dual-triangular ranking filter is illustrated in Figs. 5.35 to 5.37 for the phantom image, and Figs. 5.38 to 5.40 for the real patient image. Fig. 5.35 was obtained by first convoluting the segmented phantom image with a 9×9 dual-triangular mask using a rank order of 41. This rank order is chosen such that a point missing in a line (9 pixels long) will be filled in. The image is then convoluted using the same mask, but this time with a rank order of 24. This step is used to reduce some of the noise that may be contained in the image. Finally the filtered image is dilated until all the gaps and holes are filled (which required 7 iterations). Fig. 5.36 was produced by first convoluting the image with a 27×27 dual-triangular mask using a rank order of 365. The size of 27 is employed because a binary operation with this mask size will eliminate most of the holes for both the phantom and real patient image. The image is then filtered again with the same dual-triangular mask with a lower ranking order (195) to remove some of the noise. Lastly, the differences between the first (Fig. 5.35) and second (Fig. 5.36) images are illustrated in Fig. 5.37. Here the white pixels are the extra areas identified by the first operation (9×9 dual-triangular mask then dilated). Similar results can be observed in Fig. 5.40. Based on these two Figures, one may conclude that the dual-triangular mask operation is the better choice since it does not expand the edge of the bone structure as much as the dilation method.

One possible concern with employing the dual-triangular mask operation is the fact that the size of the mask required to eliminate the holes is image dependent. Therefore, the mask size selected will be the largest size required to fill most of the gaps for the current set of images. This may lead to the problem that the mask may expand some of the edge unnecessarily; however, this will ensure that minimal bone component will be left behind. Another concern is that the triangular mask will expand the boundary of objects that are bigger than 27 pixels; consequently, some of the noise on the image may increase in size. This is the reason why a second pass with a lower ranking order is required, and the results illustrated in Figs. 5.36 and 5.39 show that the noise level should be acceptable for the current procedure.

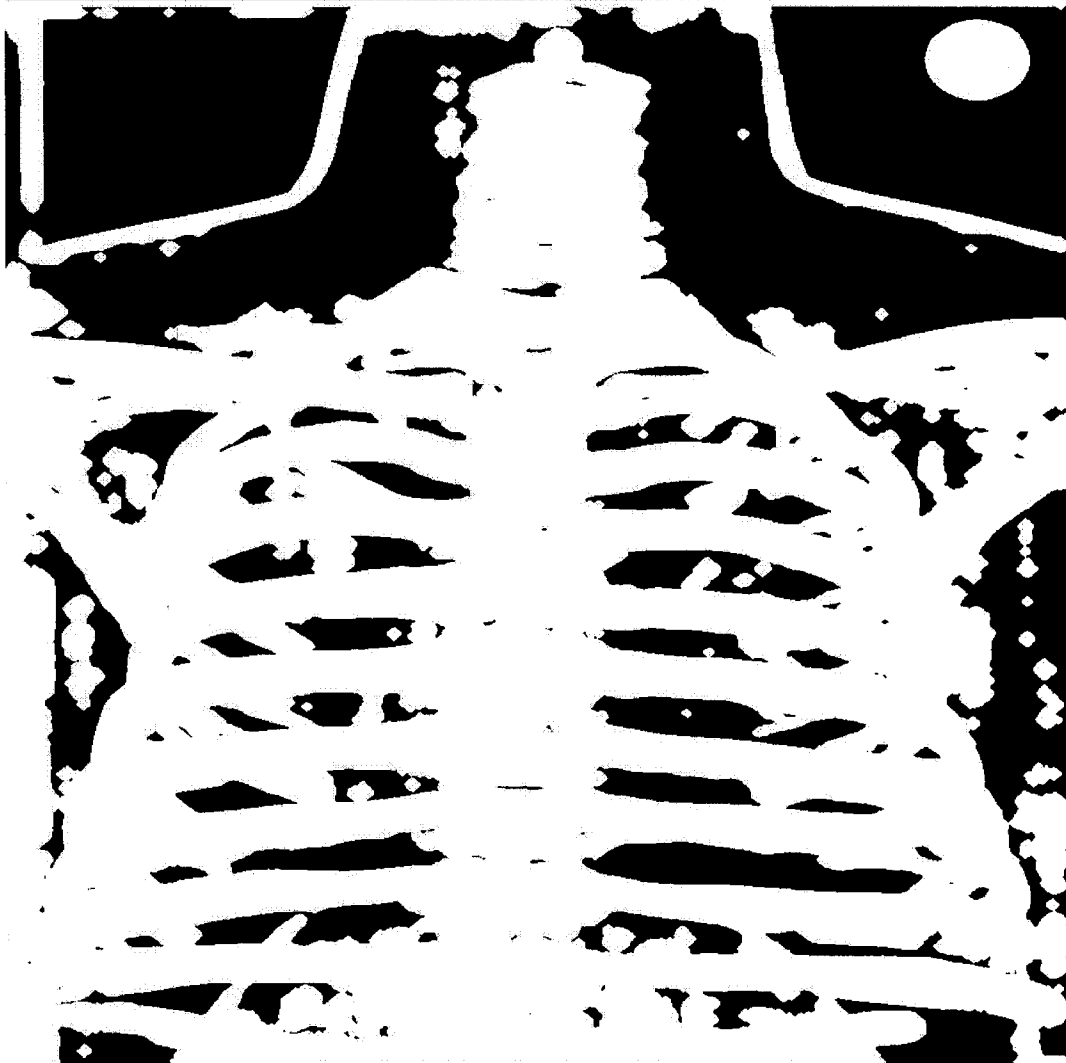


Figure 5.35. The segmented anthropomorphic chest phantom image operated with both the dual-triangular mask and dilation procedures. Here a 9×9 mask is employ twice, first with a ranking order of 41 and then with a rank order of 24. Seven dilation iterations are needed to fill in the gaps completely.

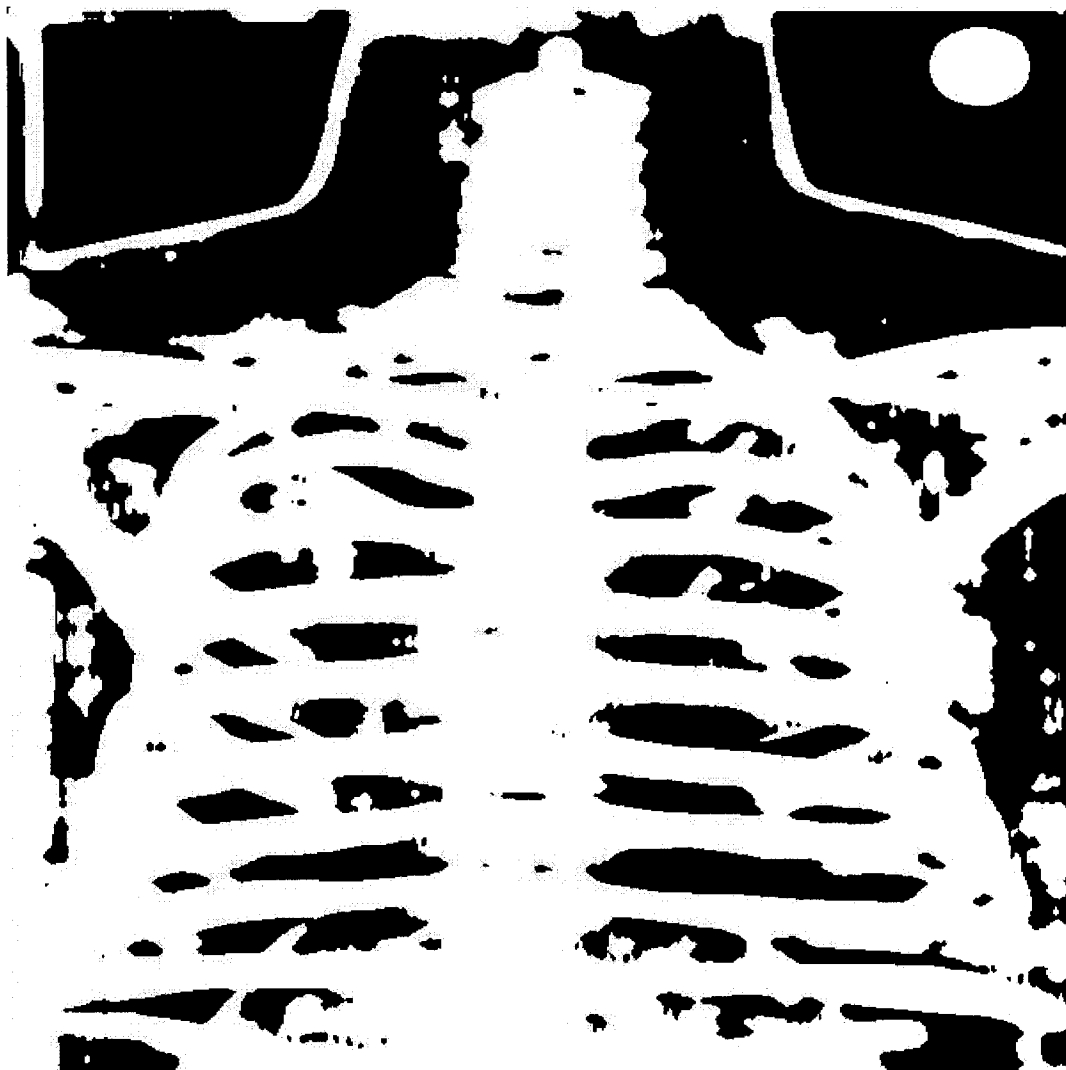


Figure 5.36. The segmented anthropomorphic chest phantom image processed with the dual-triangular mask procedure only. Here a 27×27 mask is employed twice, first with a ranking order of 365 and then with a rank order of 195.

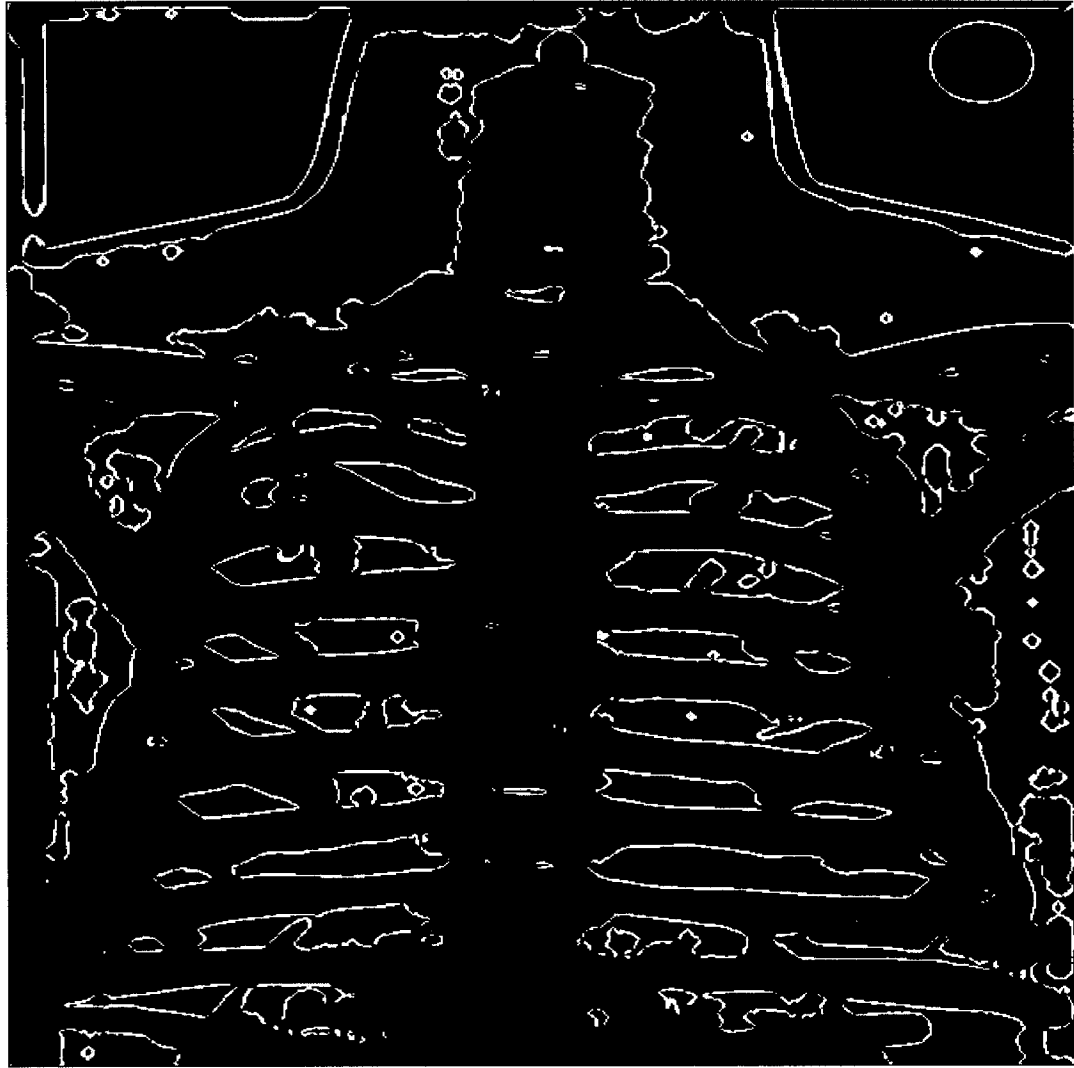


Figure 5.37. The differences between the segmented anthropomorphic chest phantom image processed by a mixture of dual-triangular mask and dilation versus dual-triangular mask alone. Here the white pixels are the extra areas identified by the hybrid method.

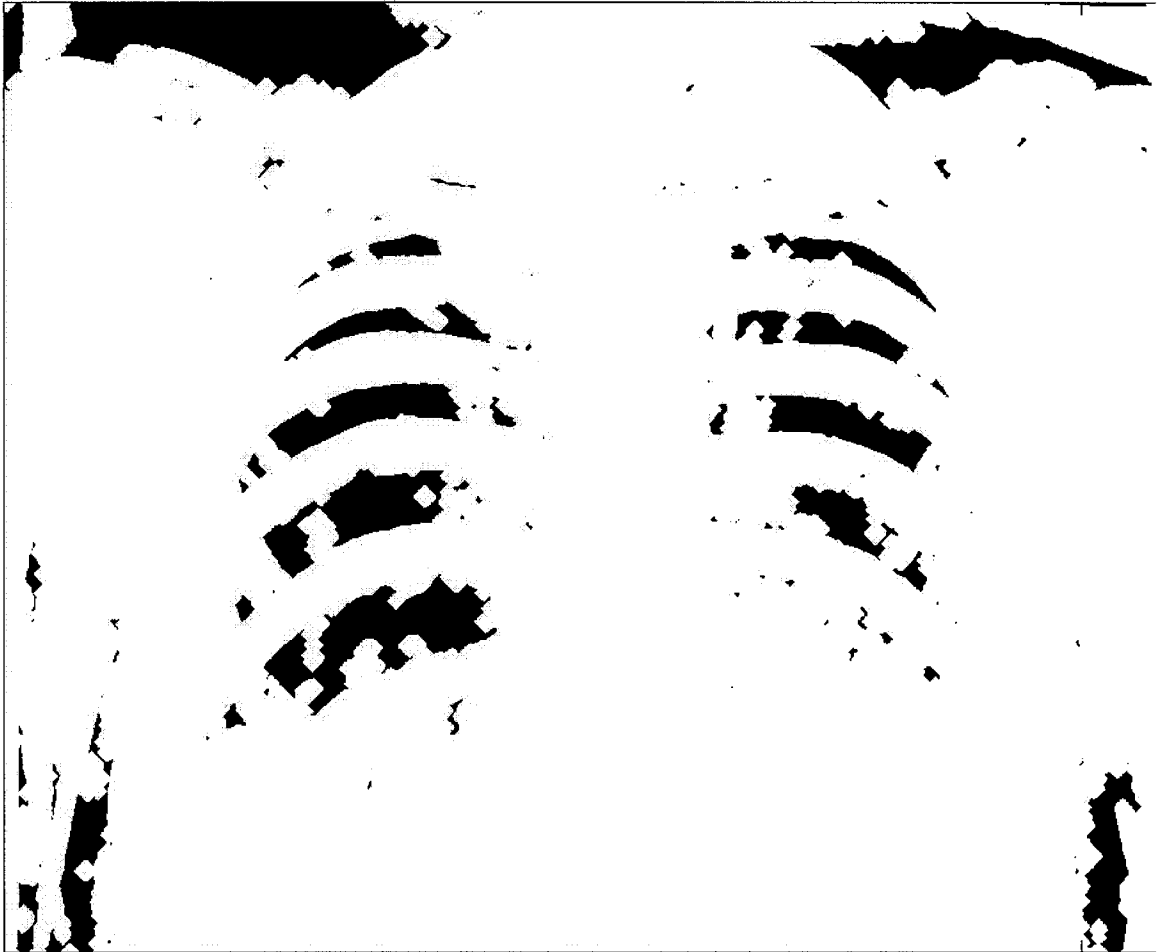


Figure 5.38. The segmented real patient image processed with both the dual-triangular mask and dilation procedures. Here a 9×9 mask is employed twice, first with a ranking order of 41 and then with a rank order of 24. Fourteen dilation iterations were needed to fill in the gaps completely.

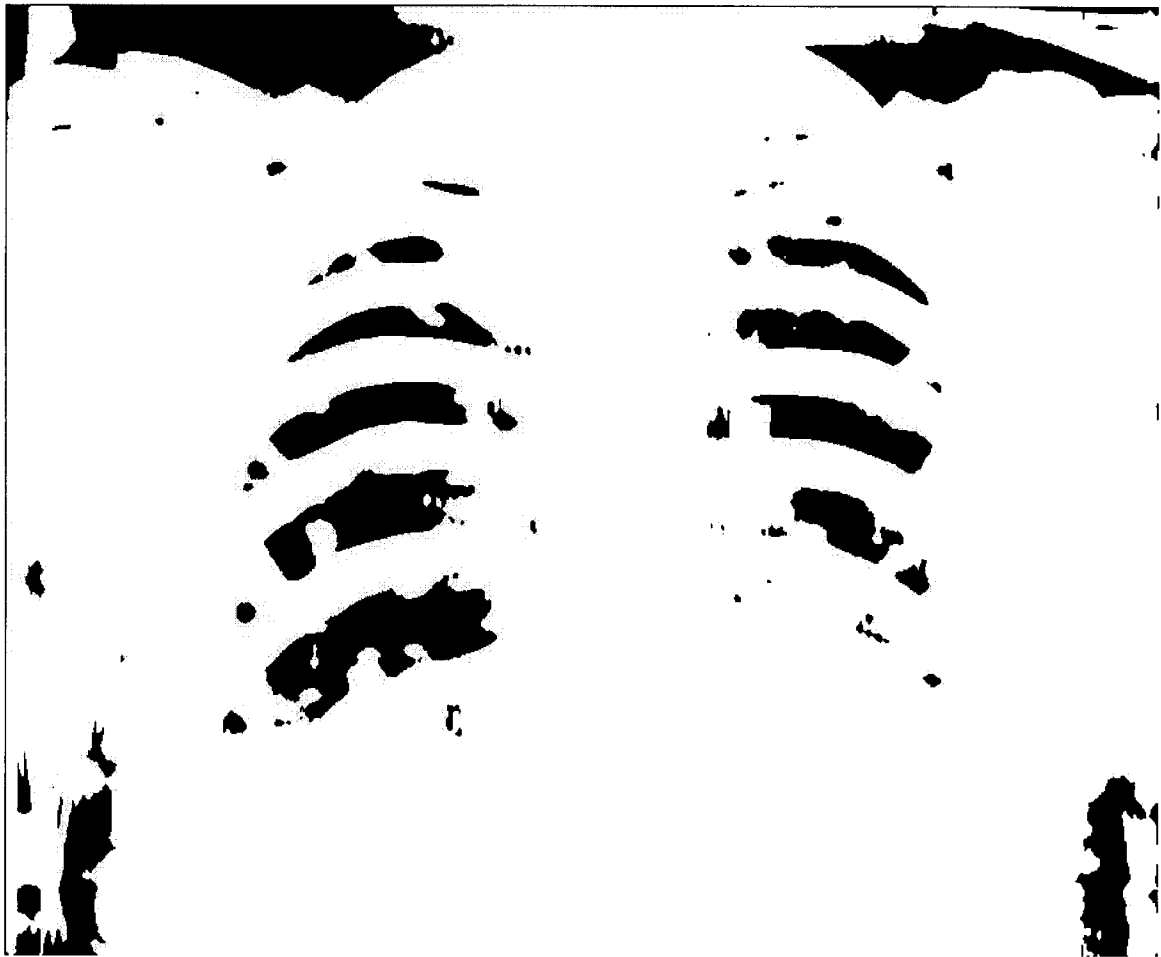


Figure 5.39. The segmented real patient phantom image processed with the dual-triangular mask procedure only. Here a 27×27 mask is employed twice, first with a ranking order of 365 and then with a rank order of 195.



Figure 5.40. The differences between the segmented real patient phantom image processed by a mixture of dual-triangular mask and dilation versus dual-triangular mask alone. Here the white pixels are the extra areas identified by the hybrid method.

5.4. The Bisection Results

The procedures described in the last three sections will now be used to identify the bone structure in one anthropomorphic chest phantom image and five real patient images. Two Figures will be illustrated for each radiograph. The first image is the original bone-only radiograph, while the second image is the area of the original radiograph identified as bone by the procedures. The phantom images are shown in Figs. 5.41 and 5.42, while the real patient radiographs are shown in Figs. 5.43 to 5.52. From Fig. 5.42, one can observe that parts of the ribs at the bottom of the image (as indicated by the white arrows) are missing. This may be due to the fact that the SNR for these rib sections is very low, and the algorithm is unable to pick them up. Also, a small hole is observed in the anterior ribs. This is expected due to the lower SNR of the anterior ribs as explained before. Overall, the algorithm was able to identify most of the bone structure in the original radiograph without dilating the bone boundaries too significantly. Also, a good portion of the anterior ribs is identified, although some false positives are observed.

Similar results are observed in Figs. 5.44, 5.46 and 5.48, where the algorithm was able to identify most of the bone structure in the original radiographs without expanding the bone boundaries too significantly. However, bits and pieces of bone structure are still missing in these images, which may be due to one of the following reasons:

- 1) Overlapping of the anterior and posterior ribs can interfere with the segmentation procedures, leading to part of the bone structure being missed. This is because the overlapping region will have a higher gray-level when compared to the other surrounding areas. As a result, this may lead to the failure of the segmentation method since it relies on the gray-level of the edge, to bisect the image. This effect is illustrated for one of the ribs at the top right hand side of Fig. 5.44, as well as in Fig. 5.48. However based on the results obtained in this Section, this is not a significant issue with the current set of images.

- 2) The noise in the image may lead to the creation of holes in the identified bone structure. This is demonstrated in Fig. 5.44 for the heart region.
- 3) The anterior ribs, which are harder to identify due to their lower SNR, may be missed in some of the identified structures.

For Fig. 5.50, one can see that some sections of the posterior ribs are missing from the identified structure. Holes can also be observed in this image. This may be due to the fact that the original image, as illustrated in Fig. 5.49, is very noisy. Hence, the detected image is of inferior quality. This demonstrates the need to utilize good quality original radiographs as a starting point to increase the SNR in the bone-only image. From Fig. 5.52, it is evident that most anterior ribs, as well as two sections of the posterior ribs near the heart, are missing from the identified structure. The higher noise levels in the heart region of the original image cause the missing posterior rib sections, which reduce the SNR of the ribs at these locations.

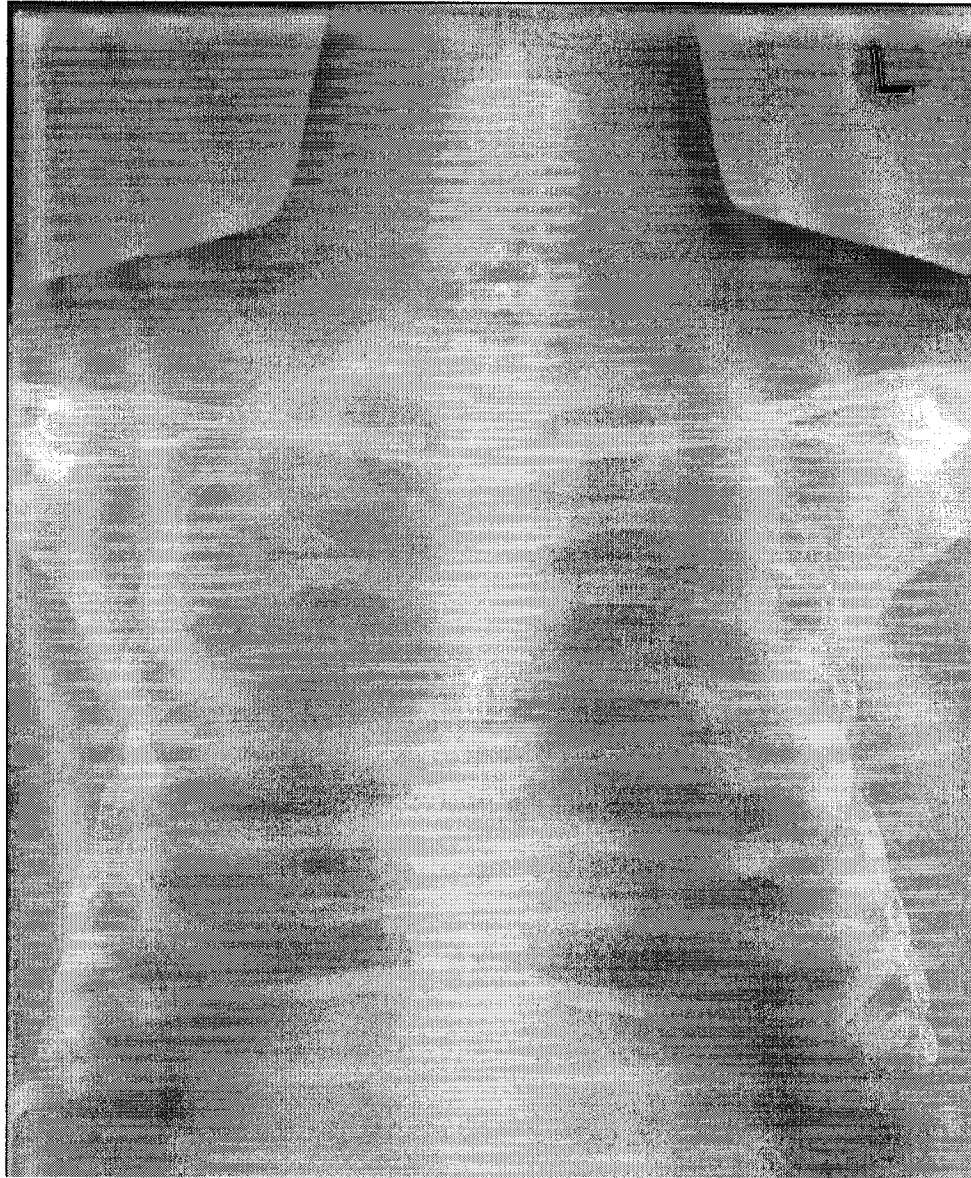


Figure 5.41. The original bone-only phantom image.

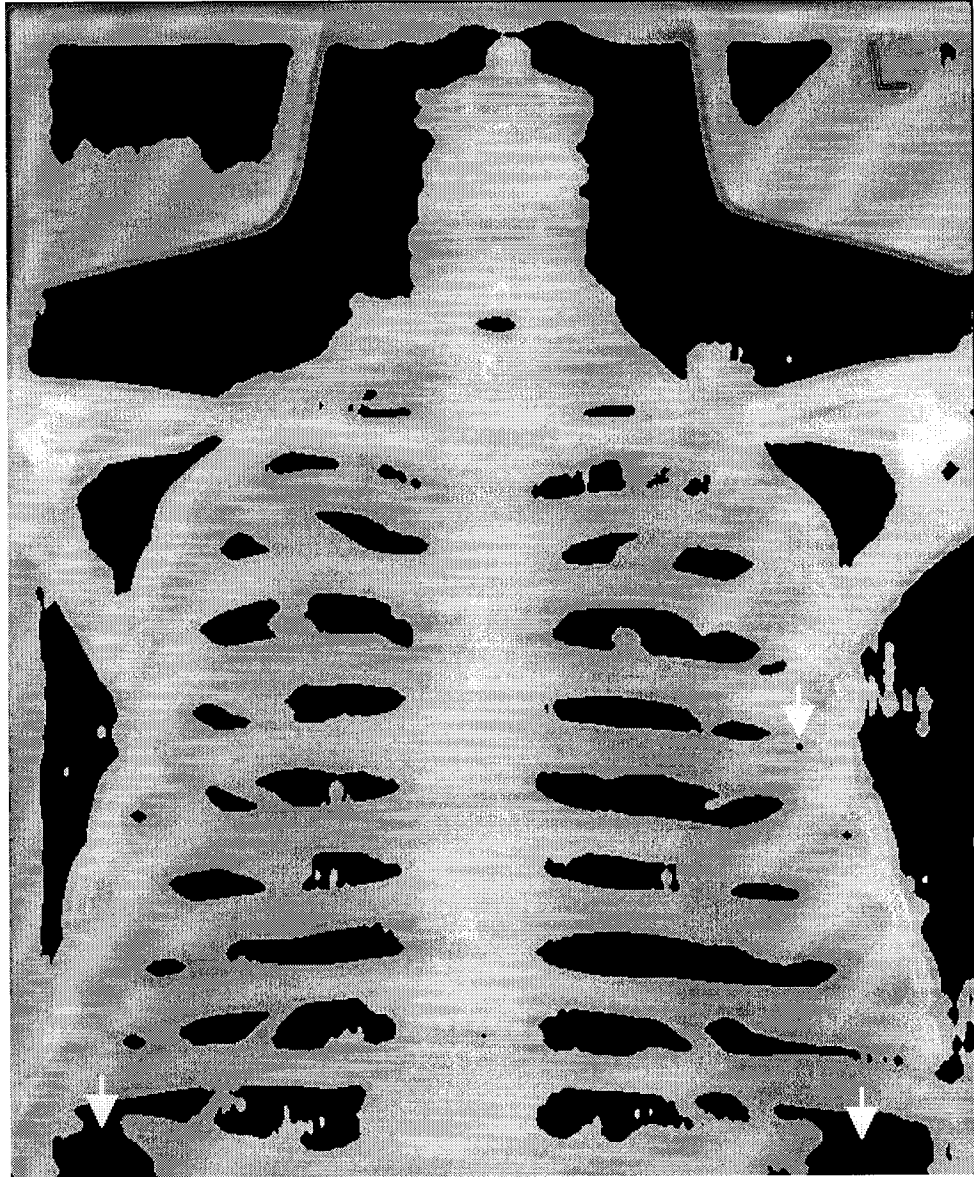


Figure 5.42. The identified bone structure of Fig. 5.41.



Figure 5.43. The original bone-only real patient A image.

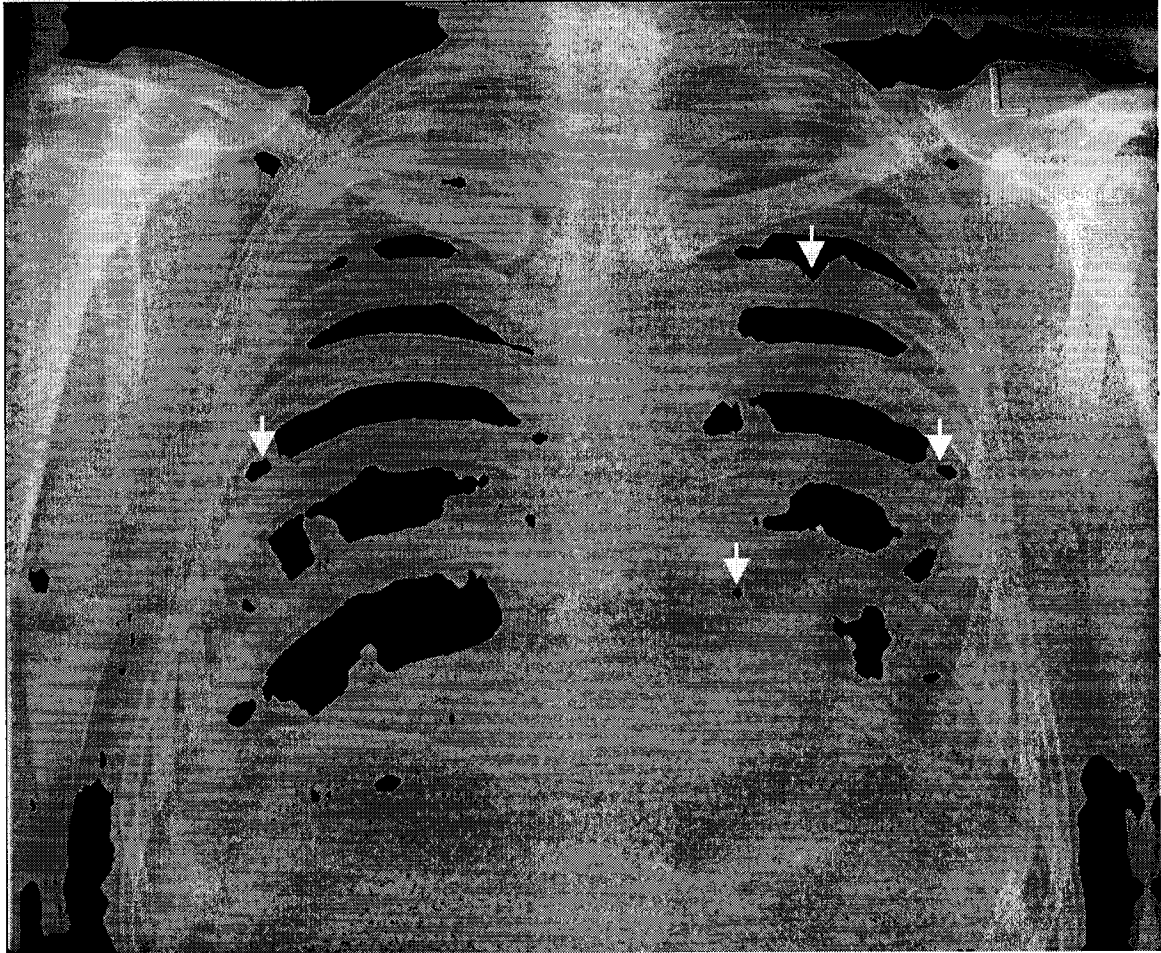


Figure 5.44. The identified bone structure of real patient A.

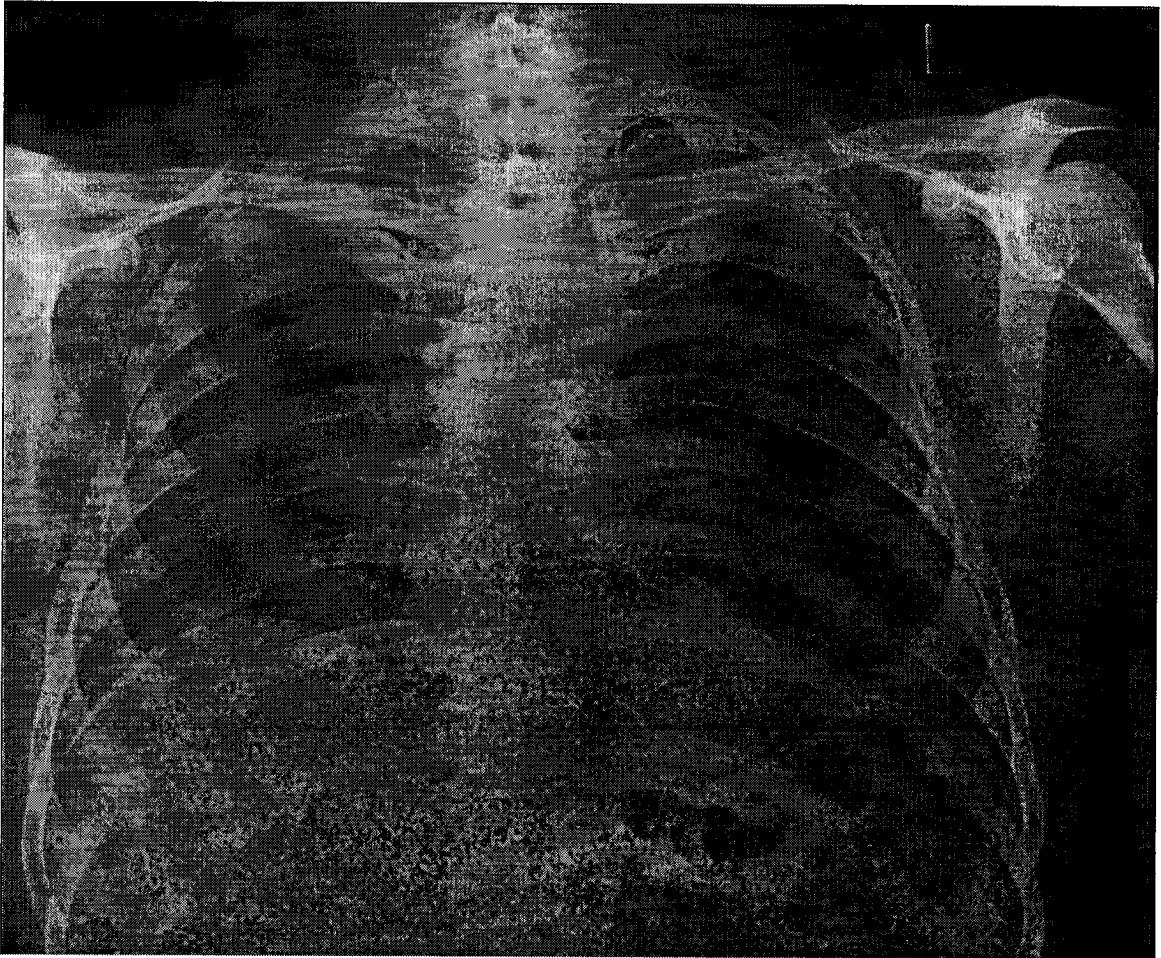


Figure 5.45. The original bone-only real patient B image.

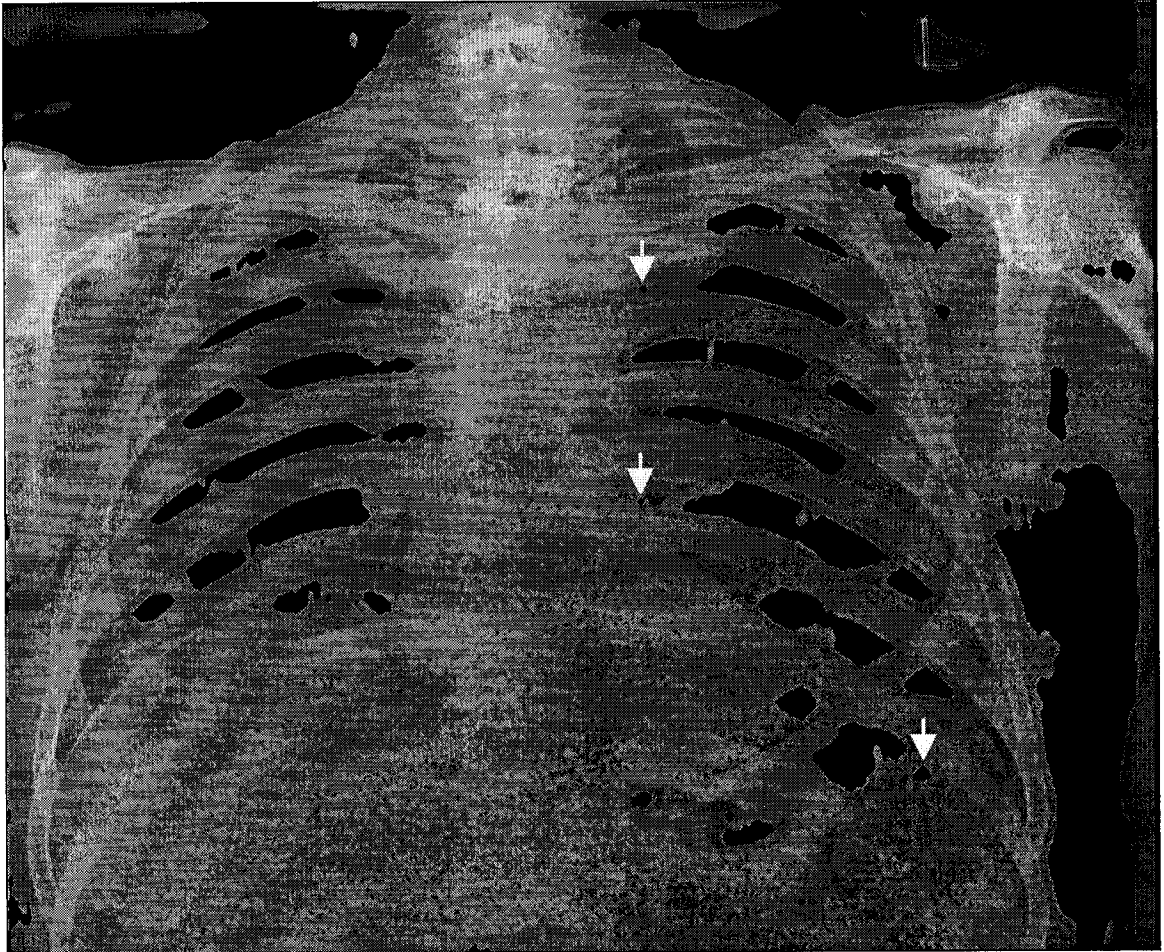


Figure 5.46. The identified bone structure of real patient B.

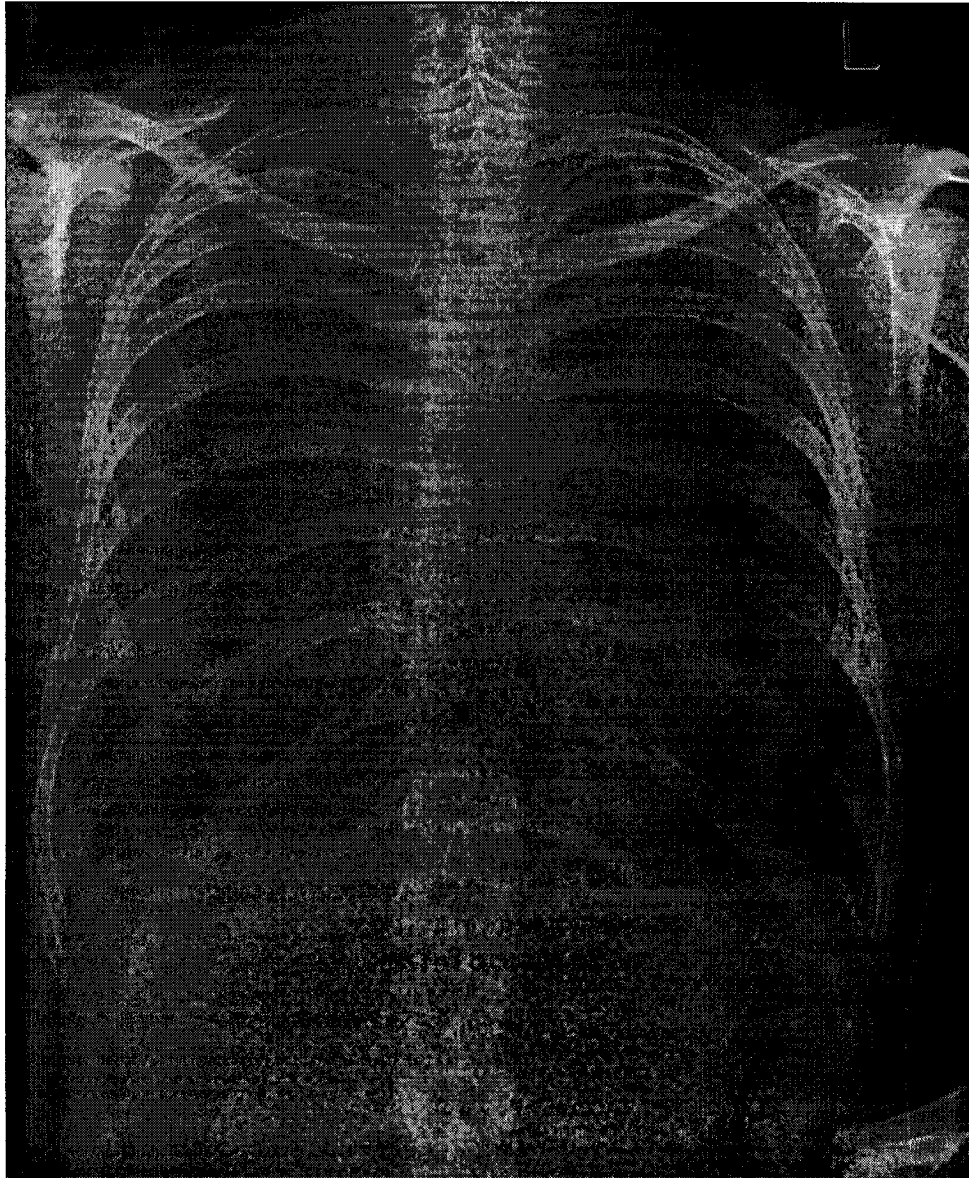


Figure 5.47. The original bone-only real patient C image.



Figure 5.48. The identified bone structure of real patient C.

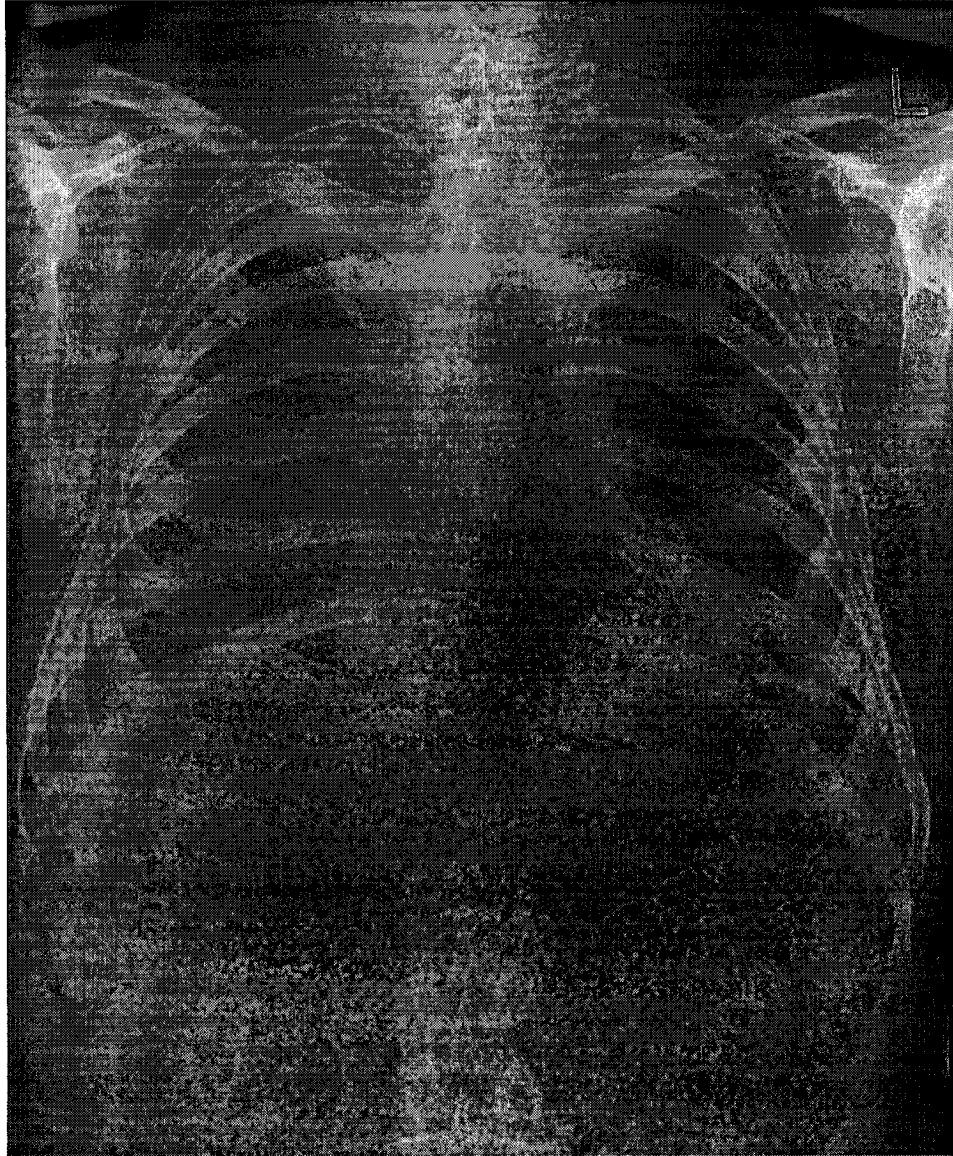


Figure 5.49. The original bone-only real patient D image.



Figure 5.50. The identified bone structure of real patient D.

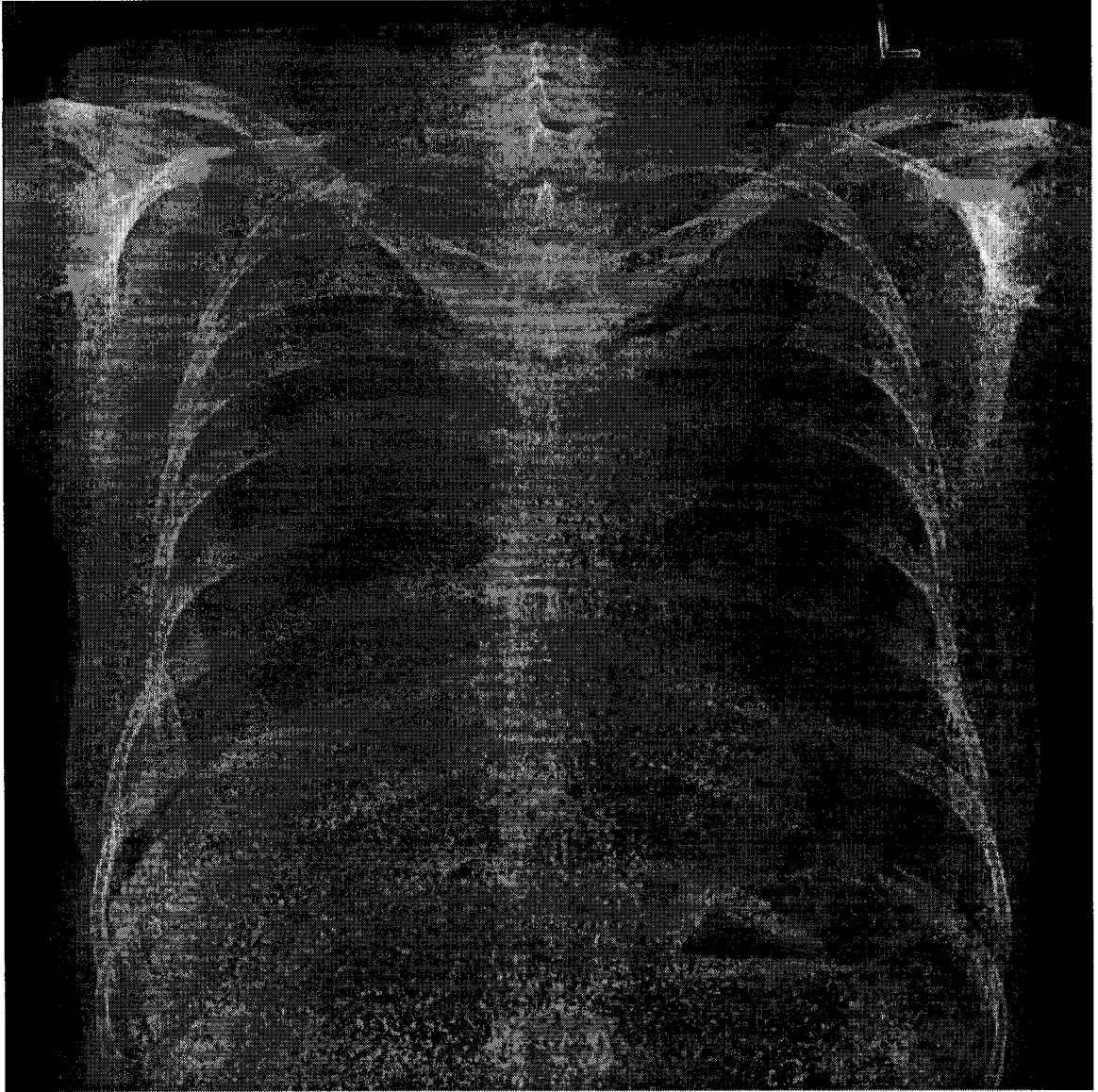


Figure 5.51. The original bone-only real patient E image.



Figure 5.52. The identified bone structure of real patient E.

5.5. The Reconstructed Image

In this section, the final soft tissue only image will be produced. The final soft tissue only image is composed of the low energy image where the chest radiograph is not obstructed by the bone structure, and the soft-tissue only image outputted by the Fuji system where the radiograph is obstructed by bone. To produce these final images, the easiest way is to generate two templates. The first template (T_b) indicates the area of the x-ray that is obstructed by bone, and is simply the binary image from the last section. The second template (T_s) indicates the area of the radiograph that is not obstructed by bone, and is calculated by

$$T_s = A - T_b, \quad (5.2)$$

where A is a matrix of ones with the size equal to the size of the image.

Once these two templates are computed, they are multiplied pixel-by-pixel with the appropriate images to obtain the areas of interest

$$I_s = T_s \times I_{LE}, \quad (5.3)$$

and

$$I_b = T_b \times I_{ST}. \quad (5.4)$$

Here, I_s is the image containing only the area that is not obstructed by bone, while I_b is the image containing the area that is obstructed by bone. I_{LE} is the low energy image and I_{ST} is the soft tissue only image produced by the Fuji system. Once I_s and I_b are computed, the final image (I_f) is produced by

$$I_f = I_b + I_s. \quad (5.5)$$

Although the process to obtain the final image is very straightforward, an extra step is required if one utilizes the image outputted by the Fuji system. This is because the soft tissue and bone-only images outputted are only one quarter the size of the low energy image, or a reduction by half in both the x and y direction. To account for this, the low energy image obtained is also reduced by 50% in both the x and y direction using the “imresize” function in Matlab with nearest neighbor interpolation. With these procedures, the reconstructed images for the previous five real patient images are computed and shown in Figs. 5.53 to 5.57 respectively.



Figure 5.53. The reconstructed soft tissue image for patient A.

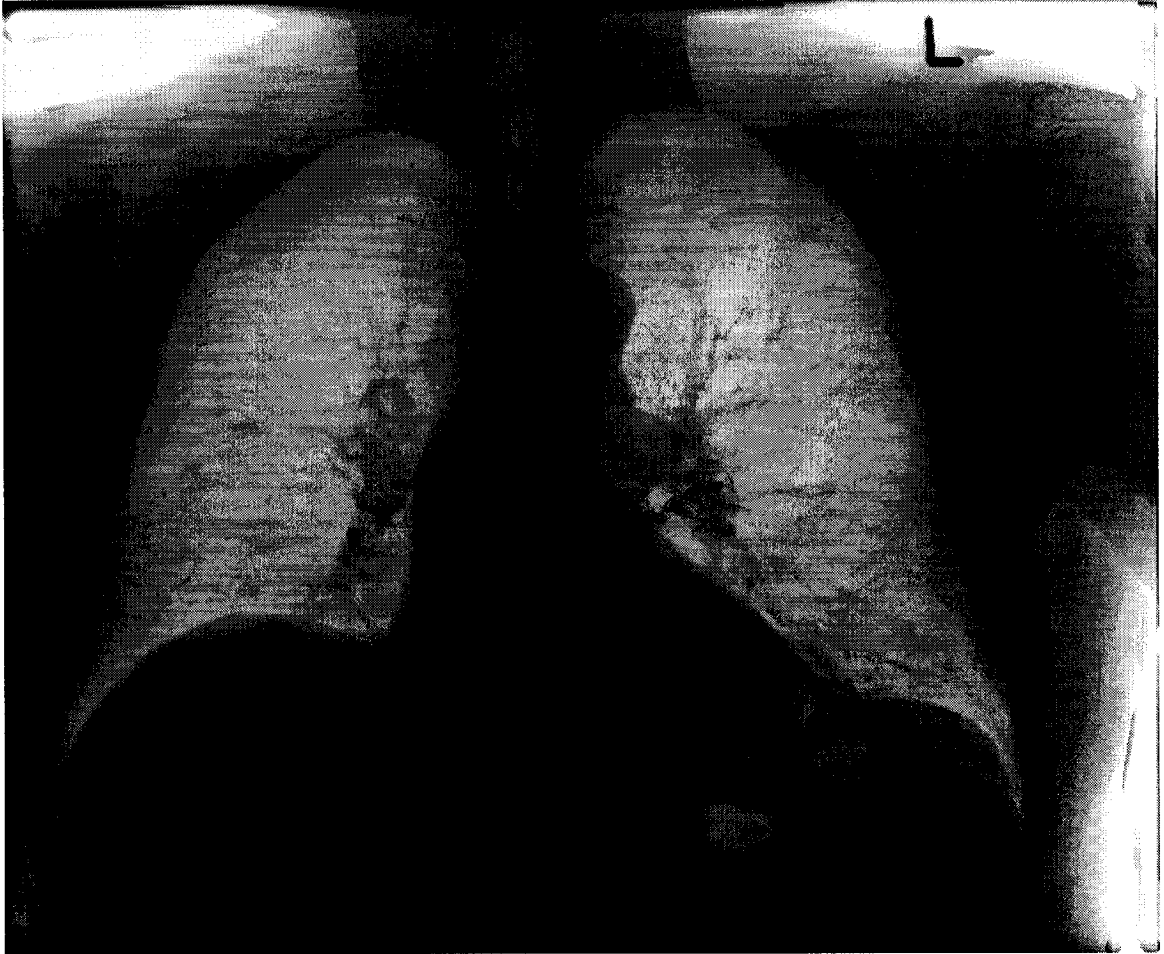


Figure 5.54. The reconstructed soft tissue image for patient B.



Figure 5.55. The reconstructed soft tissue image for patient C.



Figure 5.56. The reconstructed soft tissue image for patient D.

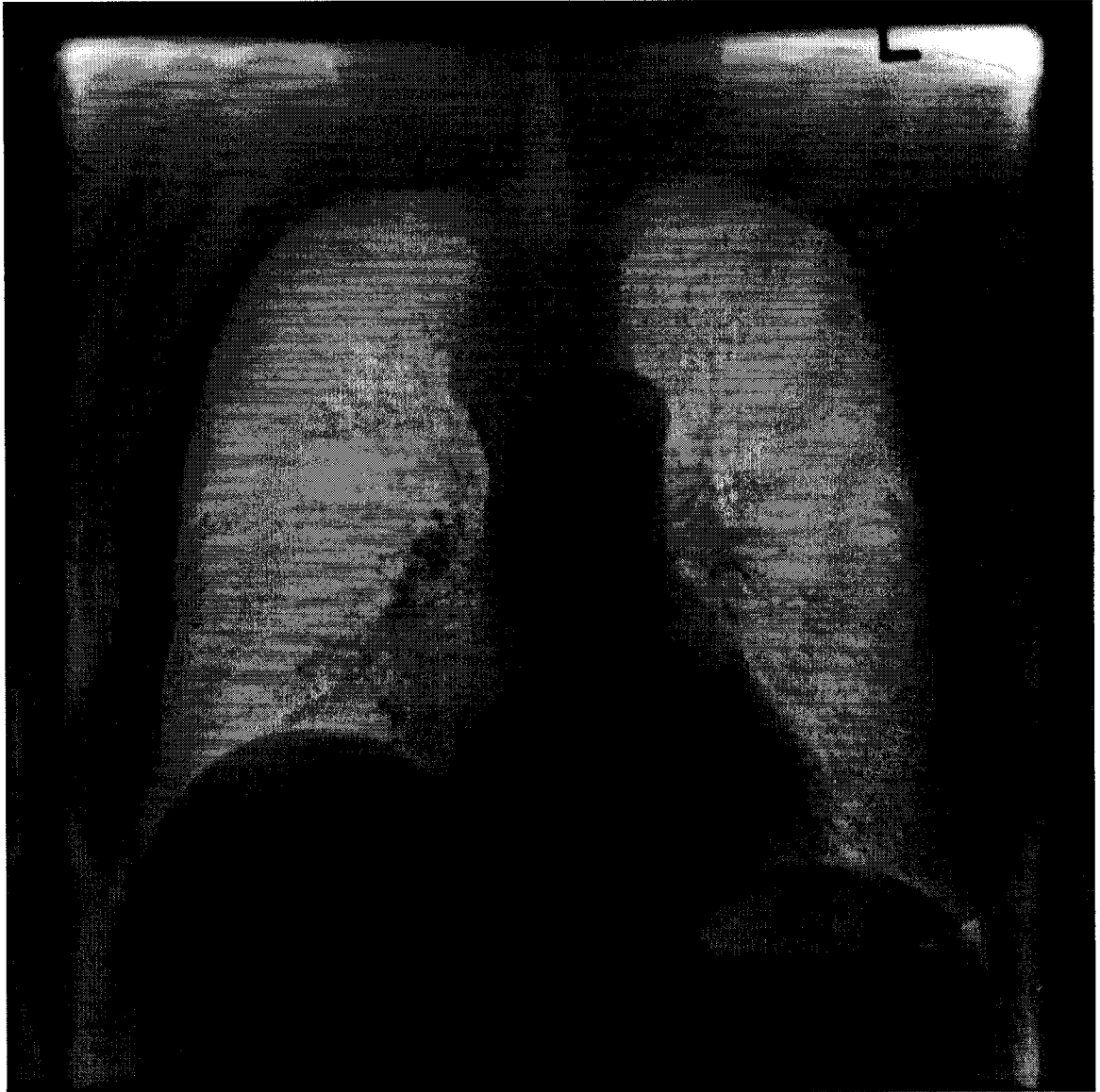


Figure 5.57. The reconstructed soft tissue image for patient E.

From these five Figures, one can conclude that the reconstruction works reasonably well. However, there is a slight “zebra” effect (light and dark regions) in these images. This is clearly visible on the right hand side of Fig. 5.53. One possible explanation for this effect is the removal of the ribs will reduce the attenuation characteristic of the regions that contain them. Thus, the number of photons detected (theoretically) by the imaging plate should be higher than the surrounding inter-rib spaces that do not contain bone. Hence, a difference exposure, or gray-level, will be produced, creating the “zebra” effect. This can be easily overcome by replacing the amount of bone removed with the same thickness of soft tissue. However, this should not be the case for the current images as the soft tissue images (outputted by the Fuji unit) do not display this “zebra” effect.

Another possibility is that due to the removal of the bone structure from the radiograph, the latitude, or the range of gray-levels, required to display the soft tissue radiograph is reduced when compared to the original radiograph. Therefore, it will be beneficial to increase the contrast of the image by re-scaling the gray-level of the soft tissue. This is likely to be the cause of the “zebra” effect for the current images. To overcome this, one will need to know the adjustment factors applied to the image. Since this is not readily available, a manual gray-level matching technique is attempted for Fig. 5.53. Fig. 5.53 is selected because this image shows the largest “zebra” effect. The left and right hand side of the image is adjusted independently since clearly the inter-rib space (dark region) on the right hand side will require a larger gray-level increase. The result of this simple gray-level matching is illustrated in Fig. 5.58. To produce this Figure, the gray-level for the pixels on the left hand side of I_s has been increased by 20 gray-levels, while on the right hand side has been increased by 80 gray-levels. From Fig. 5.58, one can see that using this simple matching method has reduced the “zebra” effect. A more refined method, such as matching each inter-rib space with its surrounding area, should yield better results, and may eliminate the “zebra” effect altogether.



Figure 5.58. The reconstructed soft tissue image for patient A with a simple gray-level matching.

6. Conclusion

A procedure that identifies the bone structure in a digital chest radiograph is presented in this dissertation. This new procedure, when employed with a dual-energy subtraction algorithm, should improve, or at least maintain, the diagnostic capability of a chest radiograph. In Chapter 3, a new type of bone equivalent material and a different soft tissue equivalent material were introduced. The bone equivalent material is a mixture of aluminum and PVC in a 1:2 thickness ratio, while the soft tissue equivalent material is composed of water enclosed by a Lucite casing. Based on the theoretical considerations and experimental results, both of these materials are expected to outperform the traditional bone equivalent material (aluminum) and soft-tissue equivalent material (Lucite).

The processes for the identification of bone structure in a bone-only image can be summarized as follows:

- 1) The edges of the bone structure are detected using the Canny edge detector, which outperforms the more traditional edge detectors such as Sobel and Prewitt.
- 2) The Yanowitz and Bruckstein image segmentation method is employed to produce a threshold surface, which is then used to separate the bone structure from the rest of the image.
- 3) The ranking filter with dual-triangular mask is used to eliminate the gaps and holes missing in the identified bone structure.

The bisection results for an anthropomorphic chest phantom image and five real patient images are illustrated in Section 5.4. From these results, one can observe that the automatic algorithm is able to identify most of the bone structure. The major concern is with the anterior ribs, which have a lower SNR due to their position. Another concern is with the expanded boundary of the bone structure, which over-estimates the true location of an edge and will lead to the subtraction of soft-tissue if employed in a dual-energy subtraction algorithm. Unfortunately, the expansion of the boundary is unavoidable due the noise level of the original bone-only image, which produces many holes and gaps in the identified bone structure that need to be eliminated.

The final reconstructed soft tissue images are illustrated in Figs. 5.53 to 5.57 in Section 5.5. In general, the reconstruction works well. However, there is a slight “zebra” effect (light and dark regions) in these images. This effect is probably caused by the gray scale processing of the subtracted soft tissue image by the Fuji system to enhance the image contrast, and may be eliminated by matching the gray-level histogram of the inter-rib space with its surrounding area.

Based on these observations, it can be seen that the current approach is a good starting point for the identification of bone structure in a digital chest radiograph. It is a good starting point because it uses a unique combination of image enhancement tools and edge detection algorithms that together minimize the problems presented by low SNR images. Further improvement of either contrast enhancement and/or edge detection processes will most likely not improve significantly upon the process used here. Improvement will come from either higher quantum detection efficiency image receptors and/or x-ray sources (both in terms of dual energy separation and photon flux).

The low SNR of the bone image is created due to the following reasons. Firstly, the number of photons detected by the high-energy (second) imaging plate will be reduced due to the attenuation by the copper filter placed in front of it. This will not only decrease the signal produced on the imaging plate, but also increase the quantum mottle, or graininess of the images, due to the statistical nature of the x-ray production. On top of this, the amount of scattering, or noise, detected by the high imaging plate will also increase due to the extra attenuated photons. Consequently, the overall SNR will decrease. This lower SNR will propagate to the bone only image with the decomposition process, producing a lower SNR bone image. Another reason for the lower SNR in the bone only image is that due to the higher attenuation characteristic of the bone, the number of photons reaching the imaging plate for the areas obstructed by the bone structure will be lower. This is illustrated in Fig. 6.1 where a typical 125 kVp x-ray spectrum (shown in Fig. 2.3) is used to compute the follow two energy spectra:

- 1) Passing through 15 cm of soft tissue.
- 2) Passing through 14 cm of soft tissue and 1 cm of cortical bone.

In other words, the second curve (bone + soft tissue) simulates a potential output spectrum in the areas of the radiograph that contain ribs. From Fig. 6.1, one can observe

that the number of non-attenuated photons is less for the curve containing bone. This implies the signal detected in areas with bone will be lower. And once again, these attenuated, or scattered, photons will likely increase the noise in the surrounding area, reducing the SNR even further.

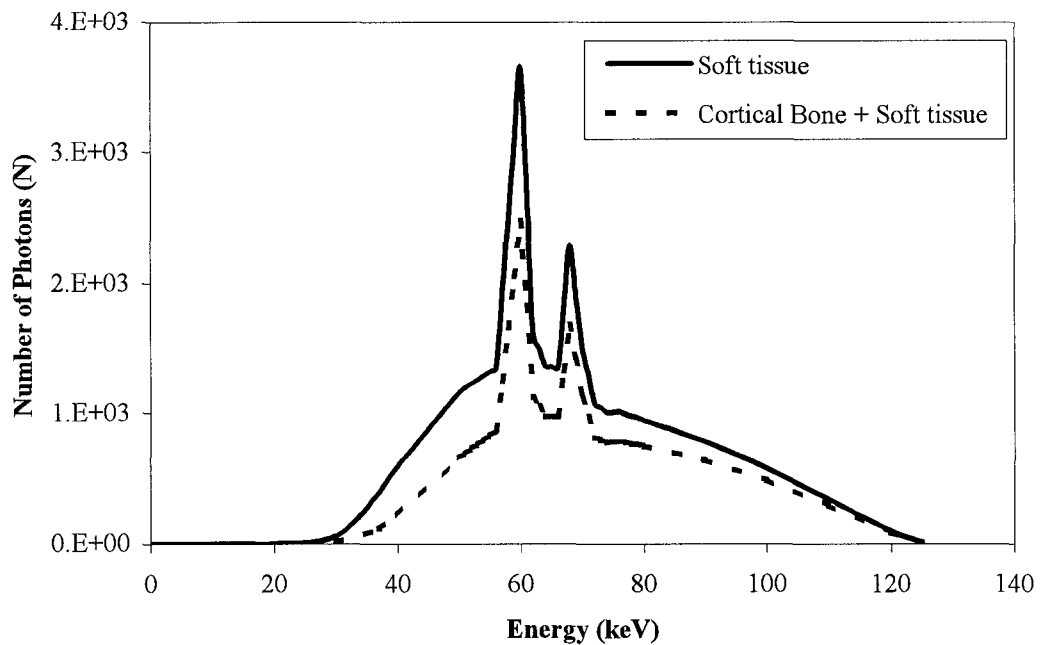


Figure 6.1. The difference between the number of non-attenuated photons passing through 15 cm of soft tissue compared with 14 cm of soft tissue plus 1 cm of cortical bone.

Additional error may be introduced during the conversion of the latent image on the imaging plate to the final image. The amplification and quantization process⁶⁶ will typically produce additional noise in the digital image. Lastly, a CR plate is more sensitive to scattered photons than a traditional screen film system, due to the low k-edge energy (of about 37 keV⁶⁷) of the europium activated barium fluorohalide compounds contained in the CR plate. This will decrease the SNR of the resulting image even

further. This is especially important for the high energy image since the copper filter in front of the second imaging plate will introduce more scattered photons.

In conclusion, the ability to identify and subtract the bone structure and only the bone structure from routine dual-energy chest images acquired using current technology and typical clinical settings is very limited. Simply, the SNR is insufficient to allow accurate detection and subtraction of bone structure. SNR will need to be improved in future equipment or in the acquisition process (ex: higher dose). Some possibilities that may enable this to happen are discussed in the next chapter.

A spin-off of this research is an algorithm that can automatically detect and compute the subject-to-noise ratio of low contrast disks inside a geometric chest phantom. This algorithm has the ability to locate the low contrast objects to an accuracy of less than one pixel, and provides results that are consistent with our understanding of SNR. This should simplify the evaluation of contrast detail phantoms by providing an accurate, quantitative analysis of the selected objects, and eliminates the subjectivity inherent in evaluating low contrast objects in current testing procedures. This research had been published in the March 2003 issue of *Medical Physics*,⁶⁸ and the article in its entirety is reprinted (with permission) in Appendix V.

7. Future Research

As demonstrated, noise in the bone-only image is one of the biggest problems affecting the identification procedures. This is because the noise does not only affect the edge detection process, but also the segmentation procedure. This problem was addressed through the implementation of a dual-triangular ranking filter, which unfortunately had a side effect of expanding the edge of the detected bone structure. One of the causes of the noise in the bone-only image is the subtraction of the high energy image, which is very noisy due to the following two reasons:

- 1) The amount of x-ray quanta reaching the second (high-energy) imaging plate is significantly less than the first one as illustrated in Fig. 2.6. Therefore, the signal will decrease and the noise level due to quantum mottle will increase.
- 2) The (Copper) filter between the two imaging plates will increase the amount of scattered photons exposing the second imaging plate. This will increase the noise level even further.

The most obvious solution is to eliminate the filtering process by acquiring the images sequentially. However, patient motion between exposures makes this solution less than ideal. Therefore, a different filter material is proposed in order to increase the SNR of the high energy image. This proposed material is tin.¹⁹

Tin is chosen because the binding energy of its K-shell electron is 29.2 keV, which leads to an increase in the photoelectric absorption of incoming photons for the energy region above 29.2 keV. This is illustrated in Fig. 7.1, where the thickness of Tin required to produce the attenuation is only 0.3 mm, while the thickness of Copper needed is 1 mm. Here the spectra are calculated using the same method used to compute the spectrum exposing the second imaging plate in Fig. 2.6. The result is that the amount of Compton scattering from the filter, which should be a significant contributor of noise to the high energy image, can be reduced. This is illustrated in Fig. 7.2, where the probabilities of Compton scattering for different filter materials are computed by

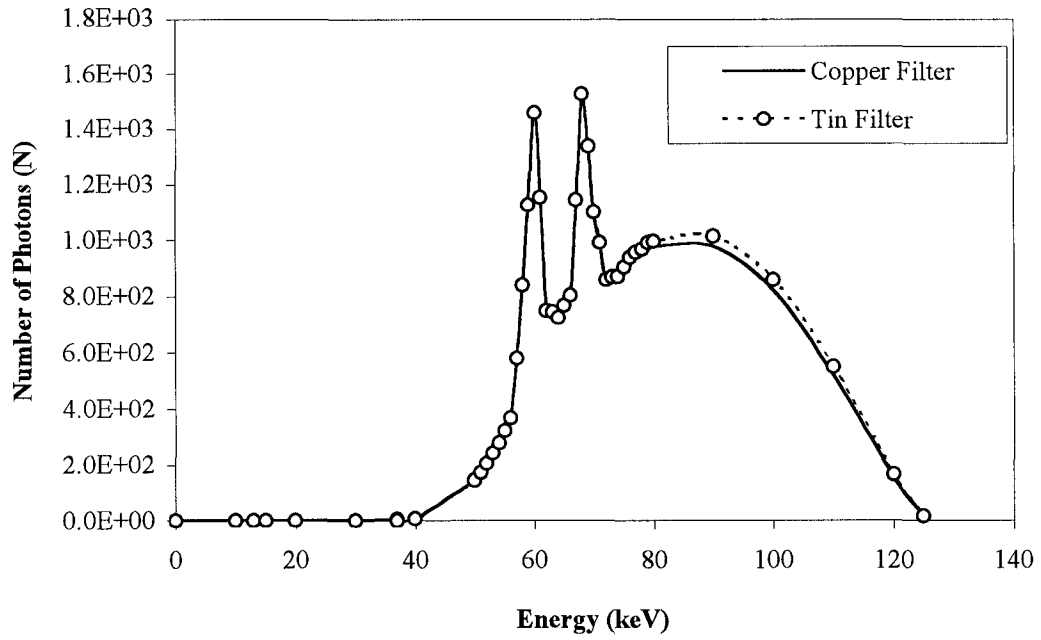


Figure 7.1. The photon spectrum exposing the second image plate after passing through different filter materials.

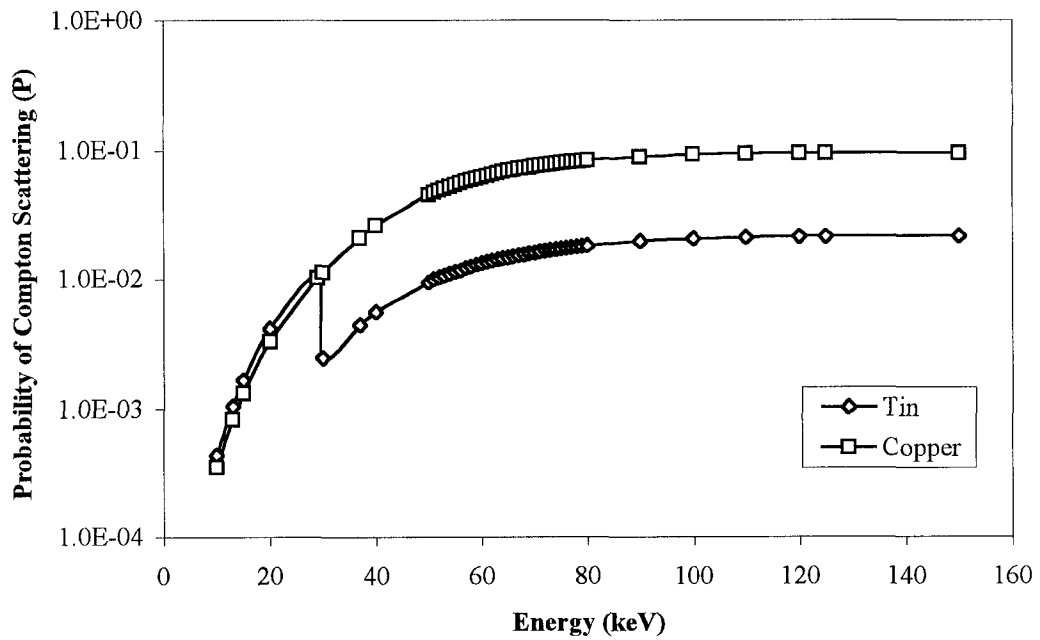


Figure 7.2. The probability of Compton scattering exposing the second imaging plate resulting from different filter materials.

$$P = (1 - e^{-\mu x}) \frac{\sigma}{\mu}. \quad (7.1)$$

Here P is the probability of the Compton scattering at a given photon energy. The μ is the total linear attenuation coefficient, while σ is the linear attenuation coefficient due to the Compton scattering interaction. Lastly, x is the thickness of the filter material required, which is equal to 0.3 mm for tin and 1 mm for copper. As illustrated in Fig. 7.2, the amount of Compton scattering for the tin filter should be less for the higher energies (≥ 30 keV). This should improve the SNR of the higher energy image.

Although the utilization of a tin filter should reduce the amount of scattering photons irradiating the second imaging plate, it does not eliminate the problem. Nor does this address the issue of lower signal (amount of photons) detected by the second imaging plate. To address these issues more thoroughly, a different acquisition approach will be required. One possibility is to use a sequential exposure method with very short time interval between the two acquired images. However, one has to be certain that patient movement (such as heart motion) is kept to a minimum. This is because, although motion between the images may be corrected for, it may create legal concerns (as discussed in Chapter 2).

Another possibility for single shot dual-energy acquisition is to pack two different phosphors (x-ray screen materials) onto a single screen as done by Boone et al.⁶⁹ In his approach, two different phosphors were uniformly distributed onto a single screen. One was more sensitive to lower energy photons and the other to higher energy photons; however, there was overlap in energy sensitivity. Yttrium oxysulfide:praseodymium ($\text{Y}_2\text{O}_2\text{S}:\text{Pr}^{3+}$) and gadolinium oxysulfide:europium ($\text{Gd}_2\text{O}_2\text{S}:\text{Eu}^{3+}$), with emission light photons centered at 514 nm (green) and 624 nm (red) respectively, were used. These light photons were then detected by two CCDs (charged-coupled devices) covered with the appropriate optical filter, producing the dual-energy images required with a single exposure. Clearly, the ideal materials will contain one phosphor completely sensitive only to low energy photons while the other is completely sensitive to only higher energy photons. However, nobody has discovered such ideal phosphors yet.

Also, one of the concerns with the above approach was that CCD (charged-coupled device) systems typically have large electronic noise. Also the detective

quantum efficiency (DQE) of the CCD system is comparable to film/screen only at limited demagnification factors.⁷⁰ The demagnification limit for lens type CCD systems is estimated to be about three, while for fiberoptic systems it is about five. This implies that the CCD chip will have to be large in order to produce satisfactory DQE since a typical chest radiograph is 43-by-35 cm (17-by-14 inches), a very difficult (expensive) proposition. However, a commercially available CCD radiographic system developed by Imaging Dynamics Corporation (Calgary, Alberta, Canada) may have overcome these problems by using a slightly different approach.

One may also try to use two different PSPs to accomplish this task, eliminating the need for the CCD chips. However, a simple uniform distribution of the two PSPs onto a single screen will not be an acceptable solution since one cannot control the movement of the electrons after the initial interaction. Hence, a compromise is proposed here. Instead of mixing the two PSPs, one may try to apply a different PSP onto each side of the imaging plate. The PSP on the side closer to the patient will be used to detect the low energy photons, while the PSP on the other side is used to detect the higher energy photons. This will eliminate the need of the copper filter between the two imaging plates, while still producing the two different energy images required. If successful, this should reduce the problem of scattering photons in the single shot “sandwiched” detector method to a minimum. The emulsion holding the two PSPs, plus the first PSP layer, will still generate some scattered photons and reduce the signal of the second layer, but it should be significantly better than utilizing a metal filter.

A number of issues will need to be addressed before one can utilize this idea. First and foremost, one will need to develop a suitable PSP for this application. This is because commercially available PSPs are based on RbCl, BaFBr:Eu²⁺, BaF(BrI):Eu²⁺, BaSrFBr:Eu²⁺, which have a maximum k-edge of about 37 keV (BaFBr:Eu²⁺) as mentioned in the last Chapter. Clearly, one should not use a PSP that is lower than 37 keV for the second PSP layer as it will be more sensitive to scattering noise in a high scatter environment.

So what is an ideal PSP for the second layer? Obviously it should have a k-edge higher than 37 keV, but what should its k-edge energy be? To answer this question, one may wish to examine the photoelectric and Compton Scattering attenuation characteristic

of bone. From the mass attenuation coefficients numbers provide by XCOM, one can calculate that the cross-over point, or the point at which the photoelectric absorption attenuation coefficient and the Compton Scattering attenuation coefficient are equal to each other, is about 56 keV for cortical bone. Hence a k-edge above 56 keV for the second PSP layer would be ideal. This is because the first imaging plate would include the photoelectric absorption of cortical bone (k-edge of BaFBr:Eu²⁺ is about 37 keV as mentioned before). In other words, one would want to incorporate materials such as Holmium (Z = 67, k-edge = 55.6 keV) or higher Z materials into the second layer. However, these materials are selected based on their k-edge characteristic, and other concerns, such as their ability to (photostimulable) luminesce and chemical stability, will also need to be considered.

Once the proper PSP materials are developed, additional technical issues, such as readout of the latent images on both sides of the imaging plate and elimination of potential optical and/or electron crossover, will need to be addressed before this concept may be implemented. Also, due to the fact that the second layer of the PSP only receives the “leftover” photons that do not get absorbed by the first layer, the signal produced will be lower. This may be overcome by increasing the dose to the patient. However in a study by Shaw and Gur⁷¹, it is estimated that in order for the SNR of the high energy image of the conventional sandwich detector technique to match that of the sequential method, the x-ray output have to be increased by a factor of up to 16 times. Therefore, a complete study of the benefit of the additional dose, such as better detection of early stage lung nodules, should be carried out in a phantom study to determine the optimal dose setting before such steps are taken.

With the advance in spectroscopy,⁷² it may be possible to obtain the complete x-ray spectrum for every pixel on the radiograph in the future. If achieved, this would allow dual-energy subtraction with only a single exposure and no filter, as the spectrograph can be easily separated into two components. This will also allow better control of the separation of the two energy levels, as one can easily pick the range of energy one prefers, to create the low- and high-energy radiographs. Also, with spectral analysis, one should be able to reduce the amount of image noise due to scattering on the final radiograph by eliminating the lower energy bins that contain photon numbers that

are much greater than the original spectrum (since these excess photons would have been scattered into the bins). Lastly, additional components (such as fat or blood) may be decomposed. This may provide additional diagnostic information for the radiologists.

Another improvement is the incorporation of the bone and soft-tissue equivalent materials into the subtraction algorithm. These equivalent materials, combined with the conic and cubic surface equations as proposed by Cardinal and Fenster³⁷, should increase the accuracy of the decomposition algorithm. Also, the algorithm currently takes about 12 hours to process one image, where the majority of time is used in the segmentation procedure. This may be due to the fact that the program is coded in Matlab, where experiments have shown that code written in Matlab might take up to 10 times longer to complete when compared with program coded in C.

Once these improvements are included, the next step will be to include techniques that may remove calcified nodules in the identified bone structure. Ultimately, the goal is to develop a highly accurate process that can automatically detect lung tumors at a resectable stage for dual-energy radiographs by combining the refined algorithm with CAD programs that can detect lung nodules (such as the one proposed by Xu et al.⁵⁴ or Baydush et al.⁷³), abnormal interstitial patterns⁵³, pneumothorax⁷⁴, and cardiomegaly⁷⁵. This may lead to an effective and accurate screening program for lung cancer, and more accurate detection of other lung disease.

Finally in a study by Friedman et al.⁷⁶, it has been shown that dual-energy chest radiography may be a viable alternative for the measurement of the mineral content of bone with ribs, which may allow for the detection of osteoporosis. This is of significant interest since smoking is suspected to be one of the causes of both lung cancer and osteoporosis. Therefore, a simple screening method, such as dual-energy chest radiography, which allows for the detection of both diseases, will be of great value.

8. References

- ¹ American Lung Association: **Trends in Lung Cancer Morbidity and Mortality**, Atlanta, USA, July 2001.
- ² National Cancer Institute of Canada: **Canadian Cancer Statistics 2001**, Toronto, Canada, 2001.
- ³ American Cancer Society: **Cancers Facts and Figures 2001**, Atlanta , USA, 2001.
- ⁴ National Cancer Institute of Canada: **Canadian Cancer Statistics 2000**, Toronto, Canada, 2001.
- ⁵ M.R. Melamed, B.J. Flehinger, M.B. Zaman, R.T. Heelan, W. A. Prechick and N. Martini, "Screening for early lung cancer," *Chest* **86**, 44–53 (1984).
- ⁶ R.S. Fontana, D.R. Sanderson, L.B. Woolner, W.F. Taylor, W.E. Miller and J.R. Muhm. "Lung cancer screening: The Mayo program," *Journal of Occupational Medicine* **28**, 746–750 (1986).
- ⁷ Canadian Cancer Society-Ontario (<http://www.ontario.cancer.ca>)
- ⁸ G. Hillerdal, "Long-term survival of patients with lung cancer from a defined geographical area before and after radiological screening," *Lung Cancer* **15**, 21–30 (1996).
- ⁹ J.R. Muhm, W.E. Miller and R.S. Fontana, "Lung cancer detected during a screening program using four-month chest radiographs," *Radiology* **148**, 609–615 (1983).
- ¹⁰ Y. Baba, M. Takahashi, S. Tominguchi and S. Kiyota, "Cost-effectiveness decision analysis of mass screening for lung cancer," *Academic Radiology* **5**, S344–S346 (1998).
- ¹¹ J.H. Woodring, "Pitfalls in the radiologic diagnosis of lung cancer," *American Journal of Roentgenology* **154**, 1165–1175 (1990).
- ¹² M.L. Giger, K. Doi, H. MacMahon, C.E. Metz and F.F. Yan, "Pulmonary nodules: Computer-aided detection in digital chest images," *Radiographics* **10**, 41–51 (1990).
- ¹³ C.J. Herold, A.A. Bankier and D. Fleischmann, "Lung metastases," *European Radiology* **6**, 596–606 (1996).

- ¹⁴ R.A. Kruger, J.D. Armstrong, J.A. Sorenson and L.T. Niklason, "Dual energy film subtraction technique for detecting calcification in solitary pulmonary nodules," *Radiology* **140**, 213–219 (1981).
- ¹⁵ H. Nishitani, Y. Umezu, K. Ogawa, H. Yuzuriha, H. Tanaka and K. Matsuura, "Dual-energy projection radiography using condenser x-ray generator and digital radiography apparatus," *Radiology* **161**, 533–535, (1986).
- ¹⁶ T. Ishigaki, S. Sakuma, Y. Horikawa, M. Ikeda and H. Yamaguchi, "One-shot dual-energy subtraction imaging," *Radiology* **161**, 271–273 (1986).
- ¹⁷ T. Ishigaki, S. Sakuma and M. Ikeda, "One-shot dual-energy subtraction chest imaging with computed radiography: clinical evaluation of film images," *Radiology* **168**, 67–72 (1988).
- ¹⁸ B.K. Stewart, "Single exposure dual-energy digital radiography," *Computer Methods and Programs in Biomedicine* **30**, 127–135 (1989).
- ¹⁹ B.K. Stewart and H.K. Huang, "Single-exposure dual-energy computed radiography," *Medical Physics* **17**, 866–875 (1990).
- ²⁰ S. Kido, J. Ikezoe, H. Naito, S. Tamura, T. Kozuka, W. Ito, K. Shimura and H. Kato, "Single-exposure dual-energy chest images with computed radiography," *Investigative Radiology* **28**, 482–487 (1993).
- ²¹ S. Kido, J. Ikezoe, H. Naito, J. Arisawa, S. Tamura, T. Kozuka, W. Ito, K. Shimura and H. Kato, "Clinical evaluation of pulmonary nodules with single-exposure dual-energy subtraction chest radiography with an iterative noise-reduction algorithm," *Radiology* **194**, 407–412 (1995).
- ²² S.J. Riederer, "Digital radiography," *Critical Reviews in Biomedical Engineering* **12**, 163–200 (1985).
- ²³ H. Rougeot, "Direct x-ray photoconversion processes" in *Medical Physics Monograph No. 22: Digital Imaging*, edited by W.R. Hendee and J.H. Trueblood, Medical Physics Publishing Corporation, Madison, 49–96 (1993).
- ²⁴ J.H. Trueblood, S.E. Burch, K. Kearfott and K.W. Brooks, "Radiographic film digitization" in *Medical Physics Monograph No. 22: Digital Imaging*, edited by W.R.

- Hendee and J.H. Trueblood, Medical Physics Publishing Corporation, Madison, 97–122 (1993).
- ²⁵ J.A. Seibert, “Film digitizers and laser printers” in *Medical Physics Monograph No. 25: Practical Digital Imaging and PACS*, edited by J.A. Seibert, L.J. Filipow, K.P. Andriole, Medical Physics Publishing Corporation, Madison, 107–133 (1999).
- ²⁶ G.T. Barnes, “Digital x-ray image capture with image intensifier and storage phosphor plates: Imaging principles, performance and limitations” in *Medical Physics Monograph No.22: Digital Imaging*, edited by W.R. Hendee and J.H. Trueblood, Medical Physics Publishing Corporation, Madison, 25–48 (1993).
- ²⁷ S.M. Kengyelics, J.H. Launders and A.R. Cowen, “Physical imaging performance of a compact computed radiography acquisition device,” *Medical Physics* **25**, 354–360 (1998).
- ²⁸ K.P. Andriole, “Computed radiography overview” in *Medical Physics Monograph No. 25: Practical Digital Imaging and PACS*, edited by J.A. Seibert, L.J. Filipow, K.P. Andriole, Medical Physics Publishing Corporation, Madison, 135–157 (1999).
- ²⁹ D.L. Lee, L.K. Cheung, L.S. Jeromin and E. Palecki, “Imaging performance of a direct digital radiographic detector using selenium and a thin-film-transistor array”, in *Computer Assisted Radiology*, edited by K.U. Lemke, M.W. Vannier, K. Inamura and A.G. Farman, Elsevier, Amsterdam, 41–46 (1996).
- ³⁰ J. Rowlands and S. Kasap, “Amorphous semiconductors usher in digital x-ray imaging,” *Physics Today* **50**, 24–30, (1997).
- ³¹ W. Zhao, I. Blevis, S. Germann, J.A. Rowlands, D. Waechter and Z. Huang, “Digital radiology using active matrix readout of amorphous selenium: Construction and evaluation of a prototype real-time detector,” *Medical Physics* **24**, 1834–1843 (1997).
- ³² W. Zhao and J.A. Rowlands, “Digital radiology using active matrix readout of amorphous selenium: Theoretical analysis of detective quantum efficiency,” *Medical Physics* **24**, 1819–1833 (1997).
- ³³ W. Zhao, D. Waechter, and J.A. Rowlands, “Digital radiology using active matrix readout of amorphous selenium: Radiation hardness of cadmium selenide thin film transistors,” *Medical Physics* **25**, 527–538 (1998).

- ³⁴ W. Zhao, J. Law, D. Waechter, Z. Huang and J.A. Rowlands, "Digital radiology using active matrix readout of amorphous selenium: Detectors with high voltage protection," *Medical Physics* **25**, 539–549 (1998).
- ³⁵ A. Kano, K. Doi, H. MacMahon, D. D. Hassell and M.L. Giger, "Digital image subtraction of temporally sequential chest images for detection of interval change," *Medical Physics* **21**, 453–461 (1994).
- ³⁶ R.E. Alvarez and A. Macovski, "Energy-selective reconstructions in X-ray computerized tomography," *Physics in Medicine and Biology* **21**, 733–744 (1976).
- ³⁷ H.N. Cardinal and A. Fenster, "An accurate method for direct dual-energy calibration and decomposition," *Medical Physics* **17**, 327–341 (1990).
- ³⁸ D.C. Giancoli, *Physics for Scientists and Engineers, 2nd Edition* (Prentice Hall, New Jersey, 1988).
- ³⁹ J.M. Boone and J.A. Seibert, "An accurate method for computer-generating tungsten anode x-ray spectra from 30 to 140 kV," *Medical Physics* **24**, 1661–1670 (1997).
- ⁴⁰ J.T. Bushberg, J.A. Seibert, E.M. Leidhold, Jr. and J.M. Boone, *The Essential Physics of Medical Imaging* (Williams & Wilkins, Baltimore, 1994).
- ⁴¹ H.E. Johns and J.R. Cunningham, *The Physics of Radiology, Fourth Edition* (Charles C. Thomas, Springfield, 1983).
- ⁴² H. Kato, "Photostimulable phosphor radiography design considerations" in *Medical Physics Monograph No. 20: Specification, acceptance testing and quality control of diagnostic X-ray imaging equipment*, edited by J.A. Seibert, C.R. Barnes, R.G. Gould, American Institute of Physics, Inc., Woodbury 731–770 (1994).
- ⁴³ D.L. Ergun, C.A. Mistretta, D.E. Brown, R.T. Bystriany, W.K. Sze, F. Kelcz and D.P. Naidich, "Single-exposure dual-energy computed radiography: Improved detection and processing," *Radiology* **174**, 243–249 (1990).
- ⁴⁴ <http://physics.nist.gov/PhysRefData/XrayMassCoef/cover.html>
- ⁴⁵ F.H. Attix, *Introduction to Radiological Physics and Radiation dosimetry* (John Wiley & Sons, Inc., New York, 1986).
- ⁴⁶ R.A. Rutherford, B.R. Pullan and I. Isherwood, "Measurement of effective atomic number and electron density using an EMI scanner," *Neuroradiology* **11**, 15–21 (1976).

- ⁴⁷ R.A. Rutherford, B.R. Pullan and I. Isherwood, "X-ray energies for effective atomic number determination," *Neuroradiology* **11**, 23–28 (1976).
- ⁴⁸ R.A. Brooks, "A quantitative theory of the Hounsfield unit and its application to dual energy scanning," *Journal of Computer Assisted Tomography* **1**, 487–493 (1977).
- ⁴⁹ L.A. Lehmann, R.E. Alvarez, A. Macovski, W.R. Brody, N.J. Pelc, S.J. Riederer and A.L. Hall, "Generalized image combinations in dual KVP digital radiography," *Medical Physics* **8**, 659–667 (1981).
- ⁵⁰ J.R. Taylor, *An Introduction to Error Analysis* (University Science Books, Mill Valley, 1982).
- ⁵¹ International Commission on Radiation Units and Measurements, *ICRU Report 44: Tissue Substitutes in Radiation Dosimetry and Measurement* (International Commission on Radiation Units and Measurements, Bethesda, 1989).
- ⁵² www.gu.edu.au/school/eng/mmt/RadDec.html
- ⁵³ T. Ishida, S. Katsuragawa, T. Kobayashi, H. MacMahon and K. Doi, "Computerized analysis of interstitial disease in chest radiographs: Improvement of geometric-pattern feature analysis," *Medical Physics* **24**, 915–924 (1997).
- ⁵⁴ X.W. Xu, K. Doi, T. Kobayashi, H. MacMahon and M.L. Giger, "Development of an improved CAD scheme for automated detection of lung nodules in digital chest images," *Medical Physics* **24**, 1395–1403 (1997).
- ⁵⁵ J.I. Toriwaki, Y. Suenaga, T. Negoro and T. Fukumura, "Pattern recognition of chest X-ray images," *Computer Graphics and Image Processing* **2**, 252–271 (1973).
- ⁵⁶ H. Wechsler and J. Sklansky, "Finding the rib age in chest radiographs," *Pattern Recognition* **9**, 21–30 (1977).
- ⁵⁷ G.F. Powell, K. Doi and S. Katsuragawa, "Localization of inter-rib spaces for lung texture analysis and computer-aided diagnosis in digital chest images," *Medical Physics* **15**, 581–587 (1988).
- ⁵⁸ F.M. Carrascal, M. Cabrera, J.M. Carreira, L. Gomez and J.J. Vidal, "Pulmonary vessels detection in digital chest radiographs applied to pulmonary vascular patterns recognition", in *Computer Assisted Radiology*, edited by H.U. Lemke, M.W. Vannier, K. Inamura and A.G. Farman, Elsevier, Amsterdam 369–373 (1996).

- ⁵⁹ R. C. Gonzalez and R. E. Woods, *Digital Image Processing* (Addison-Wesley Publishing Company, MA, 1992).
- ⁶⁰ J. Canny, "A computational approach to edge detection," *IEEE Transactions on Pattern Analysis and Machine Intelligence* **8**, 679–698 (1986).
- ⁶¹ S.D. Yanowitz and A.M. Bruckstein, "A new method for image segmentation," *Computer Vision, Graphics, and Image Processing* **46**, 82–95 (1989).
- ⁶² J.M.S. Prewitt, "Object enhancement and extraction", in *Picture Processing and Psychopictorics*, edited by B.S. Lipkin and A. Rosenfeld, Academic Press, New York (1970).
- ⁶³ J.R. Parker, *Algorithms for Image Processing and Computer Vision* (John Wiley & Sons, Inc., New York, 1997).
- ⁶⁴ W.H. Press, S.A. Teukolsky, W.T. Vetterling and B.P. Flannery, *Numerical Recipes in FORTRAN, Second Edition* (Cambridge University Press, Cambridge, 1992).
- ⁶⁵ W.K. Pratt, *Digital Image Processing* (John Wiley & Sons, Inc., New York, 1978).
- ⁶⁶ E. Mah, E. Samei and D.J. Peck, "Evaluation of a quality control phantom for digital chest radiography," *Journal of Applied Clinical Medical Physics* **2**, 90–101 (2001).
- ⁶⁷ K.L. Yip, B.R. Whiting, T.E. Kocher, D.P. Trauernicht and R.L. Van Metter, "Understanding the relative sensitivity of radiographic screens to scattered radiation," *Medical Physics* **23**, 1727–1737 (1996).
- ⁶⁸ A.L.C. Kwan, L.J. Filipow and L.H. Le, "Automatic quantitative low contrast analysis of digital chest phantom radiographs," *Medical Physics* **30**, 312–320 (2003).
- ⁶⁹ J.M. Boone, M. Tecotzky and G.M. Alexander, "Binary screen detector system for single-pulse dual-energy radiography," *Radiology* **183**, 863–873 (1992).
- ⁷⁰ S. Hejazi and D.P. Trauernicht, "System considerations in CCD-based x-ray imaging for digital chest radiography and digital mammography," *Medical Physics* **24**, 287–297 (1997).
- ⁷¹ C.C. Shaw and D. Gur, "Comparison of three different techniques for dual-energy subtraction imaging in digital radiography: A signal-to-noise analysis," *Journal of Digital Imaging* **5**, 262–270 (1992).
- ⁷² S. Miyajima, "Thin CdTe detector in diagnostic x-ray spectroscopy," *Medical Physics* **30**, 771–777 (2003).

- ⁷³ A.H. Baydush, D.M. Catarious, J.Y. Lo and C.K. Abbey and C.E. Floyd, Jr., “Computerized classification of suspicious regions in chest radiographs using subregion Hotelling observers,” *Medical Physics* **28**, 2403–2409 (2001).
- ⁷⁴ S. Sanada, K. Doi, and H. MacMahon, “Image feature analysis and computer-aided diagnosis in digital radiography: Automated detection of pneumothorax in chest images,” *Medical Physics* **19**, 1153–1160 (1992).
- ⁷⁵ N. Nakamori, K. Doi, V. Sabeti and H. MacMahon, “Image feature analysis and computer-aided diagnosis in digital radiography: Automated analysis of sizes of heart and lung in digital chest images,” *Medical Physics* **17**, 342–350 (1990).
- ⁷⁶ S.E. Friedman, E.V. Dubovsky, J. Dubovsky, C.B. Alexander, C.A. Robinson, E.A. Sabbagh, G.T. Barnes and R.G. Fraser, “Mineral content of bone: Measurement by energy subtraction digital chest radiography,” *American Journal of Roentgenology* **149**, 1199–1202 (1987).
- ⁷⁷ P. Vuysteke, P. Dewaele and E. Schoeters, “Optimizing radiography imaging performance” in *Medical Physics Monograph No. 23: The Expanding Role of Medical Physics in Diagnostic Imaging (1997 AAPM Summer School)*, edited by G.D. Frey and P. Sprawls, Medical Physics Publishing Corporation, Madison 107–151 (1997).
- ⁷⁸ P.J. Burt and E.H. Adelson, “The Laplacian pyramid as a compact image code,” *IEEE Transactions on Communications* **COM-31**, 532–540 (1983).
- ⁷⁹ B. Jähne, *Practical Handbook on Image Processing for Scientific Applications* (CRC Press LLC, Boca Raton, 1997).
- ⁸⁰ <http://medical.nema.org/dicom/2001.html>
- ⁸¹ <http://oasis.rad.upenn.edu/~grevera>
- ⁸² H.G. Chotas, C.E. Floyd, Jr., G.A. Johnson and C.E. Ravin, “Quality control phantom for digital chest radiography,” *Radiology* **202**, 111–116 (1997).
- ⁸³ A. H. Baydush, W. C. Ghem and C.E. Floyd, Jr., “Anthropomorphic versus geometric chest phantoms: A comparison of scatter properties,” *Medical Physics* **27**, 894–897 (2000).
- ⁸⁴ H. Blume, “Stimulable phosphor systems - Technical aspects” in *Proceedings of the Chest Imaging Conference, 1987*, edited by W. W. Pepler and A.A. Alter, Medical Physics Publishing Corporation, Madison, 194–207 (1988).

Appendix I. Fitting of Rib Edges

As mentioned in Chapter 4, the fitting of rib edges has been attempted for some time. In fact in 1977, Wechsler and Sklansky⁵⁶ proposed a fitting method using parabolic and elliptical equations for each rib edge. The parabolic equations are used for the more curved part of the rib edges, while the elliptical equations are used for the sections of the rib edges closer to the spinal cord. However, this process is not very accurate for the large digital images produced by the modern digital radiographic units. In this appendix, a section of a rib edge from a patient image will be used to demonstrate this limitation.

The part of the rib edge selected is the section that Wechsler and Sklansky proposed to be fitted by a parabolic equation. This edge is detected using the Canny edge detector discussed in Section 5.1. The section is then extracted and the noise on the image is removed manually. The edge is then transferred into an Excel spreadsheet where it can be fitted with a number of different equations. This processed rib edge is illustrated in Fig. A1.1.

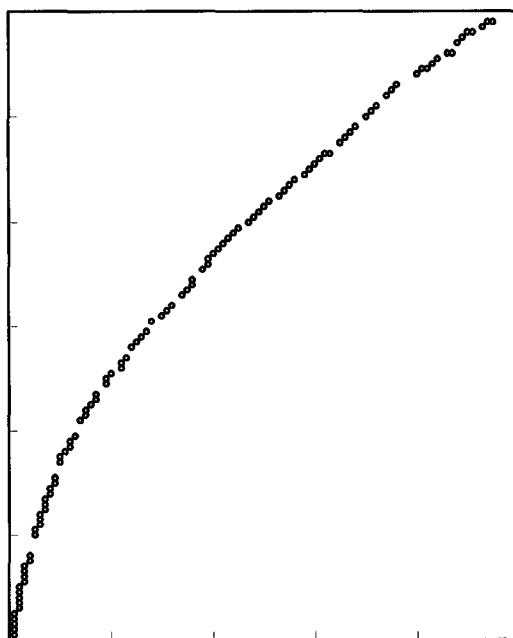


Figure A1.1. The processed rib edge.

The next step is to fit this section of the rib edge with a number of equations, which should include the parabolic equation. Although parabolic fitting is not available in Excel, it may be fitted by using a second order polynomial. The general equation for a parabola symmetric in the x direction is

$$(x - x_c) = a(y - y_c)^2, \quad (\text{A1.1})$$

where constants x_c and y_c designate the location of the vertex, while a controls the width of the parabola. If one expands the squared term and simplifies

$$x = ay^2 - 2ayy_c + ay_c^2 + x_c, \quad (\text{A1.2})$$

which can be reduced to a second order polynomial

$$x = a'y^2 + b'y + c'. \quad (\text{A1.3})$$

In order to fit the above polynomial in Excel, the x and y axis values have to be flipped such that the y axis values are plotted on the regular x axis. This is illustrated in Fig. A1.2. Besides the parabolic fit, the power, logarithmic, second and fourth order polynomial fits are also attempted in Figs. A1.3 to A1.6 respectively.

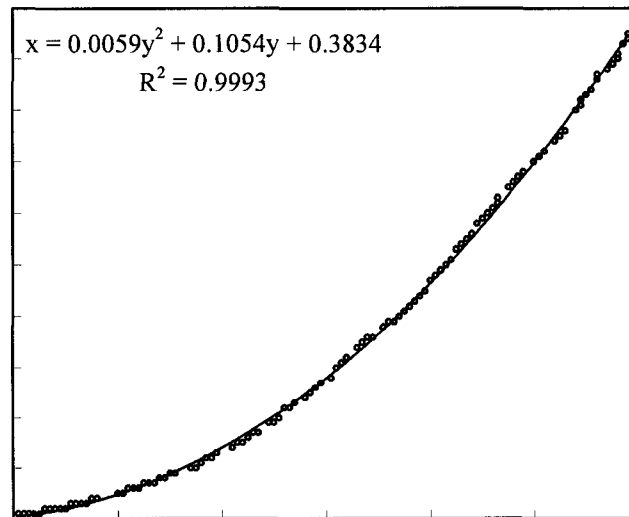


Figure A1.2. Parabolic fitting of the processed rib edge.

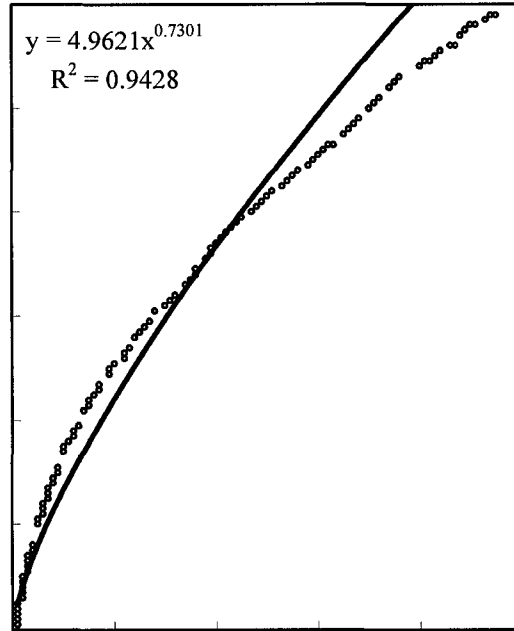


Figure A1.3. Power fitting of the processed rib edge.

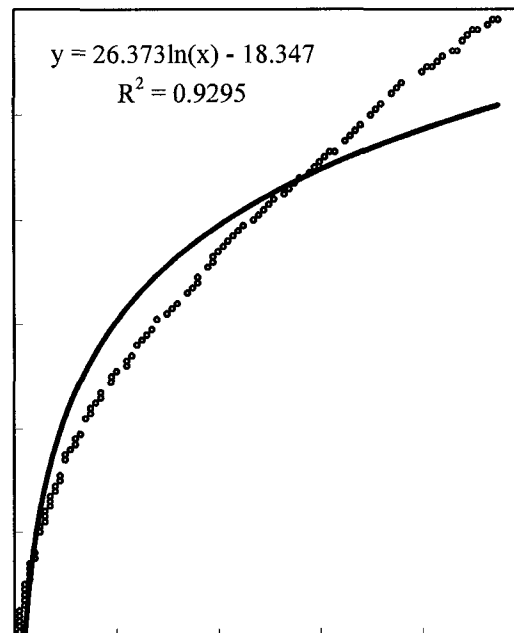


Figure A1.4. Logarithmic fitting of the processed rib edge.

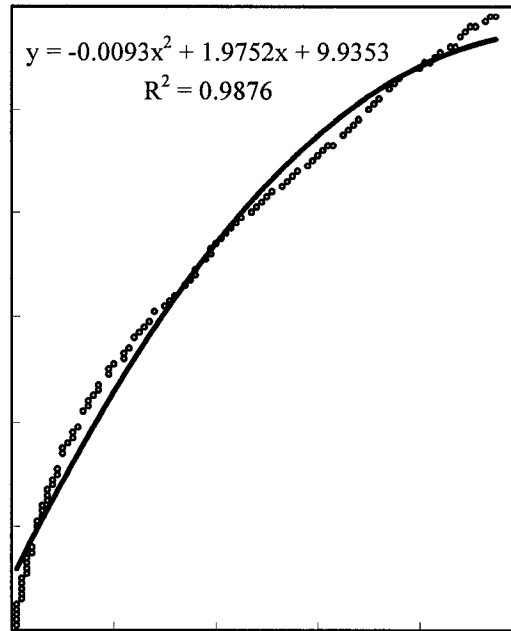


Figure A1.5. Second order polynomial fitting of the processed rib edge.

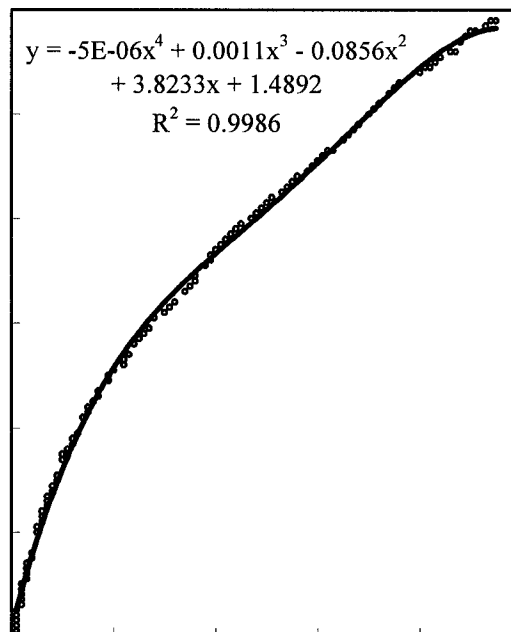


Figure A1.6. Fourth order polynomial fitting of the processed rib edge.

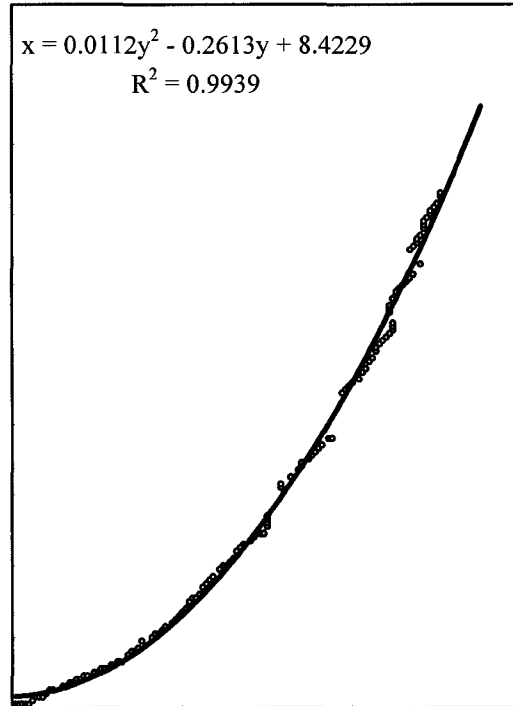


Figure A1.7. Parabolic fitting of another processed rib edge.

From these Figures, one can observe that the best fit is the parabolic one. However, one can also observe that some of the rib edges lie on top of the trend line, while others are below it even for this fit. This may be due to the fact that the edge is not a perfect parabola. Although this should not be a problem for smaller images or a small section of a bigger image that is illustrated here (The images shown here are only 100 pixels by 120 pixels), this mismatch will become an issue once more pixels are involved. This is illustrated in Fig. A1.7 for another rib section with more pixels.

Wechsler and Sklansky also proposed the use of elliptical equations for the section of a rib that is closer to the spinal cord. This is illustrated in Fig. A1.8, which demonstrates a few concerns. Firstly, the result depends on the number of pixels used for each type of fitting, which means the software has to decide when to switch from a parabolic fit to an elliptical fit. Secondly, discontinuity may occur at the pixel where the

fit is transformed from a parabola to an ellipse. Lastly, the utilization of two equations complicates the fitting procedure.

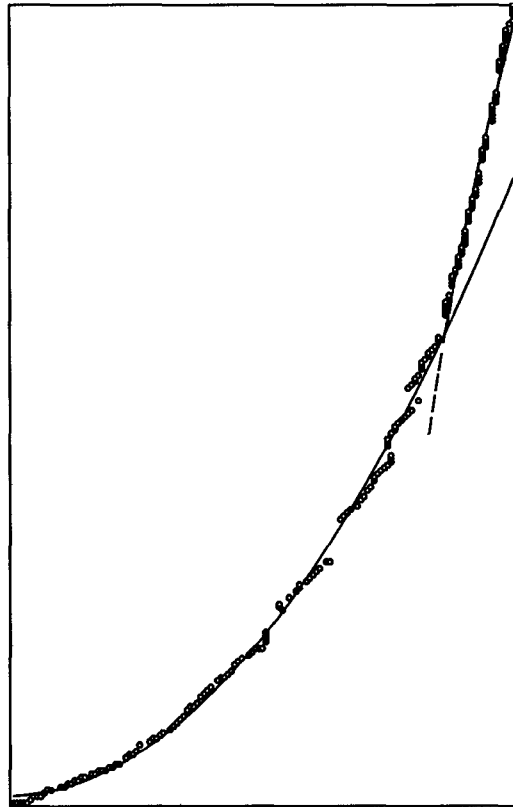


Figure A1.8. Parabolic and elliptical fitting of another processed rib edge.

Another problem with fitting the rib edges with predefined equations is the handling of the missing rib edges. As mentioned in Section 5.1, the rib edges detected usually contain some gaps. This is mainly due to the noise and interference in the radiograph. Obviously, one would need the fitting algorithm to be able to locate these missing edges. However from statistics, one knows that the bigger the gaps, the less accurate the fit will be. This is illustrated in Fig. A1.9 where part of the rib edge (x) is removed from the fit. As one can observe, the trend line does not approximate the last part of this missing section very accurately, as expected. This could pose a problem for

the fitting algorithm. Due to these concerns, the fitting technique is not utilized in the algorithm in this dissertation.

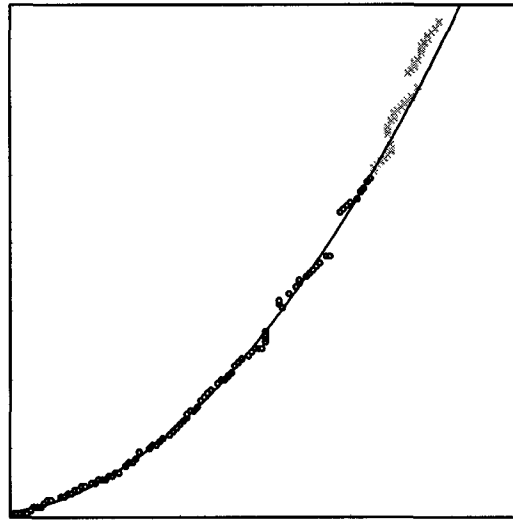


Figure A1.9. An illustration of some missing rib edges.

Appendix II. Reverse MUSICA

Multi-Scale Image Contrast Amplification⁷⁷ (MUSICA) is an image processing procedure developed by Agfa. It has the ability to enhance subtle features in an image based on the gray-level of the pixel. MUSICA consists of two major components: Laplacian pyramid decomposition^{78,79} (LPD) and the contrast equalization procedure (CE). The LPD decomposes the image into a series, or pyramid, of progressively smaller images. Each image is a band-pass filtered copy of the original image, with the finer details (higher frequency components) dominating the lower levels. The first level of the LPD is obtained by first convoluting the original image (g_0) with a 5×5 Gaussian mask, or a low-pass filter. This smoothed image is then reduced by a factor of four with sub-sampling as illustrated in Fig. A2.1.

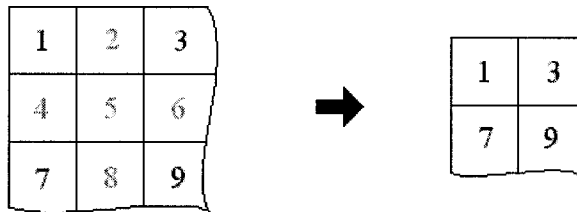


Figure A2.1. Sub-sampling of the filtered image.

The sub-sampling image (g_1) is then bilinearly interpolated to the original size (i_1), and the Laplacian pyramid layer (L_1) is the difference between the original image and the interpolated image

$$L_1 = g_0 - i_1. \quad (\text{A2.1})$$

This process will continue with the sub-sampled image (g_l) replacing the original image (g_0) until all the required Laplacian pyramid layers (LPL) are obtained.

Once all the LPL are calculated, the contrast equalization procedure is applied. Firstly, the smaller gray values in each layer represent the more subtle details. Therefore,

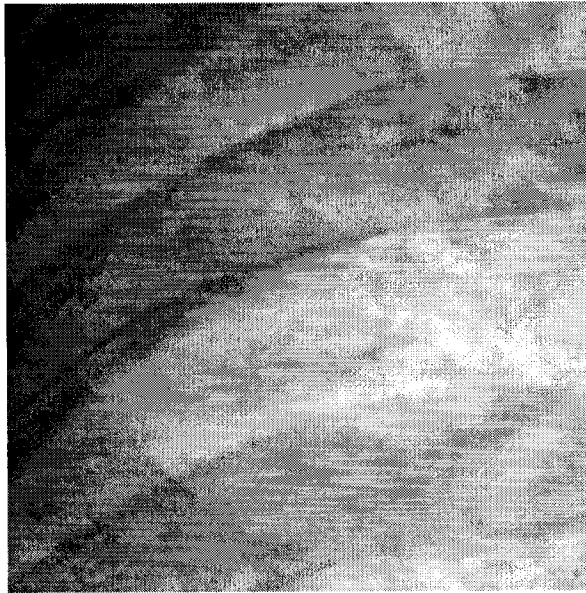
MUSICA will try to enhance these gray values. To accomplish this, each pixel in the Laplacian layer is first normalized to a range of -1 to 1 . Next the subtle detail is amplified by

$$y = a \frac{x}{|x|} |x|^p \quad (\text{A2.2})$$

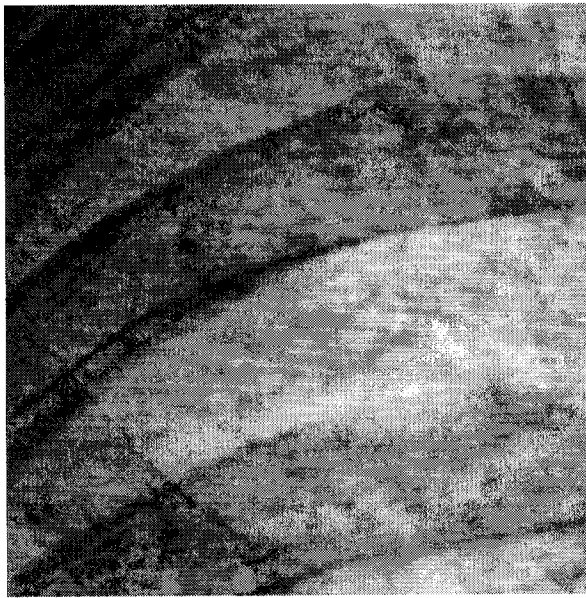
where y is the enhanced pixel value, a is the rescaling coefficient, x is the normalized pixel value and p is the amplification coefficient. MUSICA's ability to enhance subtle detail (smaller gray-level) is demonstrated in Table A2.1. Here the rescaling coefficient is assumed to be one. From this table, one can observe that MUSICA does indeed amplify the smaller gray values more than the larger ones. Also greater enhancement is achieved by applying smaller p values. Based on this information, the MUSICA algorithm has been reconstructed in Matlab. A 512×512 section of a real patient radiograph has been processed using this reconstructed code with a p value equal to 0.65 . This is illustrated in Fig. A2.2. Clearly, MUSICA is able to enhance the subtle detail in this section of the radiograph very well.

Table A2.1. A demonstration of MUSICA enhancing ability.

x	y				
	$p = 0.5$	$p = 0.6$	$p = 0.7$	$p = 0.8$	$p = 0.9$
0.1	0.32	0.25	0.20	0.16	0.13
0.2	0.45	0.38	0.32	0.28	0.23
0.3	0.55	0.49	0.43	0.38	0.34
0.4	0.63	0.58	0.53	0.48	0.44
0.5	0.71	0.66	0.62	0.57	0.54
0.6	0.77	0.74	0.70	0.66	0.63
0.7	0.84	0.81	0.78	0.75	0.73
0.8	0.89	0.87	0.86	0.84	0.82
0.9	0.95	0.94	0.93	0.92	0.91
1.0	1.00	1.00	1.00	1.00	1.00



(a)



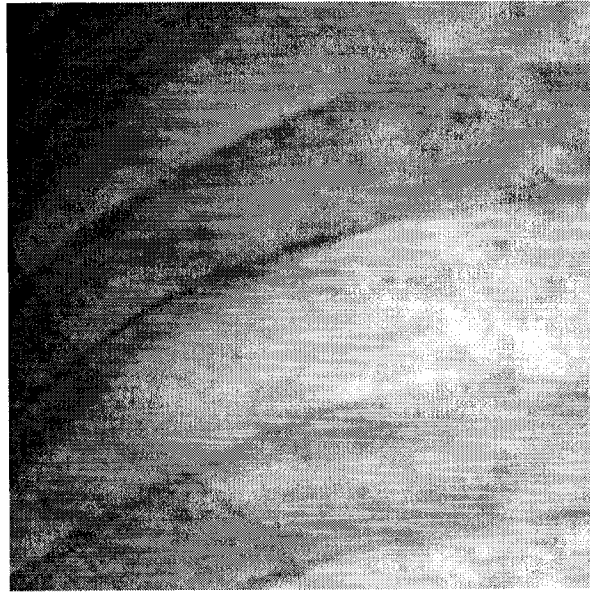
(b)

Figure A2.2. An illustration of the MUSICA's ability to enhance subtle details.
(a) Original image. (b) MUSICA enhanced image.

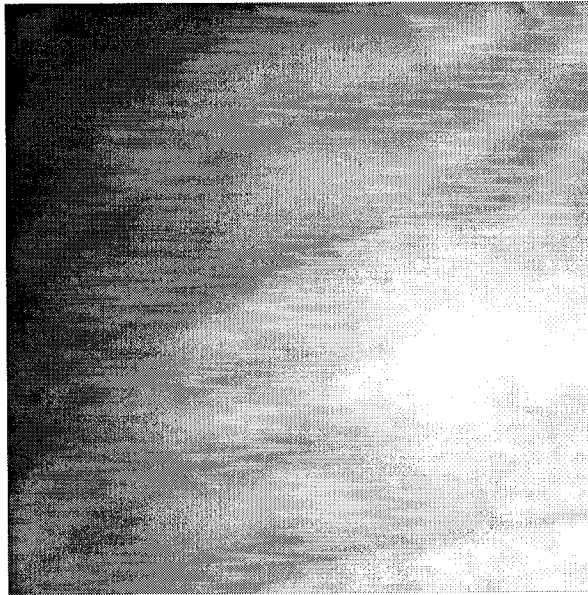
Since MUSICA enhances the subtle image details by applying a p value less than one, one should be able to suppress these features by using a p value bigger than one. This should reduce the amount of soft tissue interference with the detection of the rib boundaries. Table A2.2 is a demonstration of MUSICA's suppression ability. From this table, one can observe that the bigger the p values, the larger the suppression. This suppression ability is also illustrated in Fig. A2.3, where the p value is set to 1.5. From this Figure, one can observe that the reverse MUSICA is able to suppress the soft tissue very well. However, it also suppresses a bit of the rib edges, which will increase the difficulty of detecting these edges. Since a dual-energy subtraction Fuji CR system was made available during the later phase of this project, the reverse MUSICA is not utilized in this dissertation.

Table A2.2. A demonstration of reverse MUSICA suppression ability.

x	y				
	$p = 1.1$	$p = 1.2$	$p = 1.3$	$p = 1.4$	$p = 1.5$
0.1	0.08	0.06	0.05	0.04	0.03
0.2	0.17	0.14	0.12	0.11	0.09
0.3	0.27	0.24	0.21	0.19	0.16
0.4	0.36	0.33	0.30	0.28	0.25
0.5	0.47	0.44	0.41	0.38	0.35
0.6	0.57	0.54	0.51	0.49	0.46
0.7	0.68	0.65	0.63	0.61	0.59
0.8	0.78	0.77	0.75	0.73	0.72
0.9	0.89	0.88	0.87	0.86	0.85
1.0	1.00	1.00	1.00	1.00	1.00



(a)



(b)

Figure A2.3. An illustration of the reverse MUSICA's ability to suppress subtle details.
(a) Original image. (b) MUSICA enhanced image.

Appendix III. Reading the DICOM File

Since all modern digital chest radiographs are produced in the Digital Imaging and Communications in Medicine (DICOM) format,⁸⁰ they need to be converted it into a format that can be utilized by the computer algorithms. In other words, one would need to be able to read the data in the files. A very simple C program that obtains the required information from the DICOM file, and then converts it into a text file is utilized for this task. In this Appendix, this simple C code will be described.

This C program is based on a more complicated C code (dicom2pgm.cpp) by Grevera,⁸¹ which converts the DICOM file into the PGM format. A few assumptions are employed to simplify the code. Firstly, the radiographs are assumed to be in the DICOM 3 format. Secondly, it is assumed that the Little Endian format is used to encode the bytes. That is, the least significant byte is encoded first. Lastly, each pixel value is believed to consume 16 bits (or 2 bytes) of storage space.

In general, the DICOM file can be broken down into two parts. The DICOM header contains all the background information such as patient and image information for the radiograph. The image data is located at the end of the DICOM file after the header. Clearly, a large amount of information is stored in the DICOM header, which could be difficult to locate. Fortunately, a unique data element tag for each piece of information is included to assist the locating task. Each tag begins with two 16 bit unsigned integers: the group number and the element number. The next few bytes after these two numbers will indicate the length of the data, which is different depending on the element. Lastly, the data element is listed. Therefore, one can easily locate the required information by finding the appropriate data element tag. A section of the C code used to locate the number of rows and columns in the radiograph is listed below:

```
10     if (group == 0x0028)
11     {
12         element = unsigned int(readn(fp,2));
13         switch (element)
14         {
15             case 0x0010:
16                 vlength = unsigned int(readn(fp,4));
17                 row = unsigned int(readn(fp,vlength));
```

```

18             break;
19         case 0x0011:
20             vlength = unsigned int(readn(fp,4));
21             column = int(readn(fp,vlength));
22             break;
23     }
24 }

```

In this section, the code first locates the group number 0028H (line 10), which is the image data group. Once this group is found, the program will read the element number (line 12) using the `readn` function which will be discussed later. Once the element number is obtained, it is compared with the row element number 0010H (line 15) and column element number 0011H (line 19) using the `switch` operation (line 13). Once these elements are found, the `readn` function is used to obtain the length of the data (`vlength`). Finally, the number of rows and columns are obtained using once again the `readn` function on line 17 and 21 respectively.

The `readn` function will read “n” number of bytes from the file (`fp`) as input by the user. This function is shown below:

```

30     int readn(FILE *fp, unsigned int n)
31     {
32         unsigned short byte=0;
33         unsigned long int value;
34         unsigned long int power[4]={1,256,(256*256),(256*256*256)};
35         value=0;
36         for (unsigned int i=1; i<=n; i++)
37         {
38             fscanf(fp,"%c", &byte);
39             value += byte*power[(i-1)];
40         }
41         return value;
42     }

```

The function currently will read only up to 4 bytes, as indicated by the `power` array on line 34. Since the Little Endian format is assumed, the `power` array, which provides the multiplication factor for the bytes’ order, will start with a power of 1 and end on 256^3 (four bytes). The `for` loop starting on line 36 is used to read the bytes up to the n^{th} one. The bytes are scanned on line 38, and the byte value (`value`) is computed on line 39. On this line, the byte value is multiplied with the appropriate multiplication factor in the `power` array, and added to the `value`. The position of the array is `i-1` since C begins

addressing the array position at zero instead of one. Lastly, the computed value is returned back to the main program on line 41.

Once the number of rows and columns is obtained, the program can begin reading out the image data, which is located at the end of the DICOM file. The code employed to accomplish this task is described below:

```
50     index=-1*column*row*2;
51     fseek(fp,index,SEEK_END);
52     do {
53         pvalue = unsigned int(readn(fp,2));
54         if (!feof(fp))
55             {
56                 fprintf(op,"%d ",pvalue);
57             }
58     } while (!feof(fp));
```

On line 50, the code first computes the `index` value, which is the number of bytes the image contains. This is done by multiplying the number of rows with the number of columns and then by two. The two is needed since each pixel is assumed to be two bytes (or 16 bits) long. The `-1` on line 50 is needed since the code will search for the beginning of the image data by “rewinding” from the end of the files as shown on line 51. This is acceptable since the image data for a chest radiograph is listed at the end of the DICOM file as mentioned before. Once the file is “rewound”, the pixel values will be read on line 53 to `pvalue` using the `readn` function discussed before. The pixel value is then output into a text file on line 56. This process will continue using a `while` loop until the end of the file (`feof`) is reached on line 58. Once the text file is produced, it can be easily sent to Matlab to be used by the algorithms discussed in this dissertation.

Appendix IV. Digital Chest Phantom

Although a theoretical examination of the segmentation algorithm for the bone structure in the bone-only image is not included in this dissertation as explained in Chapter 5, a digital chest phantom was designed during this study. In this Appendix, this digital phantom (DP) will be discussed.

The digital chest phantom is based on the quality control (QC) phantom designed by Chotas et al.⁸² The design philosophy for the QC phantom is that the response of the imaging system will be similar to a chest radiograph in terms of gray-level⁸² and scattering properties,⁸³ and this phantom has been rated to be an effective QC testing tool.⁶⁶ The DP is 380 pixels tall by 350 pixels wide, which is about one tenth the size in both directions of a modern day CR image. This size is selected to reduce the processing time during the generation of the phantom, and can be increased with ease when required.

The digital phantom consists of a number of layers, similar to the QC phantom. One of these layers is the bone structure, which embodies a 0.8 cm bone structure and a 0.3 cm rib structure made up of cortical bone. This layer is illustrated in Fig. A4.1. Another layer is the soft tissue layer, which contains 15 cm of soft tissue as shown in Fig. A4.2. A heart and an abdomen layer are also included in the DP as illustrated in Figs. A4.3 and A4.4, and is composed of 1.25 cm and 2.5 cm of additional soft tissue on top of the soft tissue layer. Lastly, the DP also contains a simulated wire mesh for the lung region, and is shown in Fig. A4.5. The wire mesh consists of 0.2 cm thick wires (soft tissue) overlapping each other, which produce four different thickness (0.2, 0.4, 0.6, and 0.8 cm). The thicknesses utilized are selected such that the histogram of the final image obtained will resemble a chest CR histogram, and can be easily changed if needed.

Once the layers are computed, the digital phantom radiograph can be produced. To begin, a 110 kVp x-ray spectrum with 5% High Voltage ripple and 3 mm of aluminum tube filtering is acquired using the tungsten anode spectral model.³⁹ The generated spectrum is then divided by 100. This reduction is needed to simulate the smaller pixel area of the CR image, which typically is on the order of 100 μm -by-100 μm . This modified spectrum will then be applied to each layer on a pixel-by-pixel basis to produce the DP image.

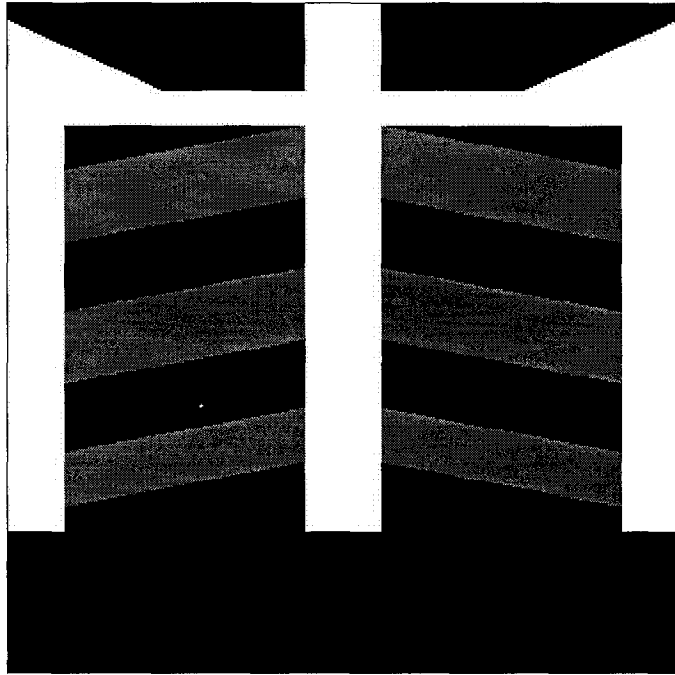


Figure A4.1. The simulated bone structure layer for the digital phantom.

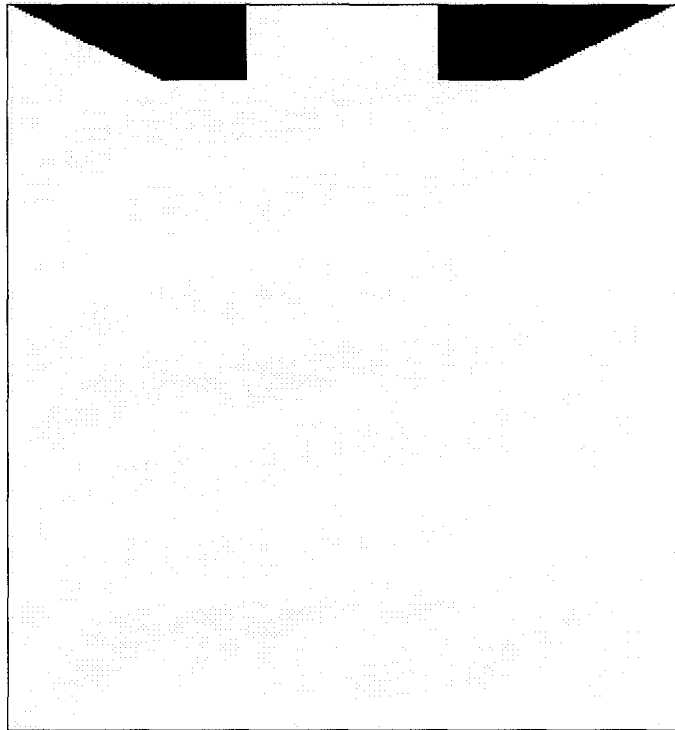


Figure A4.2. The simulated soft tissue layer for the digital phantom.

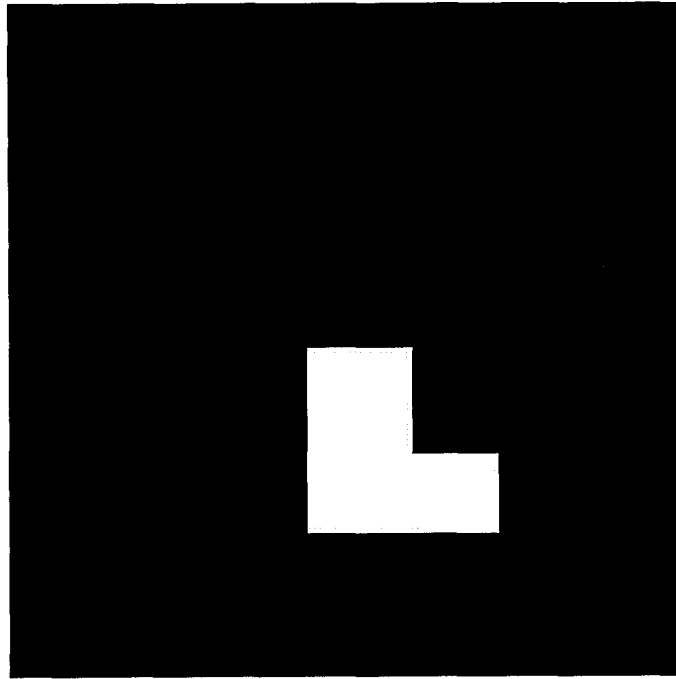


Figure A4.3. The simulated heart layer for the digital phantom.

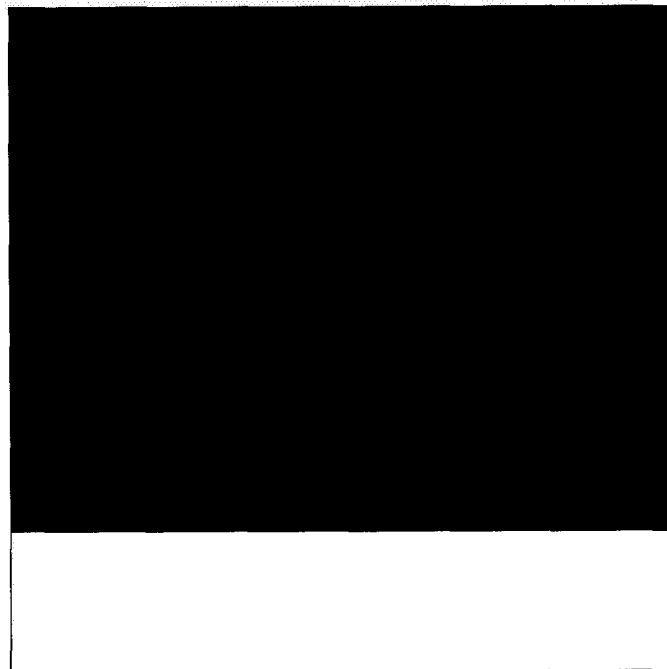


Figure A4.4. The simulated abdomen layer for the digital phantom.

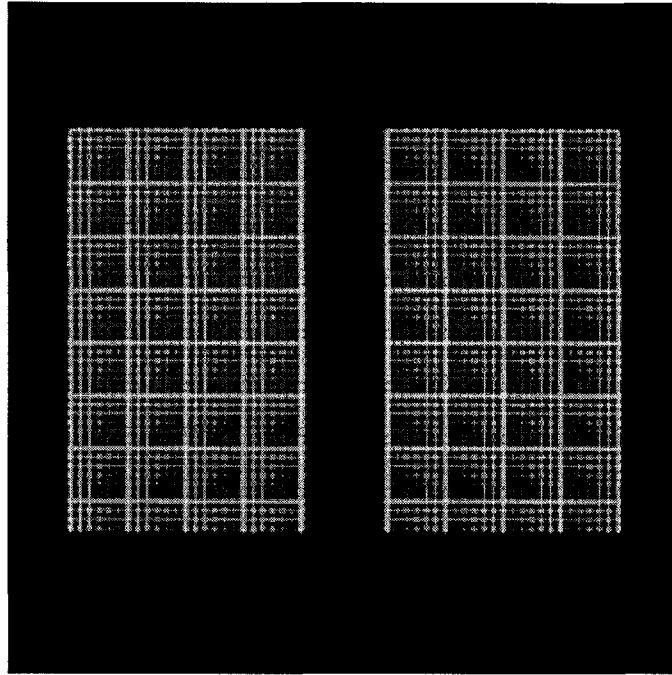


Figure A4.5. The simulated wire mesh for the digital phantom.

The linear attenuation coefficients for cortical bone and soft tissue are obtained using the XCOM program.⁴⁴ Quantum mottle is approximated using a gaussian distribution with a standard deviation of two as indicated by the MATLAB code below:

```
10 while (num <= 91)
11     [y1,y2]=randgauss(2);
12     noise(num)=y1;
13     num=num+1;
14     noise(num)=y2;
15     num=num+1;
16 end
17 noise=noise(1:91);
18 noise=noise.*sqrt(S);
19 Sn=S+noise;
```

Here 91 different gaussian distributed random numbers are generated for each energy bin of the x-ray spectrum as shown on line 10. Ninety-one bins are needed for the spectra since the calculation is only for the energy range of 20 to 110 keV. (Photons below 20 keV will rarely exit the body as discussed in Chapter 2.) Next, the noise spectrum is

rescaled to the appropriate value using the square root value of each energy bin (\sqrt{N}) on line 18, and added to the original spectrum to produce the noisy spectrum (S_n) on line 19. An illustration of the original spectrum and noisy spectrum is shown in Fig. A4.6. A different set of gaussian distributions is generated for each pixel of the image.

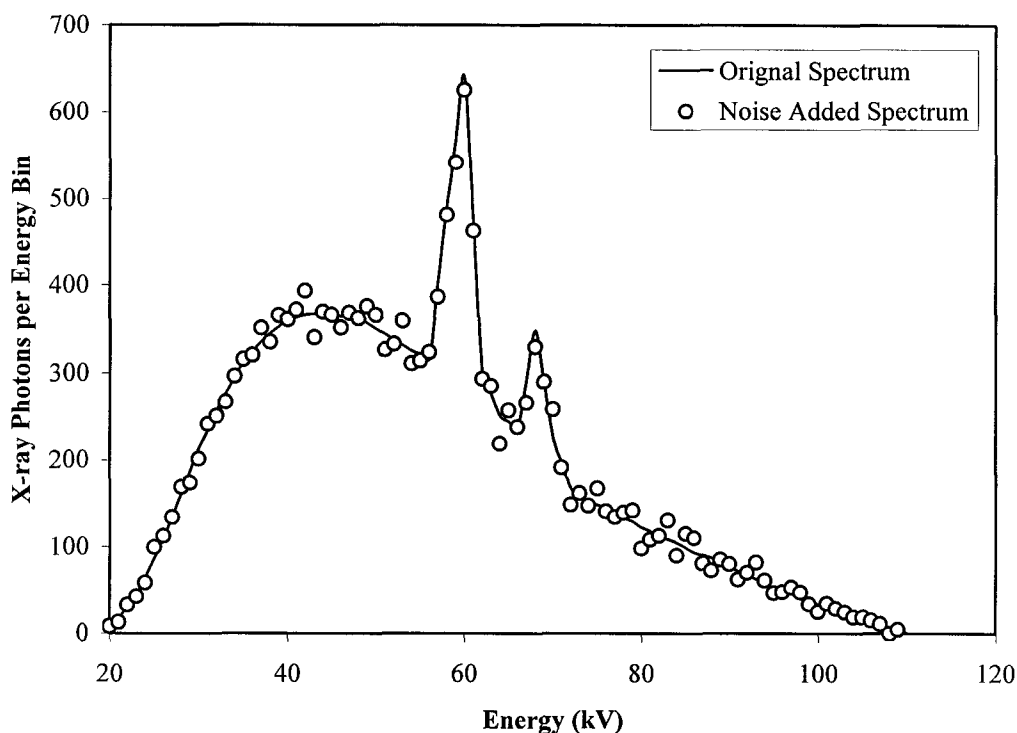


Figure A4.6. An illustration of the original spectrum and a gaussian noise added spectrum.

Once a noisy spectrum is generated for each pixel, these spectra are attenuated through the different layers to produce the DP image. The next step is to simulate the absorption of the x-ray photons by the CR plate. This is achieved by reconstruction of the absorption curve for the CR plate, which is available from a study by Blume.⁸⁴ To reconstruct this curve, a number of key points are manually extracted from curve 1 in Fig. 2 of Blume, and the values between these points are linearly interpolated afterwards. The resulting curve is shown in Fig. A4.7. Once the absorption curve is obtained, it is

multiplied with the attenuated spectrum for each pixel. The remaining photons in each spectrum are then summed together to produce the pixel value. The resulting image is illustrated in Fig. A4.8.

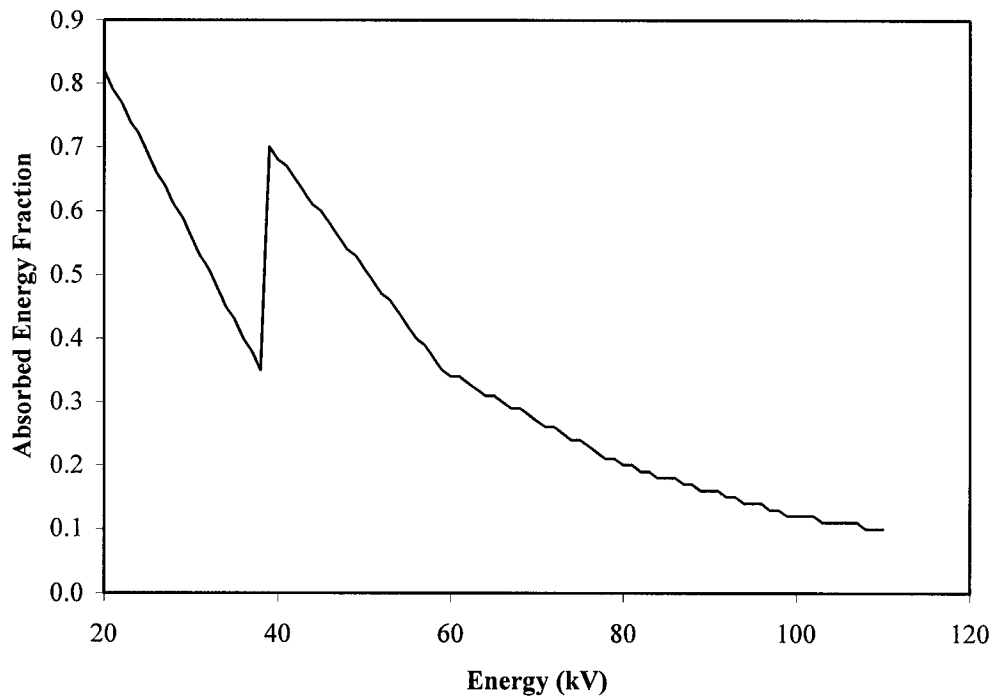


Figure A4.7. The reconstructed absorption curve for the CR plate.

In order to display Fig. A4.8 properly, the gray-levels in the image have been slightly modified. This is because the areas above the shoulders of the DP do not contain any attenuation materials. As a result, the gray-levels for these two areas are very large when compared to the rest of the image. Consequently, the gray-levels in these two areas are reduced to 256 instead of the original values of about 8,000.

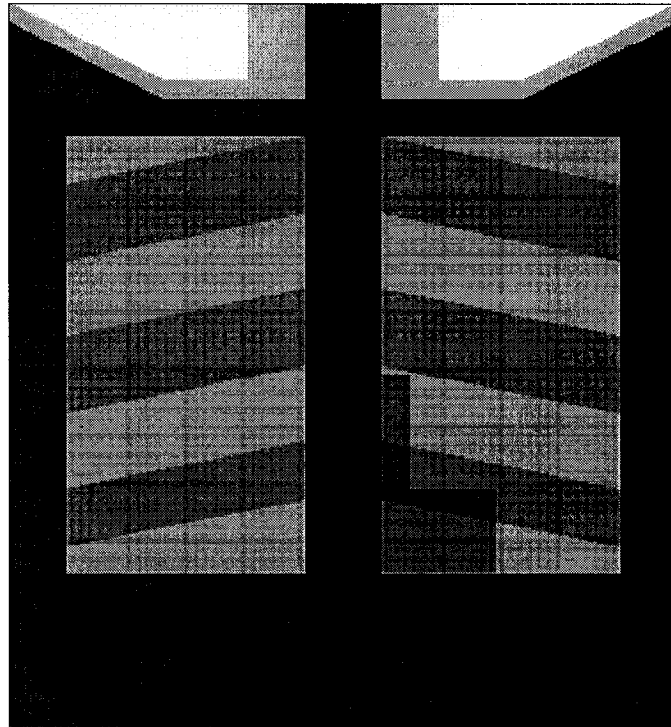


Figure A4.8. The digital phantom image.

A gray-level histogram of this DP image is shown in Fig. A4.9. From this Figure, one can observe that very distinct gray-levels exist in this histogram. In fact, the pixels at gray-level 256 are the pixels above the shoulders as discussed before. The gray-levels at about 170 to 190 correspond to the lung area of the DP, which have four distinct peaks due to the wire mesh in the phantom. (There should be five peaks but one of them is smaller and may be overlapped by other gray-level distributions.) Gray-levels 140 to 153 correspond to the ribs of the DP, and once again four peaks are observed due to the wires in the DP. Gray-levels 120 to 140 correspond to the lighter part of the heart area, and the very large peak at about 105 is produced by the bone structure (rib cage and spine) and the abdomen. Finally, the small peak at about 70 is produced by the part of the heart area overlapping the spine.

Although the simulated quantum mottle did smear the peaks in Fig. A4.9, the histogram is still not very similar to the gray-level distribution of a real chest radiograph. This is due to two main reasons. Firstly, there is only one thickness for each of the

materials in the DP such as the bone structure, while in a real patient there is a wide spread of thicknesses. Although this is partly compensated by the wire mesh in the DP, more work may be needed. Secondly, the current image does not include any scattering photons (noise), which usually accounts for a good portion of the photon flux absorbed by the CR plate.

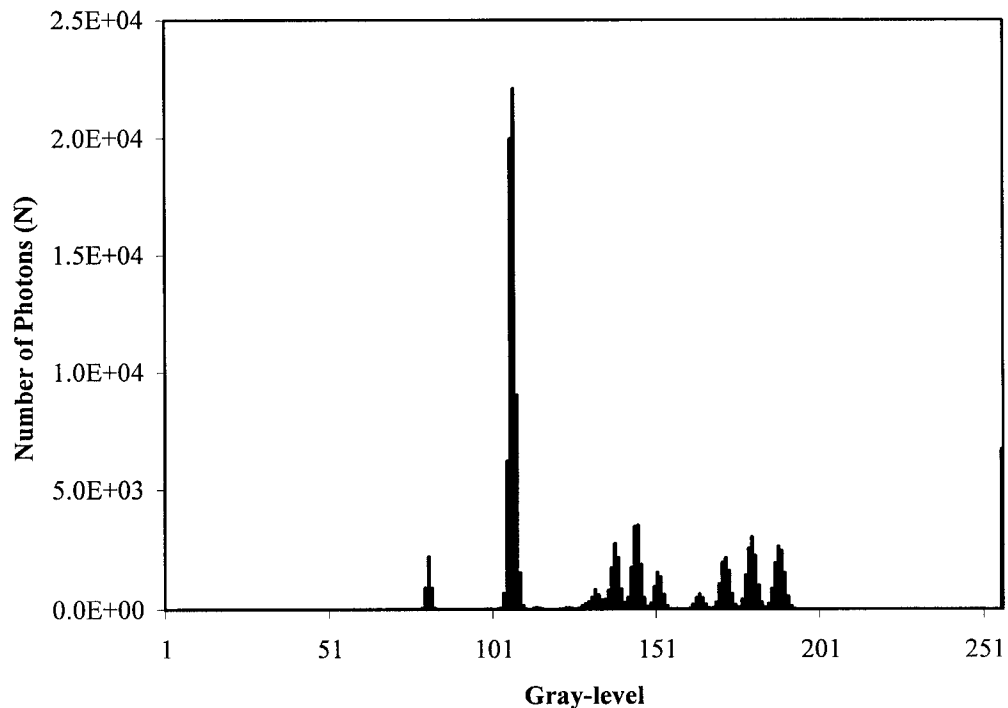


Figure A4.9. A gray-level histogram of the digital phantom image.

In order to account for these scattered photons accurately, Monte Carlo simulation is required. However, in order for the simulation to produce accurate scattering results, the design of the DP has to be similar to the structure of a real chest. This will complicate the phantom design. Consequently, an approximation is applied instead. In general, one would expect the scattered photons to be a percentage of the non-attenuated ones. Therefore, gaussian distributed noise is added to the DP image using the following Matlab code:

```

20   for i=1:numtot
21       [y1,y2]=randgauss(2);
22       noise(num)=y1;
23       num=num+1;
24       noise(num)=y2;
25       num=num+1;
26   end
27   noise=noise(1:(x*y));
28   noise=reshape(noise,y,x);
29   noise=noise.*Im.*0.1;
30   Im=Im+noise;

```

The `for` loop in lines 20 to 26 is used to generate a randomly distributed gaussian set of values, which are then reshaped into a matrix the size of the DP image on line 28. Next, the noise is rescaled to 10% of the pixel values on line 29. Finally this noise matrix is added to the original DP image (I_m) to produce the final image. This image is shown in Fig. A4.10.

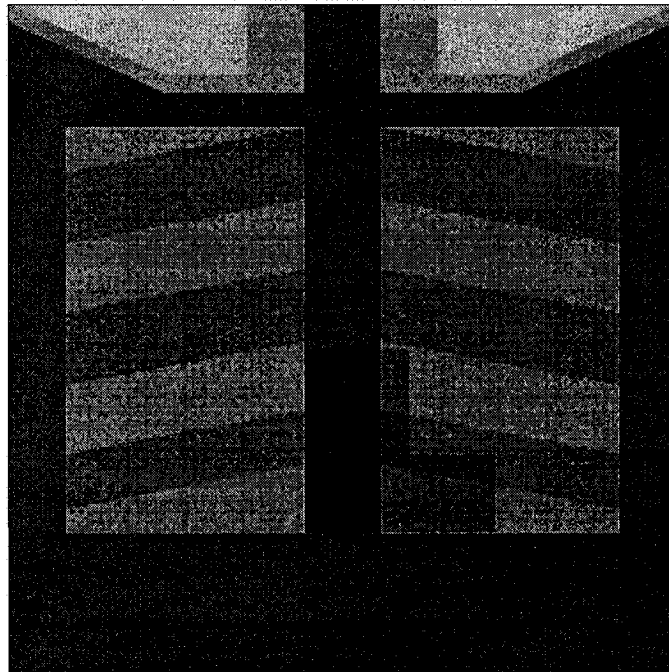


Figure A4.10. The digital phantom image with scattering noise added.

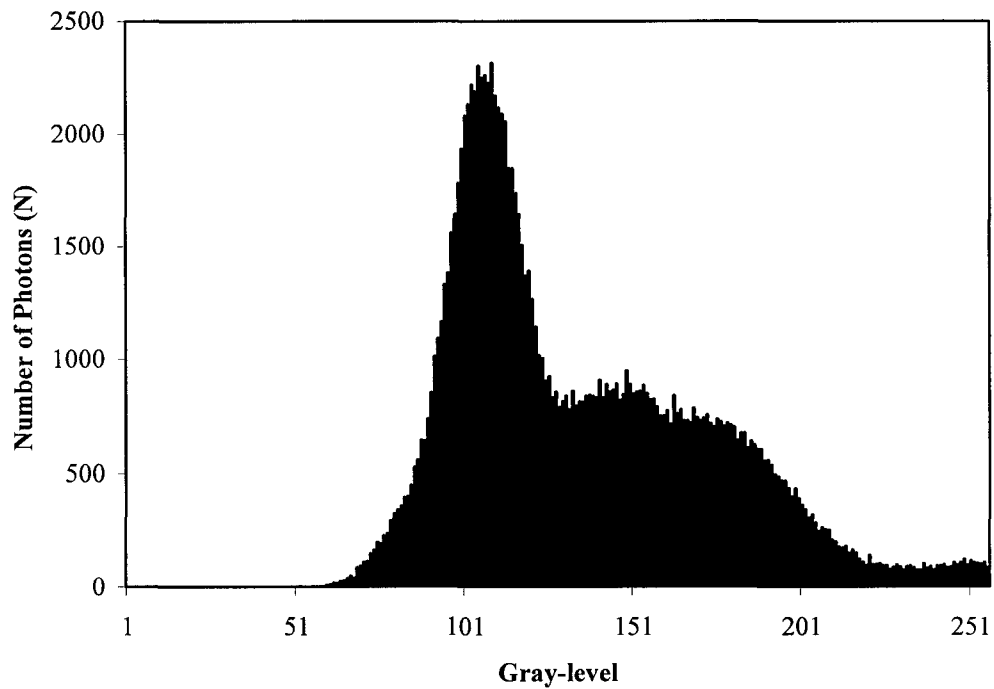


Figure A4.11. The gray-level distribution of the DP image with approximated scattering noise.

The gray-level histogram of Fig. A4.10 is shown in Fig. A4.11. When compared with a real chest CR gray-level distribution in Fig. A4.12, one can observe that the shapes of these two histograms are similar. Although the gray-levels and the number of counts are not exactly the same, these two values can be adjusted by fine tuning the thickness of the layers and by expanding the size of the DP respectively. Finally the bone structure peak in the real patient image is slightly taller when compared to the DP histogram, but this can be changed by allocating more pixels to the bone structure layer of the digital phantom.

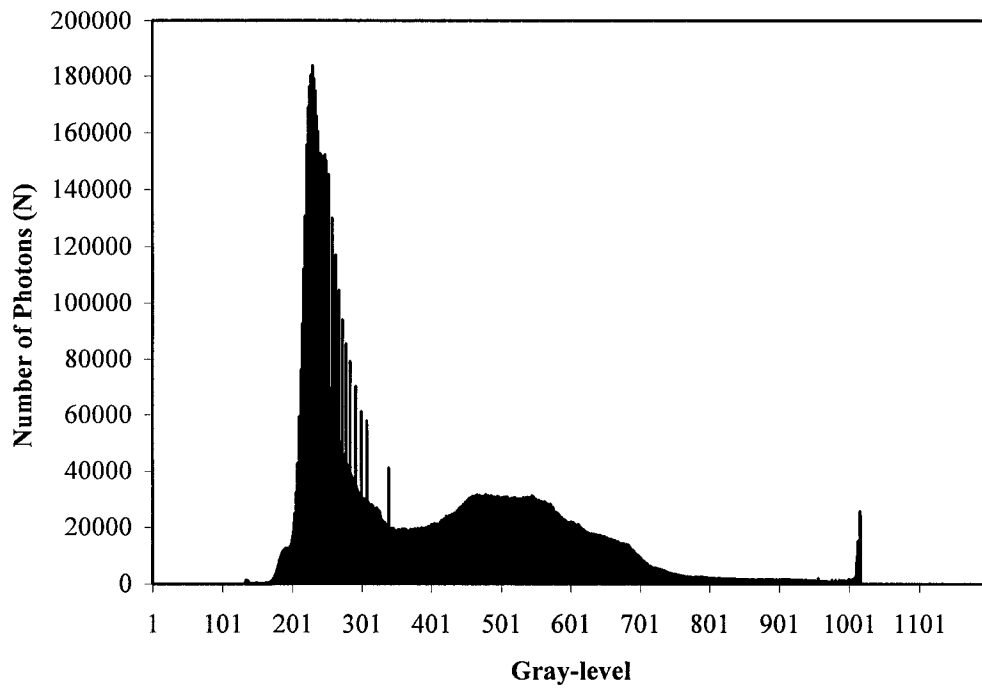


Figure A4.12. The gray-level distribution of a real chest radiograph.

Appendix V. Automatic quantitative low contrast analysis of digital chest phantom radiographs

Alexander L. C. Kwan, Larry J. Filipow,^{a)} and Lawrence H. Le
Department of Physics, University of Alberta, Edmonton, Alberta, T6G 2J1, Canada and Department of Radiology and Diagnostic Imaging, University of Alberta, Edmonton, Alberta, T6G 2B7, Canada

(Received 1 April 2002; accepted for publication 11 December 2002; published 5 February 2003)

Up to the present, the majority of low contrast object evaluations performed on phantom images have been accomplished in a subjective fashion. This is mainly due to the time and effort required to manually measure each radiograph with a densitometer to obtain quantitative results. However, with the development of digital radiographic systems, it has become feasible to automate the detection and computation processes. In this work, a method that can automatically detect and compute the subject-to-noise ratio of the low contrast disks inside a geometric chest phantom is examined. This algorithm has the ability to locate the low contrast objects to an accuracy of less than one pixel, and provides results that are consistent with the understanding of subject-to-noise ratio. This algorithm should simplify the task of quantitative evaluation of contrast detail phantoms. © 2003 American Association of Physicists in Medicine. @DOI: 10.1118/1.1543153#

Key words: automatic, quantitative, QC, low contrast phantom, image registration

I. INTRODUCTION

Evaluations performed on low contrast test phantoms have typically been accomplished in a subjective fashion.^{1,2} This is mainly due to the time, effort, and possible inaccuracies associated with manually measuring each radiograph to obtain objective results. However, studies³ have shown that the variance of quantitative measurements for microcalcifications and nodule targets in mammography phantom images is significantly smaller than that of subjective evaluation. Since there is no basis to believe that the result will be different in other types of radiographic quality control (QC) testing, it is desirable to develop a simple procedure that can provide quantitative results such as subject-to-noise ratio (SNR) or MTF⁴ for routine QC examinations. With the development of digital radiographic systems, it is now feasible to develop such computer algorithms. In this work, a procedure that can automatically detect and compute the SNR of the low contrast objects in a digital chest phantom image is investigated. This algorithm should simplify the task of quantitative evaluation of contrast detail phantoms.

II. EQUIPMENT

The geometric chest phantom (07-646) from Nuclear Associates (Hicksville, NY) was the subject of this experiment. This phantom is designed such that the response of the imaging system will be similar to that of a normal chest radiograph in terms of attenuation and gray level,⁵ as well as scattering properties.⁶ In another study, this phantom has been rated as an effective tool for routine QC testing.⁷

The Fuji FCR XU-D1 radiographic unit from Fuji Medical Systems (Tokyo, Japan) was utilized to acquire the images. The phantom images were obtained at a source-to-image distance (SID) of 182 cm for two different kVp settings, 110 and 125 kVp. For each kVp,

three different mAs settings are selected. The reference setting is established by adjusting the mAs to produce an entrance skin exposure (ESE) of approximately 25 mR. The other two images are acquired using 1/5 and 5 times the mAs of the reference setting similar to the studies of Mah *et al.*⁷ A list of the exposure parameters and the corresponding ESE are shown in Table I. These acquired images were sampled to 3520×4280 pixels with 12 bits of intensity, and then down-sampled to 10 bits. The algorithm for this project was developed using MATLAB version 5.3 on a Pentium III 667 PC running Windows NT.

III. METHOD

The segmentation based registration technique, which matches the input image with a preprocessed template, is used in this experiment. The registration produces a transformation matrix that maps the coordinates from the images to the template. The centers of the low contrast disks in the template are then mapped onto the image using the inverse of this matrix. Only the six most visible low contrast objects in the lung, heart,

TABLE I: List of the exposure parameters and the entrance skin exposure for the images acquired in this experiment. The images are named as follow: the three numbers after the "T" denote the kVp, while the remaining indicates whether the images are acquired at 1/5th the reference mAs (Rd5), the reference mAs (R), or 5 times the reference mAs (Rx5).

Image	kVp	mAs	Time (ms)	ESE (mR)	Latitude
T110Rd5	110	1.1	2.2	4.5	2.23
T110R	110	5.6	14	27.1	2.23
T110Rx5	110	28	71	125.2	2.23
T125Rd5	125	0.8	2.0	4.2	2.23
T125R	125	4.0	10	24.3	2.23
T125Rx5	125	20	50	113.5	2.23

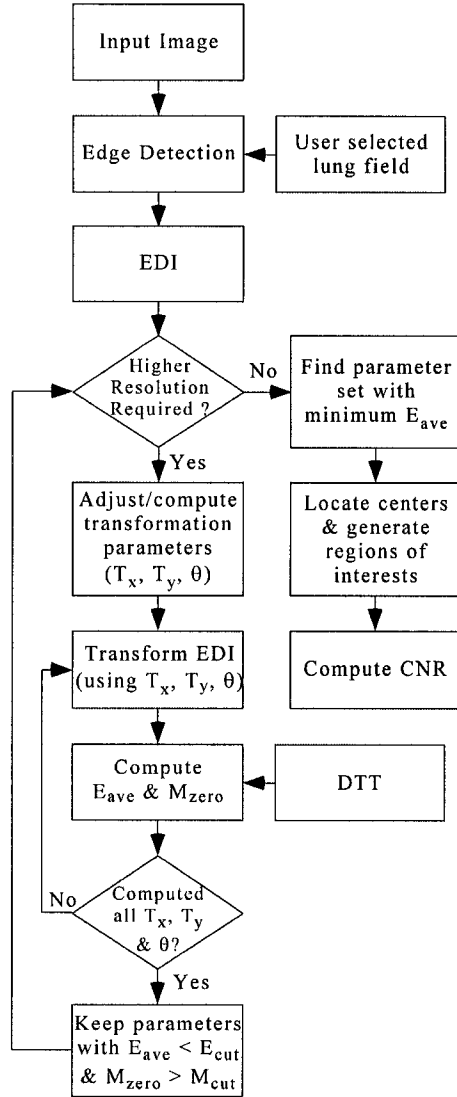


FIG 1. The automatic detection algorithm scheme. Definitions for the acronyms are listed in Table II.

and abdomen region of the phantom are examined. The mean incident exposures and the corresponding variances in the region of interest around each center of the low contrast disks are used to compute the SNR. Since this ratio is to be used in trend analysis to monitor changes over time, the initial set of low contrast objects chosen for examination should not matter provided that the same objects are monitored in subsequent testing. The basic scheme of this automatic detection algorithm is illustrated in Fig. 1, and an explanation of the acronyms in Fig. 1 is listed in Table II. The following is a more detailed discussion of the algorithm.

A. Image registration

The image registration technique employed is a modified version of the hierarchical chamfer matching algorithm (HCMA).⁸ This modified algorithm contains the following components.

TABLE II: An explanation of the acronyms utilized in Fig. 1.

Acronyms	Definition
SNR	Subject-to-noise ratio [Eq. (9)]
DTT	Distance transformed template
E_{ave}	Average distance error [Eq. (6)]
E_{cut}	Cut-off value for E_{ave} [Eq. (7)]
EDI	Edge detected image
M_{cut}	Cut-off value for M_{zero} [Eq. (8)]
M_{zero}	Number of exact edge-pixel match
T_x	The quasi-translation parameter in the x direction
T_y	The quasi-translation parameter in the y direction
θ	The rotation angle of the transformation

(1) *Distance transformed template (DTT)*. A template composed of edges from a reference image is required before the registration can begin. For the current study, the edges are chosen to be the lung field and ribs of the chest phantom. This template is obtained by first convoluting the reference image with a simplified 5×5 Canny edge detector⁹ with a unity spread ($\sigma=1$). The edge-detected image is then segmented into a binary image by selecting a value such that 90% of the gray level is below this threshold.¹⁰ Afterward, the nonedge elements are removed from the binary image and the gaps between the edge sections are filled in manually. The edges in the image are then reduced to one pixel wide using a thinning algorithm.¹¹

The next step is to compute the distance between all the pixels to the nearest edge pixel in the image. Obviously, the edge pixels should have a value of zero, and the further away a pixel is from an edge, the larger its' value. Although the exact distance can be computed in a very straightforward fashion, a huge amount of computation time is required. Fortunately, this DTT is computed only once for each acquisition configuration, and can be reused for all future matching provided that the configuration (SID) is not altered.

(2) *Detecting the edge of the input image*. Once the DTT is computed, it is stored on the QC computer for future matching. In order to register the input image, one needs to segment it. This is achieved by convoluting the lung field selected by the user with the same edge detector as mentioned before. The selection of the lung field area is the only user interaction required by the algorithm, and is to prevent the edge of the phantom from interfering with the registration procedures. The threshold level is increased to 95% to reduce the noise in the edge detected image (EDI). To further reduce the noise, the binary image is convoluted with a 3×3 median filter, thinned, and filtered again with a 3×3 ranking filter with a ranking order of 7.

(3) *Registration*. The original matching algorithm (HCMA) begins by locating the pixel values in the DTT for all the edge pixels. The average of all these values measures the difference, or error, between the two images. For the best possible fit, one needs to obtain the transformation with the minimum error. In this study, only rigid body transformations will need to be considered. To simplify the computation, only the translation and rotation about the z axis, or the source-to-image axis, will be examined. This should be a valid

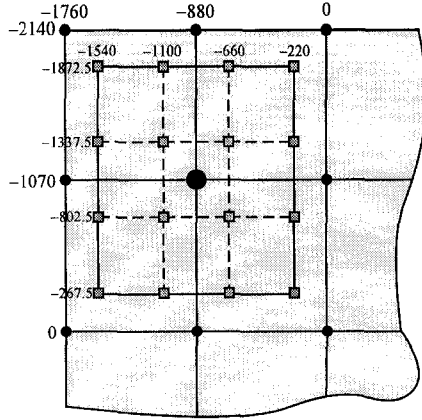


FIG. 2. The location of some of the quasi-translation parameters for the first iterations (circles) and second iteration (squares) given that point $x = -880$, $y = -1070$ (big circle) is a seed for the second iteration.

assumption since the scaling (or SID) should remain the same for all subsequent QC testing. The transformation equations for translating in the x and y directions with rotation about the z axis are defined as

$$\begin{aligned} x' &= t_x + x \cos(\theta) + y \sin(\theta), \\ y' &= t_y - x \sin(\theta) + y \cos(\theta), \end{aligned} \quad (1)$$

where x' and y' are the transformed coordinates, t_x and t_y are the quasitranslation parameters as explained in the Appendix, x and y are the original coordinates, and θ is the rotation angle. Currently, t_x is assumed to be between -1760 and 1760 and t_y to be between -2140 and 2140 . This is because a translation only transformation ($\theta=0^\circ$) in the respective direction for the given values will shift about half of the edge pixels outside the image boundary, leading to the failure of the algorithm.

The simplest approach in selecting the best set of transformation parameters is to iterate through all the possibilities. Unfortunately, this approach requires a significant amount of computation time. To reduce the workload, HCMA reduces the image into a number of resolution pyramids where each level of the pyramid is smaller than the previous level. However, the DTT for each resolution level still needs to be computed. In order to eliminate this, the "stepped chamfer matching algorithm" (SCMA) is proposed here. In this method, the first quasitranslation parameters are iterated at large steps or low resolution. Once the first iteration is completed, the data sets that fit certain criteria are kept, while the rest are discarded. The remaining data points are then utilized as the starting points for the next iteration, which will concentrate on an area 75% the size of the previous quasitranslation steps and a 50% reduction in the step size. The reason 75% of the previous step is used is to reduce the chance of eliminating the true global minimum at the gaps. The locations for some of the first and second iteration quasitranslation parameters (t_x and t_y) are illustrated in Fig. 2. This process will repeat until the steps are less than or equal to the required resolution, which is set to 1 pixel in both directions for the current study.

Since the quasitranslation parameters and the rotation angle had to be applied at the same time, one will also need to know the step of the rotation angle. However, this step depends not only on the location of the edge pixels, but also the quasitranslation steps and the rotation angle being used. As a result, an approximation is computed for each rotation angle using the furthest data point from the origin (x_{\max} , y_{\max}) similar to the HCMA. To start, one can compute the change in x' for a given rotational step ($d\theta$):

$$\begin{aligned} dx' &= [t_x + x \cos(\theta + d\theta) + y \sin(\theta + d\theta)] \\ &\quad - [t_x + x \cos(\theta) + y \sin(\theta)], \end{aligned} \quad (2)$$

which can be simplified to

$$dx' = y_{\max} \cos(\theta) d\theta - x_{\max} \sin(\theta) d\theta. \quad (3)$$

Since only the absolute value of $d\theta$ is of interest:

$$|d\theta| = \left| \frac{dx'}{y_{\max} \cos(\theta) - x_{\max} \sin(\theta)} \right|. \quad (4)$$

Here, dx' is equal to Δt_x of the given iteration since there is no incentive to compute the rotation resolution to a higher accuracy than the current quasitranslation resolution. Similarly for dy' :

$$|d\theta| = \left| \frac{dy'}{y_{\max} \sin(\theta) + x_{\max} \cos(\theta)} \right|. \quad (5)$$

Again dy' is equal to Δt_y of the given iteration.

Once $d\theta$ is computed using Eqs. (4) and (5), the smaller of the two values will be utilized as the rotation step. For the first iteration, the range of the rotation angle is limited to $\pm 45^\circ$, with $d\theta$ computed using θ equals to 0° . The rotation angle step for all other iterations will be based on the previous data similar to the quasitranslation steps, except the rotation angle range is limited to $\pm 300\%$ of the previous $d\theta$. This larger range is needed because $d\theta$ is the smallest estimate for the current set of parameters, and is to ensure that the true global minimum will not be eliminated unintentionally.

The final step is the application of the rejection criteria at the end of each iteration. Two main rejection criteria are utilized in the current algorithm. The first criterion is the average distance error (E_{ave}):

$$E_{ave} = \frac{P(D_{\max} + 1) + \sum_{i=1}^N D_i}{N + P}. \quad (6)$$

Here N is the number of edge points that are within the image boundary and P is the number of edge pixels that lies outside the boundary after the transformation. D_i is the value of the DTT at location i , and D_{\max} is the maximum value of the DTT. Clearly, Eq. (6) is just the average distance error with a penalty function for the edge pixels that get transformed outside the boundary. Once all the E_{ave} for the current iteration is determined, the cutoff value (E_{cut}) is calculated by

$$E_{\text{cut}} = E_{\text{min}} + k_1 E_{\text{std}}, \quad (7)$$

where E_{min} is the minimum of all the E_{ave} , E_{std} is the standard deviation of these average errors, and k_1 is a user predetermined constant.

The second rejection criterion is the number of exact matches (M_{zero}). This variable determines the number of zeros produced by each set of transformation parameters. The cutoff for this variable (M_{cut}) is

$$M_{\text{cut}} = k_2 M_{\text{max}}, \quad (8)$$

where M_{max} is the maximum number of exact matches for all possible guesses in the current iteration, and k_2 (which should be ≤ 1) is another user predetermined constant. Once E_{cut} and M_{cut} are computed, the transformation sets with E_{ave} larger than E_{cut} or M_{zero} less than M_{cut} are rejected. For the current image set, $k_1 = 2.0$ and $k_2 = 0.75$ is used. For the cases where a large amount of data points remain after applying the rejection criteria, only the 25 sets with the lowest E_{ave} will be used in the next iteration.

After the rejection criteria, the transformation coordinates that remain will be utilized as seeds for the next iteration. The only difference is that the E_{ave} for the rest of the iterations has to be less than the E_{cut} from the previous iteration before it will be utilized in Eq. (7). Once the desirable resolution is reached, a final rejection criterion may be needed. For the current study, the data set with the smallest E_{ave} is selected.

B. Subject-to-noise ratio

As mentioned before, only the six most visible low contrast objects in the three different regions (lung, heart, and abdomen) of the phantom will be examined. In order to calculate the SNR for these objects, the mean incident exposure for the background in the respective regions had to be known. These backgrounds are taken to be areas centered inside the wire loop near the low contrast objects, which are designed to be optical density measurement sites.⁵

The center for each of these copper disks, plus the background areas, was predetermined by mean of the Hough-based schemes for circular object detection.¹² After the centers are identified, they are stored and mapped onto the input image with the transformation parameters determined previously. Circular area with radius equal to 9 pixels is selected to be the region of interest for each object. These areas of interest are illustrated in Fig. 3 for the lung region. In each of the three regions where the low contrast phantom sets are located, the subject-to-noise ratio for each of the low contrast objects is computed as

$$\text{SNR}_i = \frac{\bar{E}_{\text{BG}} - \bar{E}_i}{\sqrt{\sigma_{\text{BG}}^2 + \sigma_i^2}}. \quad (9)$$

Here SNR_i is the subject-to-noise ratio for the i th area as illustrated in Fig. 3. \bar{E}_{BG} and \bar{E}_i are the mean incident exposures in the background area and the i th area, respectively, while σ_{BG}^2 and σ_i^2 are the corresponding variances of these means.

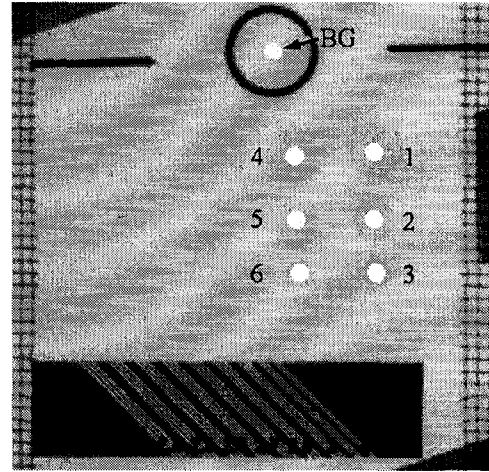


FIG. 3. An illustration of the areas of interest and the numbering for the six low contrast objects and the background area in the lung region. Here the areas in white are the regions of interest used to compute the subject-to-noise ratio.

In order to compute the mean and variance of the exposure, the pixel values (Q) in the area of interest are first converted into incident exposure. In general, the relationship between the pixel value and the incident exposure can be defined as⁷

$$\log(cE) = a \times Q + b, \quad (10)$$

where a and b are the slope and intercept of a linear function for a logarithmic-linear relationship. The constant c has a value of 1 mR^{-1} , and is used to provide the proper dimension for the logarithmic function. To obtain the regression parameters, a number of different mAs exposures are utilized for each of the two different kVp settings. The results are illustrated in Fig. 4. From Fig. 4, one can observe that the slope is equal to 0.0022 and the intercept is equivalent to 0.5661 for the 110 kVp setting, while the slope and intercept are equal to 0.0022 and 0.5571, respectively, for the 125 kVp setting. Using these relationships, one can convert the pixel values to incident exposures, which can then be used to calculate the mean and variances.

IV. RESULTS AND DISCUSSION

A. Accuracy

To determine the accuracy of the registration algorithm, the images were numerically transformed with ten different sets of rotation and translation parameters. These parameters are listed in Table III. Registration is then applied to generate the experimental transformation results. Five coordinates (the four corners and the center of the image) were then transformed with the numerical parameters, and transformed back using the experimental values. Ideally, the original and final coordinates should be the same. The distance differences between the expected location and the transformed location for these five coordinates are illustrated in Fig. 5. From this figure, the first observation is that transformation 10 for the T110Rd5 image had failed.

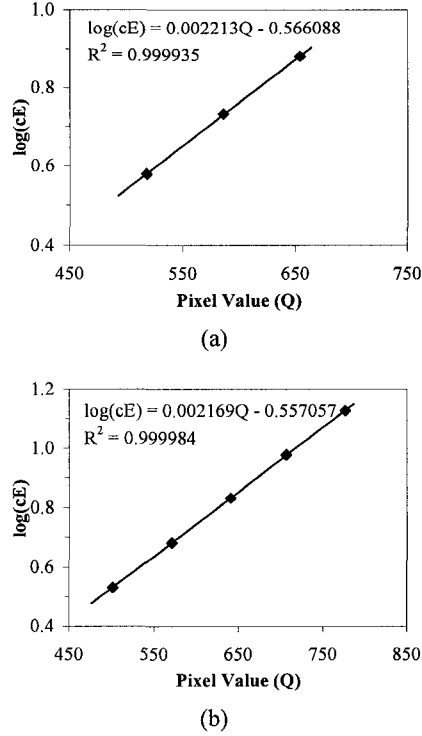


FIG. 4. The relationship between the incident exposure (E) and the pixel value (Q). Here the constant c in front of the incident exposure is equal to 1 mR^{-1} , and is used for providing the proper dimension for the logarithmic function. (a) The relationship for the 110 kVp setting. (b) The relationship for the 125kVp setting.

This may be due to the fact that part of the lung field is missing after the numerical transformation. This coupled with the extra noise in the image from the reduced mAs may have lead to the failure of the algorithm. However,

registrations for the remaining five images at this transformation do provide acceptable results. This demonstrates that the current algorithm has the ability to register images even though part of the input image is missing. This should increase the robustness of the automatic registration technique.

If one ignores the distance differences for transformation 10 of the T110Rd5 image, the maximum distance difference for the four corner coordinates is 6.40 pixels, with average distance differences of 1.54, 1.58, 1.36, and 1.39 for corners 1 to 4, respectively. One can also observe that the corner coordinates generally generate a larger error than the center region, which has an average distance difference of 0.85 pixel. Based on these results, one may conclude that the accuracy of the matching algorithm is acceptable.

A possible source of error is the slight variation in the positioning of the CR plate between different exposures. Since these variations have to be first accounted for before the numerical transformations can be applied, any error in the initial matching may be incorporated into the final result. Also due to the memory limitation of the computer, the input images have to be reduced to 1760×2140 before the Canny edge detector can be applied. Although the EDI is re-sampled back to the original size before the registration, these processes may have generated additional error. If the accuracy of the algorithm needs to be improved, the resolution may be increased slightly by iterating the quasitranslation steps (Δt_x and Δt_y) to finer values such as 0.5 pixels.

The reader may wonder why the segmentation-based registration technique is used instead of some other image registration techniques.^{13,14} The extrinsic registration methods require the use of external markers such as a ball bearing. Although these methods converge very quickly and can be automated easily, the external markers will affect the overall gray level of the image, and reduce the effectiveness of the chest phantom to mimic a normal radiograph. The landmark-based registration methods required the user to identify a

TABLE III: A list of the translation and rotation parameters used for the accuracy test. The transformation parameters are slightly different for the first six transformations between the 110 kVp and the 125 kVp image sets. For the translation parameters, T_x is the translation in the x direction and T_y is the translation in the y direction in pixels. For the rotation parameters, C_x is the center of rotation in the x direction, C_y is the center of rotation in the y direction and θ is the angle of rotation. A positive θ implies a counter-clockwise rotation. For transformations 7 and 8, the image is first translated then rotated. For transformations 9 and 10, the image is first rotated then translated.

Name of Transformation	Translation parameters		Rotation parameters	
	110 kVp	125 kVp	110 kVp	125 kVp
1	$T_x = 0; T_y = -10$	$T_x = 10; T_y = 0$	$\theta = 0^\circ; C_x \text{ and } C_y = 0$	$\theta = 0^\circ; C_x \text{ and } C_y = 0$
2	$T_x = 100; T_y = 0$	$T_x = 0; T_y = -100$	$\theta = 0^\circ; C_x \text{ and } C_y = 0$	$\theta = 0^\circ; C_x \text{ and } C_y = 0$
3	$T_x = 0; T_y = 1000$	$T_x = -800; T_y = 0$	$\theta = 0^\circ; C_x \text{ and } C_y = 0$	$\theta = 0^\circ; C_x \text{ and } C_y = 0$
4	$T_x = 0; T_y = 0$	$T_x = 0; T_y = 0$	$\theta = -0.1^\circ; C_x = 1760$ and $C_y = 2140$	$\theta = 0.1^\circ; C_x = 1760$ and $C_y = 2140$
5	$T_x = 0; T_y = 0$	$T_x = 0; T_y = 0$	$\theta = 1^\circ; C_x = 1760$ and $C_y = 2140$	$\theta = -1^\circ; C_x = 1760$ and $C_y = 2140$
6	$T_x = 0; T_y = 0$	$T_x = 0; T_y = 0$	$\theta = -10^\circ; C_x = 1760$ and $C_y = 2140$	$\theta = 10^\circ; C_x = 1760$ and $C_y = 2140$
7	$T_x = 231; T_y = 796$		$\theta = 6.68^\circ; C_x = 1760$ and $C_y = 2140$	
8	$T_x = -399; T_y = -265$		$\theta = -3.15^\circ; C_x = 1320$ and $C_y = 1605$	
9	$T_x = 678; T_y = -238$		$\theta = -12.28^\circ; C_x = 1760$ and $C_y = 2140$	
10	$T_x = 54; T_y = -492$		$\theta = 23.17^\circ; C_x = 1320$ and $C_y = 1605$	

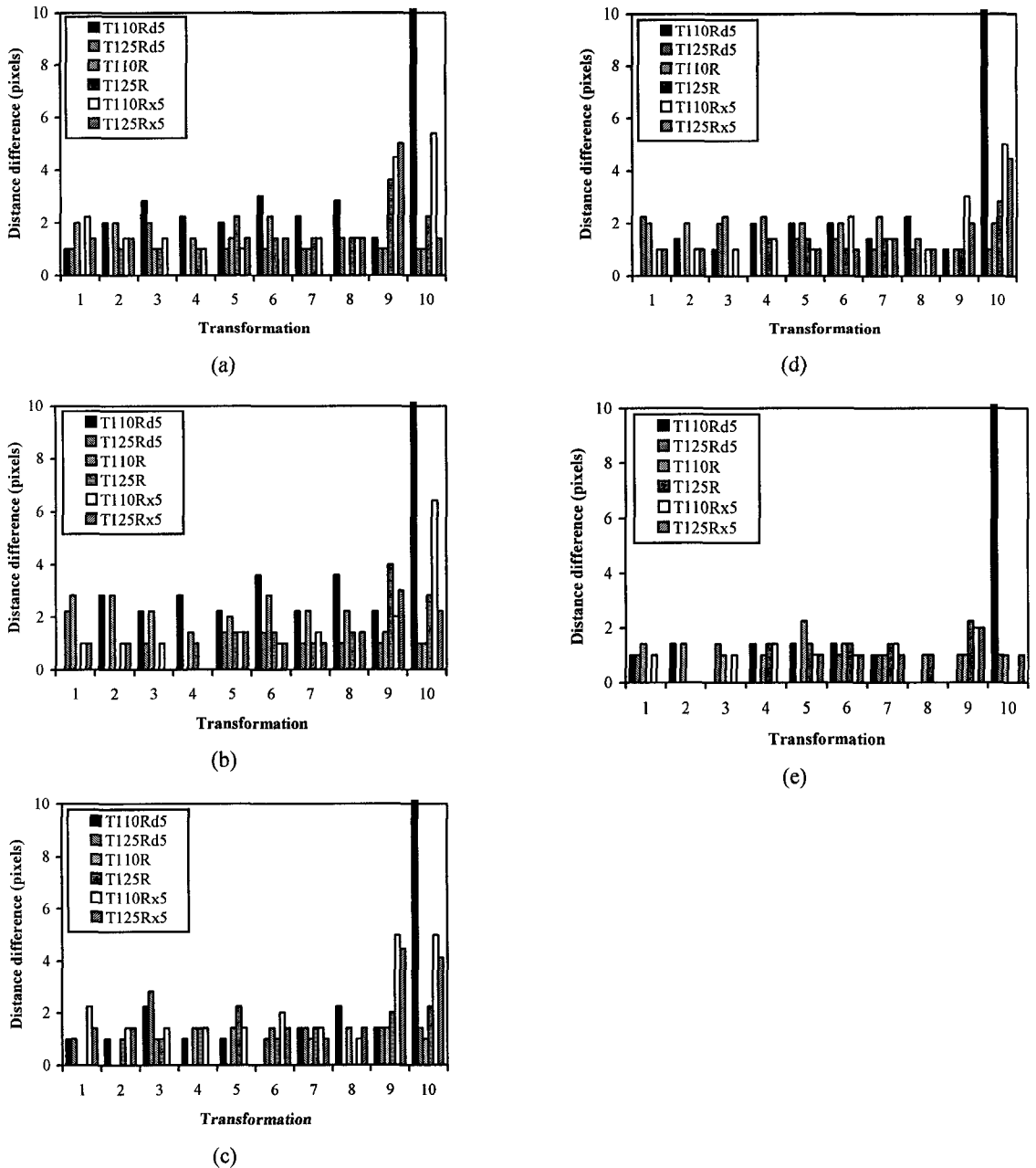


FIG. 5. The distance differences between the expected and experimental coordinates for five locations in the images (a) First corner ($x = 1, y = 1$). (b) Second corner ($x = 3520, y = 1$). (c) Third corner ($x = 1, y = 4280$). (d) Forth corner ($x = 3520, y = 4280$). (e) Center ($x = 1760, y = 2140$). The registration for transformation 10 of image T110Rd5 has failed, and the distance differences which is not shown are 78.62, 78.79, 34.21, 28.16 and 32.02 for locations a to e respectively (done to visualize small differences). The transformation parameters are listed in Table III.

number of landmarks, or salient points, on both the acquired and reference images for the registration. The obvious drawback of this method is that significant user interaction is required. This may lead to the problem that a large inaccuracy may result from mismatch by the user; consequently, a number of methods that utilized the user identified landmarks and image information were developed.^{15,16} The voxel property-based registration methods use the gray level of the image direct for

registration. Although these methods also converge very quickly, they are not very accurate. Since quality control examination is usually not a time critical procedure, speed will be sacrificed in favor of accuracy. On top of this, user interaction should be reduced to a minimum to lessen the workload to the user and to decrease the chance of error. Hence the segmentation-based registration method is selected.

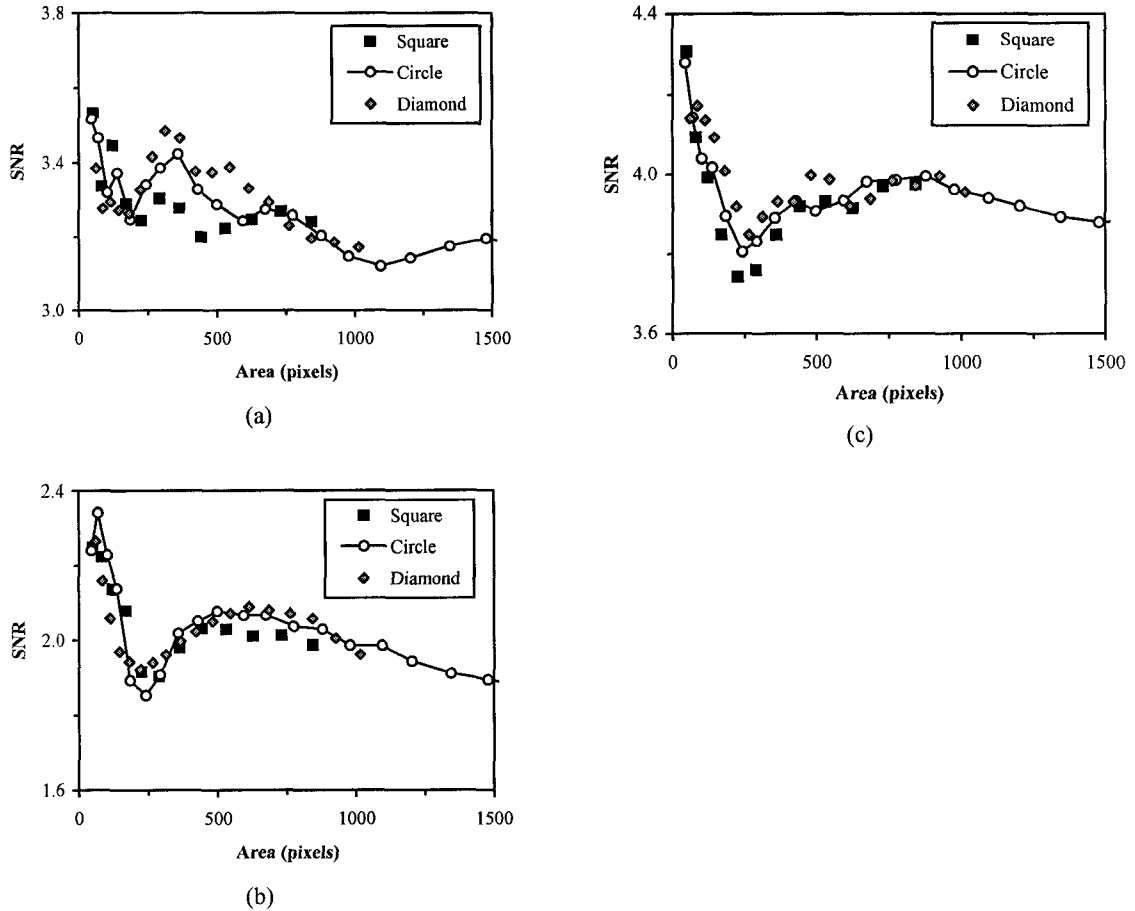


FIG. 6. The SNR for three different shapes as a function of the region of interest's area. The three different shapes are square, circle and diamond. (a) SNR for area 1 (as illustrated in Figure 3) in the lung region. (b) SNR for area 1 in the heart region. (c) SNR for area 1 in the abdomen region

B. Subject-to-noise ratio

As mentioned before, the region of interest is selected to be a circle with radius equal to 9 pixels. Circular area is chosen because there is only a minor difference in the SNR between the shape of a square, circle, and diamond of the same area for a given region of interest as illustrated in Fig. 6. Also from Fig. 6, the SNR seems to vary significantly for the smaller area. This is expected due to the smaller sample size. The SNR seems to level off for the area size of about 500–800 pixels for the abdomen and heart region, and starts to decrease with larger area. This decrease may be due to the fact that the larger areas contain pixels closer to the edge of the disks, where the SNR will be lower. Lastly, only small variations are observed in the SNR for the larger areas; therefore, the size of area selected will not be of great importance for areas bigger than 250 pixels.

The computed SNR for the six different images are illustrated in Fig. 7. From Eq. (9), one would expect the thicker objects to produce a higher SNR. This is observed where the computed SNR for thicker disks (areas 1, 2, and 3) are higher. One can also observe that

the noisier images (T110Rd5 and T125Rd5) produce a lower SNR when compared to the less noisy images (T110Rx5 and T125Rx5) as expected. Furthermore, one can observe that as the x-ray energy is increased from 110 to 125 kVp, the SNR generally decreases. This may be due to the fact that the ESE for the 125 kVp is slightly lower than the 110 kVp images.

The slight variations between the SNR for the objects of the same thickness at a given exposure are due to the variation in the incident exposure resulting from quantum mottle, as well as noise introduced by the downsampling of the image.⁷ Beside SNR, the relative signal from the studies of Mah *et al.*⁷ is also computed. The relative signals for both reference images (T110R and T125R) are found to be 0.61 ± 0.02 in the heart region and 0.25 ± 0.01 in the abdomen region. These results are similar to those published.

Currently the algorithm does not take into consideration the gray level re-scaling parameters in the DICOM header; however, the incorporation of these parameters should not affect the implementation of the algorithm. Also, the current algorithm, which is written

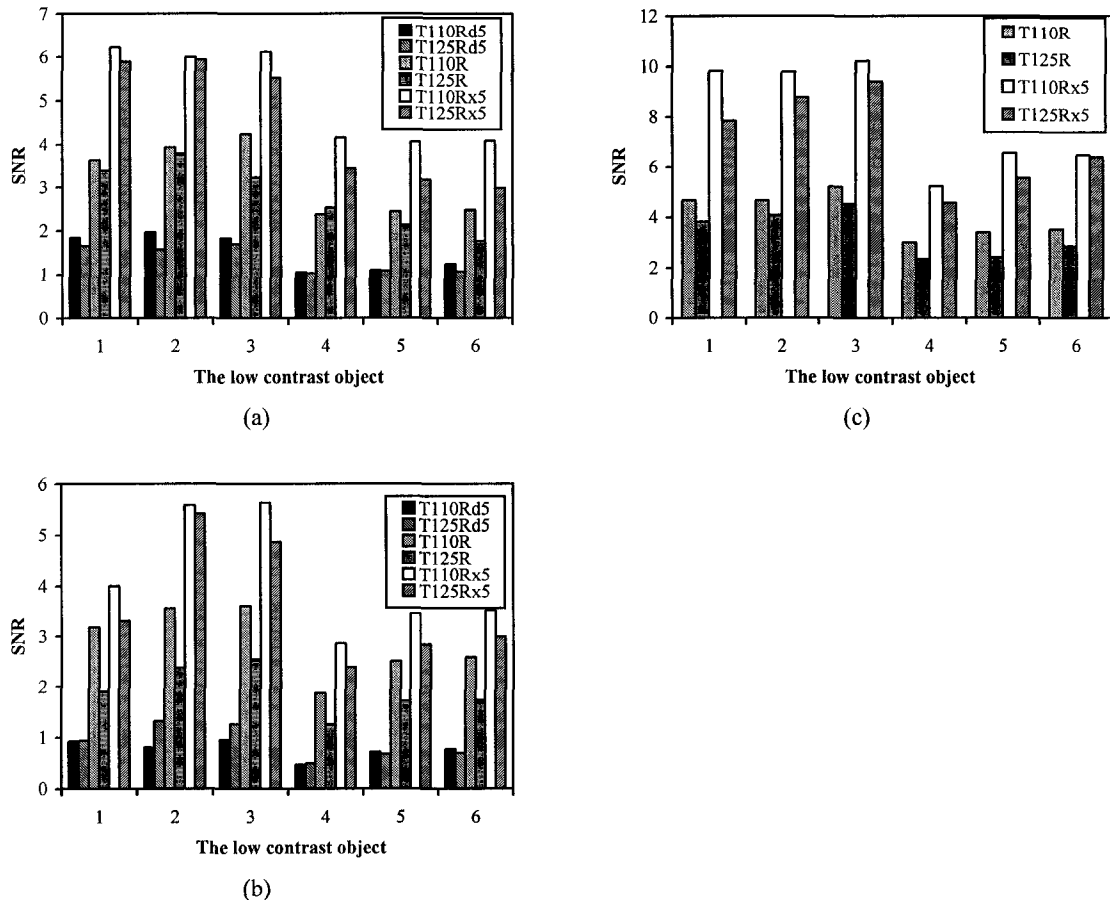


FIG. 7. The computed subject-to-noise ratio for the images acquired using different exposure techniques as stated in Table I. (a) SNR for the low contrast objects in the lung region. (b) SNR for the low contrast objects in the heart region. (c) SNR for the low contrast objects in the abdomen region. Due to the fact that no useful information is obtained from the abdomen region for the one-fifth reference mAs images, T110Rd5 and T125Rd5 SNR's are discarded in figure (c).

in MATLAB, requires 7–16 h of computation for each registration. Although slower, MATLAB is chosen due to the ease of coding. While this is manageable by running the algorithm overnight, a reduction in the operation time will be worthwhile. Fortunately, small scale testing of the algorithm coded in C has shown that a reduction in time by a factor of 10 or more is achievable. On top of this, the current algorithm runs on a 667 MHz Pentium III PC. Consequently, one would expect a fully optimized C version of the algorithm running on a Pentium 4 to complete the iterations in less than an hour for an image size of 3520 × 4280, or a reduction by a factor of 20 in time. This computational time, if achievable, should be acceptable since it is shorter than the duration of a typical QC examination in our facility.

V. CONCLUSION

In this work, an algorithm is proposed which can automatically detect and compute the SNR of the low contrast components in a digital chest phantom

radiograph. This algorithm provides an accurate, quantitative analysis of the selected objects, and eliminates the subjectivity inherent in evaluating low contrast objects in current testing procedures. Finally, this algorithm can be easily adapted to detect and compute the SNR of low contrast objects in the QC testing of other digital diagnostic modalities (such as fluoroscopy or CT), provided that sufficient edges can be acquired from the phantom images.

ACKNOWLEDGMENTS

This work is partly funded by a Province of Alberta Graduate Fellowship (A.K.). The authors would like to thank Dr. A. J. B. McEwan and Dr. S. Halls of the Cross Cancer Institution for the utilization of the Fuji radiographic system, as well as D. Bridgeman and M. Harden for the assistance in the acquisition of the radiographic images. The authors also wish to acknowledge the assistance of Eugene Mah in providing

some thoughtful insight with regards to SNR responses from CR imaging plates.

APPENDIX

For any transformation involving translation (T_x and T_y) and rotation of an angle θ about an arbitrary center of rotation (C_x and C_y), two types of transformations are possible: a translation followed by a rotation, or a rotation followed by a translation. For the first type of transformation, the transformation equations can be written as

$$\begin{aligned} x' &= (x + T_x - C_x) \cos(\theta) + (y + T_y - C_y) \sin(\theta) + C_x, \\ y' &= -(x + T_x - C_x) \sin(\theta) + (y + T_y - C_y) \cos(\theta) + C_y. \end{aligned} \quad (\text{A1})$$

Since all the transformation parameters (T_x , T_y , θ , C_x , and C_y) are constant for a given transformation, Eq. (A1) may be rearranged as

$$\begin{aligned} x' &= x \cos(\theta) + y \sin(\theta) \\ &\quad + (T_x - C_x) \cos(\theta) + (T_y - C_y) \sin(\theta) + C_x, \\ y' &= -x \sin(\theta) + y \cos(\theta) \\ &\quad - (T_x - C_x) \sin(\theta) + (T_y - C_y) \cos(\theta) + C_y, \end{aligned} \quad (\text{A2})$$

where the last three terms of both equations are constant. Therefore, one can define two constant terms:

$$\begin{aligned} t_x &= (T_x - C_x) \cos(\theta) + (T_y - C_y) \sin(\theta) + C_x, \\ t_y &= -(T_x - C_x) \sin(\theta) + (T_y - C_y) \cos(\theta) + C_y, \end{aligned} \quad (\text{A3})$$

and simplify Eq. (A2) to

$$\begin{aligned} x' &= x \cos(\theta) + y \sin(\theta) + t_x, \\ y' &= -x \sin(\theta) + y \cos(\theta) + t_y, \end{aligned} \quad (\text{A4})$$

which is Eq. (1).

Similarly for the second type of transformation, the transformation equations are

$$\begin{aligned} x' &= (x - C_x) \cos(\theta) + (y - C_y) \sin(\theta) + C_x + T_x, \\ y' &= -(x - C_x) \sin(\theta) + (y - C_y) \cos(\theta) + C_y + T_y, \end{aligned} \quad (\text{A5})$$

or

$$\begin{aligned} x' &= x \cos(\theta) + y \sin(\theta) - C_x \cos(\theta) \\ &\quad - C_y \sin(\theta) + C_x + T_x, \\ y' &= -x \sin(\theta) + y \cos(\theta) + C_x \sin(\theta) \\ &\quad - C_y \cos(\theta) + C_y + T_y, \end{aligned} \quad (\text{A6})$$

This time the last four terms of the equations are constant. Therefore if one let

$$\begin{aligned} t'_x &= -C_x \cos(\theta) - C_y \sin(\theta) + C_x + T_x, \\ t'_y &= +C_x \sin(\theta) - C_y \cos(\theta) + C_y + T_y, \end{aligned} \quad (\text{A7})$$

Eq. (A6) will simplify to

$$\begin{aligned} x' &= x \cos(\theta) + y \sin(\theta) + t'_x, \\ y' &= -x \sin(\theta) + y \cos(\theta) + t'_y. \end{aligned} \quad (\text{A8})$$

Again, this is similar to Eq. (1). Although the constant terms in Eqs. (A4) and (A8) are different, the same equation may be utilized for both types of transformation, provided that the quasitranslation parameters are fitted with the rotational angle (θ) simultaneously.

^{a)} Electronic-mail:

- ¹ E. Samei, J. A. Seibert, C. E. Willis, M. J. Flynn, E. Mah, and K. L. Junck, "Performance evaluation of computed radiography systems," *Med. Phys.* **28**, 361–371 (2001).
- ² X. J. Rong, C. C. Shaw, X. Liu, and M. R. Lemacks, "Comparison of an amorphous silicon/cesium iodide flat-panel digital chest radiography system with screen/film and computed radiography systems—A contrast detail phantom study," *Med. Phys.* **28**, 2328–2335 (2001).
- ³ D. P. Chakraborty and M. P. Eckert, "Quantitative versus subjective evaluation of mammography accreditation phantom images," *Med. Phys.* **22**, 133–143 (1995).
- ⁴ E. Samei, M. J. Flynn, and D. A. Reimann, "A method for measuring the presampled MTF of digital radiographic systems using an edge test device," *Med. Phys.* **25**, 102–113 (1998).
- ⁵ H. G. Chotas, C. E. Floyd, Jr., G. A. Johnson, and C. E. Ravin, "Quality control phantom for digital chest radiography," *Radiology* **202**, 111–116 (1997).
- ⁶ A. H. Baydush, W. C. Ghem, and C. E. Floyd, Jr., "Anthropomorphic versus geometric chest phantoms: A comparison of scatter properties," *Med. Phys.* **27**, 894–897 (2000).
- ⁷ E. Mah, E. Samei, and D. J. Peck, "Evaluation of a quality control phantom for digital chest radiography," *J. Appl. Clin. Med. Phys.* **2**, 90–101 (2001).
- ⁸ G. Borgefors, "Hierarchical chamfer matching: A parametric edge matching algorithm," *IEEE Trans. Pattern Anal. Mach. Intell.* **10**, 849–865 (1988).
- ⁹ J. Canny, "A computational approach to edge detection," *IEEE Trans. Pattern Anal. Mach. Intell.* **8**, 679–698 (1986).
- ¹⁰ R. C. Gonzalez and R. E. Woods, *Digital Image Processing* (Addison-Wesley, Reading, MA, 1992).
- ¹¹ T. Y. Zhang and C. Y. Suen, "A fast parallel algorithm for thinning digital patterns," *Commun. ACM* **27**, 236–239 (1984).
- ¹² E. R. Davis, *Machine Vision: Theory, Algorithms, Practicalities*, 2nd ed. (Academic, San Diego, 1997).
- ¹³ L. G. Brown, "A survey of image registration techniques," *ACM Comput. Surv.* **24**, 325–376 (1992).
- ¹⁴ J. B. Maintz and M. A. Viergever, "A survey of medical image registration," *Med. Image Anal.* **2**, 1–36 (1998).
- ¹⁵ J. Moseley and P. Munro, "A semiautomatic method for registration of portal images," *Med. Phys.* **21**, 551–558 (1994).
- ¹⁶ B. J. McParland and J. C. Kumaradas, "Digital portal image registration by sequential anatomical matchpoint and image correlations for real-time continuous field alignment verification," *Med. Phys.* **22**, 1063–1075 (1995).



American Association of Physicists in Medicine

One Physics Ellipse
College Park, MD 20740-3846
(301) 209-3350
Fax (301) 209-0862
<http://www.aapm.org>

March 28, 2003

Mr. Alex L.C. Kwan
5106-39B Avenue,
Edmonton, Alberta
Canada T6 1P1

Dear Mr. Kwan:

The American Association of Physicists in Medicine grants you permission to include the article "Automatic Quantitative Low Contrast Analysis of Digital Chest Phantom" in your dissertation.

Alexander L.C. Kwan, Larry J. Filipow and Lawrence H. Le et. al. Automatic Quantitative Low Contrast Analysis of Digital Chest Phantom.

Deputy Executive Director